Year : 2019

Wireless sensor networks for landslide monitoring: application and optimization by visibility analysis on 3D point clouds

Gracchi Teresa

Gracchi Teresa, 2019, Wireless sensor networks for landslide monitoring: application and optimization by visibility analysis on 3D point clouds

Originally published at : Thesis, University of Lausanne

Posted at the University of Lausanne Open Archive http://serval.unil.ch
Document URN : urn:nbn:ch:serval-BIB_E01C8F7D92077

Year : 2019

Wireless sensor networks for landslide monitoring: application and optimization by visibility analysis on 3D point clouds

Gracchi Teresa

Gracchi Teresa, 2019, Wireless sensor networks for landslide monitoring: application and optimization by visibility analysis on 3D point clouds

Originally published at : Thesis, University of Lausanne

Posted at the University of Lausanne Open Archive http://serval.unil.ch
Document URN : urn:nbn:ch:serval-BIB_E01C8F7D92077

UNIVERSITÀ DEGLI STUDI FIRENZE

UNIL | Université de Lausanne

International Doctorate in Civil and Environmental Engineering

Joint Ph.D. - Cycle XXXII

Wireless sensor networks for landslide monitoring: application and optimization by visibility analysis on 3D point clouds

Ph.D. Thesis

Presented at the

Faculty of Geosciences and Environment of the University of Lausanne

Department of Civil and Environmental Engineering of the University of Florence

by

Teresa Gracchi

To obtain the grade of

Ph.D. in Earth Sciences

Ph.D. in Civil and Environmental Engineering

Prof. Michel Jaboyedoff	Thesis director
Prof. Claudia Madiai	Thesis director
Prof. Nicola Casagli	Thesis co-director
Prof. Marco Barla	Expert
Prof. Marc-Henri Derron	Expert
Prof. Giovanni Gigli	Expert
Prof. Claudia Meisina	Expert
Prof. Claudio Borri	Coordinator

2016–2019

UNIL | Université de Lausanne
Faculté des géosciences et de l'environnement
bâtiment Géopolis bureau 4631

IMPRIMATUR

Vu le rapport présenté par le jury d'examen, composé de

Président de la séance publique :	M. le Professeur Christian Kull
Président du colloque :	M. le Professeur Christian Kull
Directeur de thèse :	M. le Professeur Michel Jaboyedoff
Co-directrice de thèse :	Mme la Professeure Claudia Madiai
Expert interne :	M. le Docteur Marc-Henri Derron
Expert externe :	M. le Professeur Giovanni Gigli
Expert externe :	M. le Professeur Marco Barla
Experte externe :	Mme la Professeure Claudia Meisina

Le Doyen de la Faculté des géosciences et de l'environnement autorise l'impression de la thèse de

Madame Teresa GRACCHI

Titulaire d'un
Master en sciences de la Terre
De l'Université de Florence

intitulée

Wireless sensor networks for landslide monitoring: application and optimization by visibility analysis on 3D point clouds

Lausanne, le 21 avril 2020

Pour le Doyen de la Faculté des géosciences et de l'environnement

Professeur Christian Kull

Table of contents

Acknowledgments

First of all, I would like to thank Prof. Nicola Casagli Prof. and Claudia Madiai for giving me the opportunity and the tools to undertake and complete my PhD program. Particular thanks are directed also to Prof. Giovanni Gigli for its constant patience and support.

During my PhD I had the chance to work together with the *Institute des sciences de la Terre de la Faculté des Géosciences et de l'Environnement de l'Université de Lausanne*, in Switzerland. I cannot possibly tell how much of an exceptional experience that was. I will always feel indebted to Prof. Michel Jaboyedoff for making it happen. Your teaching and advice allowed me to greatly improve both my competences and my attitude to research.

This thesis is the result of a 3-year doctoral program, during which I had the privilege to work and interact with many people. It is difficult to describe in a few words the credit that each one of them deserves, so may I be forgiven if I will not list them all in these acknowledgements.

All the above cannot be even closely compared to the gratitude that I owe to my parents and to the dear family of my sister Anna. Thank you for giving me full freedom to explore my passion and pursue my dreams, no matter how crazy they are. Without your unconditional support, guidance and love I would not have come this far.

Finally, my gratefulness goes to my boyfriend for believing in me and motivating me time and time again. I cannot thank you enough for everything you did for me, may your love and encouragement always be there.

Teresa

List of Abbreviations

EWS	Early Warning System
HPR	Hidden Point Removal
LOS	Line Of Sight
MN	Master Node
NLOS	Non-Line Of Sight
PAs	Priority Areas
PCT	Point Cloud Terrain
PCV	Point Cloud Vegetation
PI	Performance Index
ROI	Region Of Interest
ROI_{P1}	Region Of Interest for Point 1
SDS-TWR	Symmetric Double-Sided Two-Way Ranging
SN	Slave Node
SSN	Super-Slave Node
TOF	Time Of Flight
TRL	Technology Readiness Level
UWB	Ultra-Wide Band
WSN	Wireless Sensor Network

Abstract

Occurring in many geographical, geological and climatic environments, landslides represent a major geological hazard. In landslide prone areas, monitoring devices associated with Early Warning Systems are a cost-effective means to reduce the risk with a low environmental and economic impact, and in some cases, they can be the only solution. In this framework, particular interest has been reserved for Wireless Sensor Networks (WSNs), defined as networks of usually low-size and low-cost devices denoted as nodes, which are integrated with sensors that can gather information through wireless links.

In this thesis, data from a new prototypical ground instability monitoring instrument called Wi-GIM (Wireless sensor network for Ground Instability Monitoring) have been analysed. The system consists in a WSN made by nodes able to measure their mutual inter-distances by calculating the time of flight of an Ultra-Wide Band impulse. Therefore, no sensors are implemented in the network, as the same signals used for transmission are also used for ranging. The system has been tested in a controlled outdoor environment and applied for the monitoring of the displacements of an actual landslide, the Roncovetro mudflow in Central Italy, where a parallel monitoring with a Robotic Total Station (RTS) allowed to validate the system. The outputs are displacement time series showing the distance of each couple of nodes belonging to the same cluster. Data retrieved from the tests revealed a precision of 2–5 cm and that measurements are influenced by the temperature. Since the correlation with this parameter has proved to be linear, a simple correction is sufficient to improve the precision and remove the effect of temperature. The campaign also revealed that measurements were not affected by rain or snow, and that the system can efficiently communicate up to 150 m with a 360° angle of view without affecting precision. Other key features of the implemented system are easy and quick installation, flexibility, low cost, real-time monitoring and acquisition frequency changeability.

The comparison between Wi-GIM and RTS measurements pointed out the presence of an offset (in an order that vary from centimetric to decametric) constant for each single couple, due mainly to the presence of obstacles that can obstruct the Line Of Sight (LOS). The presence of vegetation is the main cause of the non-LOS condition between two nodes, which translates in a longer path of the signals and therefore to a less accurate distance measurements. To go further inside this issue, several tests have been carried out proving the strong influence of the vegetation over both data quantity and quality. To improve them, a MATLAB tool (R2018a, MAthWorks, Natick, MA, USA) called WiSIO (Wireless Sensor network Installation Optimizer) has been developed. The algorithm finds the best devices deployment following three criteria: (i) inter-visibility by means of a modified version of the

Hidden Point Removal operator; (ii) equal distribution; (iii) positioning in preselected priority areas. With respect to the existing viewshed analysis, the main novelty is that it works directly with 3D point clouds, without rendering them or performing any surface. This lead to skip the process of generating surface models avoiding errors and approximations, that is essential when dealing with vegetation.

A second installation of the Wi-GIM system has been therefore carried out considering the deployment suggested by WiSIO. The comparison of data acquired by the system positioned with and without the help of the proposed algorithm allowed to better comprehend the effectiveness of the tool. The presented results are very promising, showing how a simple elaboration can be essential to have more and more reliable data, improving the Wi-GIM system performances, making it even more usable in very complex environments and increasing its flexibility.

The main left limitation of the Wi-GIM system is currently the precision. Such issue is connected to the aim of using only low-cost components, and it can be prospectively overcome if the system undergoes an industrialization process. Furthermore, since the system architecture is re-adaptable, it is prone to enhancements as soon as the technology advances and new low cost hardware enters the market.

1. Introduction

Landslides are frequent and widespread geomorphological phenomena and have an enormous impact on society, economics, and environment (Guzzetti et al., 2003). They can be defined as any mass of earth material (soil or rock) displaced under the action of the gravity. In recent times, factors such as excessive land use, uncontrolled urbanization, and improper urban planning have led to an alarming worldwide increase in the frequency of landslides occurrence (Nadim et al., 2006; Petley, 2012).

In landslide prone areas, risk mitigation must often face problems related to economic resources, environmental impact and logistic issues. This is particularly true for structural countermeasures, which aim at minimising the risk by reducing the probability of failure (bolts, anchors, piles etc.), by preventing the landslide from reaching the elements at risk (barriers, ditches, retaining walls etc.) or by reinforcing existing buildings. Moreover, these defensive techniques are often not adequate to counteract the size and rapidity with which slope failures commonly occur and are also limited by economic/logistical constraints that may not be possible to overcome.

Monitoring devices associated with Early Warning Systems (EWSs) are an alternative cost-effective means to reduce the risk with a low environmental and economic impact. In some cases, they can even be the only solution, for instance when a landslide is so large that it cannot possibly be stabilized, when in an area there are too many unstable slopes and there are not enough financial resources to take care of them all individually, or when the residual risk after remediation works is still unacceptable. Indeed, sometimes the timely evacuation of the dangerous area remains the only viable procedure for protecting vulnerable communities (Kilburn and Petley, 2003). According to Medina-Cetina & Nadim (2008) EWSs are defined as “monitoring devices designed to avoid, or at least to minimize the impact imposed by a threat on humans, damage to property, the environment, or/and to more basic elements like livelihoods”, and include the following activities: monitoring, data analysis/forecasting, dissemination of alarms, and definition of response actions (Casagli et al., 2017b; Intrieri et al., 2012; Figure 1). All of these need to be calibrated and contextualized in the frame of the studied scenario. Implementing an EWS depends indeed on (i) the type of landslide; (ii) the disaster scenarios considered; (iii) the degree of awareness of the stakeholders, including populations; (iv) the allocated resources (e.g. budgetary, human).

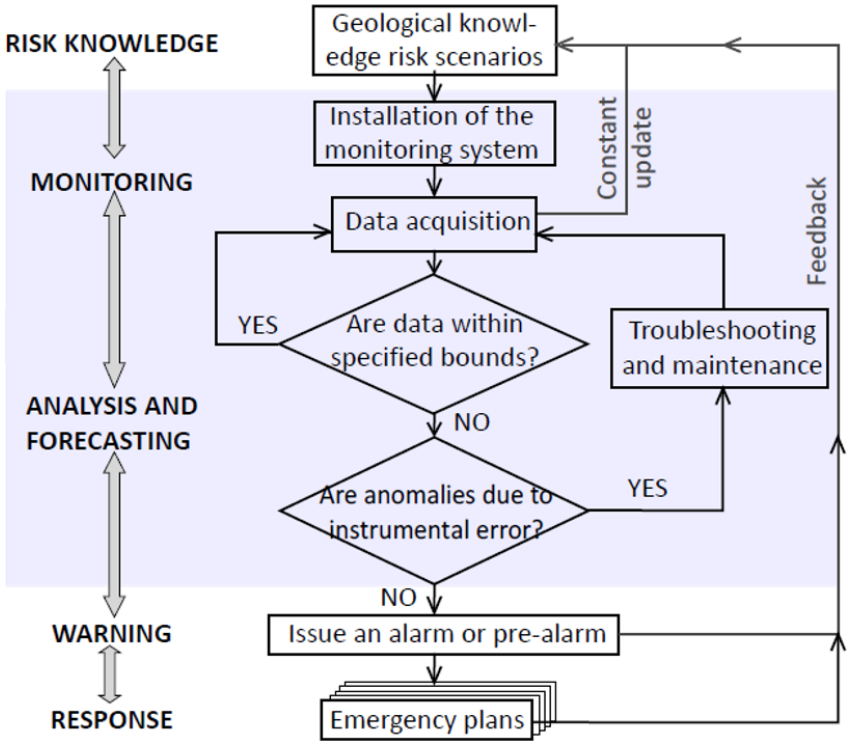

Figure 1. Flow chart of the activities of the implementation and operation of an EWS. The blue box indicates the action linked to the monitoring system (after Casagli et al., 2017b).

Landslide monitoring is therefore a key component of landslide hazard assessments, with the main objective of providing early warning of an impending failure where lives, communities, or infrastructure may be at risk (Eberhardt, 2012). The monitoring instruments typically include extensometers, borehole inclinometers, tiltmeters, topographic instruments (Petley at al., 2005), satellite interferometry (Tofani et al., 2013), Ground-based interferometric Synthetic Aperture Radar (GB-InSAR) (Barla et al., 2016; Farina et al., 2011; Lombardi et al., 2017) and robotic total stations (RTSs) (Giordan et al., 2013; Petley et al., 2005) (Figure 2).

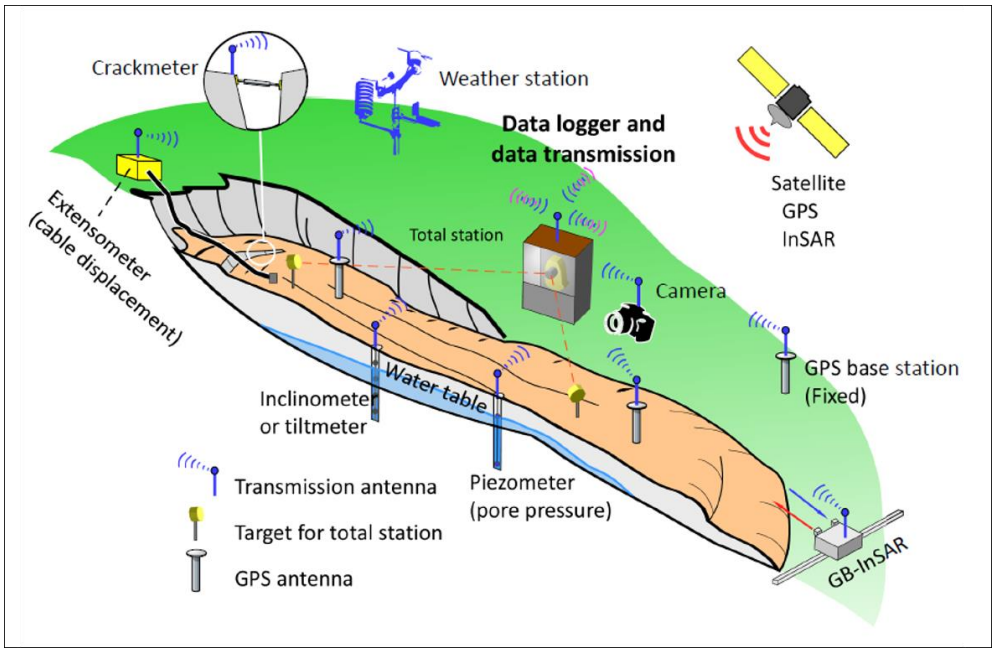

Figure 2. Main components of an Early Warning System (after Casagli et al., 2017b).

Recently, Wireless Sensor Network (WSN) technology has been often used to support environmental detection, monitoring and prediction, thanks to its capability of real-time monitoring of natural phenomena and data extraction (Estrin et al., 2002). Some of the main advantages of the adoption of WSN for environmental real-time monitoring are fast and easy deployment, low maintenance, scalability and adaptability to different scenarios. On the other hand, some drawbacks are represented by memory, power and throughput, that are in general too scarce, limiting the efficiency of the systems (Mucchi et al., 2018).

Focusing on the use of WSNs for landslide monitoring (Teja et al., 2014), several parameters, such as temperature and humidity, are gathered by multiple sensors and sent to a control centre; however, sensors are not directly used to measure the ground movement. New methodologies for ground instability measurement based on distributed and connected low cost wireless sensors have been proposed and are becoming more and more widespread (e.g. Arnhardt et al., 2007; Castillo et al., 2004; Chen et al., 2013; Intrieri et al., 2018).

In this context, an innovative WSN (Wi-GIM, standing for Wireless sensor network for Ground Instability Monitoring) based on the adoption of Ultra-Wide Band (UWB) technology for the 3D accurate superficial monitoring of ground deformations has been developed. The main idea is to detect the surface movements by acquiring the position of many sensor nodes (organized in clusters) distributed over the monitored area to perform real-time ground displacement measurements to

provide early warning. The system has been implemented in the framework of a Life+ European Program, and the first part of this thesis is devoted to the analysis of the acquired data.

Working with UWB WSNs means that the Line Of Sight (LOS) cannot be neglected. As a matter of fact, an information is properly transmitted if transmitter and receiver stations are in view of each other without any obstacle. For this purpose, the LOS of each emitting sensor is an important issue to consider when positioning two or more receivers. Depending mainly on their wavelength and the characteristics of the material to cross, waves can in fact follow several behaviours, and problems connected to non-LOS can lead to the absence of data or inaccuracy in measures, due to delay in the arrival time or multiple reflections effect (Alwan and Mahmood, 2015; Dardari et al., 2009; Schroeder et al., 2007; Wang et al., 2003). Indeed, several tests concerning vegetation have been carried out on the Wi-GIM system, demonstrating how the non-LOS condition (mainly due to vegetation) can cause a delay in the signal which can lead to an error in the distance evaluation as well as data loss, compromising the reliability of the monitoring system (Intrieri at al., 2018). For these reasons, an analysis of the inter-visibility is essential to correctly place and install a WSN requiring LOS.

With this purpose, in the second part of this thesis, an algorithm able to find the best locations to install the sensors of a WNS requiring free LOS is presented. The aim was to develop an easy algorithm that works directly with 3D point clouds instead of Digital Elevation Models (DEMs) or Digital Surface Models (DSMs), that is to say without reconstructing any surface, avoiding approximations.

The Wi-GIM system has been installed twice in the Roncovetro landslide (Emilia-Romagna region, Italy): at first, in 2016, following traditional patterns for its positioning; after, in 2019, installing the sensors in the points determined by the algorithm developed as part of this study. The comparison between data acquired from the two configurations allows to evaluate the performance of the proposed method on a real serviceable case, showing promising results.

Moreover, during the monitoring activities, several analyses have been carried out to evaluate the accuracy and feasibility of the Wi-GIM system, mostly thanks to a parallel monitoring made with a Robotic Total Station (RTS). Results points out the effectiveness of the network especially in emergency conditions, due mainly to the rapid, economic and easy installation, the flexibility of the system and the real-time monitoring.

1.1 Overview of the existing landslide monitoring techniques

Landslide monitoring is essential for the recognition of landslide occurrence as well as for early warning. A large variety of techniques is available for the monitoring of landslides, ranging from classical geodetic methods providing a local measurement of the movements to advanced laser and radar methods providing a global image of the displacements.

There are three major categories of landslide monitoring. The first one is field observations; a conventional monitoring method in which geologists measure the changing features at regular time intervals in the field. The method has a limitation in providing information on impending landslides or slope failures, because measuring changes at the site in a short time interval such as a minute or an hour scale is impossible (Chae et al., 2017). The second category includes in situ ground-based observation of slope displacement, using various instruments as extensometers, laser distance meters, GPS, total stations, terrestrial laser scanner, ground based Interferometric synthetic aperture radar (GB-InSAR), seismometers and others. The third category consists of airborne and spaceborne techniques including acquisition and analysis of satellite images, photogrammetry and synthetic aperture radar (SAR) interferometry (Figure 3).

Among these techniques, laser distance meters, total stations and Global Positioning Systems (GPS) receivers allow to precisely locate the position of targets installed within a landslide over time (Duranthon, 2000). These methods are also commonly used to georeference the images acquired with high resolution cameras, light detection and ranging (LiDAR) and radar systems.

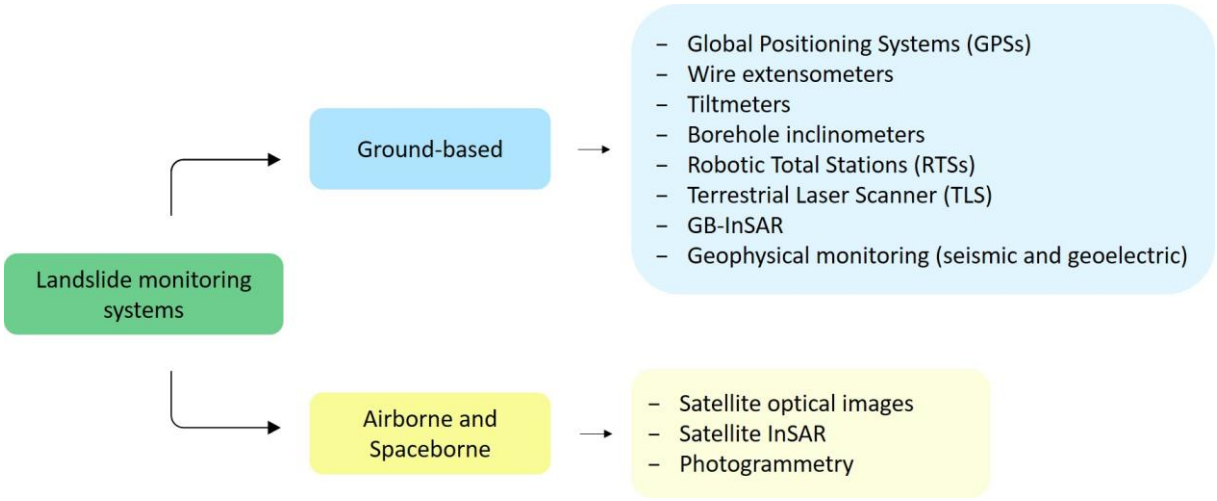

Figure 3. Some of the most common landslide monitoring systems.

1.1.1 Ground-based monitoring techniques

In situ ground-based monitoring observes slope displacement (as well as other parameters connected to the investigated movement) trough devices that are installed in boreholes and on the surface of potential landslide sites. The instruments can measure parameter changes in a regular time interval or in real time.

The Global Positioning System (GPS), a radio navigation, timing and positioning system with a wide set of applications, is one of them. By tracking the electromagnetic waves that the GPS satellites are sending continuously, the system can obtain the antenna position (longitude, latitude, and height). The use of the phase measurements allows to determine the relative positions of points located as far as several hundred kilometres apart with an accuracy of 2–5 mm in the X–Y plan and 5–10 mm in altimetry. This accuracy allows the fast detection of weak displacements and, thus the survey of the temporal evolution of natural hazards (volcanoes, tectonic faults, ice glaciers, landslides) (Bock et al., 1990; Dixon et al., 1991; Gili et al., 2000; Lowry et al., 2001). Displacements are computed comparing repeated GPS surveys (Squarzoni et al., 2005). Its application is mainly suitable for the monitoring of slow-moving landslides and the pre-failure stage rockslide. In addition, due to its high accuracy and precision, GPS offers advantages over conventional terrestrial method, e.g. measurements can be taken during night or day and under different weather conditions. However, the accuracy of GPS relative positioning depends on the geometric distribution of the observed satellites: at least four satellites must be in view with the receiver station.

Other ground-based monitoring devices are wire extensometers: instruments which give punctual and one-dimensional displacement information that can be installed on the ground surface (Bonnard and Steinmann, 1990) or into a borehole (Angeli et al., 1988), giving an automatic and continuous recording of ground displacement. In any case, the extensometer integrates the displacement occurred between two points, one fixed on a stable zone outside the landslide area (in superficial extensometers) or below the landslide mass (in borehole extensometers), and the other one located in the ground surface of the moving mass. Due to its simplicity, low cost and excellent performance, wire extensometers have been applied to a large number of landslides (Angeli et al., 1988; Corominas et al., 2000; Corominas et al., 2005). Wire extensometer readings cannot be properly interpreted unless the general pattern of the movement is known; indeed, there is no direct relationship between the displacements of the landslide and the displacements of the wire extensometer. Moreover, these instruments give punctual and one-dimensional displacement information, are quite vulnerable and their installation requires skilled personnel.

An instrument that has mainly been used for relative displacement measurements within the deformable object and its surroundings is the tiltmeter. The measurement of tilt is usually understood as the determination of a deviation from the horizontal plane (Savvaidis, 2003). Tiltmeters are instruments that can measure degrees of rotation and are usually based on electrolytic level sensors. A data logger automatically records the output of a tiltmeter at sampling periods, which can be freely adjusted by the user (García et al., 2009). The same limitations previously explained for the extensometers are still valid. Moreover, the inclination variation or angular acceleration are often too low and are covered by the instrument noise. The measure is taken only at one place and in one depth per instrument.

Conversely, borehole inclinometers are geotechnical instruments used to measure horizontal displacements along various points on a borehole. The device consists of a series of gravity sensor transducers (uniaxial or biaxial) positioned at intervals along the borehole axis or in the failure surface (Stark and Choi, 2007). The main advantages include rapid automatic data logging and real-time monitoring, but they need a borehole that must reach and go further the sliding surface (sometimes up to several meters in depth), with consequent high cost, long installation time, and logistic problems (Dunnicliff and La Fonta, 2001; Machan and Bennett, 2008).

Robotic Total Stations (RTSs) enable measurements of angles and distances to target-prisms located on the moving mass, making it possible to retrieve the absolute position of a target and, therefore, its displacement. With respect to a traditional optical-mechanical theodolite, it has an electronic distance meter and a computer for storing and calculating data. Modern systems can operate automatically with high acquisition frequency providing relative positioning in almost real-time to an accuracy of ±0.05 mm over distances of several meters and ±1–2 mm over distances of several hundred meters (Giordan et al., 2013; Liu et al., 2004; Mantovani et al., 2000; Petley et al., 2005; Rizzo and Leggeri, 2004). The distance is performed through the electronic distance meter embedded within the total station. A laser beam is generated by the telescope, hits the targeted point and is reflected. The instruments record the time occurred for the light pulse to reach the target and calculates the travelled distance accordingly. Albeit total station systems are very precise and reliable and provide 3D coordinate information of the measured points; one of the main disadvantages is the requirement to have an unobstructed Line Of Sight (LOS) between the instrument and the targeting prism (Savvaidis, 2003).

In opposition to the above mentioned conventional and point-based surveying techniques, Terrestrial Laser Scanner (TLS) provides information over the entire landslide area; enabling a more complete

understanding of the landslide displacements. A laser (standing for Light Amplification by Stimulated Emission of Radiation) is a device that produces and emits a beam of highly collimated, directional, coherent and in-phase electromagnetic radiation. These systems can be used for the acquisition of large amounts of 3D information of the terrain at an extremely fast recording rate (Jaboyedoff et al. 2012). If the sensor is ground-based, then instruments takes the name of Terrestrial Laser Scanner (TLS), conversely, we talk about Aerial Laser Scanner (ALS) when it is airborne-based. A laser scanner consists of a transmitter/receiver of laser beam and a scanning device. Two different methods for range determination are possible (Wehr and Lohr 1999): phase and pulse method. While the first one is characterized by a more accurate range determination and suffers from a limited range (Petrie and Toth 2008), the latter allows a greater range. For this reason, the pulse method is the one usually used for Earth surface observations, including landslide studies (Baltsavias 1999; Wehr and Lohr 1999). The result of a scan is a 3D point cloud representing the surveyed surface, expressed in polar coordinates with respect to the centre of the apparatus (range r, horizontal angle θ, vertical angle ϕ). The produced point cloud is directly the 3D digital model of the scanned object and founded several applications for landslides mapping and characterisation. Rowlands et al. (2003) used a TLS -DEM to map the limits of a shallow landslide; Dunning et al. (2009) analysed a rockslide scar by TLS and estimated its volume; Jaboyedoff et al. (2009) demonstrated that shallow landslides in river banks are characterized by spherical failure surfaces. TLS surveys has also been exploited on rockfalls and rockslides for the extraction of 3D rock mass properties (orientation, spacing, persistence, roughness of discontinuities) (Gigli and Casagli, 2011; Jaboyedoff et al., 2007). Finally, landslide displacements can be efficiently monitored by multi-temporal TLS acquisitions computing the distance between matching points in two TLS point clouds, as proposed in several studies (Jaboyedoff et al., 2009; Oppikofer et al., 2009; Pesci et al., 2011; Teza et al., 2007).

While monitoring by means of multi scan acquisition requires manual processing (i.e. the distance evaluation), ground-based interferometry (GB-InSAR) is a remote sensing technique that allows the real time determination of 2D deformation maps with high accuracy automatically. One of the great advantages of this technique is that measurements of the surface displacements are carried out remotely, being helpful for the observation of the ongoing phenomena as well as for checking the efficiency of consolidation interventions (Atzeni et al., 2015; Romeo et al., 2015). GB-InSAR is an interferometric technique based on the synthetic aperture radar (SAR) technique, similar to those used on satellites, but implemented in a mobile system with a terrestrial platform. In the last years this technique has been demonstrated as a reliable tool to monitor slope instability. Luzi (2010) presented an extensive literature about the working principle of this instrument and some of its applications.

Recently it has been shown that GBInSAR can be used in several geological contexts as well as with new approaches (Barla et al., 2017; Barla et al., 2010; Casagli et al., 2010; Farina et al., 2013). Moreover, it is very useful for monitoring of wide areas since it is suitable to cover long distances (Casagli et al., 2010; Tapete et al., 2012). However, only the component of displacement along the line of sight is measured, shadow areas cannot be detected, vegetation cover and atmospheric disturbance negatively influence the measurements, and the cost of the apparatus is very high.

Some of the ground-based techniques allow to measure geophysical parameters, e.g. the seismic and the geoelectrical monitoring. Concerning the landslide geoelectrical monitoring, it can be performed by means of three different techniques: electrical resistivity tomography, self-potential and induced polarization. The Electrical Resistivity Tomography (ERT) technique, based on the measurement of the electrical resistivity values and their spatial distribution in the subsoil, is an active method largely applied in order to investigate landslide areas (Godio et al., 2006; Lapenna et al., 2005; Meric et al., 2005; Pazzi et al., 2018). This technique provides useful information both on the lithostratigraphic sequences and the geometry of the landslide body (lateral extension and thickness), identifying the sliding surfaces between the slide material and the underlying bedrock, and individuating high water content areas (Perrone et al., 2014). Self-potential (SP) technique is applicable for the monitoring of underground fluid motion based on the electro-kinetic effect. The method (defined as a passive one) measures the presence of naturally occurring charges in the Earth surface, primarily streaming potentials and electrochemical potentials, which are measured between pairs of electrodes to create areal maps of variation in self-potentials. In the context of landslides, this is used to determine areas of subsurface flow within the subsurface material (Witheley et al., 2018). The Induced Polarization (IP) is a phenomenon stimulated by an electric current, observed as a delayed response to voltage in natural materials (Sumner, 1976). By establishing an electrical current flow through the electrodes A and B on the surface, a primary potential difference is established (Martins et al., 2016). This parameter could eventually provide information on changes in pore geometry due to deformations of the landslide body. Although Auken et al. (2006) considered IP as a possibly emerging method, this technique has been applied on landslides quite rarely (Jongmans and Garambois, 2007).

In recent years, seismic monitoring of active landslides detected a variety of seismic signals triggered by the unstable slope. Seismic monitoring appears therefore as a promising approach to complement surveillance and early warning systems of active landslides. In this framework, many researchers are focusing on the use of seismic sensors (e.g. seismometers, geophones, accelerometers, acoustic emission transducers) to monitor passively potential events. The extent of the investigated area varies from some centimetres to thousands of kilometres, depending on the magnitude and depth of the

events, the possible attenuation of the seismic waves travelling through the material, the type of seismic devices and the design of the seismic array. The technique founded numerous applications in rock cliffs (Amitrano et al., 2005; Feng et al., 2019; Gracchi et al., 2017; Kolesnikov et al., 2003); fracture processes in hard rocks (Brückl et al.,, 2006a; Roth et al., 2006; Spillmann et al., 2007); and debris flows (Itakura et al., 2005; Mainsant et al., 2012). On the other hand, for mass movements developed in soft rocks such as mudslides, the high attenuation of the seismic waves due to the nature of the material generally does not allow the use of seismic monitoring.

1.1.2 Airborne and spaceborne monitoring techniques

Airborne and spaceborne monitoring systems are widely used in the field landslides, especially dealing with large volumes of mobilised material. Among them, the most common are satellite optical, satellite radar, photogrammetry and aerial laser scanner.

Satellite images in the optical region with high spatial resolution are used for producing landslide inventory maps and for mapping factors related to the occurrence of landslides such as surface morphology, structural and lithological properties, land cover, and temporal changes of these factors (Fiorucci et al., 2011; Hervás et al., 2003; Savvaidis, 2003; Weirich et al., 2007). Data from satellite images are used in addition to aerial photos or as a single tool, due also to their low-cost in case of regional or national scales compared to other techniques. The big advantage of satellite-based remote sensing is the capability to repeat observations, which results in more frequent update of information on landslide characteristics compared to the conventional data sources. The method has been used for measuring long-term landform evolution of both rock glaciers and landslides from multitemporal digital elevation models (DEM) derived from sequential photo (e.g. Brunsden and Chandler, 1996; Kääb et al., 1997). Moreover, differencing of multi-temporal DSMs generated from satellite images can be used to estimate involved volumes and/or vertical surface settlements. As a lack, only extremely large landslides can be identified directly, and the landslide susceptibility of an area can be only determined indirectly from some of the features that are identifiable at small scales (Savvaidis, 2003).

Another spaceborne technique increasingly used for landslides monitoring purposes is the SAR (Synthetic Aperture Radar) system, which sends radar pulses to the ground and measures both the amplitude and the phase of the backscattered signal. A SAR image is indeed composed of pixel characterized by amplitude and phase values. Phase values of a single SAR image partly depends on the sensor-target distance and this is the key element to detect ground displacement. SAR Interferometry is the technique focused on the measure changes of signal phase over time through the analysis of at least two SAR images (Casagli et al., 2017a; Fruneau et al., 1996; Singhroy et al., 1998). A suitable method to exploit phase variation could be done indeed considering only two radar images, (Bamler and Hartl, 1998; Rosen et al., 2000). However, since the use of two single images could lead to geometrical and temporal decorrelation (Berardino et al., 2002), usually the Multitemporal Interferometric Techniques (MIT) approaches is preferred (Ferretti et al. 2001; Crosetto et al, 2016). In the past years, several MIT approaches have been developed. Between them, the signal analysis of a network of coherent radar targets (Permanent Scatterers, PS) allows to estimate occurred displacement, acquisitions by acquisition. Line Of Sight (LOS) deformation rate can be estimated with

an accuracy theoretically better than 0.1 mm/yr (Casagli et al., 2017a). In the field of landslide investigations the potential of SAR data has been exploited at different scales: from national (Adam et al., 2011) to regional (Ciampalini et al. 2016; Meisina et al., 2008;) slope (Frodella et al., 2016) and building scale (Bianchini et al., 2015; Ciampalini et al., 2014; Nolesini et al., 2016), as well as in different phases of landslide response (Canuti et al., 2007). On the other hand, significant difficulties have been found to use this technique as an effective and operational tool in emergency management situations due to the acquisition parameters of the current satellite SAR missions, especially in terms of temporal coverage and incidence angle.

Photogrammetric techniques have been extensively used in determining ground movements, especially with the development of Unmanned Aerial Vehicle (UAV) (Colomina et al., 2014; Rossi et al., 2018). The main advantages of using photogrammetry are the reduced time of fieldwork; simultaneous three-dimensional coordinates; the huge number of points that can be monitored (Brückl et al., 2006b; James et al., 2012; Savvaidis, 2003). The technique consists in the extraction of three-dimensional measurements from two-dimensional data (i.e. images). The final products are mainly DEM, DSM, 3D point clouds and orthoimages. The comparison of the above mentioned outputs acquired in different times is useful for monitoring purposes (Bitelli et al., 2004; Cardenal et al., 2008; Mora et al., 2003; Rossi et al., 2017), since the more recent photographs can be compared with old ones to examine the progressive development of slides. The accuracy of photogrammetric point position determination has been much improved in last years together with the advancement of high resolution cameras, making it attractive for high accuracy deformation measurements.

The use of airborne Light Detection and Ranging (LiDAR), also called Airborne Laser Scanning (ALS), for topographic mapping is rapidly becoming a standard practice for landslide investigations (Ardizzone et al., 2007; Corsini et al., 2007; Eeckhaut et al., 2007; Xiong et al., 2018), also due to its ability to measure terrain surface elevations beneath a vegetated canopy (Glennie et al., 2013; Wang, 2013). Duel mainly to the high costs, this technique is used mainly for landslides modelling, but it can be also used for monitoring purposes. Multi-temporal ALS surveys have indeed become indeed a method for the detection of mass movements and the monitoring of land surface deformation processes (DeLong et al., 2012; Mora et al., 2018). As discussed in Shrestha et al. (1999) and Montealegre et al. (2015), depending on many issues, the accuracy of ALS measurements could range from a couple of decimetres to over one meter for large-scale topographic mapping applications. ALS permits an improvement in the landslide inventory mapping (Borlat et al. 2007), but the processing still requires significant experience and manual efforts to produce highly accurate ground surface measurements (Xiong et al., 2018).

1.2 Wireless Sensor Networks

With the development of Micro-Electro-Mechanical Systems (MEMS) technology, which has facilitated the development of smart sensors, Wireless Sensor Networks (WSNs) have gained worldwide attention (Yick et al., 2008). They can be defined as networks of devices (also called nodes) that can communicate the information gathered from a monitored field by means of wireless links (Figure 4). These sensors are low size, with limited processing and computing resources, and low cost compared to traditional sensors (Estrin et al., 2002).

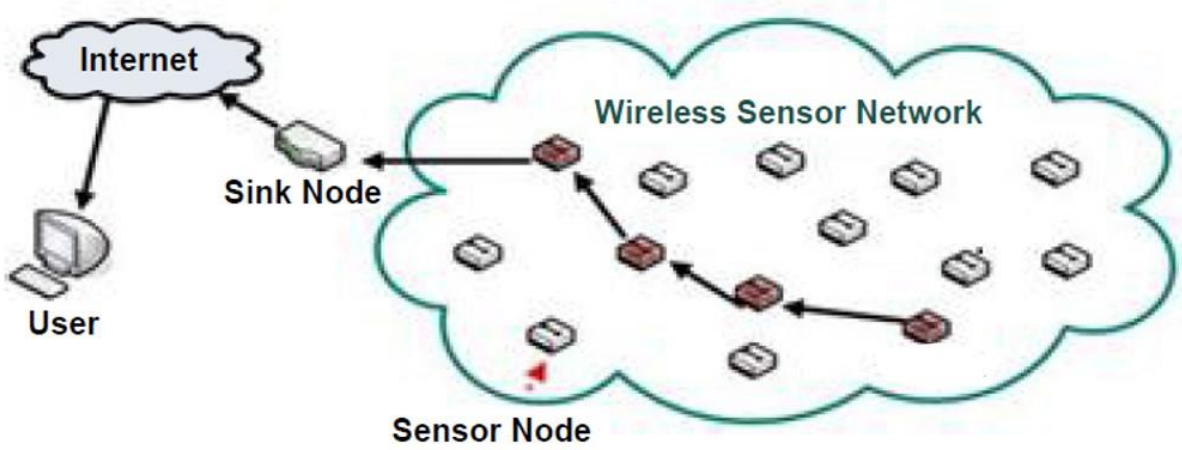

Figure 4. Schematic structure of a Wireless Sensor Network. Modified after Khara (2017).

WSN technology has the capability to quickly capture, process, and transmit data real-time (Intrieri et al., 2018). After their deployment in the environment, wireless sensors create a network by inter-connecting to each other, with the advantage of being highly flexible. Sensors can indeed be distributed as needed and adapted to the environment.

The use of WSN dates back to the Cold War, when the USA developed a system of acoustic sensors to place on the ocean bottom as a sound surveillance to detect and track Soviet submarines (Bhardwaj et al., 2014). Since then, they found application in several fields, e.g. robotics, domestic, military, health care, environmental and as traffic detectors (Figure 5), as explained in detail in Akyildiz et al. (2002).

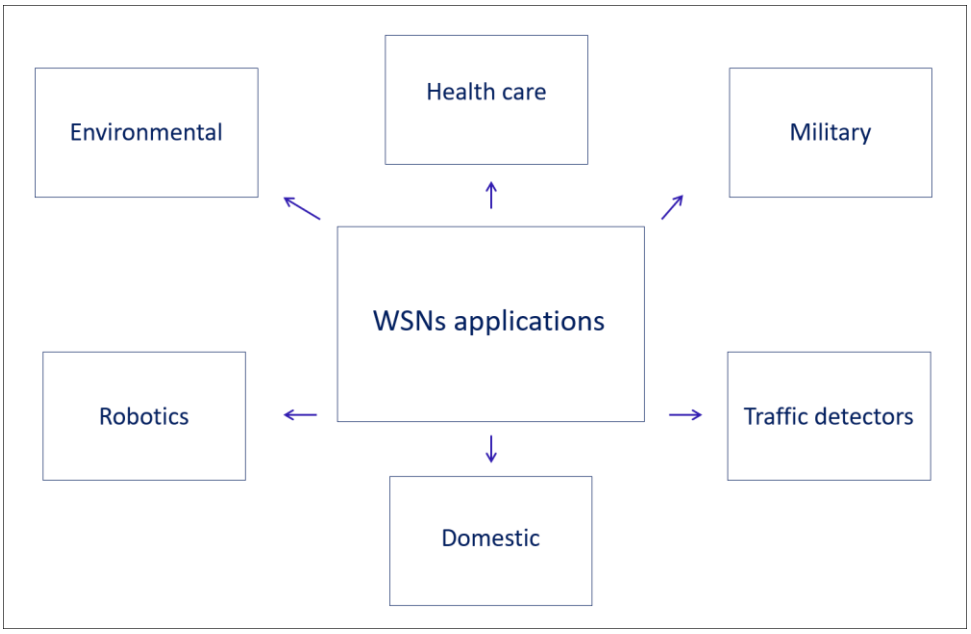

Figure 5. Some Wireless Sensor Networks applications.

In recent years, WSNs have been employed in engineering geology, with the aim to help in preventing the millions of the losses due to natural hazard. In particular, they are considered a powerful tool for monitoring natural phenomena in hostile and remote environments as for example glaciers (Martinez et al., 2004), active volcanoes (Werner-Allen et al., 2006) and landslides (Bhardwaj et al., 2014; Cho et al., 2008; Giorgetti et al., 2016; Sheth et al., 2007), as confirmed by the increasing worldwide interest in this field (Rosi et al., 2011).

Wireless transmission permits to interpret data from any remote location in order to perform a real-time hazard assessment. Moreover, these systems can generally acquire data with variable rates: the frequency can be modified anytime according to the criticality level reached by the monitored phenomenon at a certain time. This fulfils an important need for real-time monitoring, especially in hazardous or remote conditions. In this framework, WSNs can play a great role for landslide monitoring. The choice of the sensors used within the network depends on the parameters to measure, their variability, the required accuracy (function of the characteristics of the monitored phenomenon) and on the network compatibility to the site, with respect to energy efficiency. This technology can be in fact employ for the monitoring of several parameters such as temperature, sound, pressure, displacement etc... Furthermore, it can be applied to several geological conditions, geometries and environments.

A distributed strain sensors system for landslide prediction is presented in Sheth et al. (2005), while a WSN capable of measuring the strain in the rock due to the accumulated pressure is proposed in Mehta

et al. (2007). In that work, slope movements are detected thanks to an accelerometer included in each node, as well as temperature, pressure and humidity, which are monitored by additional integrated instruments. In Dai et al. (2009), the ground motion is measured by means of three-axial accelerometer units. Benefits and limits of WSN and methods implemented and deployed in the northern Italy Apennines for landslide monitoring are described in Rosi et al. (2011). Their use has been tested on several lithological and geological conditions, as for example rockslide (Intrieri et al., 2012), floods (Castillo et al., 2004) and debris flow (Cho et al., 2008).

The above mentioned experiences highlight important advantages of WSN over traditional ground-based monitoring techniques, such as:

i. the capability of collecting, aggregating and analysing, from a multi-point perspective, diverse and distributed data (Rosi et al., 2011);
ii. the possibility to be very quickly deployed without requiring any pre-existing infrastructure (Kamal and Hamid, 2013);
iii. the limited-cost wide area coverage, thanks to the exploitation of multi-hop communications;
iv. the existence of low-cost energy-efficient algorithms to allow the network to run for months without human intervention;
v. the capability to reach harsh environments thanks to the absence of wired structures (Zanella and Zorzi, 2006);
vi. the reduced vulnerability and environmental impact thanks to the use of wireless communications with respect to physical wiring among sensors and data loggers;
vii. the possibility of coexistence and integration with existing instruments, acting as an infrastructure to collect, process, and transmit data to a remote-control centre (Akiyldiz et al., 2002; Arampatzis and Manesis, 2005).

On the other hand, the diffusion of WSN for landslide monitoring purposes has been limited by four main factors: the energy consumption; the need of post-processing of acquired data; the capability of monitoring only a few points; the accuracy and the precision of the measure (i.e. the closeness of the measurements to the true value, and the closeness of the measurements to each other, respectively).

It is important to note that WSNs have been mainly used to move information, not to measure the movements with a radio frequency technology. The measure of the ground movement is made by inertial sensors, or classical extensometers, or other traditional device, which is then interconnected by the WSN to a data logger.

1.2.1 Ultra-Wide Band technology for distance estimation in WSN

As stated in the previous section, WSNs presented in literature mainly exploit radiofrequency signals to provide connectivity to the sensor nodes and not to measure the distance between nodes (Intrieri et al., 2018). In contrast, it is possible to use particular WSNs that use an impulsive radiofrequency technology, such as Ultra-Wide Band (UWB), to measure the distance between the nodes of a WSN, thus creating a "grid" over the soil surface to be used to monitor landslide movements.

Ultra-Wide Band systems are defined as those which have an absolute bandwidth larger than 500 MHz and a frequency larger than 2.5 GHz (Yavari et al., 2014). Numerous applications of UWB ranging includes logistics, security, healthcare, search and rescue, control of home appliances, automotive safety, and military applications (Dardari et al., 2009). In particular, this technology has been proved to be a viable candidate for enabling accurate localization capabilities through Time Of Arrival (TOA) based ranging techniques (Sahinoglu et al., 2008; Gezici et al., 2005).

In this framework, the UWB technology is extremely efficient for the monitoring of fast, moderate and slow moving landslides thanks to its main characteristics, such as low energy power consumption, high-bandwidth communications over a large portion of the radio spectrum (>500 MHz) and immunity to electromagnetic interference generated by element present on the soil. The impulse-based UWB enables an accurate ranging and high-precision localization of the network nodes (Win et al., 2009; Win et al., 1998).

The distance estimation is based on the Time Of Flight (TOF) measurement of a radio impulse sent from one UWB module to another. Since the radio impulses travel at the speed of light, the distance between the two modules can be easily estimated, by converting the TOF into a distance. The accuracy of the estimation of the distance is due to the exploitation of the wide band of the transmitted signal, which translates on small impulses over time. The fine timing resolution of the transmitted impulsive signal drastically limits the signal overlapping at the receiver, allowing an accurate ranging even in places characterized by many reflectors, as in the case of landslides.

Two primary methods can be considered for estimating the distance between a pair of nodes: the first one, based on a single communication between the nodes, expects a strictly fine time synchronization; however, the second one exploits several exchanges of information between the nodes, but does not need any time synchronization (Groves, 2013). We will now focus our attention on the latter solution, i.e. the one used for the deployment of the Wi-GIM System. This methodology considers an advanced two-way ranging method called symmetric double-sided two-way ranging (SDS-TWR) (Mucchi et al.,

2018). In particular, it uses the delays that naturally occur in the signal transmission for evaluating the distance. Figure 6 illustrates the SDS-TWR protocol, which exploits three communication messages (poll, response and final) between the Node A and Node B to determine the TOF.

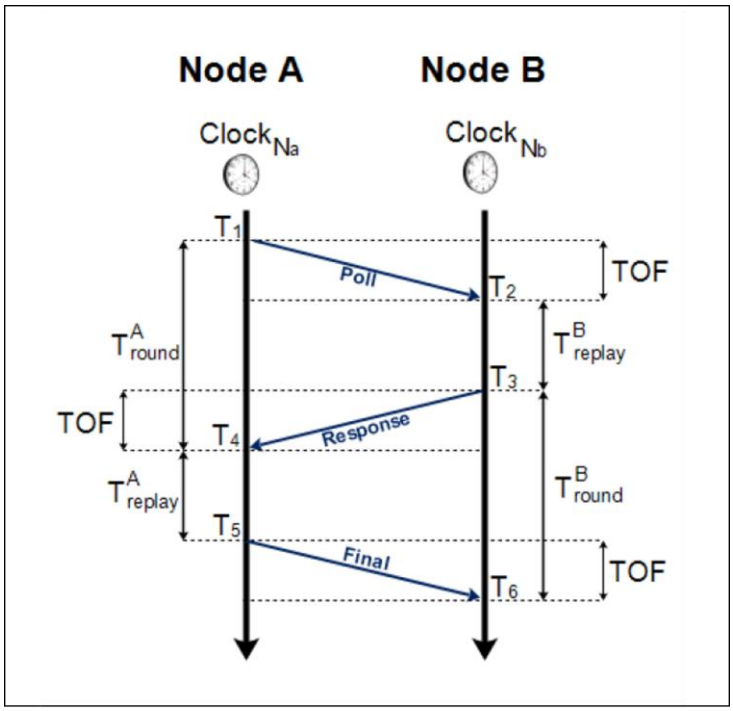

Figure 6. Symmetric double-sided two-way ranging (SDS-TWR), after Mucchi et al. (2018).

If we consider $T^A_{round} = T_4 - T_1$ and $T^A_{replay} = T_5 - T_4$, the round trip time and the reply time which refer to the Node A clock, respectively, and $T^B_{round} = T_6 - T_3$ and $T^B_{replay} = T_3 - T_2$ the round trip time and the reply time which refer to the Node B clock, the TOF between the Node A and Node B can be expressed as follows:

$$TOF_{SDS} = \frac{(T^A_{round} - T^B_{replay}) + (T^B_{round} - T^A_{replay})}{4} \quad \text{(eq.1)}$$

1.3 Rationale of the research

Ground displacement monitoring is one of the most important aspects of early warning systems and risk management strategies when addressing phenomena such as landslides. The overview on the main existing survey techniques revealed that among the most commonly used and versatile instruments, there was a lack of a low-cost, low-maintenance, feasible and easy to install tool suitable for emergency monitoring, i.e. for those situations where the priority is to rapidly gather preliminary information concerning the kinematics of a slope in order to help decision makers. The existing instrumentations able to provide real-time warnings on multiple time series are in fact typically based on expensive technologies that requires maintenance and specialised personnel.

Therefore, a wireless network based on ultra-wideband impulse radiofrequency technology has been realized. This activity has been carried out in the framework of the Wi-GIM project (Wireless sensor network for Ground Instability Monitoring) within the European Life+ financing program for the environment (Wi-GIM official website - http://www.life-wigim.eu) in collaboration with the Department of Information Engineering of the University of Florence and the private company Arsilicii s.r.l that actually developed the prototype performing the Technology Readiness Levels (TRLs) from 1 to 3 (Table 1). The main goal of the project was to obtain a geological monitoring system that reduces the installation time with respect to the more traditional instruments, and consequently reduces the risks for operational personnel involved in the field activities, as well as promptly warns the civilians in areas at risk. The main features of the system are easy and quick installation, flexibility and capability to adapt to different application scenarios and cost effectiveness. The novelty of this network consists indeed of its ability to measure the distance between nodes using the same signals used for transmission without the need for an actual measurement sensor, reducing costs considerably.

In this thesis, all data acquired by the Wi-GIM system have been post processed and analysed in depth. The first part of this thesis describes the network and the extensive experimental campaign that was performed to test its efficiency and capability. More in detail, after a test in Arcetri that can be related to a technology validation in lab (i.e. TRL 4), the system has been tested twice in a relevant environment at the Roncovetro Landslide (TRL from 5 to 7). During the acquisition period, some experiments focused on the network's inter-visibility and highlighted the importance to know a priori the visibility condition from one sensor to another one.

TRL level	Description
TRL 1	Basic principles observed
TRL 2	Technology concept formulated
TRL 3	Experimental proof of concept
TRL 4	Technology validated in lab
TRL 5	Technology validated in relevant environment
TRL 6	Tecnology demonstrated in relevant environment
TRL 7	System prototype demonstration in operational environment
TRL 8	System complete and qualified
TRL 9	Actual system proven in operational environment

Table 1. The Technology Readiness Levels, TRLs.

With the aim to go further inside the issue, the second part of this thesis focuses on the implementation of an algorithm able to find the best locations to install a WSN requiring inter-visibility. The code has been developed on Matlab software environment (R2018a, MAthWorks, Natick, MA, USA) and works directly with 3D point clouds, usually obtained by TLS, ALS or photogrammetry. Nowadays many researches in the field of urban design, landscape planning as well as GIS technology focus on the study of visibility analysis, but most of them are based on the use of gridded digital terrain and elevation models (DTM and DEM) (Fisher, 1991; Murgoitio et al., 2013). With the development of LiDAR and SfM technologies, there is an opportunity to use directly 3D point cloud data to perform visibility analyses. Doing so, many disadvantages of traditional modelling and analysis methods can be bypassed. This leads to skip the process of generating a surface model avoiding errors and approximations (Dodd, 2001; Guth et al., 2009; Katz et al., 2007; Zhang et al., 2017). Furthermore, point cloud data can provide much more detailed information than traditional gridded raster terrain data or triangulated mesh terrain data (TIN), especially in case of steep, hummocky, vegetated or/and overhanging terrain.

The main objective of this research is therefore the analysis of data acquired by an innovative Wireless Sensor Network and its optimal employment through a developed deployment tool based on inter-visibility analysis.

2. The implemented Wi-GIM system

In the framework of a European Life+ project (LIFE12/ENV/IT001033) called Wi-GIM (Wireless Sensor Network for Ground Instability Monitoring), an innovative Wireless Sensor Network based on Ultra-Wide Band technology for 3D accurate superficial monitoring of ground displacements has been implemented. As already mentioned in Section 1.3, the prototype has been developed in the first months of 2016 other than this thesis, in collaboration with the Department of Information Engineering of the University of Florence and Arsilicii s.r.l., a private company located in the province of Siena (IT). The activities of this thesis began with data post-processing and interpretation. However, it is essential to describe in detail the network, to better comprehend the work that has followed.

The Wi-GIM system was specifically designed with the aim of exploiting as much as possible its employment within Early Warning Systems in emergency situations. Among the main key features, which will be described in detail in the following sections, there are its easy and quick installation and high acquisition frequency, both requirements for early warning-oriented devices. More in general, the system was developed with the goal to overcome the limit that are still present in the conventional systems for ground deformation monitoring, introducing some advantages such as flexibility, cost effective, absence of wired structures and low environmental impact.

The main design criteria for Wi-GIM was ultimately to produce a low-cost system that was reliable enough to be applied to different situations, trying to fill the gaps of the various existing monitoring techniques as much as possible. The achievement of the above mentioned objectives will be verified by analysing and comparing the experimental results obtained for the case studies that will be presented later in this thesis.

2.1 Operating principles

2.1.1 Architecture

The system is designed as an ad hoc wireless sensor network based on a modified star topology (Figure 7). The master and slave paradigm, together with clustering technique, is adopted to allow a versatile and energy-aware estimation of the distances among the network nodes. A cluster is defined as a group of slave sensors (up to 16) managed by a single master sensor. It is defined by a single master when the scanning procedure starts during the configuration of the sensor network. During the scanning procedure, the master sensor uses the communication control channel sending a request signal. Slave sensors around the master answers to this signal with an ACK (acknowledge) and the estimated distance. Once the master has collected all the ACKs, it defines its network (cluster) of sensors, which are managed by itself from that time on.

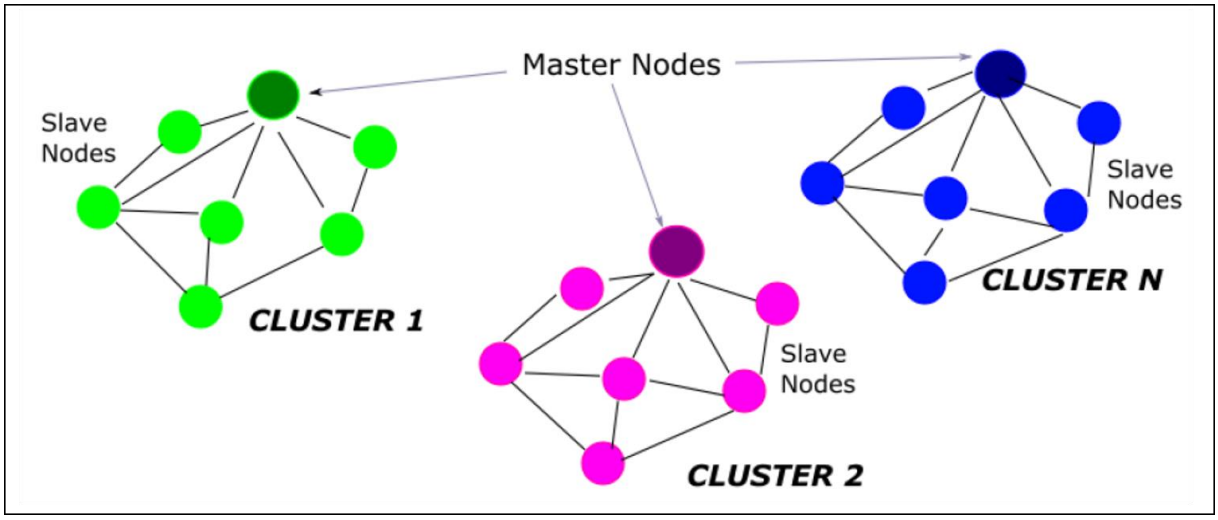

Figure 7. The master-slave paradigm (after Mucchi et al., 2018).

As will be deeply explained in Section 2.1.2, each master node periodically estimates the distances of the slave nodes belonging to its cluster through the adoption of the UWB technology and a pre-processing of the received signals. The obtained information is then transmitted to the remote server via a 3G link for a complete post-processing of all the data coming from the different clusters distributed over the monitored area. As a result, the variation of the distances among the network nodes over time is computed to evaluate the ground movements (Figure 8).

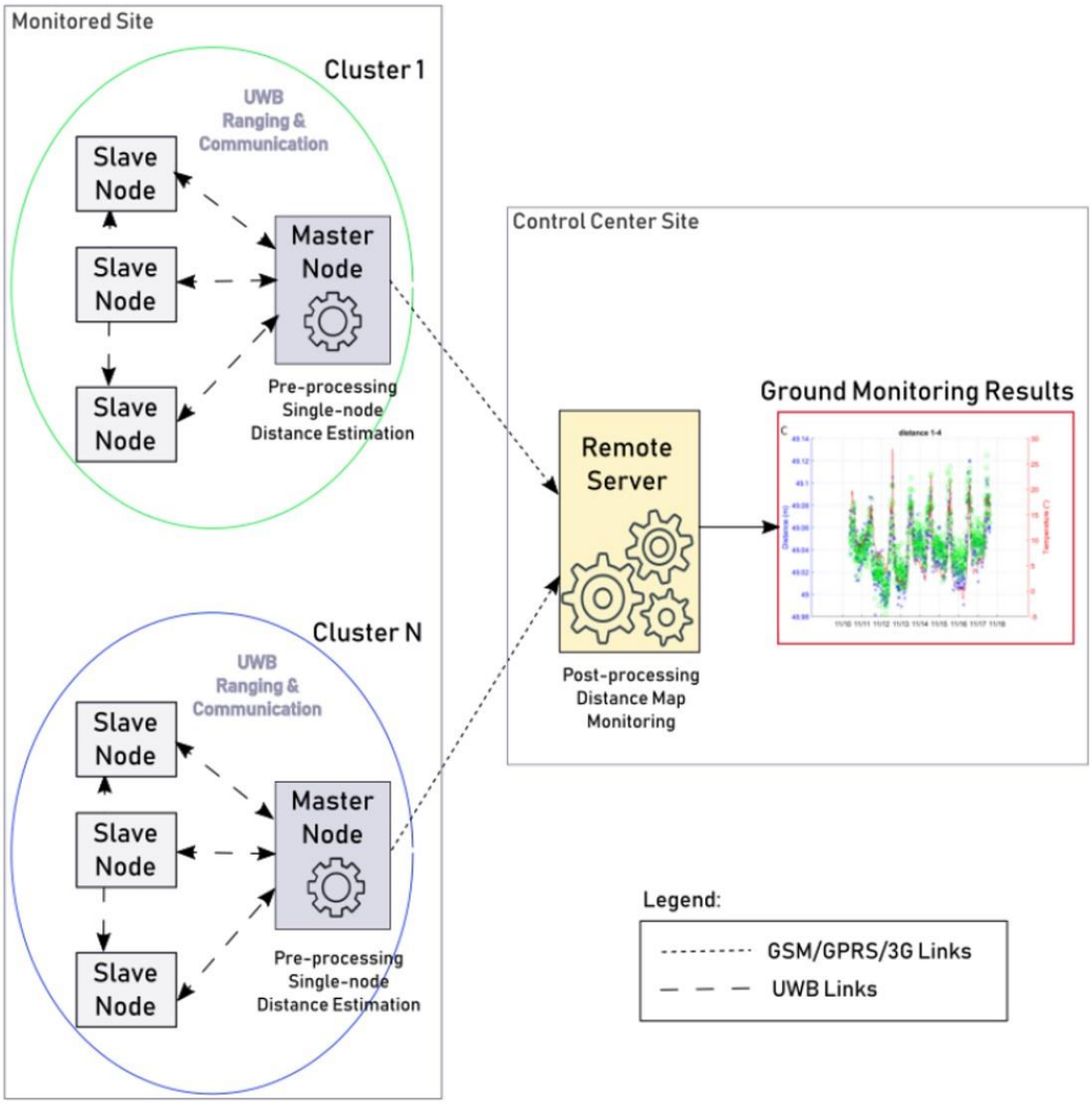

Figure 8. Wi-GIM system architecture (after Mucchi et al., 2018).

Each Wi-GIM network's node consists of an electronic board with a micro-controller ARM Cortex M3, a battery (12 V, 7.2 Ah lead acid battery), a UWB module (Decawave Sensor DWM1000) and different additional modules, that characterize the specific node function within the network architecture. Furthermore, some boxes are equipped with a thermometer, useful to make some correlations with the other parameters, as explain later. Three types of node are defined:

i. the Slave Nodes (SNs), i.e. the basic one, that include ports to plug Decawave and battery supply;
ii. the Master Nodes (MNs), which are additionally equipped with a SD memory card, a GPS, a GSM/GPRS/3G communication modules and an internal thermometer;
iii. the Super-Slave Nodes (SSNs), optionally equipped with GPS.

A list of the network nodes components and their functions is provided in Table 2, while their pictures are reported in Figure 9. Concerning the communication modules, please note that the connection depends mainly on the SIM card used and therefore, at the moment, it would be already possible to replace them with a 4G or 5G card.

Component	Function	MN	SSN	SN
Micro-controller	ARM Cortex M3 micro-controller	X	X	X
Battery	A 12 V, 7.2 Ah lead acid battery for node power supply	X	X	X
UWB	Decawave Sensor DWM1000 Module (2017a) for communication and ranging	X	X	X
SD memory card	Storage of the Ids of SNs and SSNs and the number of hops to reach them	X	X	
GPS	TAOGLAS DXP.02.A for time reference signal, required for slave coordination	X	X	
GSM/GPRS/3G	Long-range communication modules for data transmission to a remote server	X		

MN: Master Node; SSN: Super-Slave Node; SN: Slave Node.

Table 2. Wi-GIM nodes components and relative functions.

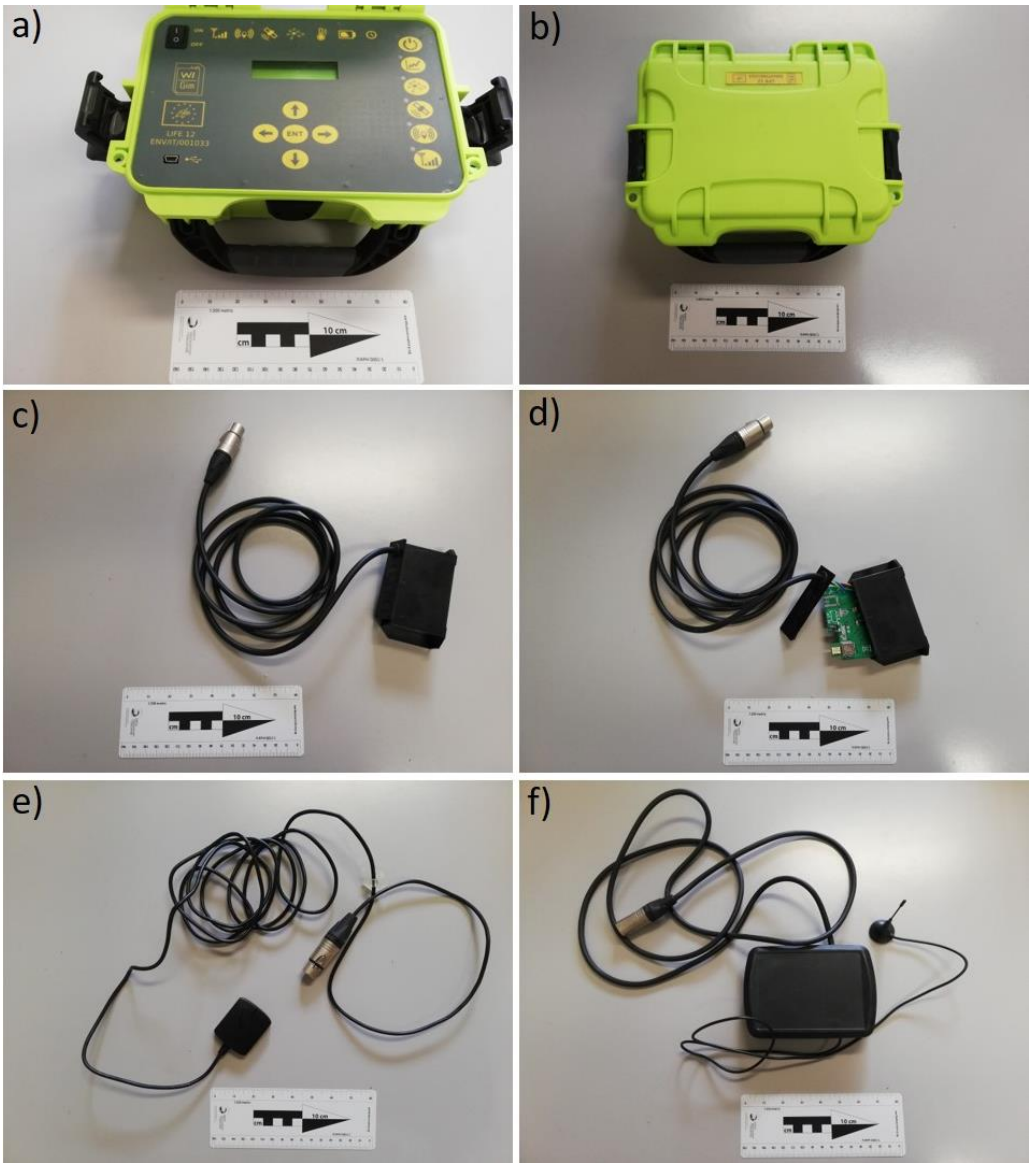

Figure 9. Wi-GIM main components: a), b) micro-controller; c), d) UWB Decawave sensor; e) GPS; f) modem.

The chosen UWB module, Decawave (Dublin, Ireland) Sensor DWM1000 Module (2017a) (Figure 10) uses signals with bandwidth of 500 MHz resulting in 0.16 ns-wide pulses. The Decawave Module integrates: the Abracon (Spicewood, TX, USA) ACA-107-T dielectric chip antenna (3200–7200 MHz frequency range), all radio frequency circuitry, power management and clock circuitry. It can be used in two-way ranging or TOF location systems to locate assets to a precision of 10 cm and it supports data rates of up to 6.8 Mbps.

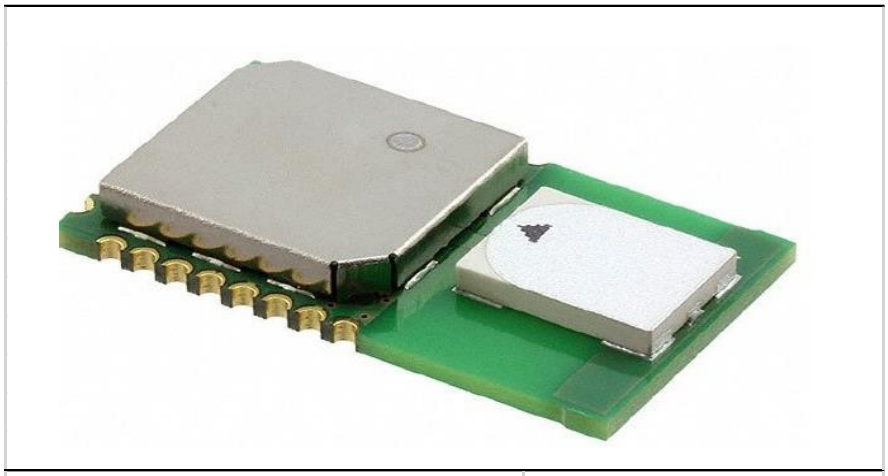

Precision	10 cm (indoor)
Data rate communications	6.8 Mb/s
Communications range	300 m
Frequency	3.5 GHz - 6.5 GHz
Dimension	23 mm x 13 mm x 2.9 mm
Supported location schemes	TOF and TDOA
Temperature Range	-30°C to +85°C
Power consumption - Transmit mode	from 31 mA
Power consumption - Receive mode	from 64 mA
Support packet sizes	up to 1023 bytes

Figure 10. Detail of the Ultra-Wide Band module used in the Wi-GIM system, the Decawave Sensor DWM1000. For more detail, please visit the Decawave website (https://www.decawave.com/product/dwm1000-module).

The GPS is not required for positioning but for a time reference. The master node spreads the GPS time reference among the slaves before starting the ranging measurements. The one implemented in the system is a TAOGLAS DXP.02.A SMD L1/L2/L5 SAW Diplexer using the GPS/GALILEO L1, L2 and L5 bands. It is housed in a compact 5 mm x 5 mm x 1.7 mm laminate package and its specifications are reported in Table 3.

BAND 1 (L1)			
	Min.	Typ.	Max.
Center Frequency (MHz)		1582.1875	
Insertion Loss (dB)		3.8	4.6
Amplitude Ripple (dB)		0.6	2.0
Return Loss (dB)		-13.0	-6.0
Attenuation (Reference level from 0dB)			
10 ~ 1330 (MHz)	32	38	
1660 ~ 2000 (MHz)	27	33	
BAND 2 (L2 and L5)			
	Min.	Typ.	Max.
Center Frequency (MHz)		1206.9225	
Insertion Loss (dB)		4.2	5.2
Amplitude Ripple (dB)		1.2	2.5
Return Loss (dB)		-8.0	-6.0
Attenuation (Reference level from 0dB)			
10 ~ 1100 (MHz)	17	23	
1320 ~ 2000 (MHz)	20	28	
BAND 1 and BAND 2			
	Min.	Typ.	Max.
Isolation (1196.9~1248.625MHz)	22	35	
Isolation (1574.22~1576.62 dB)	22	31	
Environmental			
Operating Temperature	-40°C to 85°C		
Input Power Level	10 dBm		
DC Voltage	3 V		

Table 3. TAOGLAS DXP.02.A SMD L1/L2/L5 SAW Diplexer table of specification. For more detail please see the product website page (https://www.taoglas.com/product/dxp-02-a).

Since battery consumption is a critical point for the WSN, a sleep mode has been implemented for the nodes. The master node is programmed to periodically measure the distances throughout the day, e.g., every 10 min over 24 h. When a node is activated by the master, it sends an UWB impulsive signal to each near node with whom it is able to communicate. The neighbour node receives it and sends it backwards. The active node thus can estimate the inter-node distance by calculating the two-way TOF. Once the TOF is estimated, the distance is obtained by multiplying the TOF times the speed of light. This computation is made by the master, and once the procedure is complete, it deactivates all the sensor (including itself) restoring them in the sleep mode.

Considering a cluster made by 10 nodes, a single entire measurement cycle (from activation to back in sleep mode) lasts around 90 seconds. For an earth flow, given its slow temporal evolution, the measurement frequency can be 2–4 acquisition per day in order to save batteries. For a longer use of the WSN on a landslide, the battery of each node can be changed without moving the node.

2.1.2 Installation procedure and pre-processing

The presence of obstacle between transmitter and receiver, i.e., Non-Line Of Sight (NLOS), implies a bias in the estimation of the distance. For this reason, it is important to try to install all the Decawave sensors so that they are visible one to each other. In case a Sensor Node (SN) needs to be placed behind an obstacle for monitoring purposes, so that the Master Node (MN) is in NLOS condition, another SN shall be put in Line Of Sight (LOS) with that SN and with the MN enabling the MN to still reach the "blocked" SN. In fact, each MN scans the network to gather information of those SNs that are in LOS condition, then asks these SNs to inform it about the SNs in LOS with them (but in NLOS with the MN). This procedure allows the MN to have a map of all the SNs which are in LOS and the ones reachable through 1 hop thanks to SNs relaying mechanisms.

Once the best topology has been found, then the nodes can be installed on the field and the MN can start the initial scan to know which sensors are part of the network. Once the MN has completed its SNs map, the cluster is defined, and those nodes will be considered for the monitoring strategies. It is worth highlighting that, after the initialization phase, the cluster cannot be modified: the introduction of an additional node requires a new scan of the network. From that time on, the MN continuously controls the status of each SN of its cluster (e.g., battery level, correct functioning), as better described in the following.

In order to manage the network resources allocation, the MN sends the activation control signal to an SN, enabling it to occupy the channel and perform the ranging operations. The SNs are activated one at a time. Upon reception of the activation signal, the SN sends an UWB impulsive signal to all its neighbour nodes (LOS nodes), which respond. As the SN completes the distance measurements, by calculating the two-way TOF, it sends the results to the MN and then releases the channel. The MN can now send the activation control signal to another SN and the process is repeated until all the SNs are activated.

As above mentioned, an initial network scanning allows the MN to draw a sketch of the network connections between the nodes, identifying also those SNs that are not directly reachable from the MN. The activation of those SNs is performed by means of a relay mechanism: the MN activation command is relayed by a LOS SN to the NLOS SN. The IDs of the SNs and the number of hops to reach each specific node are stored in the MN memory card. As the complete scan of the nodes is finished, the MN sends the sleep command and the wake-up time to the slaves. All the SNs deactivate all their power-consuming modules and then reactivate them at the programmed time. The scheduled

measurements activation/deactivation allows an efficient management of the nodes' battery consumption. The acquisition rate is set by the user during the installation procedure, and it is a consequence of the monitored phenomenon, always considering the battery consumption.

The proposed distance measurements system requires a time reference. For this purpose, the MN is equipped with a GPS module, whose function is to provide the GPS time reference to be spread among the SNs before starting the ranging measurements. After collecting all distances, the MN sends a report file to the remote server via 3G connection. The periodical report on the status of the cluster/network includes: the distances measured by all the pairs of sensors that are in LOS (directly or through a relay process) and the corresponding time stamp; each node battery level and the temperature recorded by the internal thermometer.

2.1.3 Data remote post-processing

The information collected by the master node are stored in the internal SD card and send at the same time to the remote server by using the GSM/GPRS/3G module. The resulting ASCII data file name is assigned based on the cluster name and acquisition time, and it is formatted as the following example:

11.06.16 01:07:50.132 DWV_RNG 001 002 80.9211

11.06.16 01:07:50.071 DWV_RNG 001 003 0.0000

11.06.16 01:07:51.250 DWV_RNG 001 004 72.4136

11.06.16 01:07:51.198 DWV_RNG 001 005 56.4527

11.06.16 01:07:51.147 DWV_RNG 001 006 82.3447

11.06.16 01:07:51.096 DWV_RNG 001 007 42.4421

11.06.16 01:08:18.067 GPS_FIX 001 110616,010731.594, A, 4431.4290, N, 01023.4090, E

11.06.16 01:08:18.047 GPS_FIX 002

11.06.16 01:08:27.219 ANG_V&T 001 12.815 V 7.001 V 26.126 °C 13.912 °C

11.06.16 01:08:27.195 ANG_V&T 002 12.079 V 17.255 V 51.454 °C -35.770 °C

where DWV_RNG stands for Decawave ranging; GPS_FIX for GPS position and ANG_V&T for sensor's values such as battery charge and device temperature.

A specific MATLAB (R2016a, MAthWorks, Natick, MA, USA) script has been compiled for the database creation by reading data from SD card and joining data from ftp server. Once data are available, they

are processed by a second specific MATLAB script which yield the following graph types for each pair of communicating nodes:

i. raw distance values (Figure 11a);
ii. distance values without invalid measurements (i.e. with no zero or non-numerical values) (Figure 11b);
iii. distance validated values (outliers' removal) (Figure 11c);
iv. distance daily mean values (Figure 11d).

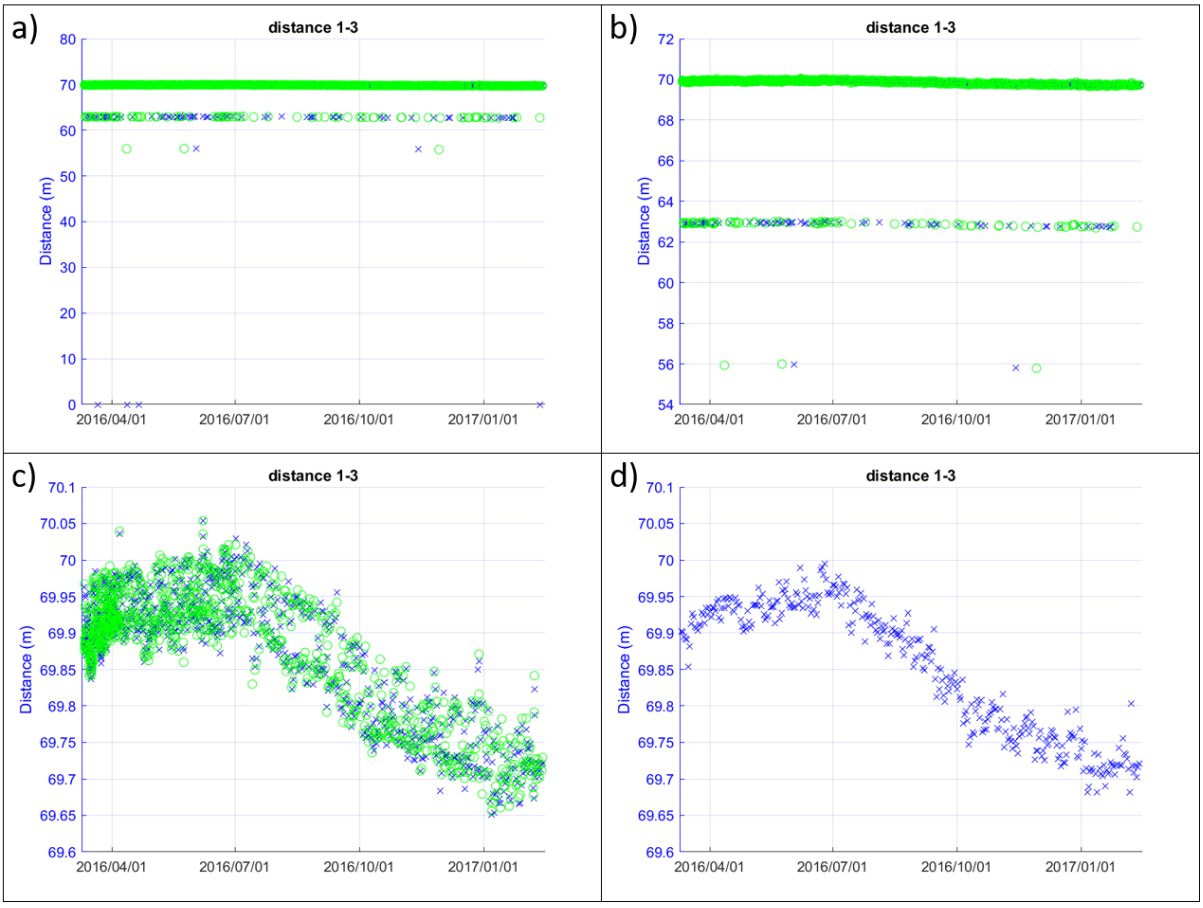

Figure 11. Displacement time series of a pair of nodes (1–3). Green circles and blue crosses represent the distance measured from one node to the other and vice versa. Where measurement points are extremely dense, the blue crosses are overlaid by the green circles. a) raw distance values; b) distance values without invalid measurements; c) distance validated values, considering a threshold of 1 m for the outlier's removal; d) distance daily mean values.

The outlier removal (iii) consists in the identification and removal of the unreliable measurements, which can be defined as those values with a distance for example bigger than 1 m compared to the previous value, avoiding also some possible multipath effects. Raw data presented indeed some offset repeated at different intervals (Figure 11 a, b). In particular, in some points the measured ranging resulted to be underestimated of a constant quantity respect to the real distance. The observed

phenomena affected data from all the test sites and was not related to the distance, since it had the same characteristics both for short and long distance, and for this reason it was considered as a problem of multipath. To avoid this problem, a correction was applied to all data considering the general trend of the measured distances. Firstly, the modal value of the first acquired data was calculated, and data exceeding a predefined threshold respect to this were considered as invalid data. Subsequently, after some days of monitoring, having regard to the possibility of a real movement, each valid value was considered as reference value, and data were considered as outliers if they exceed more than a predefined threshold with respect to the previous valid one. Note that the threshold changes in function of the kinematic of the landslide and the involved distances. Considering the latter, it is in general modified in a shorter value in case of smaller distance (for example in case of a measured distance equal to 3 m, a standard value of 0.4 m can be taken into account to remove the multipath effect).

Each pair of nodes is represented by one of the above mentioned graphs, in which distance values in both directions are plotted (e.g. for pair 1–3 distance values measured from 1 to 3 and vice versa are plotted, Figure 11). In addition, it is possible to add battery level and/or temperature values in the graphs, allowing the user to check the battery life and to eventually correlate data with temperature values (Figure 12).

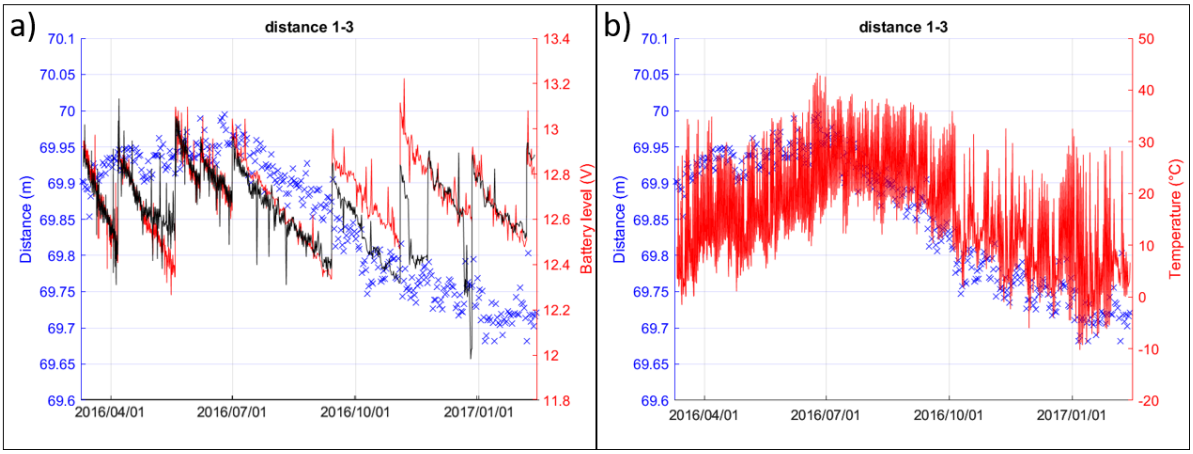

Figure 12. Distance daily mean values of a pair of nodes (1–3). a) Displacement time series and battery level. Black and red lines show the battery level of node 1 and 3 respectively. b) Displacement time series and temperature values.

2.2 Tests

To carry out some tests on the Wi-GIM technology, six clusters have been installed for a field test in a controlled open environment located in Arcetri, Florence (Central Italy). The test site has been chosen due both to logistic reasons, namely easy accessibility, and to the site features: being an outdoor setting with a heterogeneous vegetation, it allowed us to test the effects of obstacles and temperature on the measurements. For every specific test a different cluster was installed, taking advantage both of site characteristics and available distances (Figure 13).

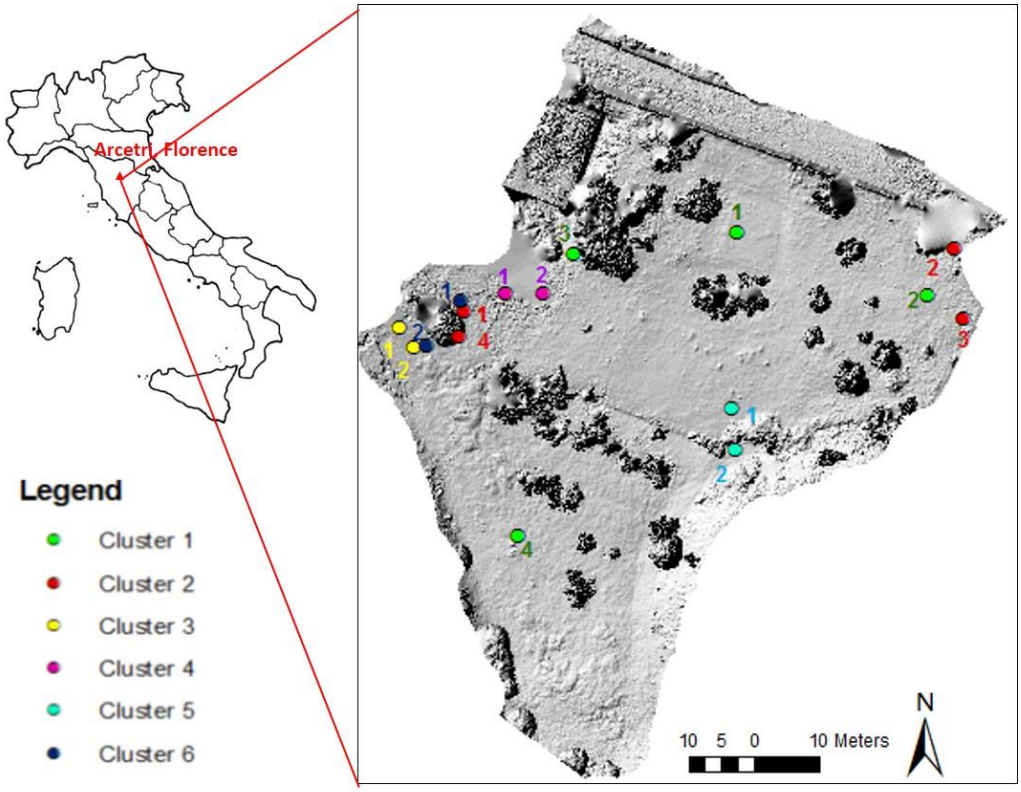

Figure 13. Location of the experimental test site in the controlled environment of Arcetri. Clusters are displayed on the Digital Surface Model (DSM) of the area. Number close to each coloured dot is the node label.

The first cluster (named Cluster 1), composed by a master node and three slaves, has been installed on 2016/10/13 and removed on 2017/02/06 with the aim to test inter visibility between pairs of nodes belonging to the same network. Each antenna was fixed on temporary wood stakes planted in the ground (Figure 14), and the acquisition frequency was set equal to 10 minutes. All the distances have been measured with a laser distance meter to have a prompt method of comparison and to better evaluate both precisions and reliability of the technology.

Figure 14. Wi-GIM installation at Arcetri.

Cluster 2, composed by a master node and three slaves, has been installed in the area on 2016/11/11, with the aim to investigate the relation between measured ranging and temperature. Nodes position has been chosen appositely to have long and short distances to analyse the relation. Acquisition frequency was fixed at 10 minutes and the cluster has been removed on 2017/01/20.

Other four clusters (named Cluster 3, 4, 5 and 6) have been installed in the area with the aim to test the system behaviour with the presence of obstacles. In all cases, clusters were composed by one master and one slave node only, and their installation and removal times are reported in Table 4.

	Installation	**Removal**
	(yyyy/mm/dd)	(yyyy/mm/dd)
Cluster 3	2016/10/11	2016/12/27
Cluster 4	2017/01/03	2017/02/01
Cluster 5	2017/01/20	2017/02/06
Cluster 6	2017/02/01	2017/02/16

Table 4. Arcetri clusters installation and removal times.

2.2.1 Inter-visibility test

Studies about inter-visibility have been carried out firstly thanks to the installation of Arcetri Cluster 1. A first test has been performed by tying the sensors on stakes about 25 cm high, so that the antennas resulted only a few centimetres from the ground level. The experiment gave as result the no vision between all the pairs of nodes, due probably to the presence of abundant grass cover combined with small slopes and soil irregularities. For this reason, on 2016/10/17 the entire cluster has been reinstalled keeping the same position but setting the antennas on stakes 1 meter high. After changes, it followed the reciprocal visibility between all nodes but the pair 2–4 was affected by the presence of discontinuous vegetation. Therefore, it was necessary to move node 2 of some decimetres to let all node communicate between them. Figure 15 and Figure 16 show the 2–4 pair line of sight before and after the applied changes.

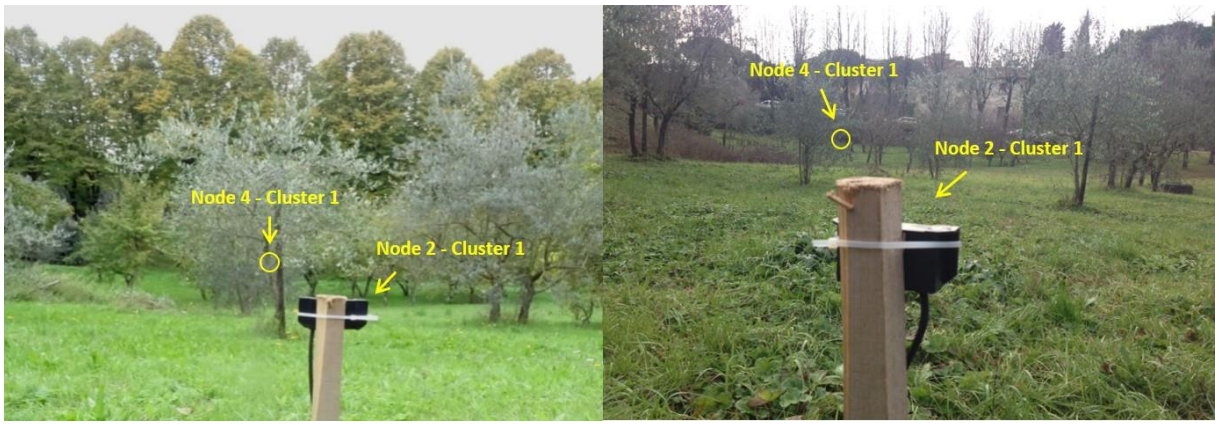

Figure 15. Line of sight between antennas 2-4 of Arcetri Cluster 1 before and after changes (respectively on the left and on the right).

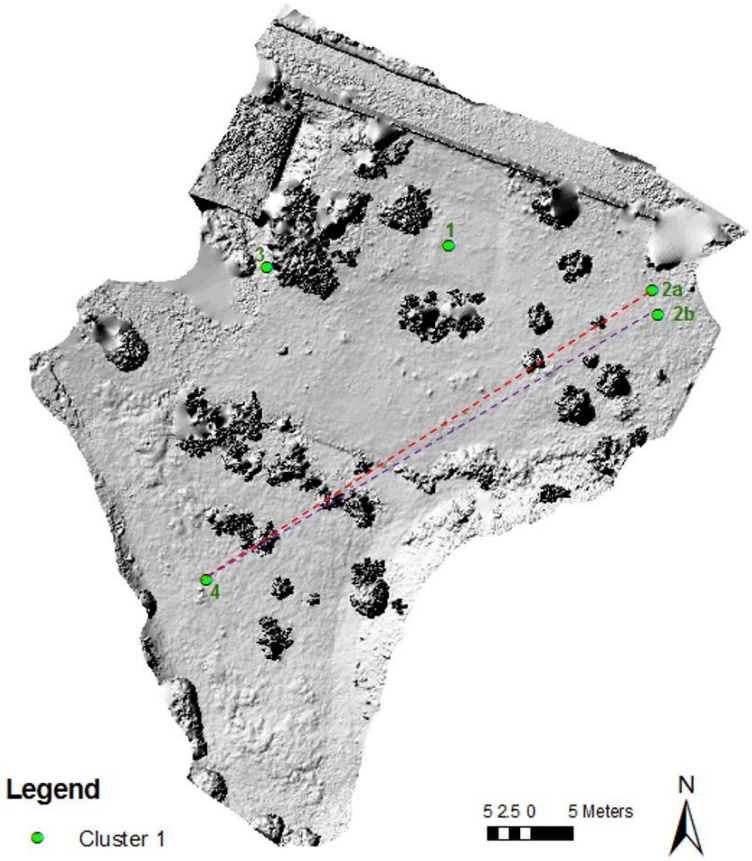

Figure 16. Arcetri DSM with the position of Cluster 1 node 2 before and after changes (respectively 2a and 2b). The dotted lines show the line of sight. Note that the dashes red line (which corresponds to the pre changes positioning) is more affected by vegetation than the purple one.

As second test consisted in flipping antennas of cluster 1 of 180° on their vertical axis to see if this affected the measurements. This experiment has been important as it was necessary to prove if a node could effectively make measurements even with respects to other nodes behind it, a common configuration in a fully connected monitoring network. This resulted in a shift in ranging measurements of about 10 cm, explainable by the different wave paths that rebounded several times on obstacles before arriving at the receiving antenna. As showed in Figure 17, in correspondence of 2016/11/28 there has been a shift of about 15 cm on average, that has been might due to the different wave paths that rebounded several times on obstacles before arriving at the receiver sensor. Figure 18 shows the real distances of the whole network of Cluster 1, measured by means of a laser distance meter.

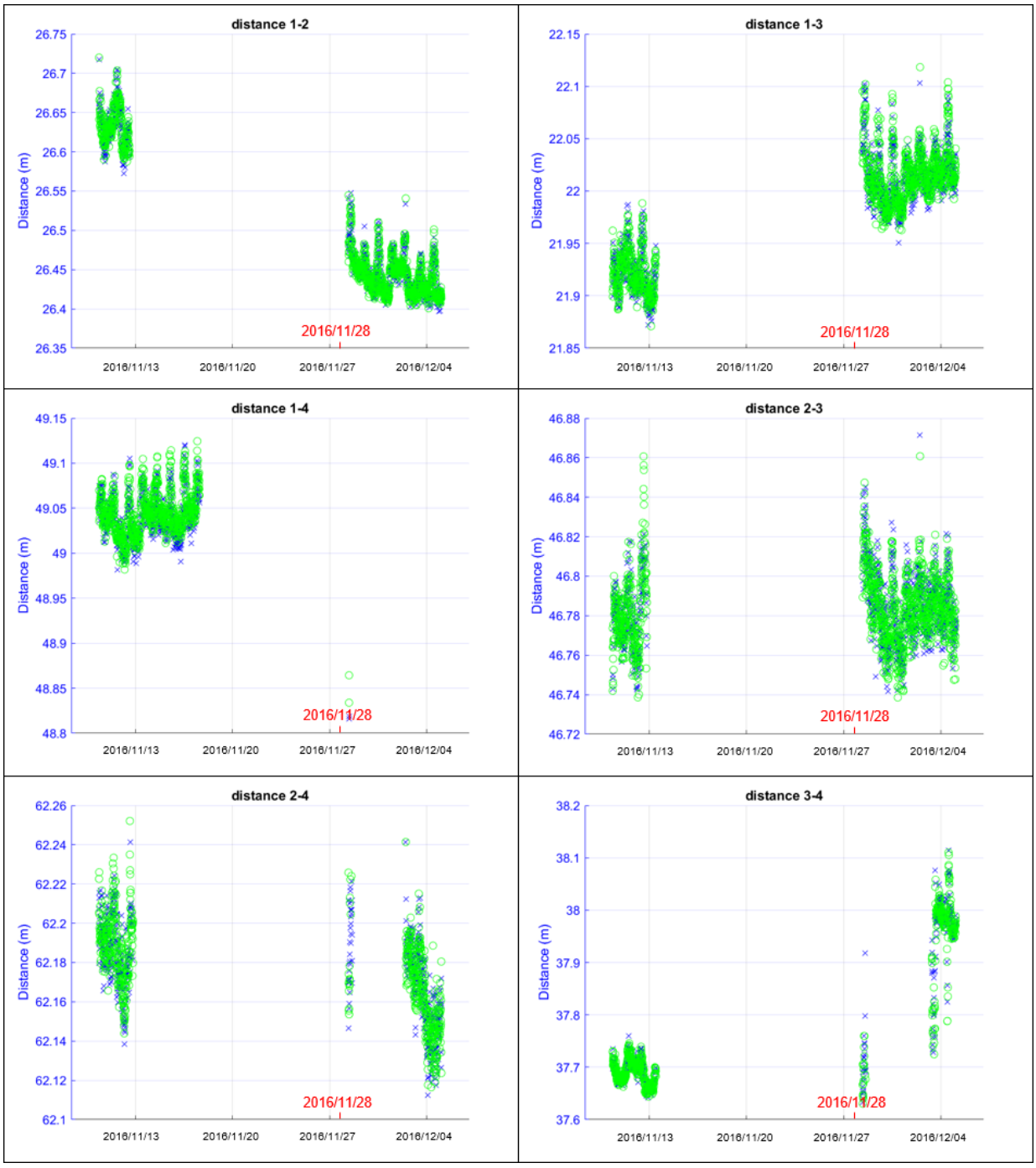

Figure 17. Arcetri Cluster 1 correct valid data from 2016/11/10 to 2016/12/05. On 2016/11/28 the system has been restarted turning 180° the antennas on their vertical axis. The absence of data in the middle time is due to the lack of power. Green circles and blue crosses represent the distance measured from one node to the other and vice versa.

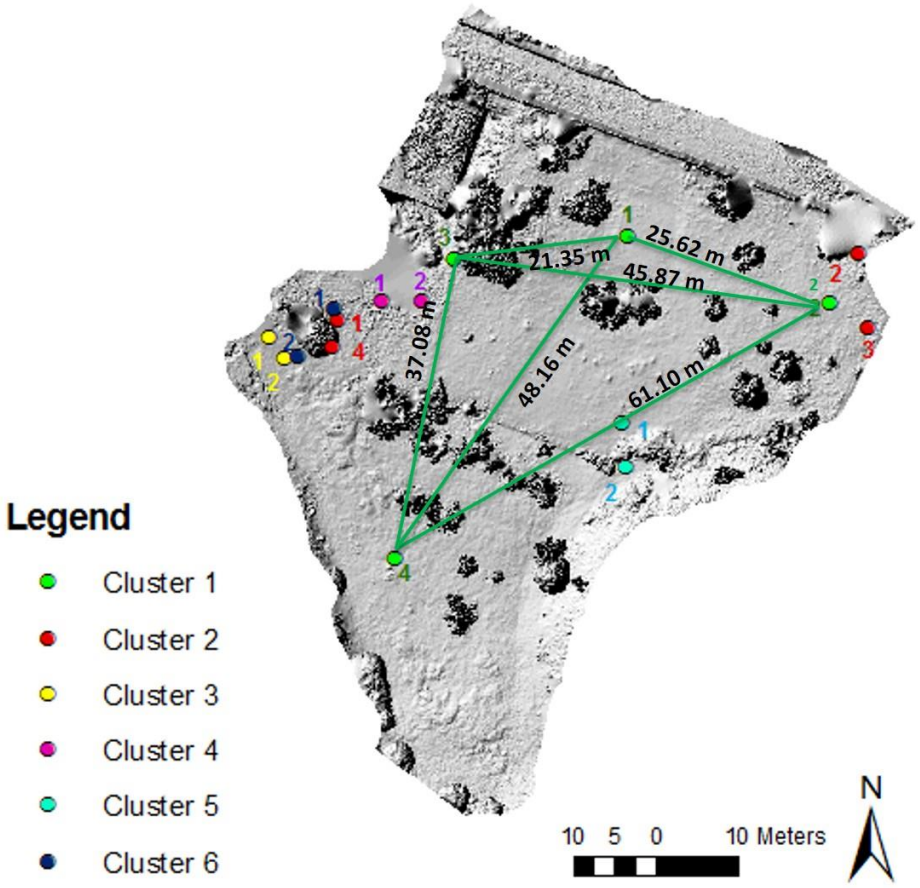

Figure 18. Arcetri DSM in which are shown the real distances relative to Cluster 1. Distances have been measured with a laser distance meter.

Further tests have been carried out to verify reliability and precision of the monitoring system in presence of obstacles. For this purpose, all clusters composed by only one master and one slave node have been exploited, and the acquisition rate has been set equal to 1 acquisition every 10 minutes, in order to have as much data as possible.

First of all, to observe the influence of an obstacle on the measurements, a 40 cm wide, 2 m high, hollow plastic cylinder has been installed between two nodes (cluster 3) that were 3.30 m far away (Figure 19a).

After 8 days of acquisition, the obstacle has been removed, and data highlight the influence of the obstacle on the ranging measurements (Figure 20a).

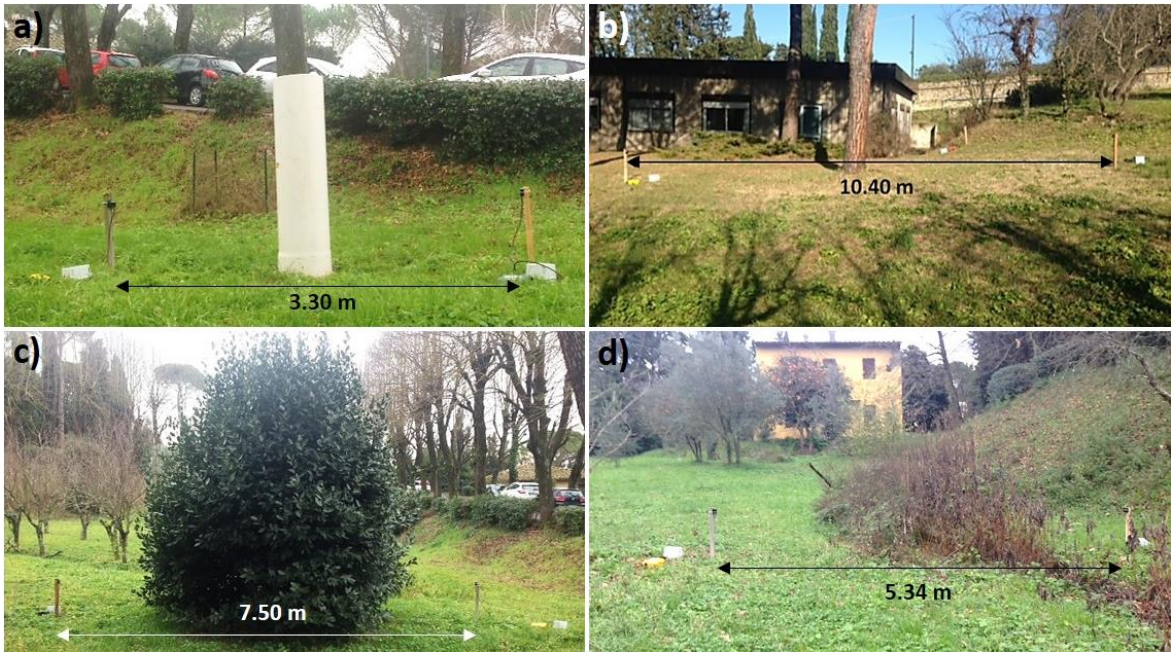

Figure 19. Photographs of different configurations for the inter-visibility tests with a PVC pipe (a), a tree (b), a vegetated bush (c) and a dry bush (d).

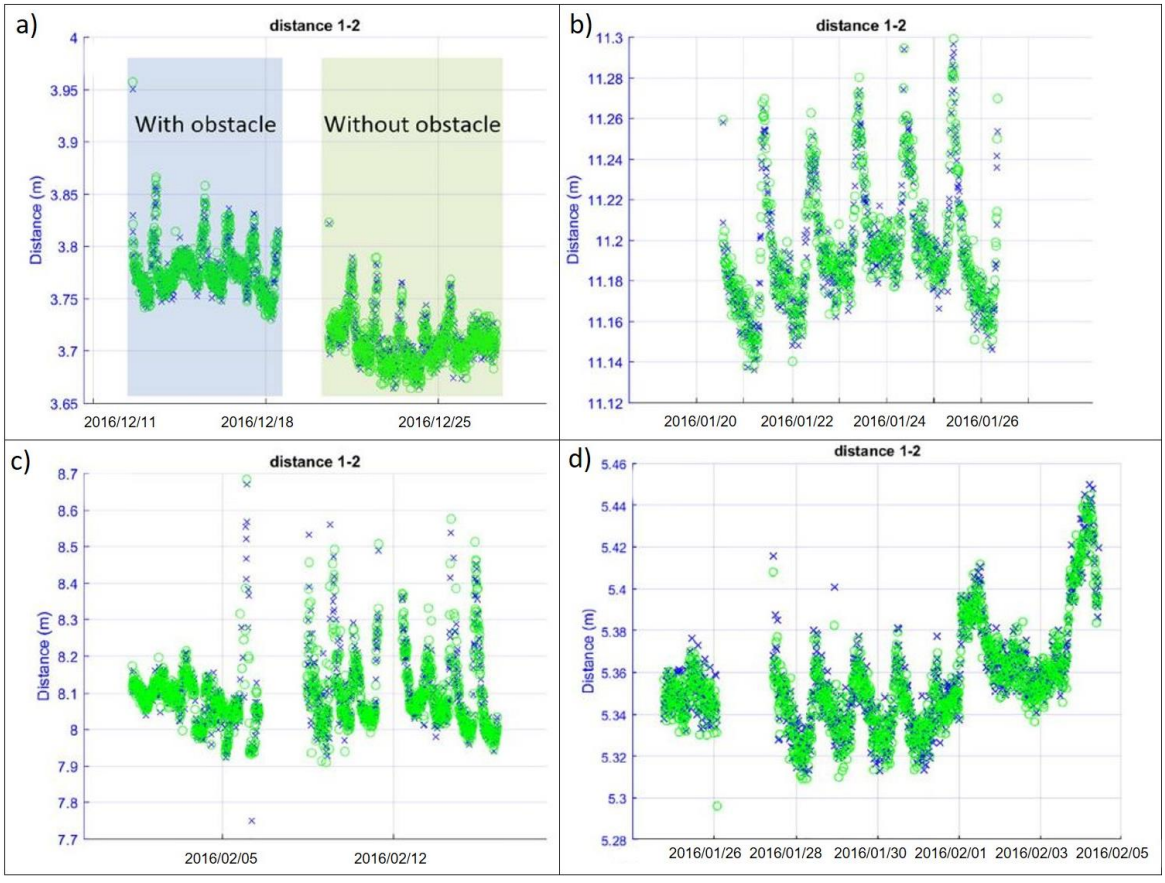

Figure 20. Measurements of the distances between nodes with time. Each graph (a, b, c, d) corresponds to the respective experiment shown in Figure 19a, b, c, d. Periods of non-acquisition were due to a lack of power. Green circles and blue crosses represent the distance measured from one node to the other and vice versa. Where measurement points are extremely dense, the blue crosses are overlaid by the green circles (after Intrieri et al., 2018).

Despite precision did not show any changes, a shift of few centimetres between measurements made before and after the object removal has been observed, thus affecting the measurements accuracy. Specifically, in the first days of acquisition (when the obstacle was in place), longer and less reliable distances have been measured by the monitoring system. This phenomenon has been interpreted as due to a difference in the path travelled by the waves that, due to the NLOS condition, are still able to reach the antennas but only after one or more rebounds.

Notably, even without any obstacles, the ranging distance measured by Wi-GIM is still affected by a systematic error resulting in an offset with respect to the actual distance. This value is constant for a specific pair of nodes but varies from pair to pair. It is probably due to a mistake during the calibration of the circuits at factory level, caused by a wrong estimation of the time needed for the signal to cover the distance between its generation and its amplification. However, the determination of absolute distance is not relevant for the applications of Wi-GIM, since the relative inter-node distance still allows the user to map the displacements.

Further tests have been performed to evaluate the system behaviour with different types of obstacles, such as a 40-cm wide tree trunk (Cluster 4). The antennas have been initially positioned at the sides of the trunk, each at a distance of 1.20 m. After a week, the antennas have been moved an additional 1m from the obstacle for a total distance between them of 4.40 m. They have been then moved again and reinstalled 5m from the trunk, for a total distance of 10.40 m (Figure 19b). Data showed how the signal was able to transmit despite the presence of the trunk (Figure 20b). The same results have been observed for each evaluated distance, without an evident relation between the obstacle influence and its distance from the nodes. The effect of different vegetation types has been then analysed taking into account a densely vegetated 7 m tall, 4 m wide shrub (monitored by Cluster 6) and a 1.5 m tall dry bush (monitored by Cluster 5). In both cases, the antennas have been positioned at opposite sides of the obstacle at 7.50 m (Figure 19c) and at 5.34 m (Figure 19d) and the signal was able to bypass the obstacle despite the antennas being close to the obstacle (Figure 20c, d). Notably, the test performed using Cluster 5 showed a sensible ranging shift starting from February 1st, indicating an increased distance between nodes, which can be interpreted as a variation in the geometry of the branches within the shrub. The comparisons between the actual distances between the nodes (measured with a laser distance meter) and the mean distances measured with Wi-GIM are reported in Table 5. Note that, for every case, the LOS was never completely free of obstacles, although their nature and dimension varied from case to case. The pair 2–4 of Cluster 2 is not included since not visible by Wi-GIM.

	Nodes	Actual distance (m)	Wi-GIM distance (m)				Difference (m)
			Min.	Max.	Mean	σ	
Cluster 1	1–2	25,62	25,08	25,23	25,16	0,025	0,46
	1–3	21,35	22,65	23,15	22,90	0,022	–1,55
	1–4	48,16	49,03	49,13	49,08	0,021	–0,92
	2–3	45,87	45,64	45,76	45,70	0,021	0,17
	2–4	61,10	62,14	62,27	62,23	0,017	–1,13
	3–4	37,08	37,70	37,80	37,75	0,022	–0,67
Cluster 2	1–2	66,70	64,16	64,25	64,21	0,013	2,49
	1–3	65,50	67,28	67,40	67,30	0,023	–1,80
	1–4	2,56	2,80	2,90	2,85	0,030	–0,29
	2–3	8,47	8,70	9,10	8,80	0,028	–0,33
	3–4	66,36	66,98	67,07	67,02	0,028	–0,66
Cluster 3	1–2	3,30	3,74	3,85	3,76	0,030	–0,46
Cluster 4	1–2	10,40	11,13	11,28	11,20	0,026	–0,80
Cluster 5	1–2	5,34	5,30	5,42	5,35	0,037	–0,01
Cluster 6	1–2	7,50	8,00	8,60	8,20	0,050	–0,70

Table 5. Measurements relating to each pair of each cluster: actual distance between the nodes (measured with a laser distance meter), minimum, maximum, mean and standard deviation (σ) of Wi-GIM measurements and difference between actual and Wi-GIM mean distance (modified after Intrieri et al., 2018).

2.2.2 Atmospheric effects

Air temperature measurements are performed at every measuring cycle using a sensor placed on every master node. This value showed a strong correlation between the measured distances and temperature on a daily scale (Figure 21 – Figure 22), and the data analysis highlighted a linear correlation between these parameters described by a trend line (Figure 23 – Figure 24).

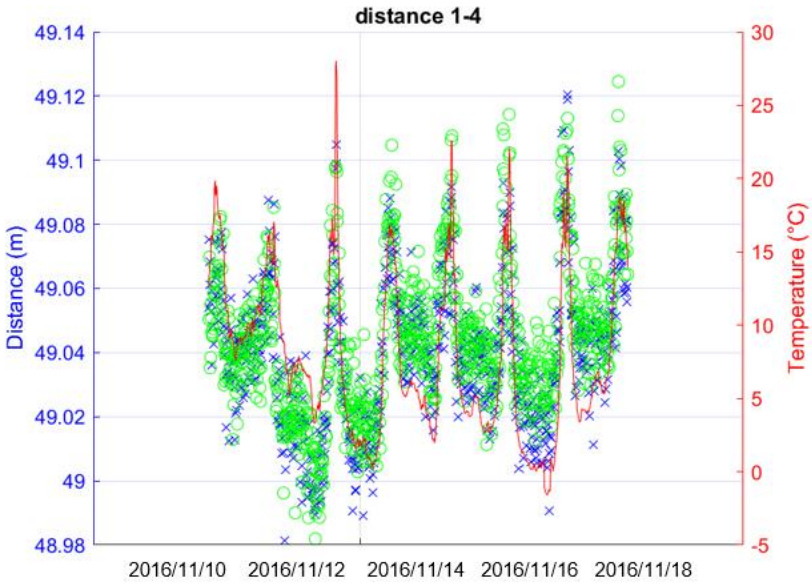

Figure 21. Distance values without invalid measurements acquired by nodes 1–4 of Arcetri Cluster 1 and temperature values from 2016/11/10 to 2016/11/18. The graph highlights the strong correlation between ranging measurements and temperature.

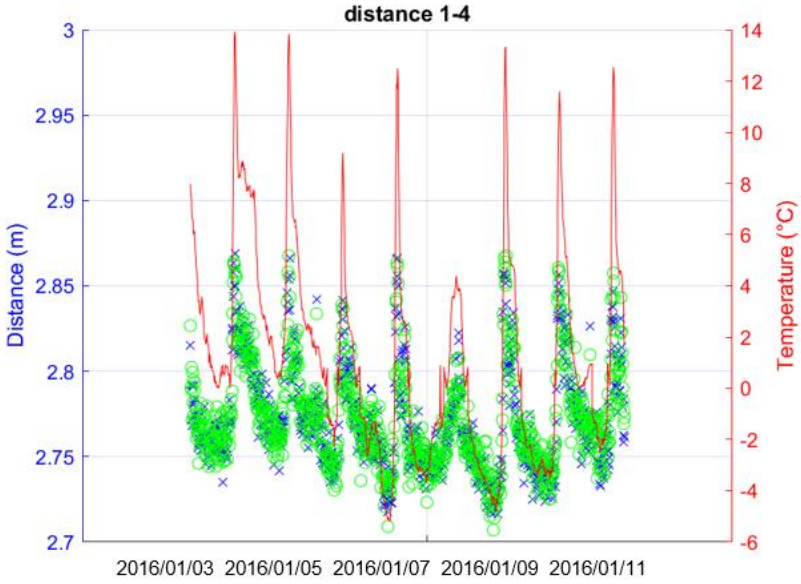

Figure 22. Distance values without invalid measurements acquired by nodes 1–4 of Arcetri Cluster 2 and temperature values from 2017/01/03 to 2017/01/12. The graph highlights the strong correlation between ranging measurements and temperature.

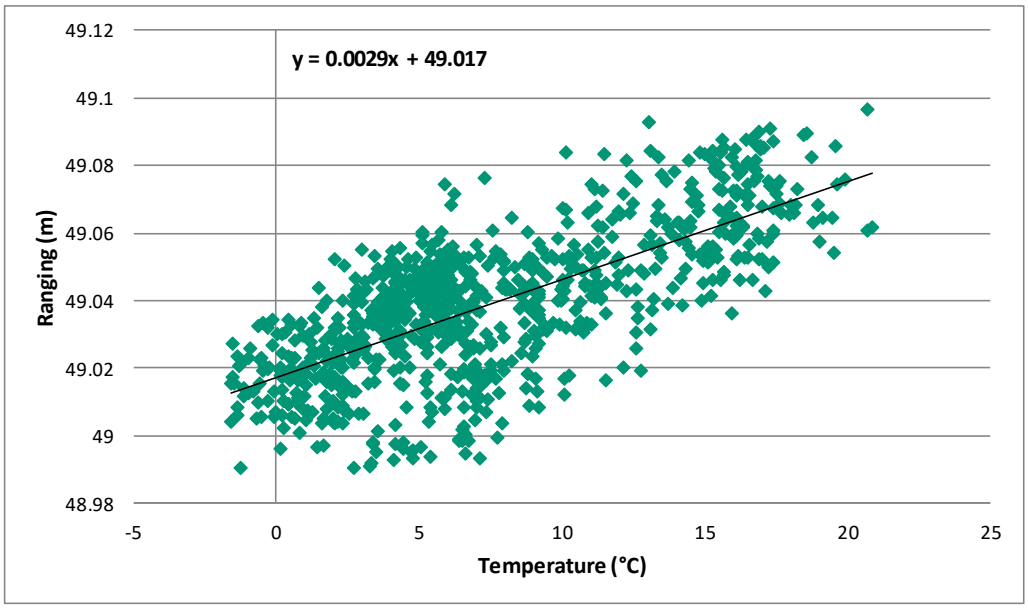

Figure 23. Scatter plot between the temperature and the measured ranging, calculated for the pair of nodes 1–4 belonging to Cluster 1 (Figure 21). The equation in the upper part refers to the black trend line.

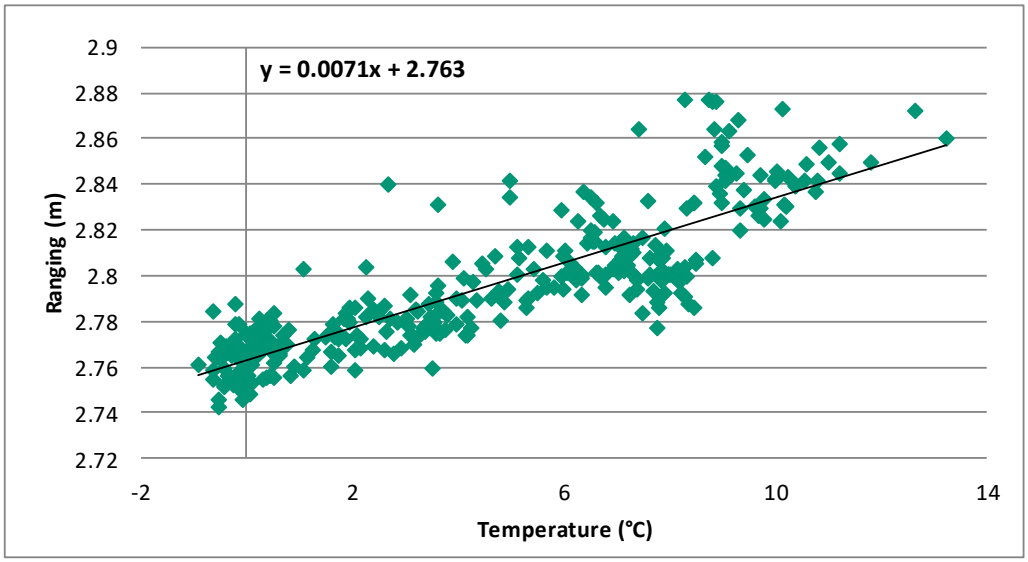

Figure 24. Scatter plot between the temperature and the measured ranging, calculated for the pair of nodes 1–4 belonging to Cluster 2 (Figure 22). The equation in the upper part refers to the black trend line.

For this reason, a linear empirical relation between ranging and environmental temperature has been proposed. A correction considering a reference temperature of 20 °C was made using a correction factor Ki for each displacement value:

$$K_i = (T_i - 20) * m \qquad \text{(eq. 2)}$$

where *m* is the trend line slope (angular coefficient). It is constant in time for each pair of nodes, but it varies from pair to pair. T_i is the temperature measured at the time (t_i) of the acquisition that is going to be corrected. The choice of a temperature of 20°C as a reference one has been made since generally

it is the average temperature at which devices are implemented. The correction has been applied by subtracting K_i from each value, resulting in a consistent reduction of the data variance:

$$D_i = D_0 - K_i \qquad \text{(eq. 3)}$$

where D_0 is the raw measured distance (that is the output value before the temperature correction) and D_i the corrected value of the distance. The satisfactory result of this correction is evident in Figure 25 and Figure 26, which show how data are no more following the temperature oscillations.

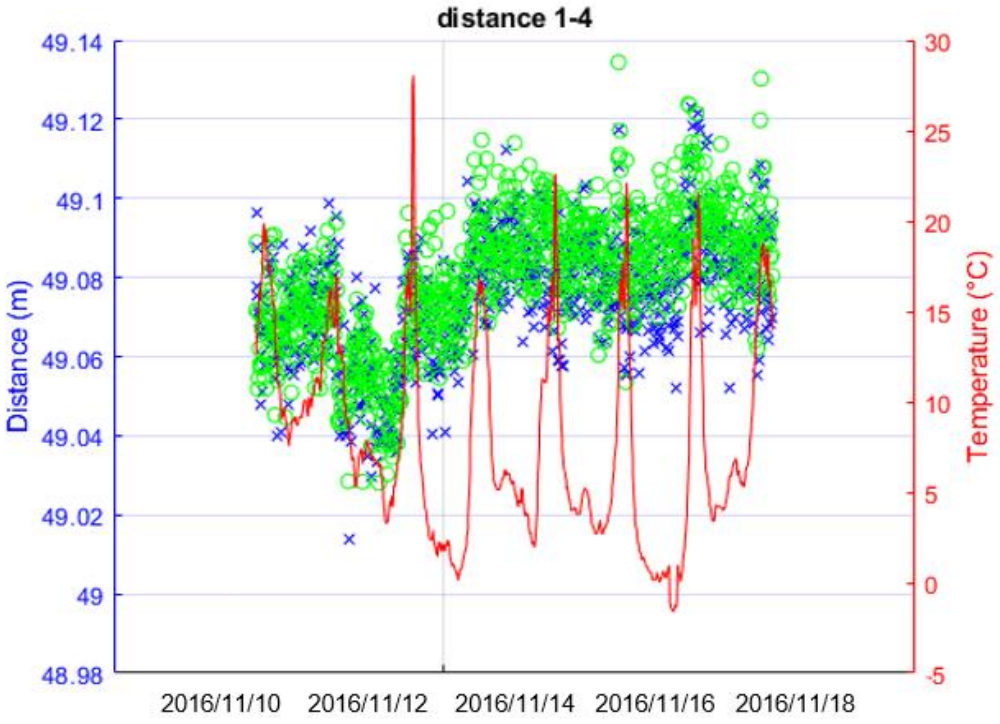

Figure 25. Results obtained applying the temperature correction on data acquired by nodes 1–4 of Arcetri Cluster1 (Figure 21). According to the trend line slope (Figure 23), the *m* value has been set equal to 0.0029.

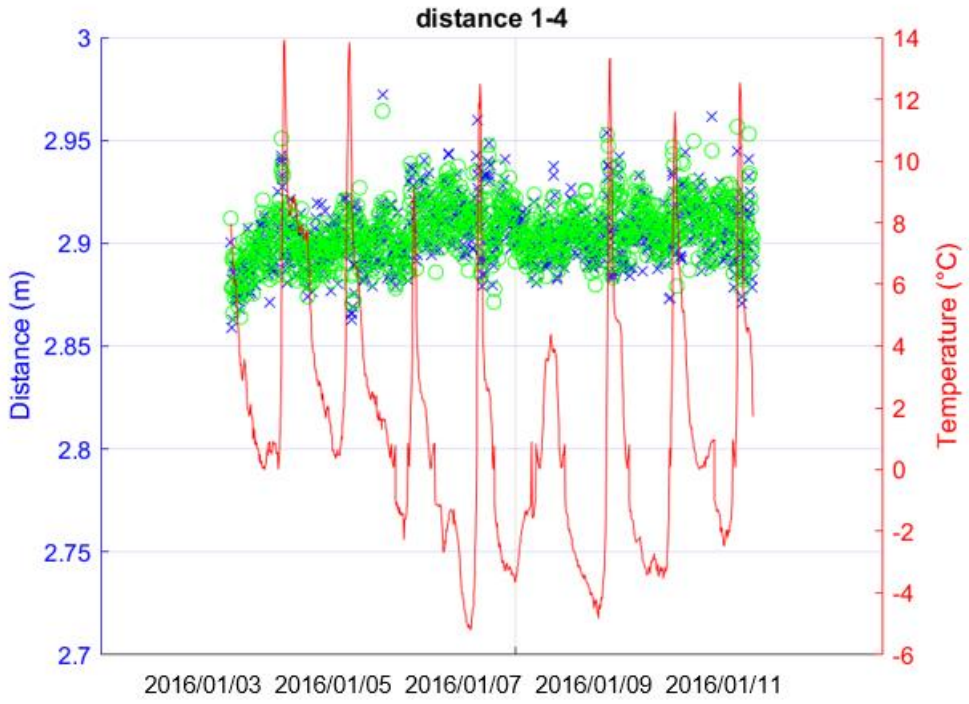

Figure 26. Results obtained applying the temperature correction on data acquired by nodes 1–4 of Arcetri Cluster2 (Figure 22). According to the trend line slope (Figure 24), the *m* value has been set equal to 0.0071.

Furthermore, to verify whether this relation depending on distance, data from Cluster 2 have also been analysed since its nodes provide the possibility to examine both long and short distances (Table 6). It was not possible to analyse nodes 2–4, the most distant from each other, because their inter-visibility was compromised by vegetation. It appears that the values of the angular coefficient are similar between different pairs within the same cluster (regardless of their respective distance) while they vary from a cluster to another (Table 6).

	Nodes	Distance (m)	*m**	R^2**
Cluster 1	1–4	49	0,0029	0,5340
	3–4	38	0,0025	0,3091
	1–3	22	0,0030	0,4803
Cluster 2	1–4	3	0,0070	0,7394
	3–4	67	0,0060	0,7063
	1–3	67	0,0063	0,8151

* Angular Coefficient
** Coefficient of determination

Table 6. Distances and trend line slopes of pair of nodes for Arcetri Cluster 1 and 2.

Therefore, other factors than the inter-nodes distance probably influence the relationship between temperature and ranging measurement. For example, it is possible that *m* is also affected by the

internal temperature of the nodes or by local atmospheric effects (such as variation of humidity or turbulence), especially where the LOS is close to the ground. On the other hand, it is still not clear if it is due to the deformation of the instrument as well as the supporting elements or if it has an influence on the signal itself (El Houssaini et al., 2019; Meng et al., 2009).

Moreover, this relation could be due directly to the temperature, or it could be caused by the batteries that with high temperatures give different charge to the Decawaves. To go further inside this aspect, some batteries have been equipped with a voltage regulator to stabilise the input at the sensors despite the temperature fluctuations. However, since these tests are in the early stages, they are not object of this thesis, but will be deepened in future.

For a proper filtering of temperature effects, the value of m cannot be assumed but needs to be calibrated for each pair in every application. In order to apply a temperature correction, a preliminary period of acquisitions is necessary to calibrate the relationship between temperature and measured distance. Once m is calculated for each pair of nodes, it can be used to correct the value of D_0 after calculating K_i. This correction can be done in real-time and therefore does not invalidate early warning applications. Moreover, a medium value of about 0,005 can be used obtaining a good result without misrepresenting data, since all the calculated values range from 0,0029 to 0,0070 (Table 6).

3. Wi-GIM application to Roncovetro landslide

A detailed experimental survey on an actual case of instability was performed to stress test the system. The chosen site was the Roncovetro landslide, a 2.5 km long complex landslide, with a volume of 3 million m^3, first described by Almagià (1907). It is located in Emilia Romagna Region (Central Italy) and carves the southern slope of Mount Staffola (where the crown is located) down to the Tassobbio stream (at the toe), where it partially dams the water creating a small seasonal lake (Figure 27).

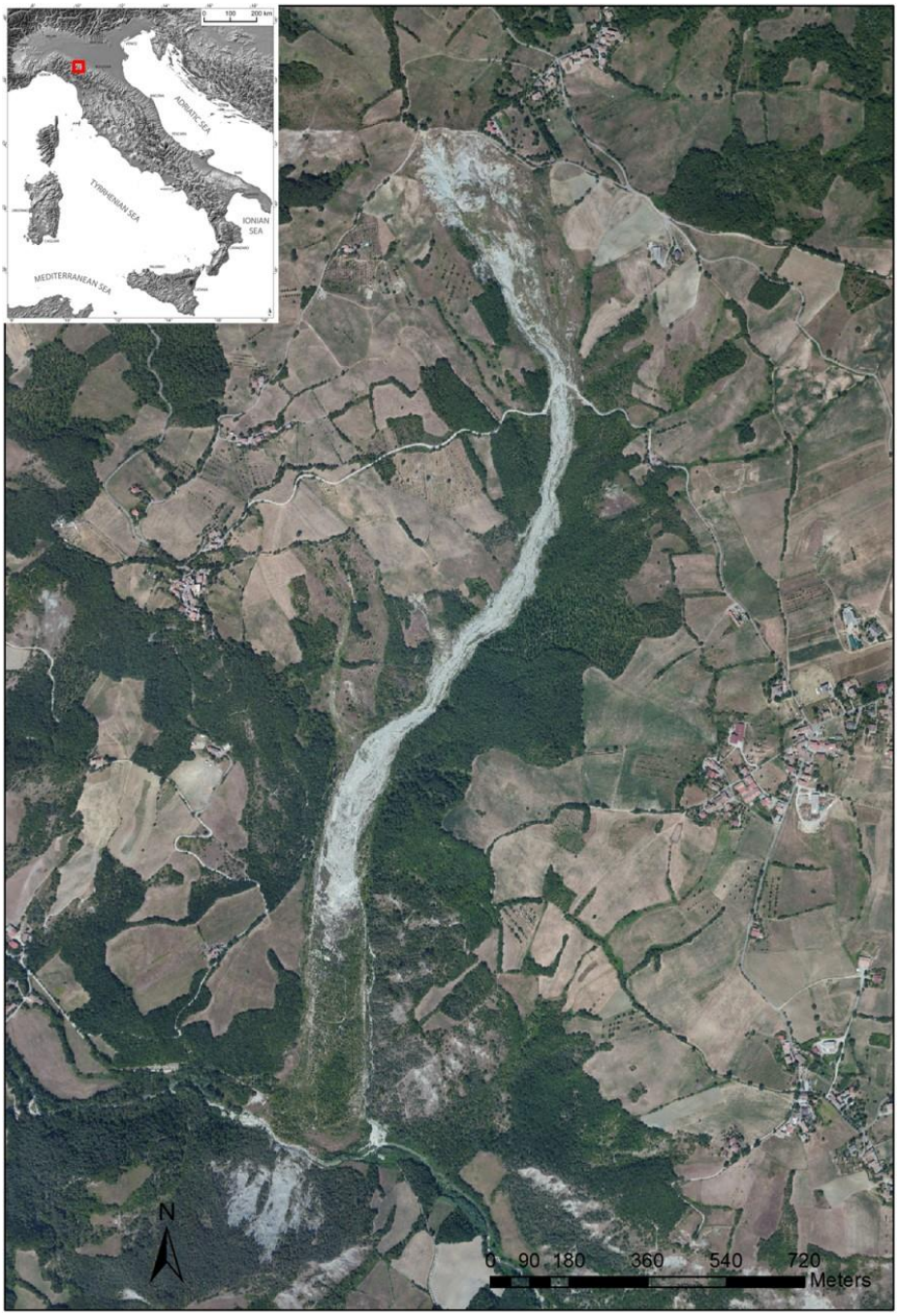

Figure 27. Aerial photo of the Roncovetro landslide.

The upper and central parts of the Roncovetro landslide appeared to be optimal for the Wi-GIM experimental survey, thanks to several factors:

i. the landslide shows almost continuous movements;
ii. the existing different mechanisms of rupture (deep creep, sliding, flowing) due to the upper area of the landslide shows a very large range of displacements;
iii. it is possible to place sensors in the whole width of the landslide in the central part;
iv. the variety of field conditions allow to experiment the inter-visibility of the monitoring network nodes;
v. the size is sufficient to test the range limit of the network;
vi. it is possible to implement a parallel system of monitoring (automated geodesy) by positioning a robotized total station to cross-check and validate Wi-GIM data.

3.1 Roncovetro landslide features

The first notices of the Roncovetro landslide dates back to the 1907, when Almagià coined the term of "Lavina di Roncovetro", where *Lavina* meant *Landslide* in local idiom, in the first Italian inventory of landslides (Almagià, 1907). At that time, the landslide was already well known among the local people, but for what we know the morphological features of this landslide were not so evident in more ancient times, since the oldest existing cartographies, dating in 1821, 1828 and 1858, did not represent it.

Figure 28. The Roncovetro landslide.

As already mentioned, it is a 2,5 km long mudflow (Figure 28) that carves the southern slope Monte Staffola from its top to the Tassobbio River where it causes the formation of a small lake.

The slope is formed by sub-ligurian clayey calcareous-arenaceous flysch belonging to the Mount Staffola Formation, Cretaceous-Eocene (Figure 29 – Figure 30).

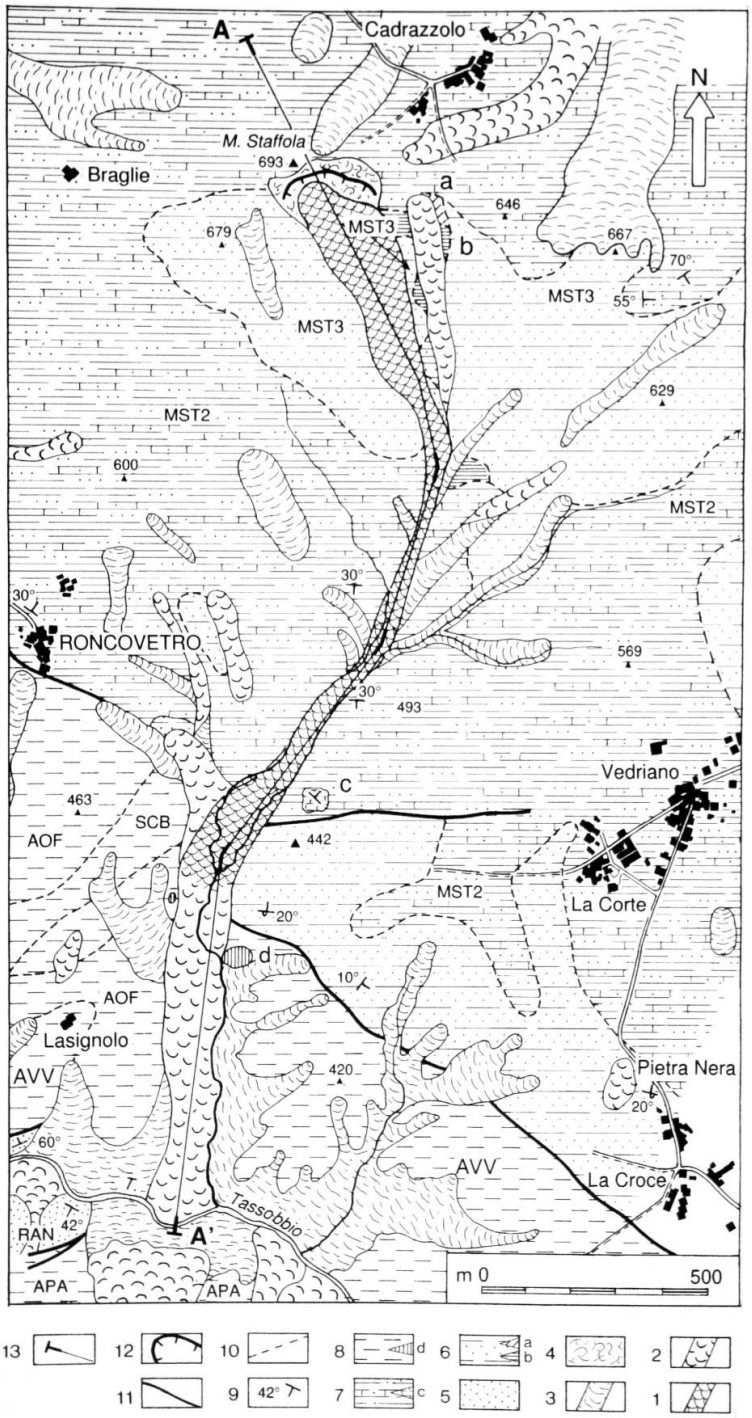

Figure 29. Geological Map. LEGEND - 1) Reactivated earth-flow landslide; 2) Reactivated earth-slide landslide; 3) earth flow, dormant; 4) rotational/translational slide, active; 5) RAN: Ranzano Formation (Eo-Oligocene); 6) MST3: Mount Staffola Formation (Vedriano); 7) MST2: Mount Staffola Formation (Upper Paeocene - Middle Eocene); 8) Units pertaining to the Ligurian Domain: APA: Palombini Shales (Lower Cretaceous); SCB: Scabiazza Arenites (Lower Campanian); AOF: Ophiolitic Shales (Upper Cretaceous); AVV: Cassio "Varicolori" Shales (Santonian-Campanian); d: ophiolites; 9) strike and dip of bedding planes; 10) tectonically-originated unit boundary; 11) fault; 12) landslide main scarp; 13) trace of geological cross-section A-A'. After Bertolini & Gorgoni (2001).

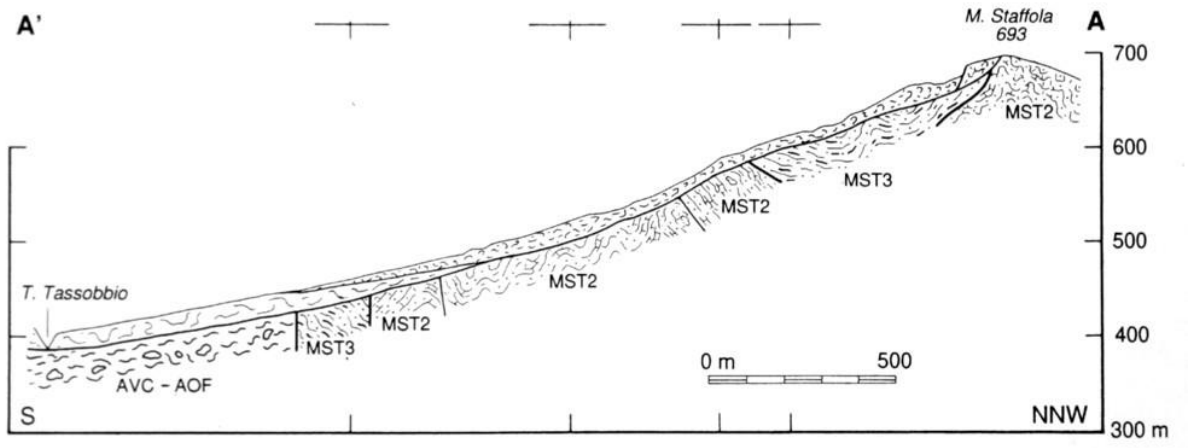

Figure 30. Geological section, referred to the A-A' section reported on the geological map of Figure 29. Symbols are the same used in Figure 29. After Bertolini & Gorgoni (2001).

The clay fraction is dominant from the mechanical point of view, causing the landslide to behave in its upper portion as a very active fluid-viscous mudflow, with maximum velocities up to 10 m/day. The total volume of the landslide is about 3 million m^3. The landslide reactivated completely in autumn 1993 and, since then, it alternates seasonal phases of suspension (i.e. during summer periods) with phases of activity.

The body of the landslide can be divided in three main sectors:

i. The upper part, that comes from the main scarp, i.e. the crown area, located at about 660–670 m a.s.l., where the bedrock is moving valleyward through rotational surfaces of rupture. The rate of movements is here in the order of magnitude of centimetres/decimetres per year.

ii. The middle part. At the altitude of about 550 metres a.s.l., the landslide material enters into a narrow channel about 1 km long, 30 m wide and 20 m deep carved inside the flysch bedrock. This channel has no other function than transport the mud from the depletion to the accumulation area, maintaining in confined conditions the fluidity of the mud. The state of fluidity here varies in time and space, causing varying flow velocities inside the moving mass.

iii. The lower part is located at about 415 m a.s.l. and moves a few decametres per year. From here, the material evolves in more plastic physical behaviour, well represented by the convex shape of the landslide in this sector (Figure 28–Figure 30), whose thickness is about 15 meters. Reaching the Tassobbio River, the landslide material forms a dam and a seasonal small lake. The damming is facilitated also due to the subterranean collision of the tip of the Roncovetro landslide with the tip of another landslide moving in opposite direction on the other side of the valley.

According to Bertolini & Gorgoni (2001), the permanent fluid state that characterizes the upper part is caused by high porewater pressures maintained by the highly mineralised groundwater mixed with methane.

During the last 20 years, the average speed of the mudflow has been of 33.6 m/year. The maximum observed velocity, in the upper part of the landslide, was 9 m/day (Bertolini & Gorgoni, 2010; Bertolini & Fioroni, 2013). The rapid evolution of this landslide during the last century is also demonstrated by recent documents and images, as shown in Figure 31. In particular, the rapid retrogression of the crown, now reaching the mountaintop, is evident (Figure 31 c, d).

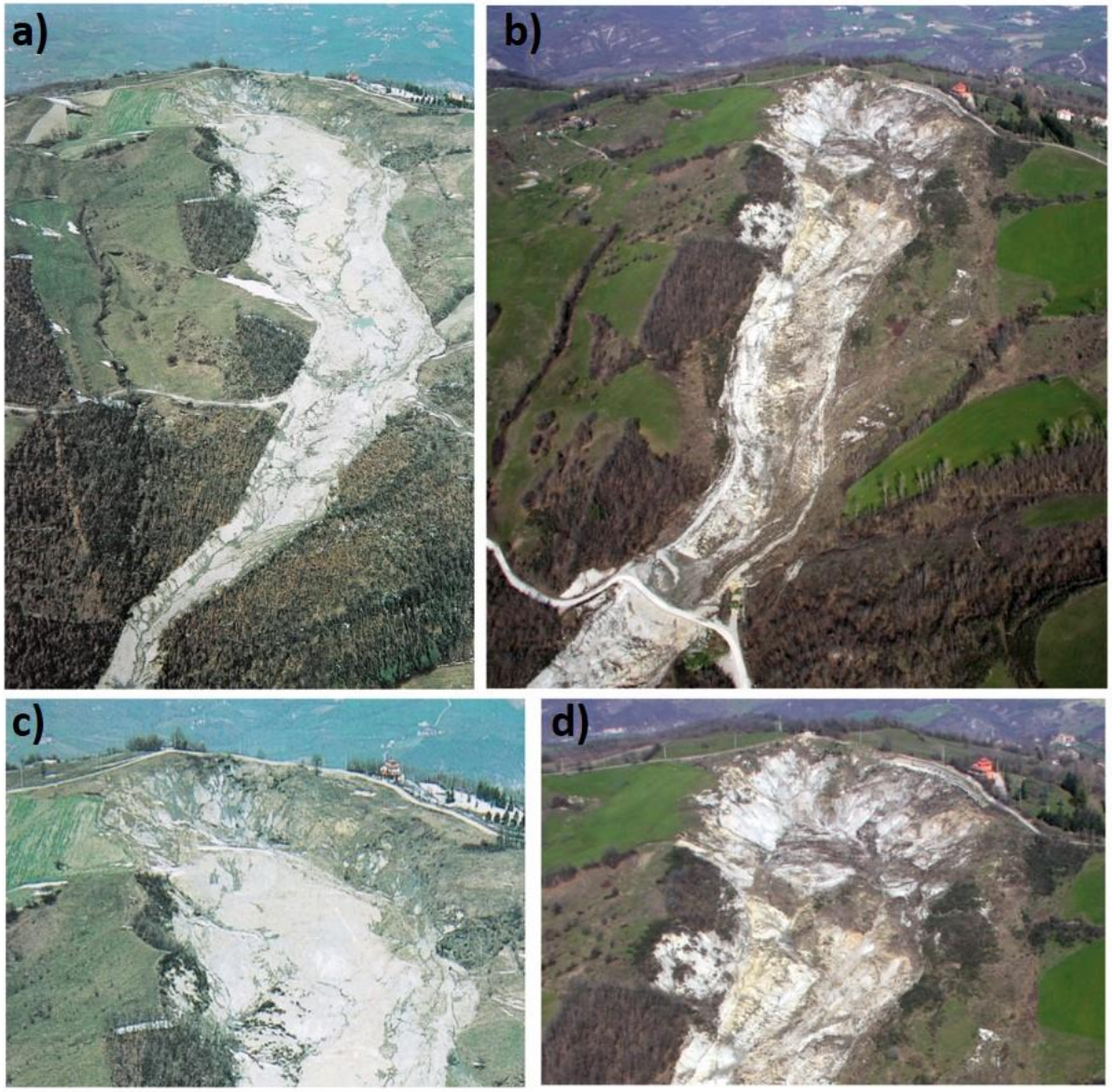

Figure 31. Pictures of the Roncovetro landslide taken in 2001 (a, c) and in 2014 (b, d). a) and b) shows the upper part of the landslide, while c) and d) highlight a detail of the crown noticeably in retrogression.

3.2 Installation of the Wi-GIM system

Two clusters have been installed respectively on the fastest moving sector of the depletion zone (Cluster 3) and on the narrowest part of the mudflow (Cluster 1), as shown in Figure 32.

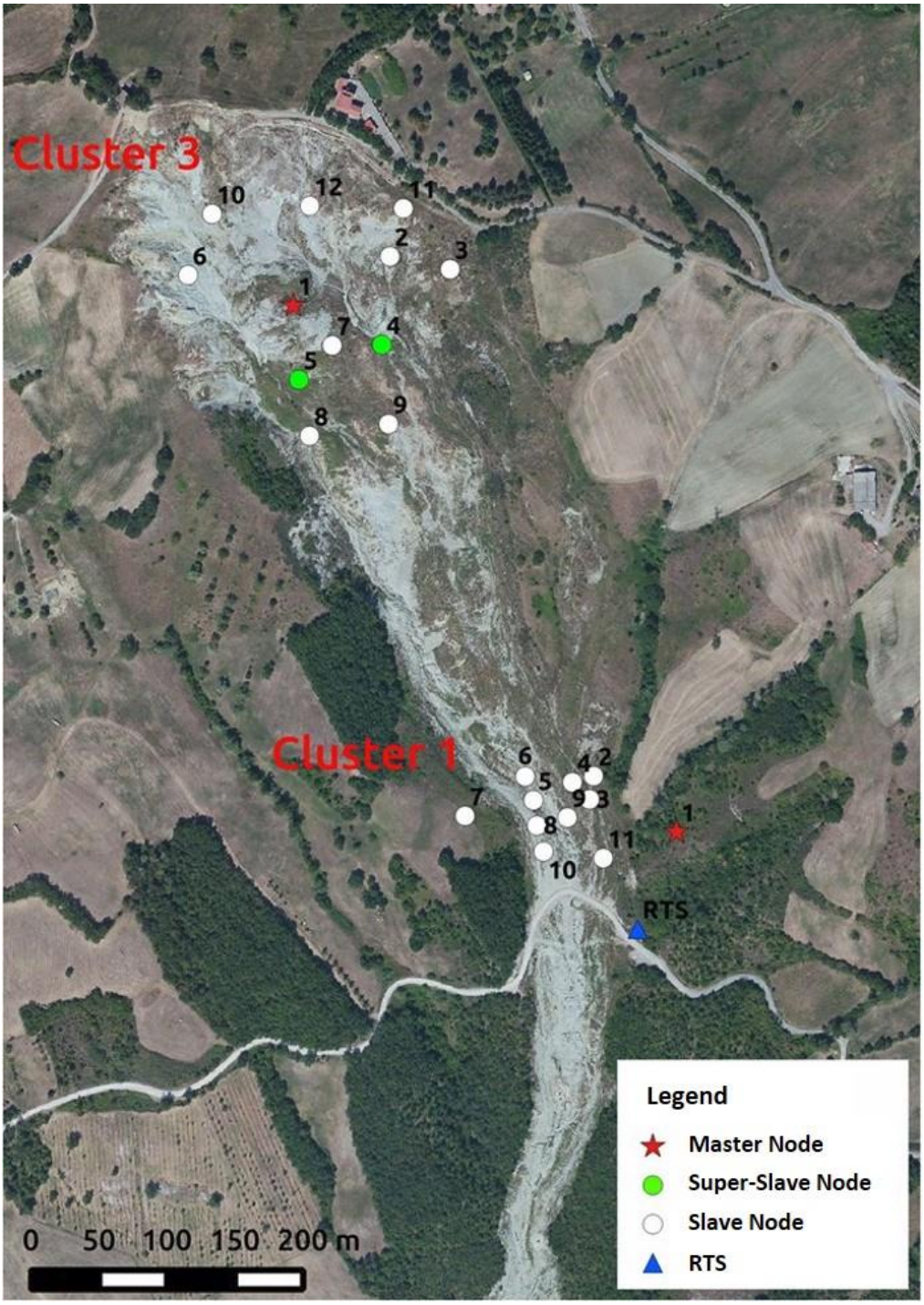

Figure 32. Location of the two clusters installed on the Roncovetro landslide.

Each node has been leaned on the ground on the top of the batteries, and the Decawave sensors have been fixed on iron poles 2.5 m high anchored in the terrain for 1 meter, so that the sensors were all at 1.5 meter from the ground (Figure 33).

Figure 33. Example of a Wi-GIM node installed on the landslide. At the top of the pole a target for the Robotic Total Station.

Cluster 1 was constituted by 11 nodes, with 3 of them placed outside of the landslide (i.e. nodes n. 1, 2 and 7, Figure 34a). Figure 34b shows the distances at which nodes have been installed, ranging from 14.4 m to 135.1 m. Cluster 3 was composed of 12 nodes (Figure 35a) placed at inter-node distances ranging from 35.1 m to 201.9 m, so to cover all the crown area (Figure 35b).

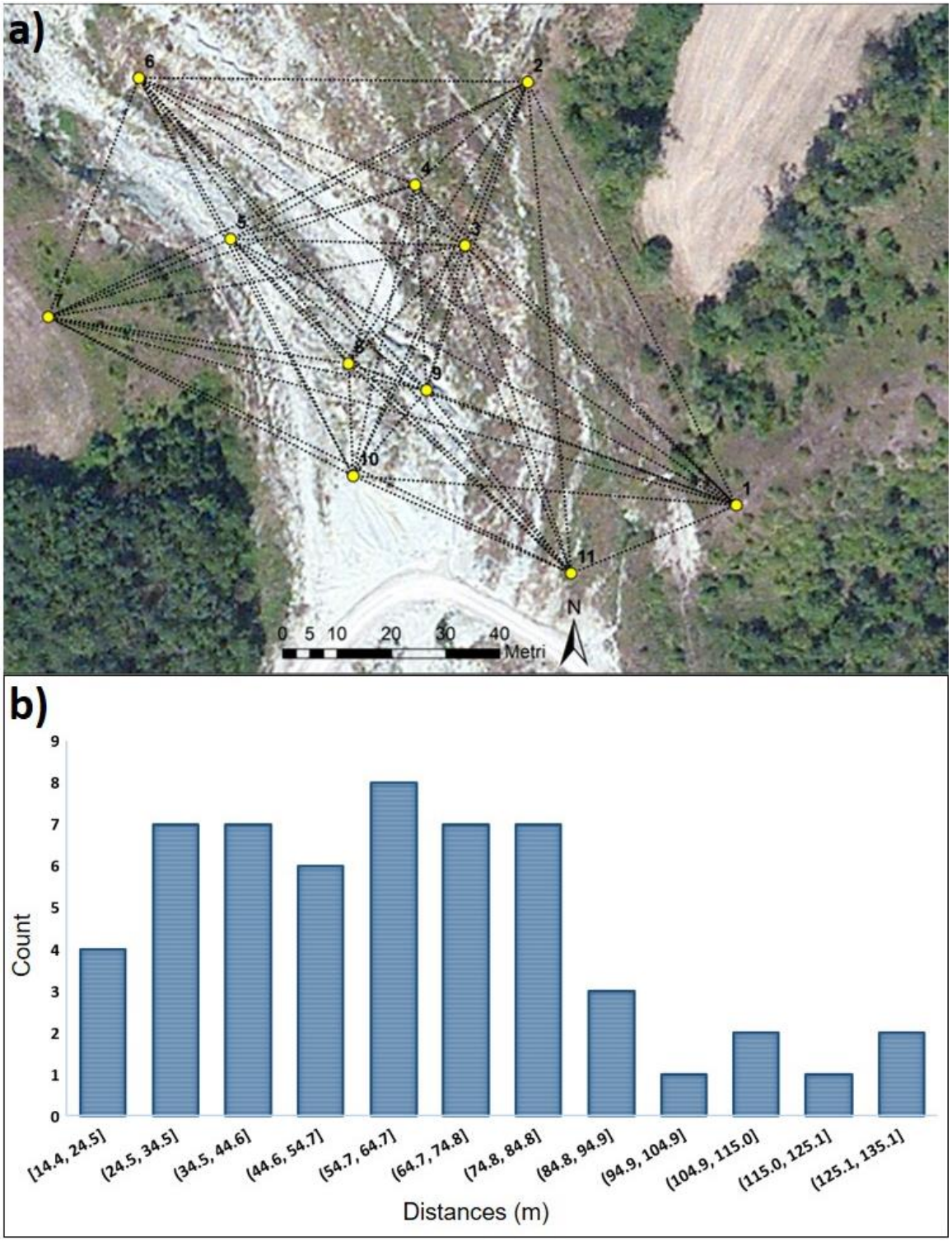

Figure 34. Roncovetro Cluster 1. a) Location of all the Cluster 1 nodes and their links (point 1 indicates the Master Node - MN); b) Distribution of node distances.

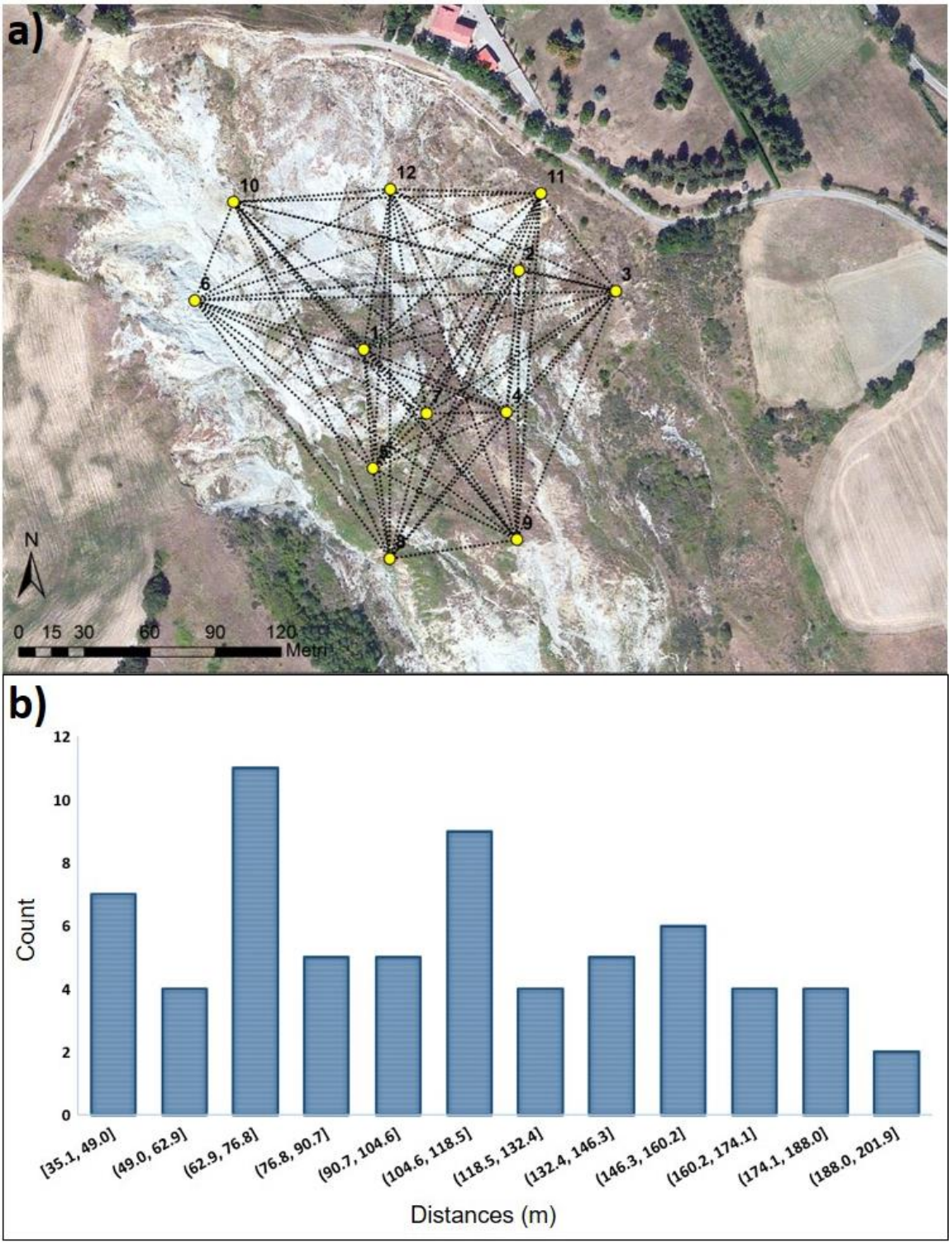

Figure 35. Roncovetro Cluster 3. a) Location of all the Cluster 3 nodes and their links (point 1 indicates the Master Node - MN); b) Distribution of node distances.

The acquisition frequency has been calibrated based on the velocity of the mudflow and set to 1 reading every 12 hours. Since measurements are redundant (as they are performed from one node to another and vice versa), this allows one to calculate daily averaged by using a total of 4 reading to reduce noise.

In detail, on February 1st, 2016 the first cluster (Cluster 3) was installed in the landslide crown area. The position of the nodes was chosen allowing to cover the entire area of interest and trying to ensure a distribution as equal as possible. Moreover, with the aim of acquire numerous and reliable data, the installation was done trying to position all the nodes in LOS, despite it was not easy due to the large distances involved and to the presence of several shrubs. The master node (node 1) was placed in the centre of the cluster (Figure 35).

Following the same criteria, on March 11th, 2016 a new cluster (Cluster 1) has been installed in the middle sector of the landslide. Here the earthflow is channelized, and the lower width allowed to cover the area of interest with 11 Nodes. As already mentioned, the master node (Node 1), Node 2 and Node 7 were located outside the unstable area (Figure 34). In this way it is possible to use their position as fixed reference, allowing to update the position of the other nodes within the earthflow. Moreover, the relative distance between the nodes of this Cluster is much smaller than in Cluster 3; consequently, it was also possible to analyse displacement accuracy with respect to node distance.

For both clusters, the acquisition started the same day of the installation and lasted until March 7th, 2017, day of the system removal.

Measurements validation has been performed using a LEICA NOVA MS50 Robotic Total Station (RTS) (Figure 36). The instrument has the same functionality as a total station integrated with a sensor for high precision in a completely automatic measurement procedure. It has a panoramic wide-angle camera and a 30x autofocusing coaxial camera. It provides real time video data on the embedded display in order to enable the visualization of high quality images. It was installed in a stable area near Cluster 1 in a location from where all nodes were visible (blue triangle, Figure 32). With the aim to validate the Wi-GIM system, prism targets and Decawave antennas have been installed on the same poles (Figure 37).

The RTS have been considered in this thesis also for the cost-benefit analysis presented in Section 6.1.4 together with a Ground-Based Interferometric Synthetic Aperture Radar (GBInSAR). However, the parallel monitoring has been done only with the RTS for the following reasons:

i. the measurements obtained with a RTS are punctual as the one's by the Wi-GIM system, while data from a GBInSAR are referred to pixels that, even with high resolutions, are far from being punctual. Therefore, the RTS allows a more proper comparison.

ii. Due to the strong presence of vegetation and to the complex morphology of the Roncovetro landslide, several areas investigated by the GBInSAR would have been not reliable or hide, respectively for the first and the second cause.

iii. To be installed, a GBInSAR system requires a planar surface with enough space for the binary on which it slides. Looking at the areas surrounding the Roncovetro landslide, there were not available spaces to correctly install the radar if not the street crossed by the landslide itself, that was not an adoptable solution.

iv. Finally, the high costs of the GBInSAR system (see Section 6.1.4 for further details about it).

Figure 36. The Leica Nova MS50 used for Roncovetro landslide traditional monitoring.

Figure 37. Prism targets installation on the same pole of the Wi-GIM antennas.

3.2.1 Data acquisition and processing

As explained in Section 2.1.3, the acquired data, once downloaded from the server or in situ from the SD cards, have been processed with the help of two specific MATLAB script. The result is a displacement time series whose noise can be further reduced by simple data averaging (daily averaged data), taking advantage of the system redundancy.

Before presenting some examples of data acquired in the Roncovetro site, focus is needed on the effect of the seasonal thermal excursion on measurements.

Looking at the analysed data, it was noted that measurements were influenced by temperature on a large scale, as showed by the displacement series of the Cluster 1 pair of nodes 5–10 (Figure 38). In detail, data followed a curve trend instead of a linear one despite no significant movement interested the area. In particular, the curve traced the seasonal temperature cycle, with its peak at the hottest months. As for the daily scale (see Section 2.2.2) ranging measurements have been put in relation with temperature values, showing a strong linear correlation (Figure 39).

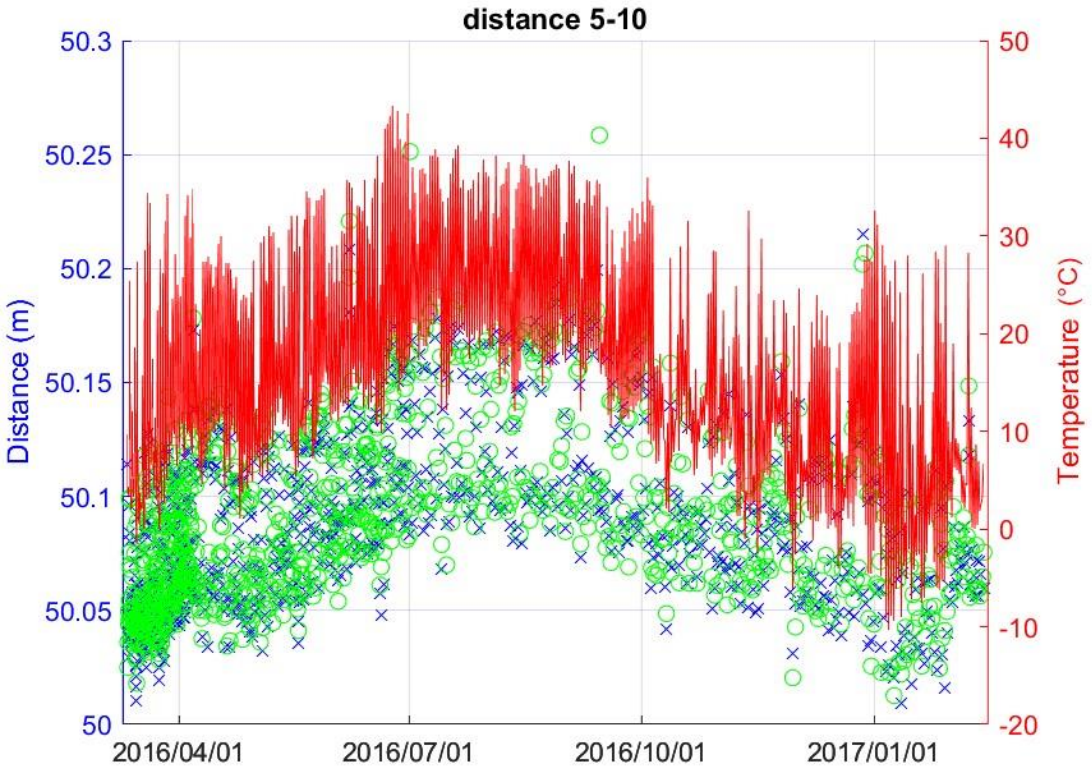

Figure 38. Displacement time series from the pair of nodes 5–10 of Roncovetro Cluster 1 with distance validated values considering a threshold of 2 m for the outliers' removal. The red line shows the temperature recorded by the master node during the whole monitoring period. Green circles and blue crosses represent the distance measured from one node to the other and vice versa. Where measurement points are extremely dense, the blue crosses are overlaid by the green circles.

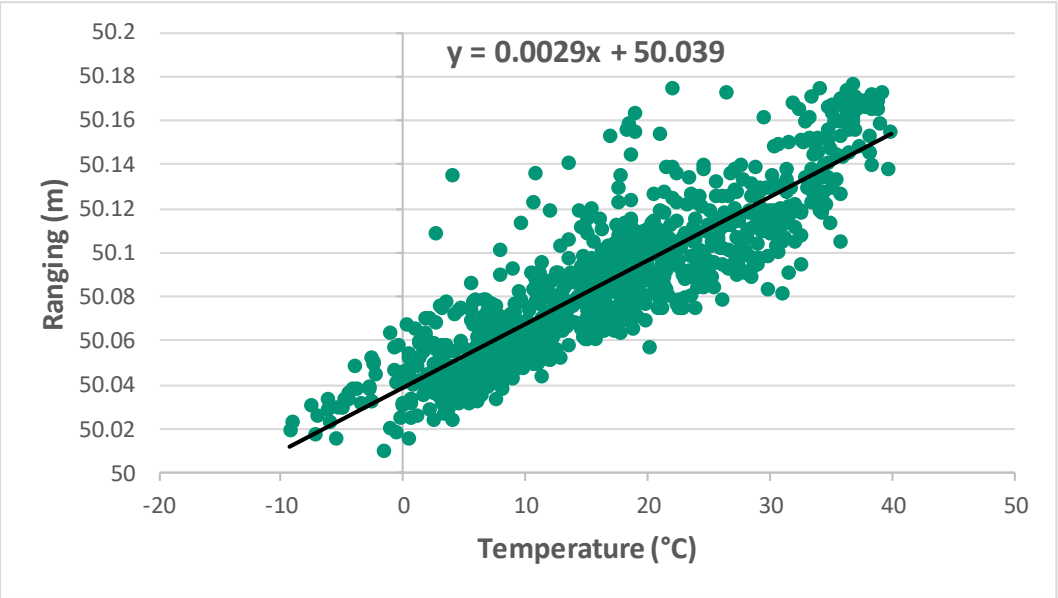

Figure 39. Scatter plot between measured ranging and temperature for the pair of nodes 5–10 of Cluster 1 (Figure 38). The equation in the upper part refers to the black trend line.

As previously described, a correction based on temperature (eq. 2 and eq. 3) was applied to the ranging values, showing a significant improvement of data quality, removing the effect of the temperature influence at a seasonal scale (Figure 40 – Figure 41). For each pair, *m* value was calculated and applied for its own correction.

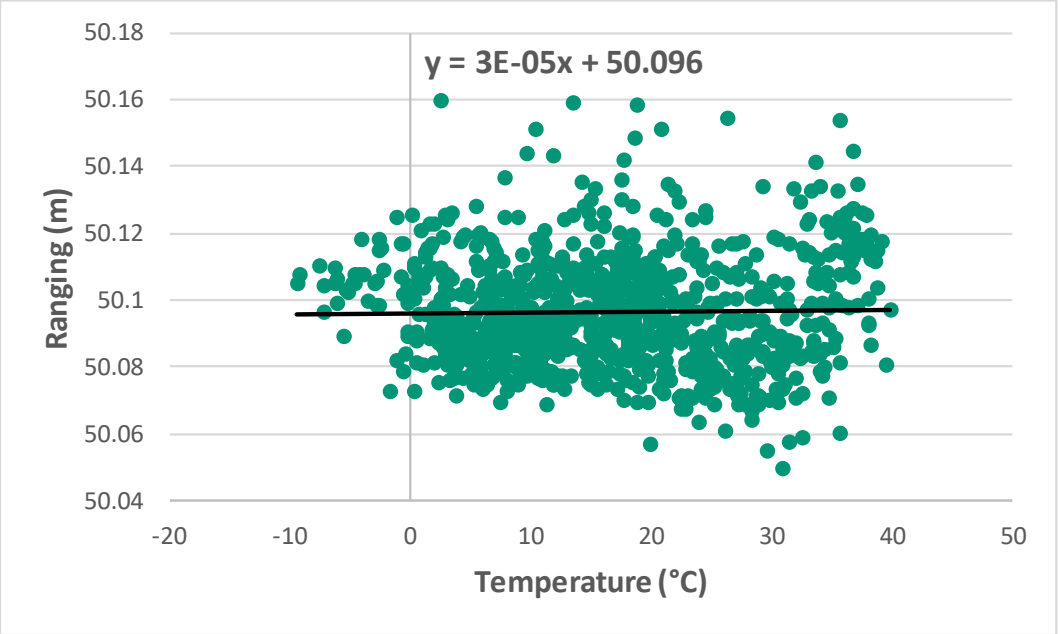

Figure 40. Scatter plot between corrected ranging values and temperature for the pair of nodes 5–10 of Cluster 1 after applying the correction presented in eq. 2 and eq. 3, setting *m* equal to 0.0029. Data present a Standard Deviation (σ) of 0.015 m. The equation in the upper part refers to the black trend line.

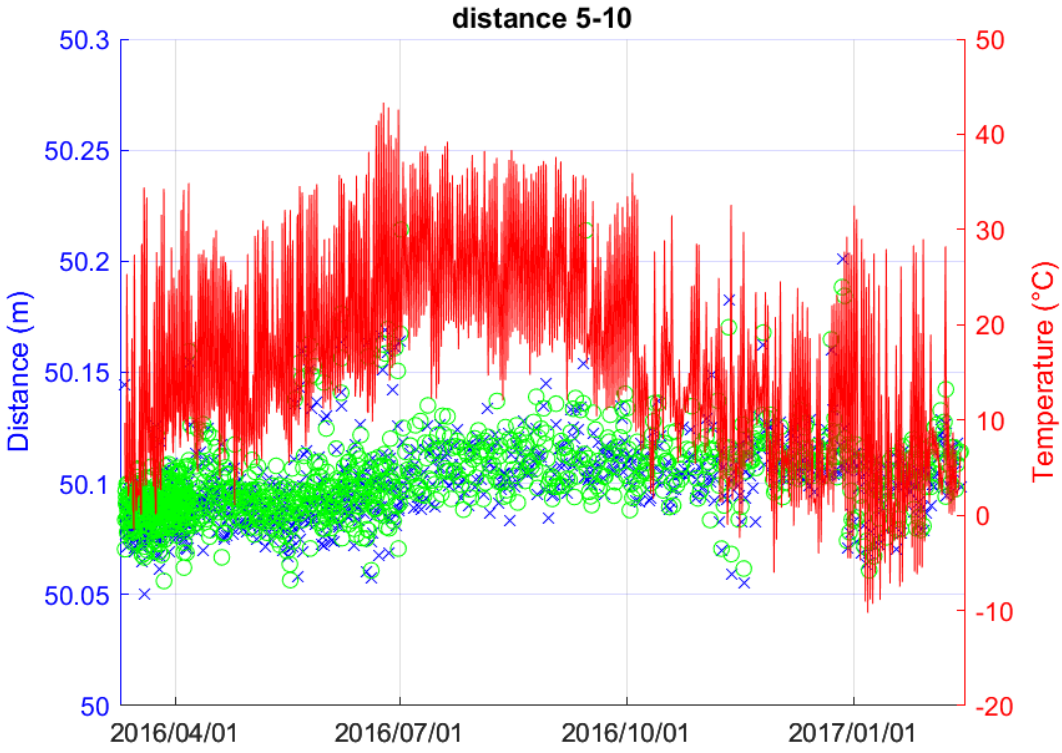

Figure 41. Displacement time series from the pair of nodes 5–10 of Roncovetro Cluster 1, after correction to remove temperature effects (eq. 2 and eq. 3 setting *m* equal to 0.0029), with distance validated values considering a threshold of 2 m for the outliers' removal. The red line shows the temperature recorded by the master node during the whole period. Green circles and blue crosses represent the distance measured from one node to the other and vice versa. Where measurement points are extremely dense, the blue crosses are overlaid by the green circles.

In the following paragraphs, some significant cases from Roncovetro test site, i.e. the pairs of nodes 1–3 belonging to Cluster 1 (from Figure 42 to Figure 47) and 1–10 belonging to Cluster 3 (from Figure 48 to Figure 53), are reported. Concerning the correction to remove temperature effects, data have been corrected setting *m* value equal 0.0030 for the former and 0.0044 for the latter.

In both cases, to eliminate the outliers, a threshold of 2 meters has been used, meaning that all values having a distance higher than 2 meters compared to the previous one have been considered as invalid data. Doing so, also the multipath effect is removed, as highly visible in Figure 44 and Figure 50.

Data can be plotted with the values of the Robotic Total Station (RTS), so to compare the measurements acquired from the two monitoring systems, as shown in Figure 47 and Figure 53. Please note that in this section data are only presented, as they will be deeply discussed in Section 6.1.1.

Furthermore, the daily mean values together with the battery level are reported in Figure 46 and in Figure 52. The voltage trend fluctuates from the maximum (about 13 V) to the minimum (up to 11 V). Once the voltage is very low, the batteries are replaced with some full charged ones and thus in the

graph the voltage values return to be high. The battery life was function of several values such as temperature and UMTS signal, but it generally lasted a bit more than one month, as explained in detail in Section 3.2.2.

Figure 42 – Figure 47 show the displacement time series from Nodes 1–3 of Roncovetro Cluster 1. The removal of invalid values and outliers allows to identify a displacement of 20 cm after a period of stability lasted until 2016/07/01. One can note a decrease of the acquired data (Figure 44 – Figure 45) when the movement started. This is due probably to a temporary loss of the LOS between the sensors subsequently restored. The precision of the measurements is about 10 cm (Figure 44), but it can be reduce at about 2.5 cm if considering a daily average (Figure 45).

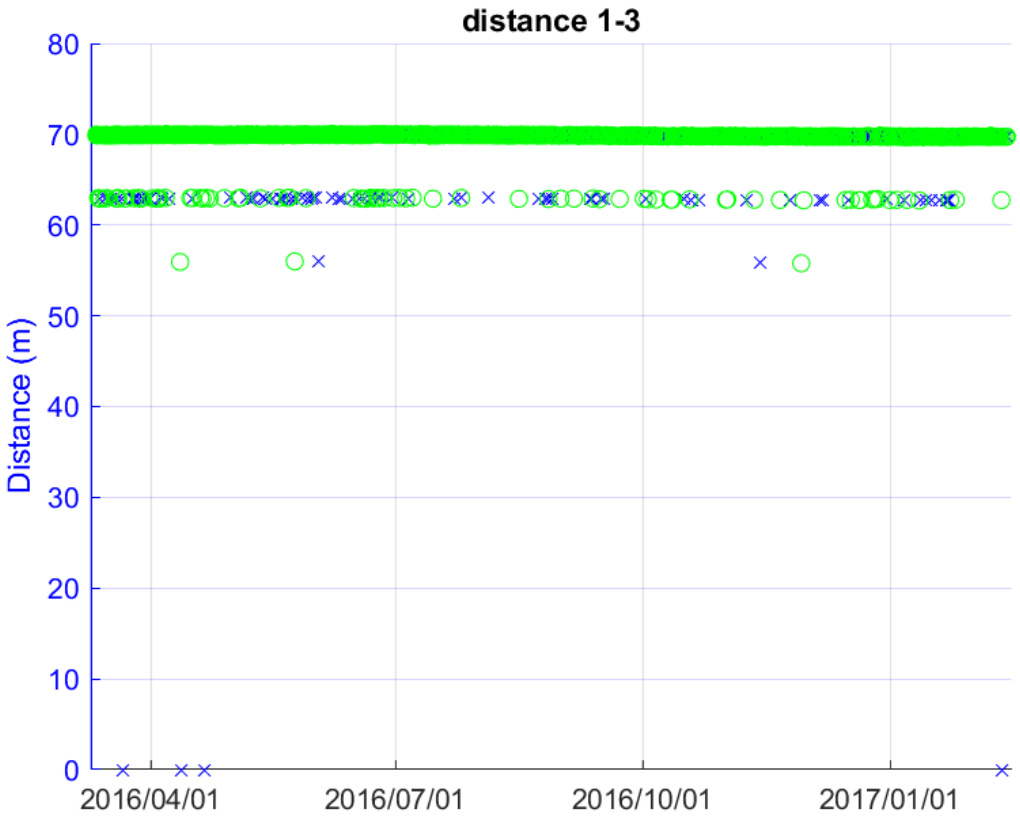

Figure 42. Displacement time series from the pair of nodes 1–3 of Roncovetro Cluster 1, raw distance values. Green circles and blue crosses represent the distance measured from one node to the other and vice versa. Where measurement points are extremely dense, the blue crosses are overlaid by the green circles.

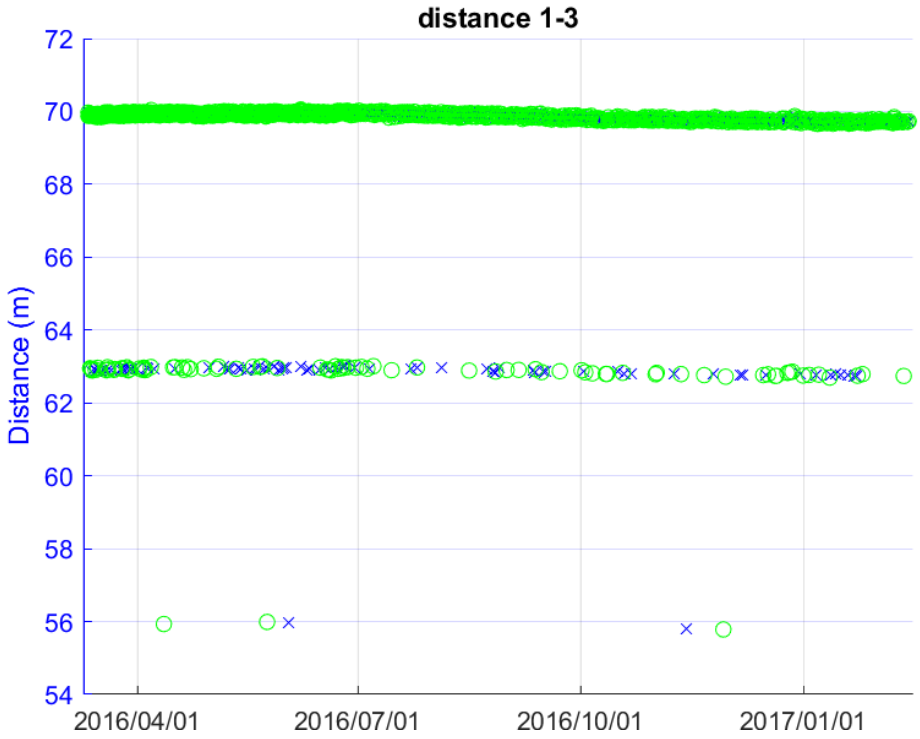

Figure 43. Displacement time series from the pair of nodes 1–3 of Roncovetro Cluster 1, distance values without invalid measurements (i.e. nonvalues and zero values). Green circles and blue crosses represent the distance measured from one node to the other and vice versa. Where measurement points are extremely dense, the blue crosses are overlaid by the green circles.

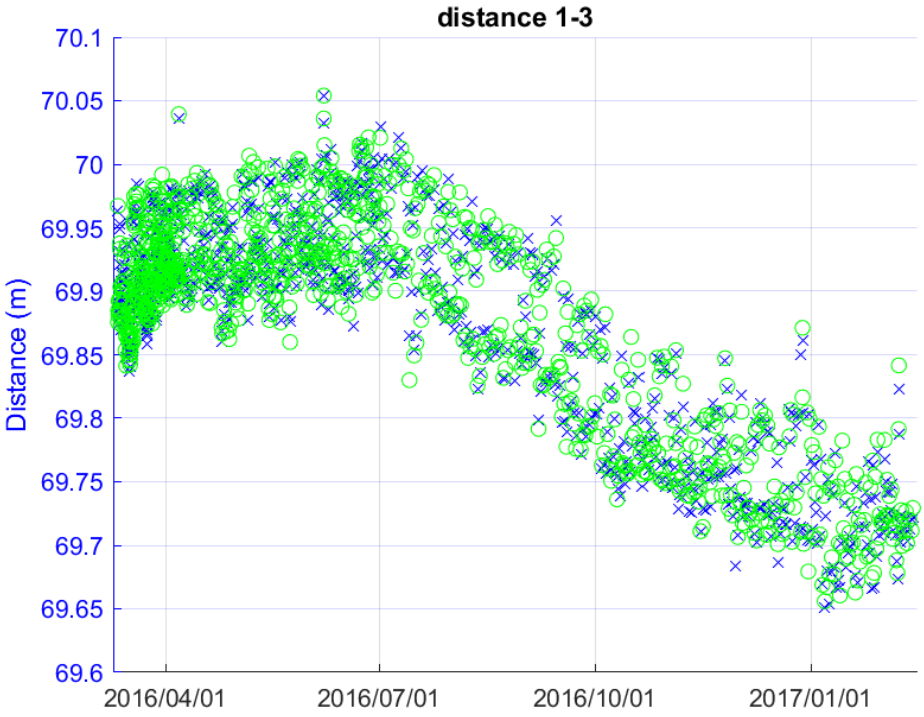

Figure 44. Displacement time series from the pair of nodes 1–3 of Roncovetro Cluster 1, distance validated values, considering a threshold of 2 m for the outlier's removal. Green circles and blue crosses represent the distance measured from one node to the other and vice versa. Where measurement points are extremely dense, the blue crosses are overlaid by the green circles.

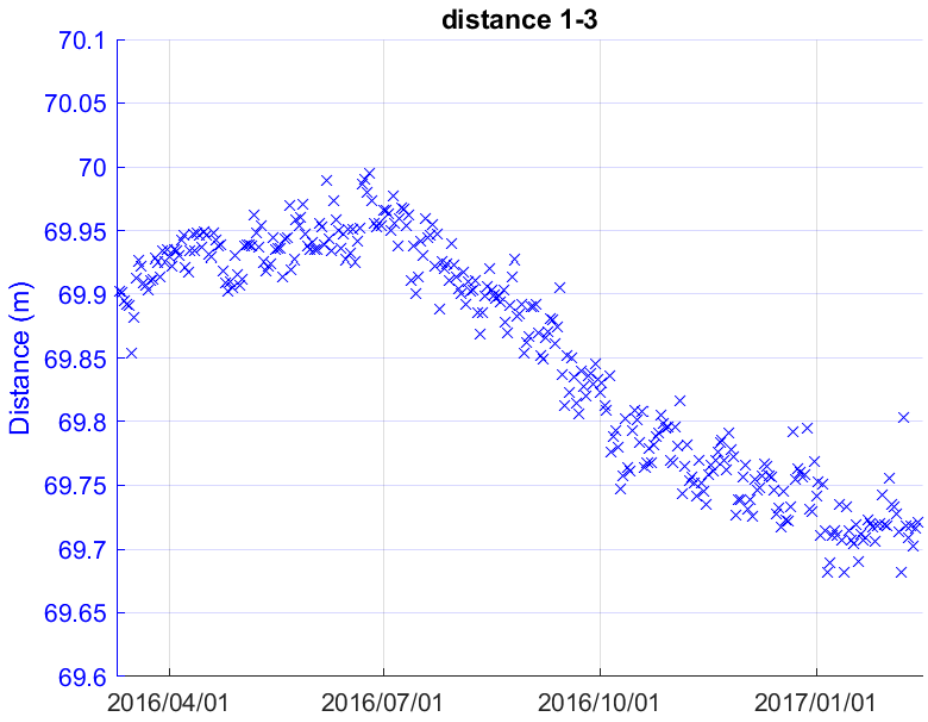

Figure 45. Displacement time series from the pair of nodes 1–3 of Roncovetro Cluster 1, distance daily mean values.

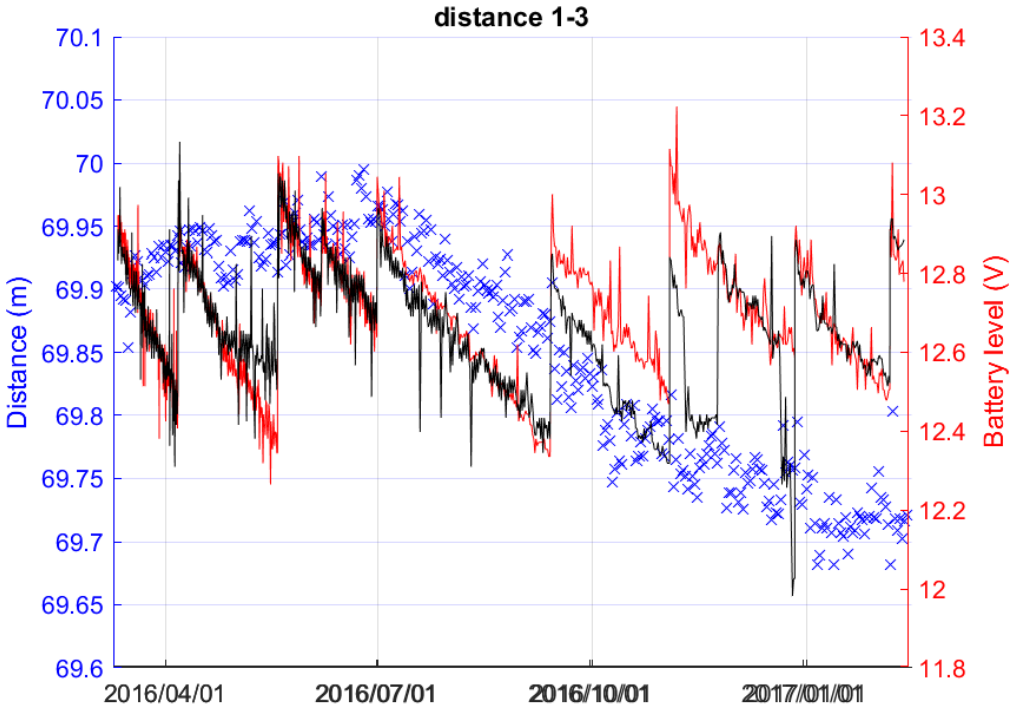

Figure 46. Displacement time series from the pair of nodes 1–3 of Roncovetro Cluster 1, distance daily mean values and batteries level. The red line refers to the battery level of Node 1, whereas the black one refers to the Node 3 one.

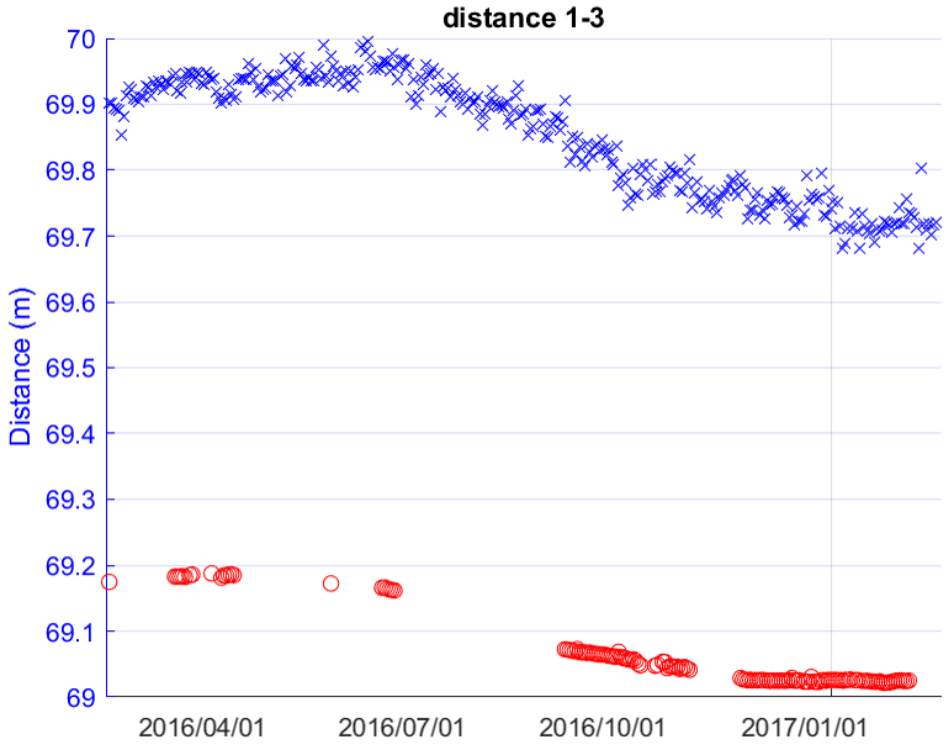

Figure 47. Displacement time series from the pair of nodes 1–3 of Roncovetro Cluster 1. Blue crosses: distance daily mean values measured by Wi-GIM. Red circles: RTS data.

Similarly, Figure 48 to Figure 53 show the displacement time series from Nodes 1–10 of Cluster 3. In particular, in Figure 50 the ranging measurements after the outlier's removal procedure are reported. Here, a displacement of about 4.5 m occurred in the period March–December 2016 is estimated, with a strong acceleration started in May 2016, during which, a shift of 1 m is evident in the graph. This apparent movement is actually due to the pole that slowly tilted and finally fell down. June 2016 records then an abrupt increase of the distance due to the correct repositioning of the pole.

A lack of data characterizes the time series from the end of June to the beginning of July 2016. This correspond to the life end of the battery, which was replaced with a full charged one on 2016/07/01 (Figure 52).

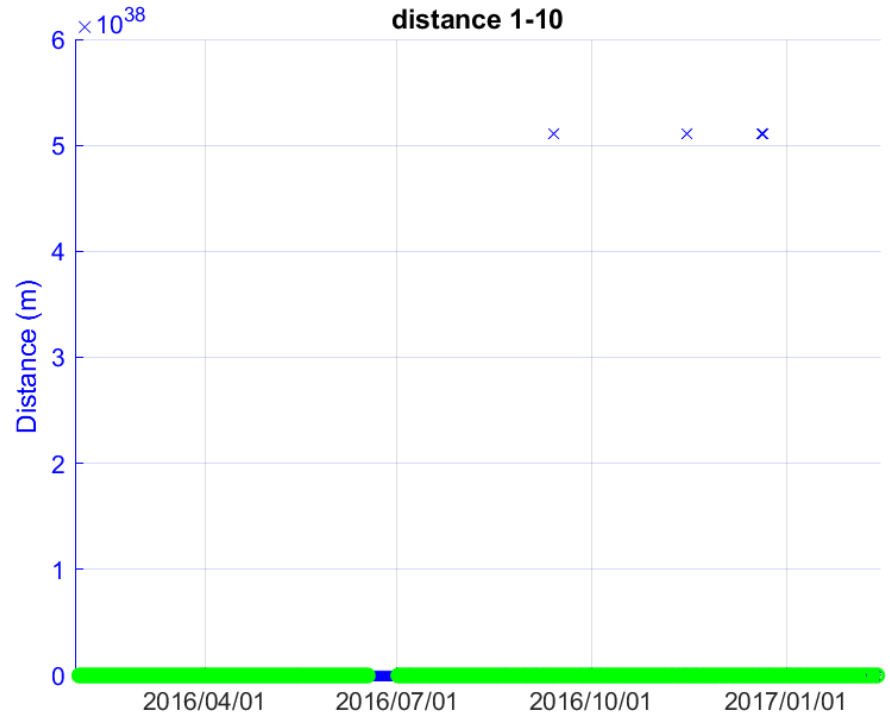

Figure 48. Displacement time series from the pair of nodes 1–10 of Roncovetro Cluster 3, raw distance values. In this case, raw data present an impressive error (distances in the order of 10^{38} m) that has been removed filtering the non-valid measurements (Figure 49). Green circles and blue crosses represent the distance measured from one node to the other and vice versa. Where measurement points are extremely dense, the blue crosses are overlaid by the green circles.

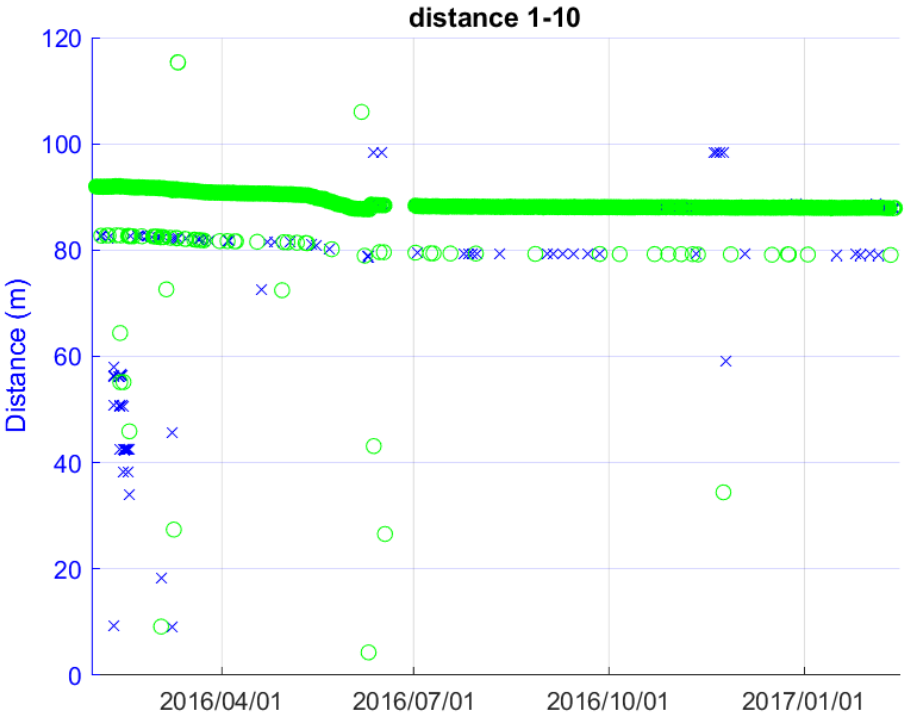

Figure 49. Displacement time series from the pair of nodes 1–10 of Roncovetro Cluster 3, distance values without invalid measurements (i.e. nonvalues and zero values). Green circles and blue crosses represent the distance measured from one node to the other and vice versa. Where measurement points are extremely dense, the blue crosses are overlaid by the green circles.

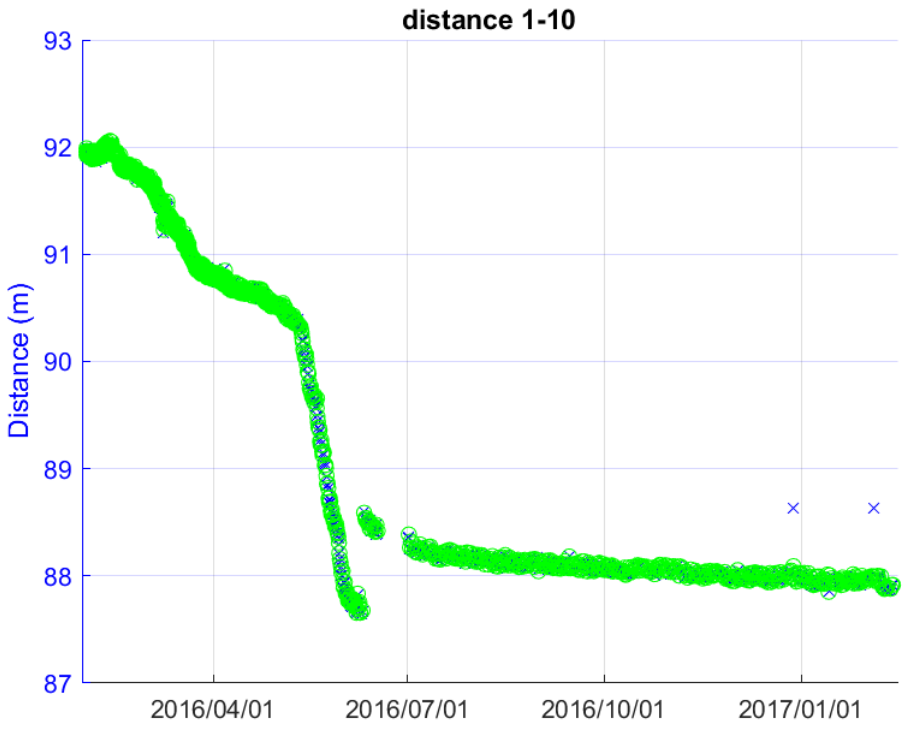

Figure 50. Displacement time series from the pair of nodes 1–10 of Roncovetro Cluster 3, distance validated values, considering a threshold of 2 m for the outliers' removal. Green circles and blue crosses represent the distance measured from one node to the other and vice versa. Where measurement points are extremely dense, the blue crosses are overlaid by the green circles.

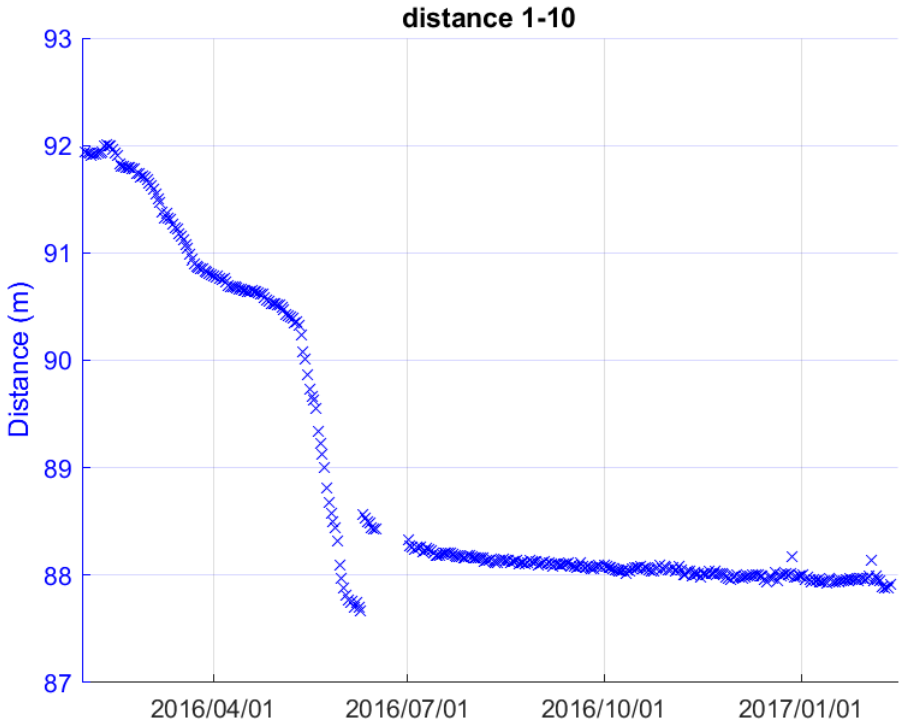

Figure 51. Displacement time series from the pair of nodes 1–10 of Roncovetro Cluster 3, distance daily mean values.

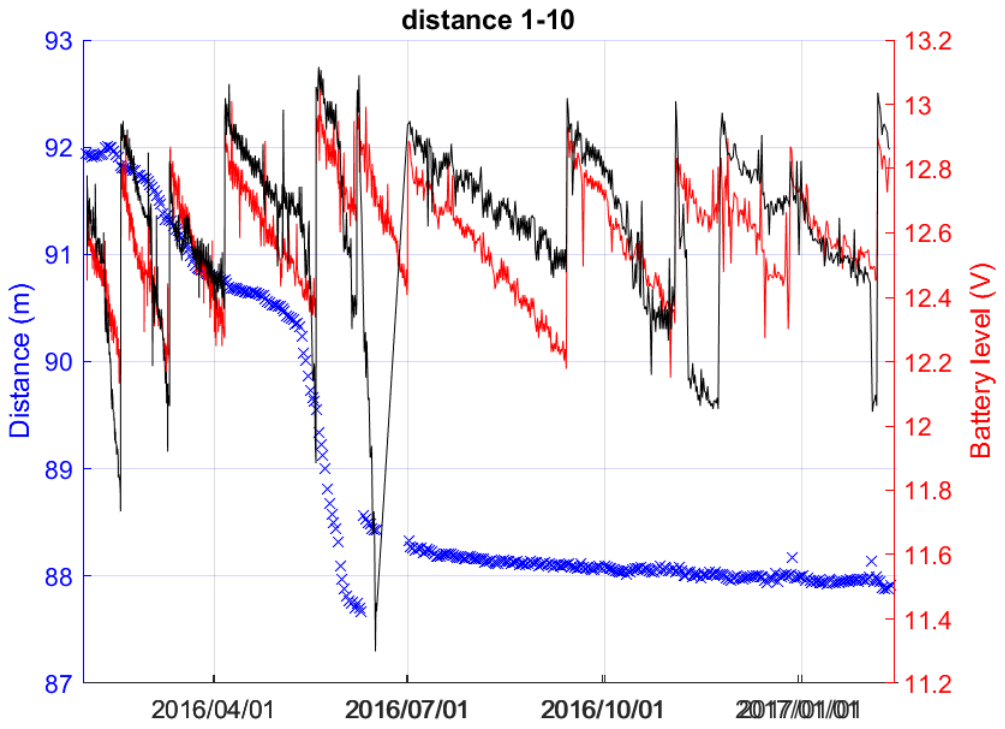

Figure 52. Displacement time series from the pair of nodes 1–10 of Roncovetro Cluster 3, distance daily mean values and batteries level. The red line refers to the battery level of Node 1, whereas the black one refers to the Node 10 one.

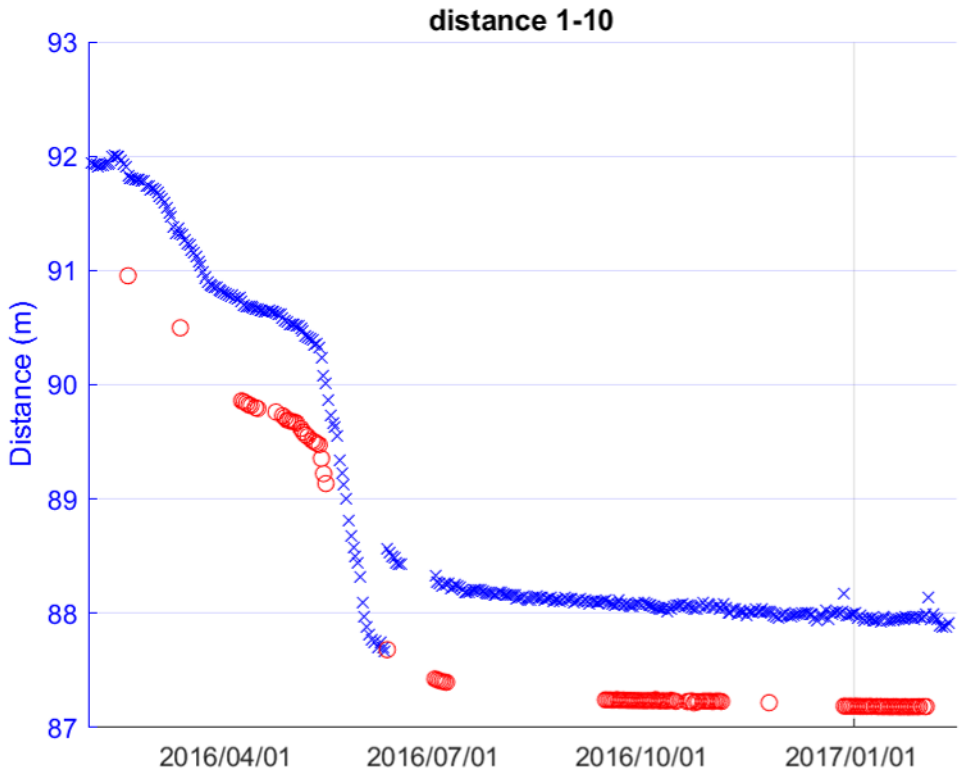

Figure 53. Displacement time series from the pair of nodes 1–10 of Roncovetro Cluster 3. Blue crosses: distance daily mean values measured by Wi-GIM. Red circles: RTS data.

Concerning the precision, it is the same observed for the previous analysed pair, i.e. about 10 cm for the complete displacement time series (Figure 50) and about 2.5 cm for the daily mean values (Figure 51). This precision is confirmed also when using of a Savitzky-Golay smoothing process, in this case more appropriate than a daily average due to data dispersion and trend (Figure 54–Figure 55). This method performs a polynomial regression to the data in a moving window, preserving in this way the peaks that would be smooth by a simple average, that is particularly true for case as the one of Figure 54, where the absence of significant movements cause a higher dispersion in data visualisation. Wider is the chosen window (defined by points), higher the smoothing is (and therefore lower the definition of the peaks). In the case here presented, a moving window of 40 point has been selected, a value that allows to make a smoothing without losing information and to better evaluate the precision of the system.

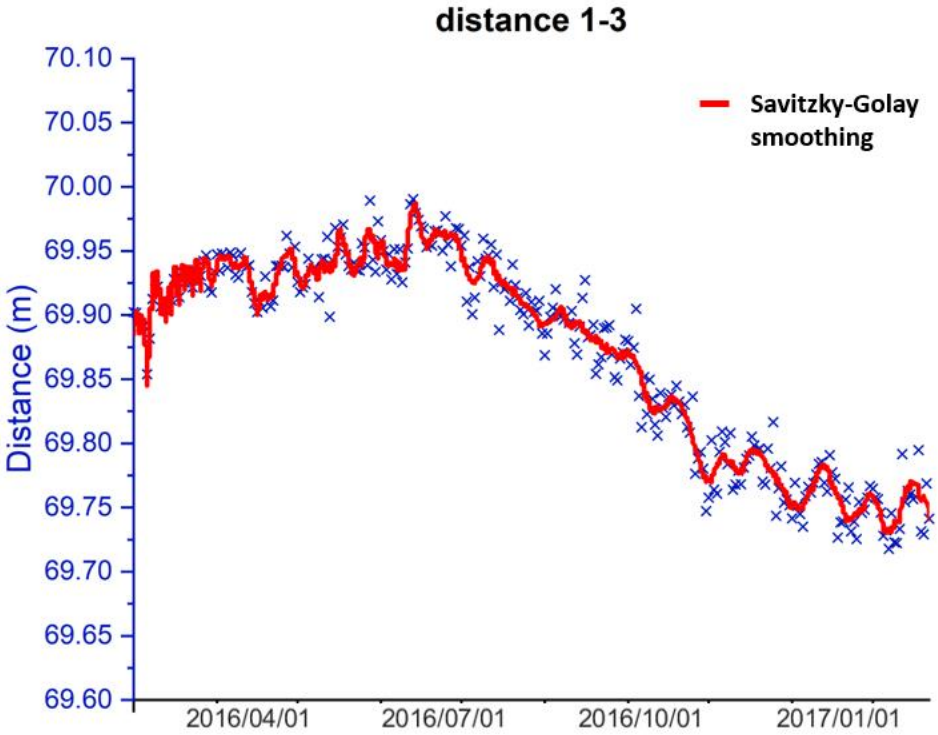

Figure 54. Displacement time series from the pair of nodes 1–3 of Roncovetro Cluster 1. Blue crosses: distance daily mean values. Red line: Savitzky-Golay polynomial regression line.

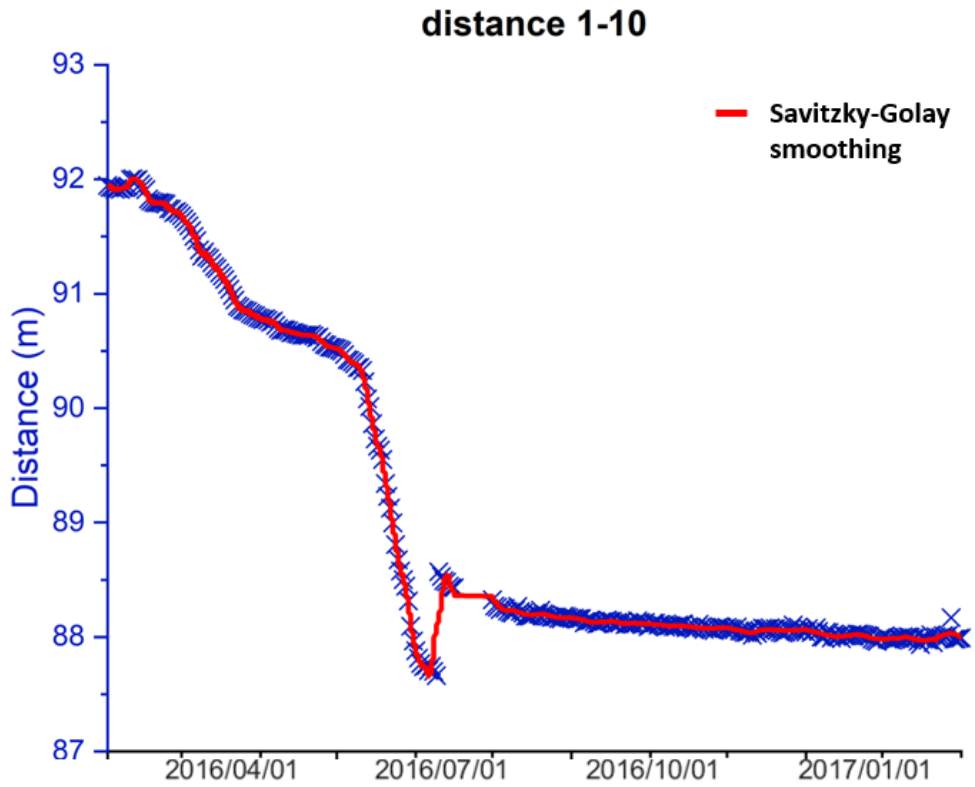

Figure 55. Displacement time series from the pair of nodes 1–10 of Roncovetro Cluster 3. Blue crosses: distance daily mean values. Red line: Savitzky-Golay polynomial regression line.

Roncovetro experimental survey also permitted to assess the effects of long distances on the overall performances of the system. Even if distances longer than 100 m resulted in more difficult transmissions, they did not affect the precision and accuracy of the measurements. More specifically, the distance between nodes has been studied in relation with data precision by calculating the standard deviation (σ) of measurements made at different distances. Pairs 3–4, 1–3 and 1–7 for cluster 1 and pairs 2–11, 1–2 and 5–12 for cluster 3 have been examined (Figure 56 – Figure 57 – Figure 58 – Figure 59 – Figure 60 – Figure 61).

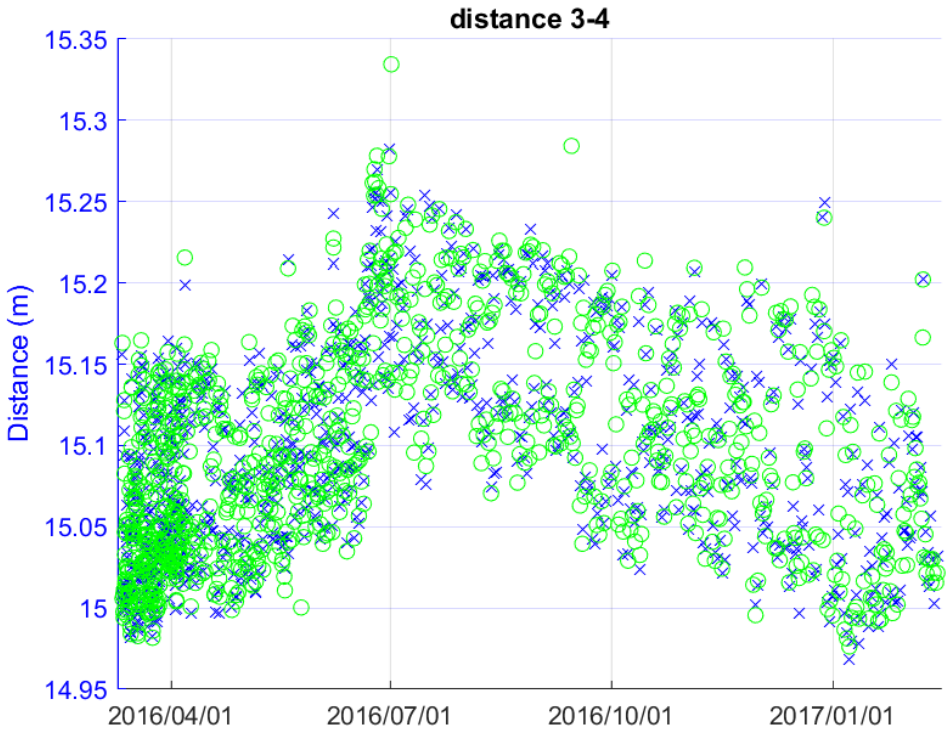

Figure 56. Displacement time series from the pair of nodes 3–4 of Roncovetro Cluster 1, distance validated values, considering a threshold of 2 m for the outliers' removal. Green circles and blue crosses represent the distance measured from one node to the other and vice versa. Where measurement points are extremely dense, the blue crosses are overlaid by the green circles.

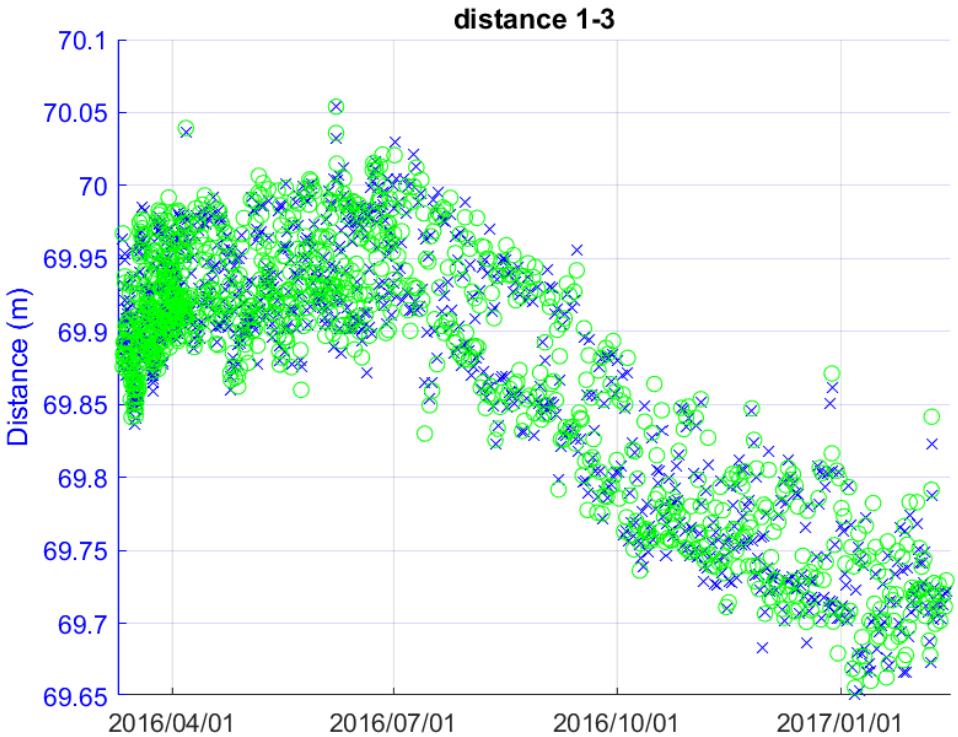

Figure 57. Displacement time series from the pair of nodes 1–3 of Roncovetro Cluster 1, distance validated values, considering a threshold of 2 m for the outliers' removal. Green circles and blue crosses represent the distance measured from one node to the other and vice versa. Where measurement points are extremely dense, the blue crosses are overlaid by the green circles.

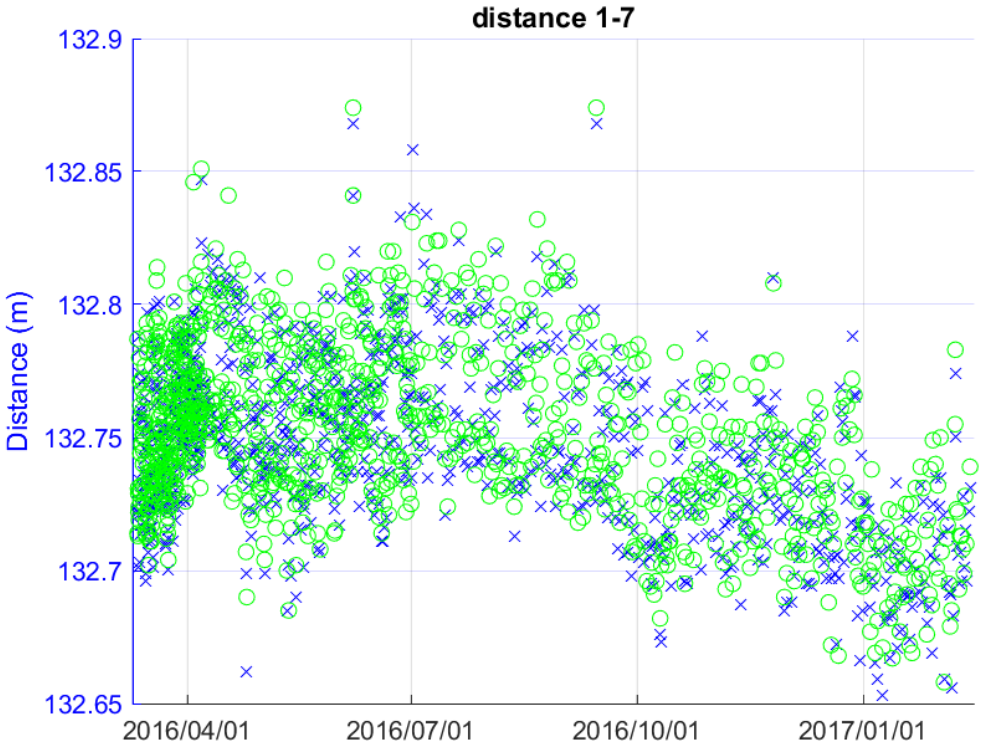

Figure 58. Displacement time series from the pair of nodes 1–7 of Roncovetro Cluster 1, distance validated values, considering a threshold of 2 m for the outliers' removal. Green circles and blue crosses represent the distance measured from one node to the other and vice versa. Where measurement points are extremely dense, the blue crosses are overlaid by the green circles.

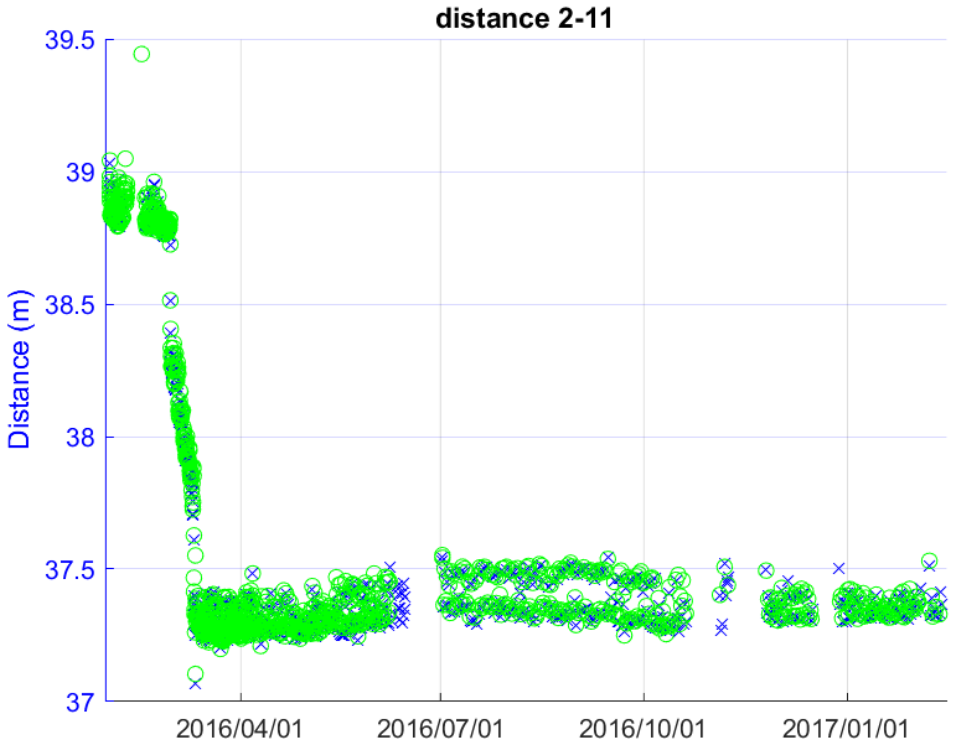

Figure 59. Displacement time series from the pair of nodes 2–11 of Roncovetro Cluster 3, distance validated values, considering a threshold of 2 m for the outliers' removal. Green circles and blue crosses represent the distance measured from one node to the other and vice versa. Where measurement points are extremely dense, the blue crosses are overlaid by the green circles.

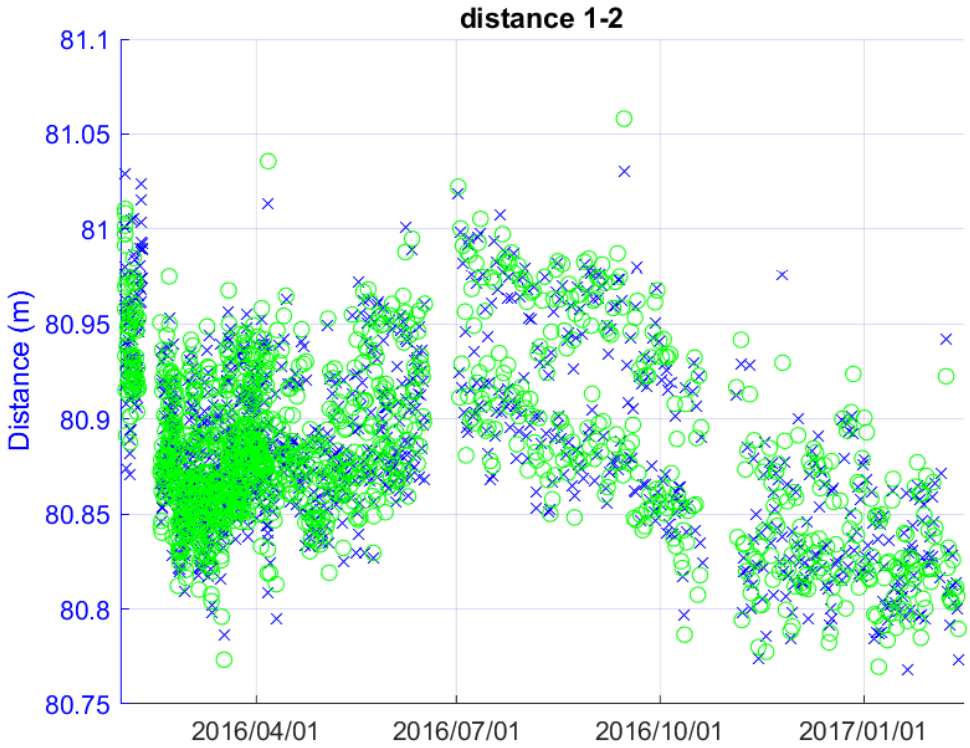

Figure 60. Displacement time series from the pair of nodes 1–2 of Roncovetro Cluster 3, distance validated values, considering a threshold of 2 m for the outliers' removal. Green circles and blue crosses represent the distance measured from one node to the other and vice versa. Where measurement points are extremely dense, the blue crosses are overlaid by the green circles.

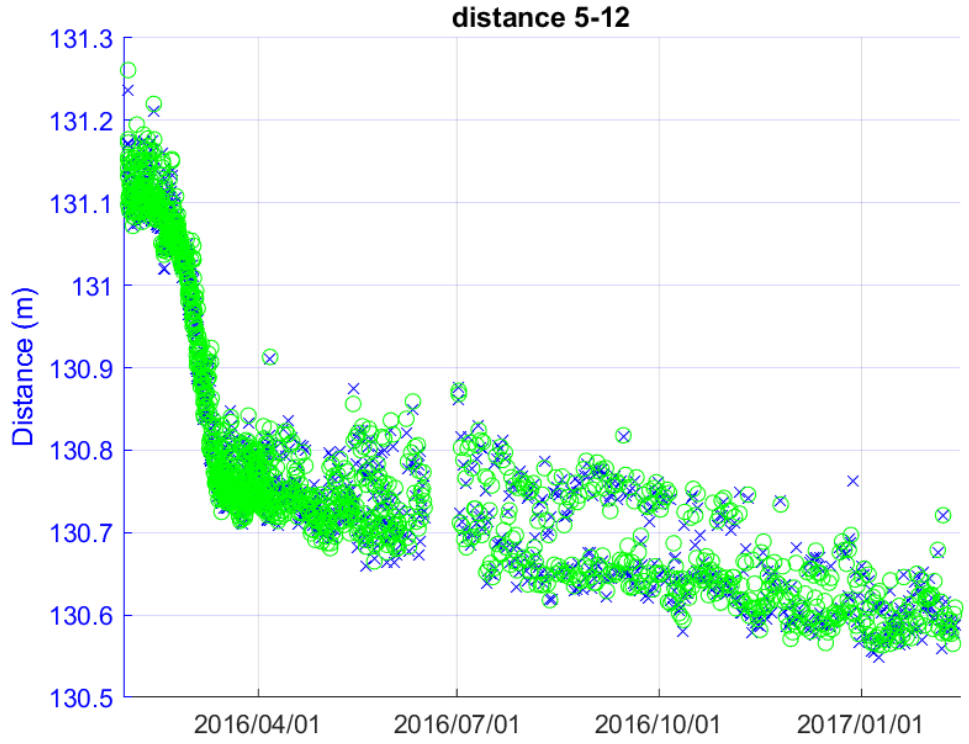

Figure 61. Displacement time series from the pair of nodes 5–12 of Roncovetro Cluster 3, distance validated values, considering a threshold of 2 m for the outliers' removal. Green circles and blue crosses represent the distance measured from one node to the other and vice versa. Where measurement points are extremely dense, the blue crosses are overlaid by the green circles.

To evaluate their dispersion, data have been analysed during periods of stability for each pair (from 11 March 2016 to 31 May 2016 for cluster 1 and from 1 December 2016 to 6 February 2017 for cluster 3), to be sure that the measurements were not relative to actual movements. All the pairs selected were characterized by a percentage of received data higher than 80% and of valid data higher than 60%. The results of this analysis did not highlight any correlation between distance and Wi-GIM precision (Table 7).

	Nodes	Wi-GIM mean distance (m)	σ (cm)
Cluster 1	3–4	15.09	4.7
	1–3	69.88	3.5
	1–7	132.75	2.6
Cluster 3	2–11	37.35	3.6
	1–2	80.83	3.0
	5–12	130.61	3.4

Table 7. For each pair is reported the mean distance measured with Wi-GIM and the standard deviation (σ) of the measurements. For the standard deviation evaluation, only data belonging to period of stability have been considered.

3.2.2 Power Consumption

As previously mentioned, the component of the Wi-GIM system have been designed in order to reduce the power consumption and maximize the batteries' life. Since the battery consumption is a critical point for a Wireless Sensor Network, a proper protocol/algorithm (i.e. the sleep mode) to save energy has been implemented. For a longer use of the WSN on a landslide, the battery of each node can be replaced with a full charge one without moving the node. However, field measurements revealed a battery life shorter than that expected; this was mainly due to:

i. low temperature (cold season);
ii. low UMTS signal, which required a longer wake up time to try sending the acquired data to the ftp server;
iii. long node to node distances, which sometimes implied several communication attempts.

For these reasons the acquisition rate was calibrated during the Wi-GIM monitoring campaign, to get an optimal balance between data continuity and logistic capability to maintain the whole system active. Table 8 summarizes the battery replacement activities related to monitoring duration for each cluster; note that the shortest life at Roncovetro Cluster 3 is due to the maximum mean node to node distance.

Cluster id	From	To	Monitoring duration (days)	Battery replacements	Mean battery life (days)
Cluster 1	11/03/2016	24/04/2017	409	10	41
Cluster 3	01/02/2016	24/04/2017	447	12	37

Table 8. Battery replacement activities related to monitoring duration for each cluster.

4. WiSIO: Wireless Sensor networks Installation Optimizer

The monitoring at both test sites (Arcetri and Roncovetro), highlighted the influence of the LOS condition on data properties.

To make the most of a WSN, an optimal deployment of sensors is indeed essential, namely an equal and thoughtful distribution. In this context, sensor deployment problems have been studied in a variety of environments (Tan et al., 2009). Wang et al. (2003) geometrically analysed the relationship between coverage and connectivity in a WSN considering an obstacle-free environment; Zou and Chakrabarty (2003) proposed a virtual force algorithm as a sensor deployment strategy after an initial random placement of sensors. In the case of UWB WSNs this issue is emphasised by the need to have the sensors in LOS. An obstacle between transmitter and receiver, i.e., non-line-of-sight (NLOS), implies a bias in the estimation of the distance. For this reason, it is important to install all the sensors so that they are visible to each other, since respecting the inter-visibility can lead to more numerous and reliable data.

In this framework, in this study an algorithm able to find the best locations to install sensors part of a WNS requiring LOS called WiSIO (Wireless Sensor network Installation Optimizer) has been implemented based on the following three criteria. (i) inter-visibility between sensors is guaranteed by exploiting a modified version of the Hidden Point Removal operator by Katz et al. (2007); (ii) equal distribution of devices is ensured; (iii) different weights are preferentially assigned to critical portions of the investigated landslide. Weighted areas are significant portions of a landslide and can be previously selected by the user (e.g. areas most at risk, areas with higher displacement values, easily reachable areas or stable areas).

4.1 General structure

The final aim of the algorithm is to geometrically find the best locations to install a WSN requiring visibility, i.e. i^{th} Point (P_i). To pursue this goal, WiSIO has been implemented as a simple, fast, and easy code in MATLAB (R2018a, MAthWorks, Natick, MA, USA), but it can be run also in open source program such as GNU Octave (GNU Octave, John W. Eaton) that has an exact compatibility (Figure 62, Annex A). It can be applied to several natural scenarios such as vertical cliffs, gentle and steep slopes, and terraces. Its employment can also be extended to buildings, small objects, and, more generally, to every artificial structure without geometrical or size limits.

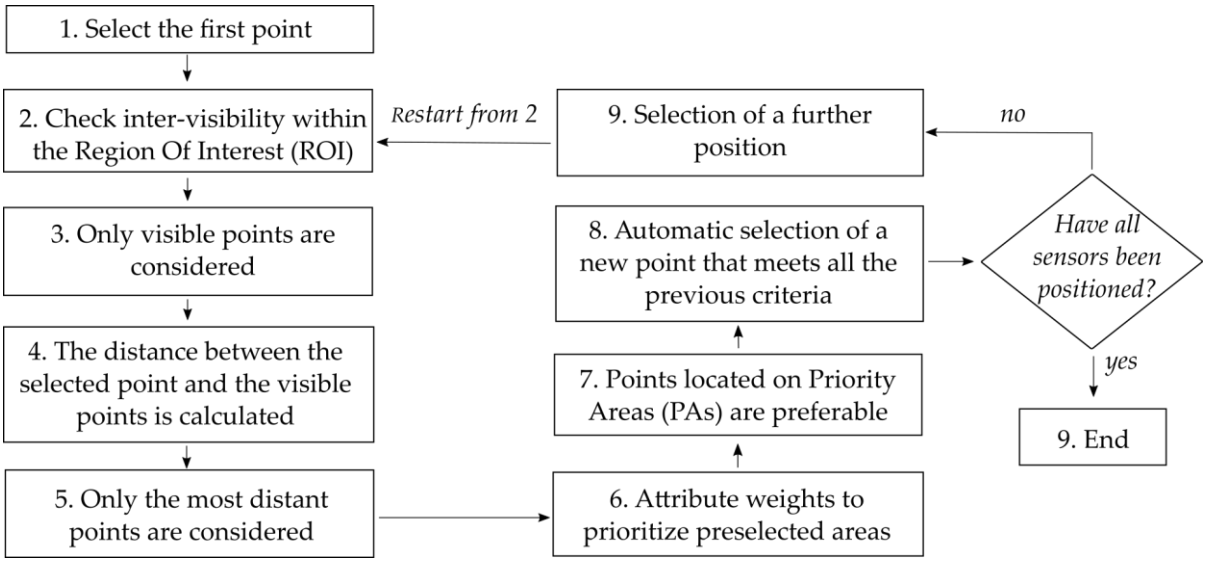

Figure 62. WiSIO operating scheme. The selection of the first point occurs in a semi-automatic way. Depending on the quantity of devices the user wants to install, once a new Pi is pointed out (box n. 8), the code ends or restart from box n.2.

The central point of the algorithm is visibility analysis. Similar analyses are the common function of most Geographic Information System software, but in all cases they are based on the digital elevation model. This kind of analysis uses the elevation of each cell of the model to detect if they are visible or not from a given point of view. Line of sight from the point of view to the target cells is substantially planned, and when cells of higher elevation intersect them, the view is considered obstructed. It goes without saying that the method works well when dealing with straight lines, as is the case of buildings and roads, and this is why these viewshed analyses are usually made on the digital elevation model and not on the digital surface model. Dealing with vegetation in fact, constrains these methods to significant geometrical approximations even when models have good resolution. With the aim of keeping all original information, the input data of the proposed algorithm are high-resolution 3D point clouds. Working directly with point clouds, as in the case of WiSIO, aims to be able to work with harsh

environments, including not only vegetation but also steep, rough, and overhanging terrain. The algorithm works without reconstructing any kind of surface, avoiding errors and approximations usually caused by traditional modelling. The heterogeneity and the resolution of 3D point clouds are consequently main limitations of the developed code: the lower the resolution of the input data is, the less reliable the output is. In this regard, input data should be a cloud obtained by merging data acquired from different positions to avoid shadow areas and to have regular distribution of points in space.

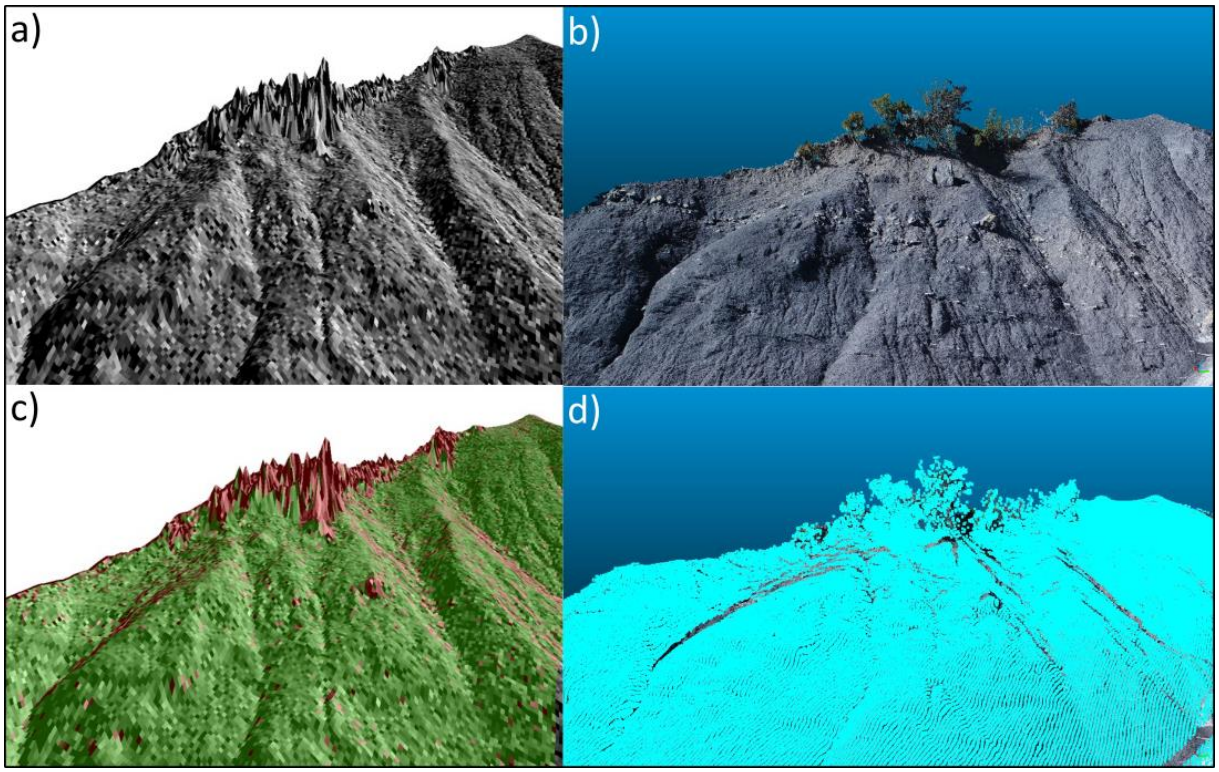

Figure 63. Comparison between viewshed analysis on a digital surface model and Wireless Sensor network Installation Optimizer (WiSIO) on a 3D point cloud using a particular of a landslide's 3D model and point cloud. For better comparison, both analyses were carried out considering the same point of view. a) Hillshade of digital surface model with 1 cm resolution. b) Three-dimensional point cloud with 1 cm resolution. c) Application of ArcGIS 3DAnalyst Viewshed applied on digital surface model. Visible and nonvisible areas are marked, respectively, in green and red. d) Application of visibility analysis carried out in WiSIO on the 3D point cloud. Visible points are highlighted in cyan.

To appreciate the importance of working with 3D point clouds instead of the digital surface model for viewshed detection, a comparison between the two processes made on the same dataset was carried out (Figure 63). In the one case, the Viewshed 3D analyst tool of ArcGIS was applied on a digital surface model with a resolution of 1 cm; in the other, WiSIO was run on the 3D point cloud (1 cm resolution), obtained by photogrammetry and source of the above mentioned surface model. Figure 63 shows the results in detail, allowing an easy comparison. It is evident that working with points instead of surfaces produces more reliable results.

Given a landslide' s 3D point cloud, only the points respecting the following criteria are considered as the best locations:

i. inter-visibility: each selected point is in LOS with the others;
ii. inter-distance: nodes are equally distributed in space;
iii. once the previous conditions are satisfied, it is preferable if P_i is positioned into pre-selected areas, hence Priority Areas (Pas).

Once these principles are met, a WSN make his most, which translates into an accurate landslide displacement map and efficient real time monitoring system, to:

i. have numerous and reliable data, since a complete inter-visibility is guaranteed for the whole network;
ii. obtain a reliable and complete deformation map;
iii. constrain the deployment of the WSN in areas pre-selected by the user.

To avoid the involvement of useless data and the consequent increase of elaboration time, the algorithm automatically calculates a Region Of Interest (ROI) for each node. Only points located inside this region are then considered for subsequent elaborations. The ROI extension depends on the landslide geometry and on the used monitoring system, but it generally coincides with the maximum distance at which two sensors can communicate properly (D_{max}). Given C, the point of view of X, Y, Z coordinates, the region is defined by a cube whose farthest are (X-D_{max}; X+D_{max}; Y+D_{max}; Y-D_{max}; Z+D_{max}; Z-D_{max}).

The best positions are thus selected automatically, except for the first one that is chosen in a semiautomatic way. The user manually selects by clicking on the point cloud with pointer P_1. The algorithm automatically calculates a second ROI (hence ROI_{P1}), smaller than the previous one, inside which the first point is chosen. The choice is made by means of an iterative procedure, during which *n* P_1 within ROI_{P1} (i.e., the Region of Interest around P_1) are selected randomly. For each of them, visibility analysis is computed. As a result, the point from which more points are visible is selected as the first point. This helps in positioning P_1 close to the desired area but having a high visibility. The choice of P_1 with low visibility could indeed compromise the results.

4.1.1 Viewshed analysis

To face the problem of inter-visibility between nodes, the Hidden Point Removal (HPR) operator proposed by Katz et al. (2007) has been applied. The operator is a simple algorithm to determine visibility in point clouds without rendering them or performing surface reconstruction. It first transforms the points of the cloud by means of spherical flipping inversion, and then computes the convex hull of the set containing the viewpoint and the transformed points (Silva et al., 2014). A point is then marked visible from a given point of view if its inverted point lies on the convex hull (Katz et al., 2007) (Figure 64). The operator is easy and fast, and it gives back points that are actually visible. Straightforward solutions are in fact bound to fail and working calculating the LOS between two point is not helpful, since except for extreme cases, a point is always visible, even with high resolution point clouds.

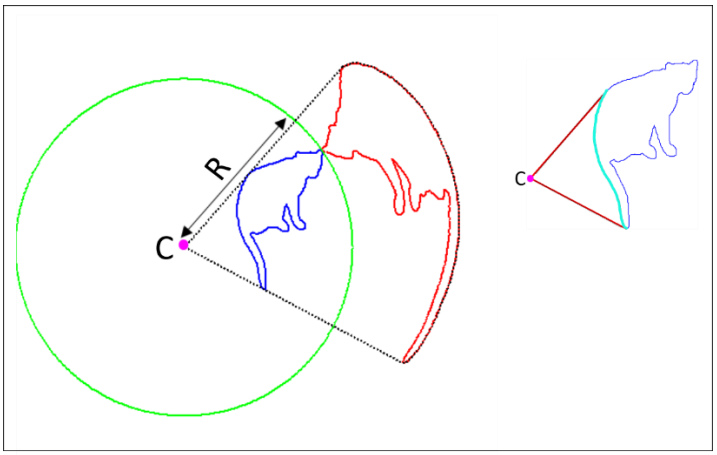

Figure 64. Hidden Point Removal operator. Blue, investigated point cloud; green, sphere with radius R used to invert points by spherical flipping (left side). Points residing on convex hull of inverted points (cyan at top-right) are marked as visible from C (point of view). (Modified after Katz et al., 2007).

The method has found numerous applications in several domains, is supported by theoretical guarantees and has been explained in depth in Katz et al. (2007; 2015).

R, the radius of the sphere for spherical flipping, is the only parameter to set. As it increases, more points pass the threshold of the convex hull and are hence market visible (Katz et al., 2007). Consequently, a large radius is recommended for dense point clouds and the other way around. It is evaluated by an iterative procedure that considers two points of view at opposite sides, with respect to the object centre. R is then defined as the value that maximizes the total number of disjoint visible points (Machado e Silva et al., 2014).

The HPR operator was developed for little objects like small sculptures. In the proposed method, dealing with huge point clouds, *R* is not constant but changes by increasing the distance from C (point of view) to the target, and it is not only a function of point density (homogeneous in ideal cases). As showed in Figure 65d, given a point cloud (P), obviously the number of involved points grow with the distance. Higher D/2 is, higher is the amount of points. In this sense, to correctly apply the HPR operator, the distance has the same role as the density: for points closer to C, a small R is recommended, while for further points, a larger R is more suitable, as demonstrated in Figure 65, where the same R is not an optimal one for both closer and furthest points. Too high values of R produce false positive (i.e. non visible point marked visible, Figure 65b) and too low values give origin to false negative (i.e. visible point marked non visible, Figure 65a). Choosing a medium value for R is not a good solution since it involves a high number of false positive for short distances and false negatives for longer distances.

To solve the problem, the point cloud is split in s cubic sector centred in C, and for each of them R is evaluated. As a result, the optimal R increases moving away from C (Figure 65d). If the point cloud is divided in *s* sector, the visibility analysis is computed *s* time, for each of them all the points between C and sector *i* (included) are considered, but only the ones that are within sector *i* are marked as visible or not-visible.

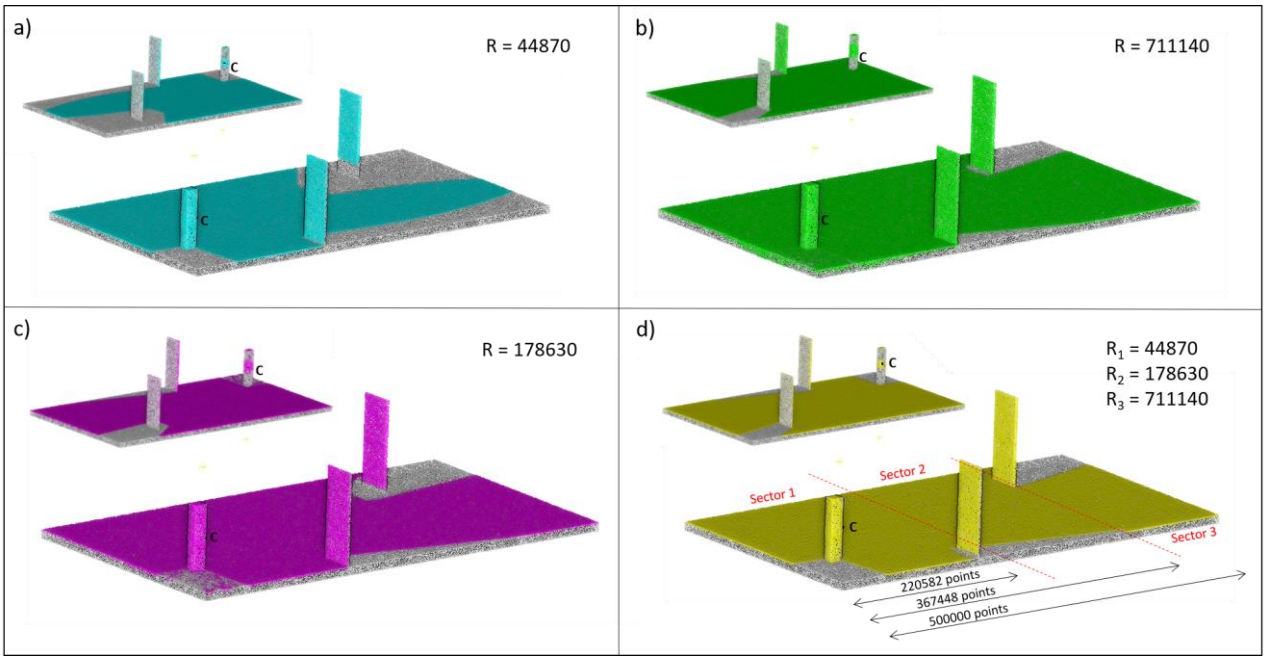

Figure 65. Test to evaluate the optimal radius R. The points marked visible from C changing the radius are shown in cyan, green, magenta and yellow. d) Use of different R for each sector.

Obviously, more are the sectors in which P is split, more accurate are the results of the visibility analysis, high is the computational time. To reach the goal of present work, the HPR operator has been applied to a landslide 3D point cloud. Since monitoring sensors (regardless of the type) generally lies on the ground, it is necessary to split the original point cloud in terrain and vegetation point clouds, to avoid the placing of sensors on points representing vegetation. Indeed, in the landscape field the major obstacle in terms of visibility is the vegetation, and monitoring devices are usually installed on the terrain. Therefore, the HPR operator is applied to the whole point cloud, but only the terrain points are considered as points where the network could be installed. For the distance calculation and the computation concerning the pre-selected areas, the terrain point cloud is also the required datum. Vegetation is involved only in the visibility analysis. As a result, providing as inputs the vegetation point cloud (PCV), the terrain point cloud (PCT) and the point of view coordinates (C), the algorithm returns visible point of PCT from C.

Furthermore, in some cases sensors are not directly in touch with the ground, but they are fixed on supports (e.g. poles, tripods). The proposed algorithm gives the possibility to consider the height of the support, placing points where the sensors will actually be placed, that is fundamental for the visibility analysis. Given h the support's height, the visibility analysis is performed by adding h to the Z component of P_i. If the installation on *n* nodes is required, for each of them the HPR operator is applied for all sectors. Since a complete inter-visibility of the network is required, one can note that nodes location is selected between points that are visible from P_1 to $P_{(i-1)}$; e.g. the choice of P_4 is among points that are visible from P_1, P_2 and P_3.

It is worth to note that obtained visible points lie on the ground, while in the field sensors must be in LOS with other sensors, raised in turn of *h*. The assumption is that a point raised of *h* is visible from a given point of view if the point on the same verticale lying on the ground is visible. Problems come in harsh situations where there is a lot of dense vegetation, such as tall grass, and a minimal amount of terrain points is visible from C. In this case, the algorithm could underestimate the visible points from C, and it could be necessary to ask the algorithm which terrain points would be visible if they were raised of *h*. To solve this problem, it should be necessary to raise each PCT point (i.e., the terrain point cloud), one by one, verifying if they lie on the point cloud convex hull. This means that, if PCT is made by one million points, the operator should be applied one million times for each point of view: each time a different PCT point should be raised of *h*, visibility should be computed and the same point should be lowered of *h*. This could be the best solution in areas with low visibility as well as not many suitable points to install a device, but it obviously takes too much elaboration time, especially when

dealing with big clouds. For this reason, considering the size of the employed point cloud, in this study the algorithm was tested rising only P_i by *h.*

4.1.2 Distance evaluation

For the geometrical deployment of the sensors, with the aim to have equal distribution in space, the Euclidean distance with already selected ones for each P_i was computed. Only the farthest points were then considered to avoid two or more close monitoring devices, or areas with no sensors at all. The procedure was carried out by associating weights to node inter-distances.

Given $X_{(i-1)}$, $Y_{(i-1)}$, $Z_{(i-1)}$ the coordinates of $P_{(i-1)}$ and X_i, Y_i, Z_i the coordinates of P_i, Euclidean distance is given by:

$$Distance = \sqrt{\left(X_{(i-1)} - X_i\right)^2 + \left(Y_{(i-1)} - Y_i\right)^2 + \left(Z_{(i-1)} - Z_i\right)^2} \quad \text{(eq.4)}$$

P_i is selected among the farthest points of PCT from the already chosen points. The remoteness is evaluated by calculating the product of all the distance obtained with eq.4, between P_1, …., P_{i-1} and all the points of PCT. This allow to weight a cluster a portion to PCT (namely the farthest points) among which Pi will be chosen.

4.1.3 Priority Areas

A step that allows to prioritize sensors deployment in selected portions of the point cloud was added to the algorithm. It aims to give different relevance to distinct areas of a landslide, avoiding the absence of monitoring devices in significant areas. The boundary of these sections (Priority Areas, PAs) is made manually by the user, and a file with the XYZ coordinates of points located inside these areas must be uploaded as an input. In detail, the *m* farthest points obtained from the distance evaluation (Equation 4) are pointed out. If some points are located in PAs, then P_i is selected among those ones. If there is no intersection between the farthest points of PCT (i.e. the terrain point cloud) and PAs, then P_i is the farthest point of PCT from P_1, …, P_{i-1}. It goes without saying that the choice of *m* depends on how much important the inter-distance is with respect to the identification of priority areas.

This makes sure that the experience and knowledge of the user play an important role on the procedure despite the automatic nature of the tool. As areas with priority, can be selected areas closer to element at risk, region with higher displacement values, most accessible zones, stable points or any areas where the user would like to place devices.

4.2 Validation on an artificial 3D model

To check the reliability of the proposed algorithm and with the aim to make the function of the code easy to understand step by step, a 3D model was produced and subsequently transformed into a 3D point cloud. The model was built to have low visibility and to highlight the WiSIO ability in positioning a network, ensuring complete inter-visibility. Furthermore, it allows to easily perceive visibility from a given point of view (Figure 66). The model corresponds to a complex artificial scene representing a room with scattered vertical obstacles in the form of beams and sections of walls designed in AutoCAD 3D (Autodesk, v. 20.0) and transformed into a 3D point cloud with CloudCompare (v. 2.10). This is a challenging scene because of the difficulty of finding lines of sight in crowded obstacle scenes. In addition, obstacles with simple shapes made the scene easy to visually interpret, making it a good first example to understanding the functioning of the code. A first validation was done selecting a generic point of view C, evaluating the visible points from C and exploiting the camera/eye centre visualization function of CloudCompare software (Figure 66). As shown in Figure 66d, all points detected as visible from WiSIO are indeed visible from C (in cyan), since there is no overlap of points. On the other hand, a small number of false negatives are reckoned up, due to the precautionary R chosen for the test trough the iterative process described in Section 4.1.1. The problem of false negatives can be easily solved increasing the number of sectors. More the sectors are, less is the number of false negative, higher is the time of running, as shown in Table 9, where data of three different approach are reported. Note that Test 1 is the approach whose results are shown in Figure 66.

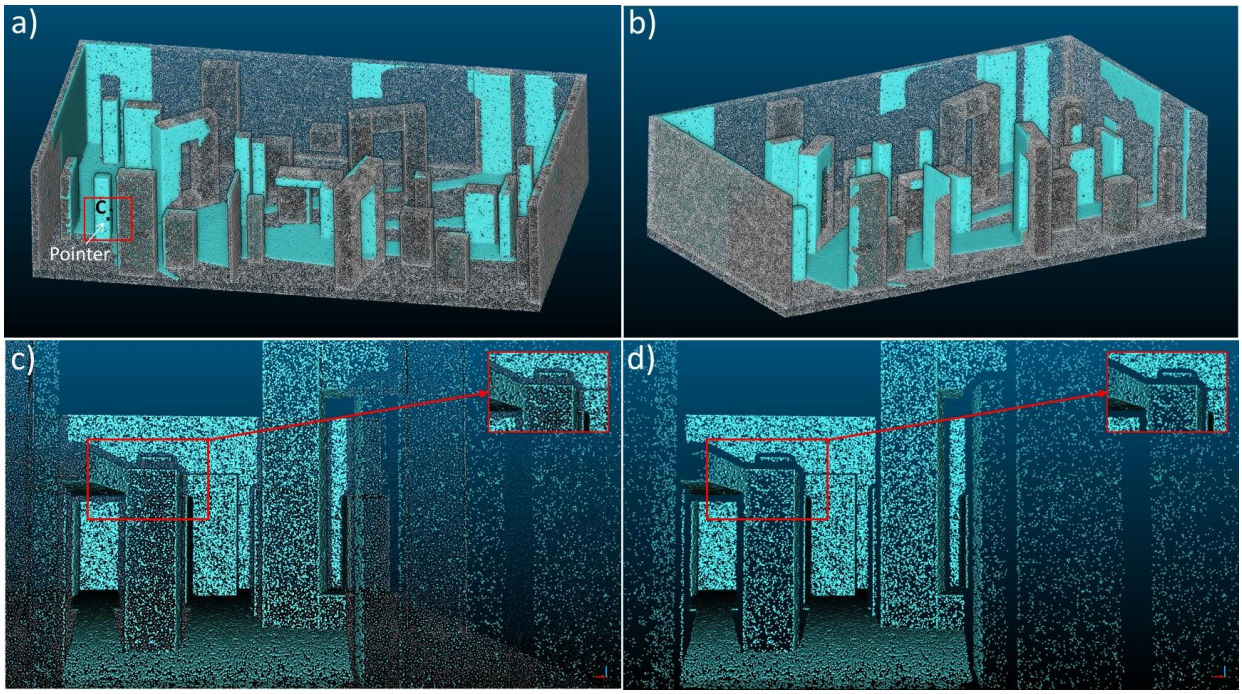

Figure 66. 3D model developed to simulate a harsh environment in terms of visibility. a) Visible points from C highlighted in cyan. The dark blue dot represents the point selected with the pointer as first choice, and the red box the small ROI inside which C has been semi-automatically detected. b) Visible points from C highlighted in cyan from a different angulation. c) View from C of points marked visible (in Cyan) and the whole point cloud (grey points). d) View from C of only points marked visible; the zoom at the right bottom allow to better comprehend the amount of false negatives, i.e. visible points marked as non-visible.

Test 1	**Radius, *R* (m)**						**False negatives**	**Running time**
	Sector 1	Sector 2	Sector 3	Sector 4	Sector 5			(min)
	44568	354019	1119508	1774301	4456843		10504	0.350
Test 2	**Radius, *R* (m)**						**False negatives**	**Running time**
	Sector 1	Sector 2	Sector 3	Sector 4				(min)
	44568	354019	706362	2812078			25120	0.317
Test 3	**Radius, *R* (m)**						**False negatives**	**Running time**
	Sector 1	Sector 2	Sector 3	Sector 4	Sector 5	Sector 6		(min)
	44568	223371	706362	2233713	4456843	5610833	4131	0.393

Table 9. Numbers of false negative obtained varying sectors. Test 2 is the one whose results are shown in Figure 66.

Only one generic point cloud P made by 1.972.852 points was used, since no vegetation is present in the model. Figure 67 illustrates the whole elaboration made by WiSIO to point out 7 nodes positions, carried out in 3,33 minutes. With respect to Figure 66, where walls helped in the comprehension of visible areas, in Figure 67 they were removed to better display all the involved P_i. To detect P_1 the iterative procedure was replied three times. The automatically evaluated ROI_{P1} is depicted as a black

box in Figure 67a. Moreover, some objects were randomly selected in the model and uploaded as priority areas (in red in Figure 67e,f).

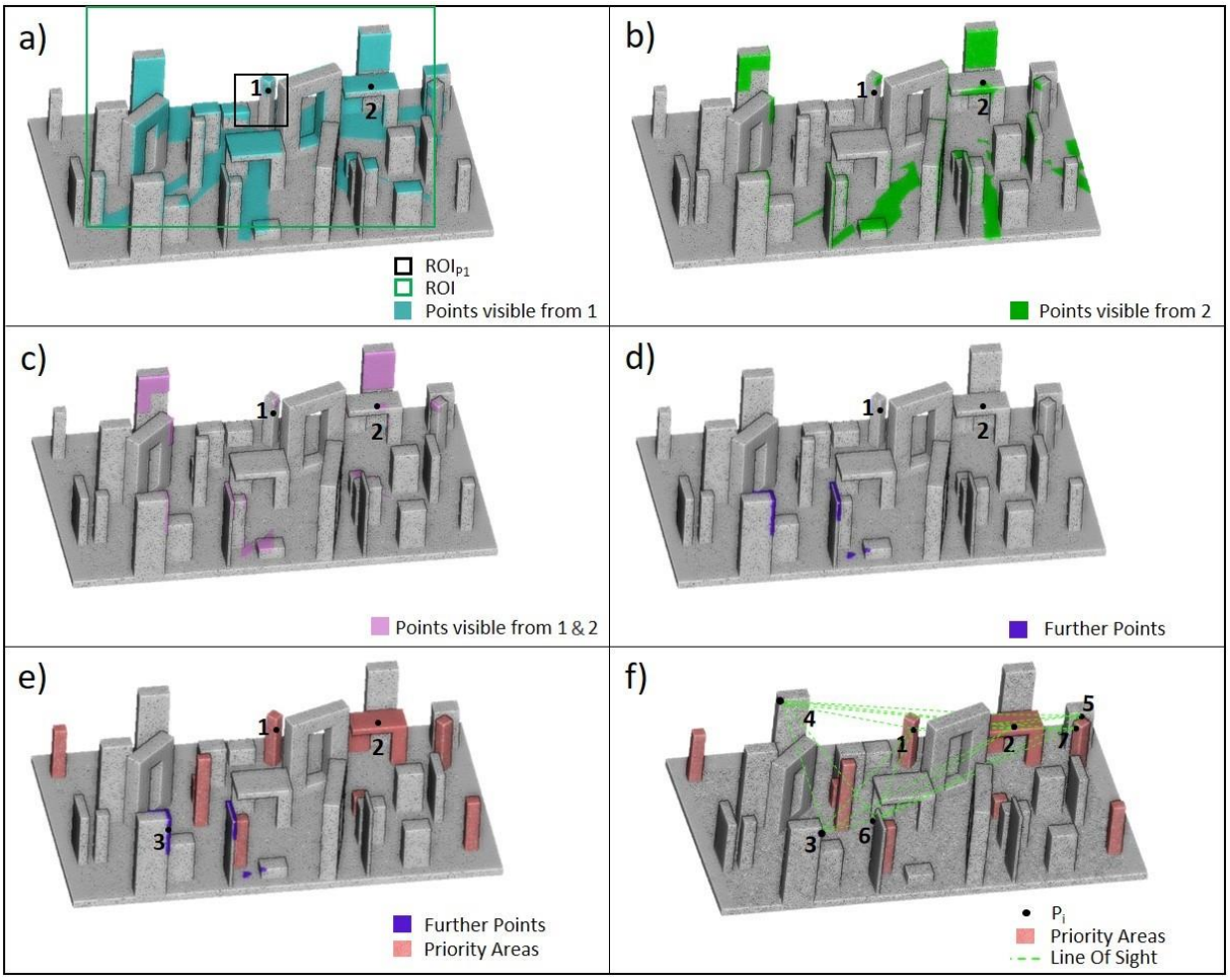

Figure 67. Results pointed out by WiSIO for the installation of 7 nodes using the developed 3D model. From a) to e) all the steps computed by WiSIO for the automatic detection of P_3; in detail: a) choice of P_1 inside ROI_{P1}, consequent selection of the ROI and detection of points visible from P_1; b) detection of points visible from P_2; c) detection of points that are visible from both P_1 and P_2; d) identification of the furthest points from P_1 and P_2 among the ones marked pink in (c); e) uploading of the PAs and automatic selection of P_3; f) final result with the location of all the 7 Points.

Five sectors were used, whose respective radius are the ones reported in Table 9, Test 1. The test was also replied changing the quantity of point to evaluate the amount of time required varying the size of the point cloud (Table 10).

N. points	427920	1972852	2000000
Running time	0.85 min	3.33 min	3.61 min

Table 10. Different time of running for different amount of points.

It is worth to note that P_3, P_4 and P_6, are out of priority areas, since no further points are overlapped to them (Figure 67e). It is also interesting to note that in the area at the right bottom of the model there are no sensors, in spite of the presence of PAs. This is due to the absence of points visible from both P_1 and P_2 (pink points in Figure 67c), that is an essential condition.

All the selected Points are in LOS with respect to the others, are equally distributed in space and 4 of them reside on the areas marked as PAs, despite the harsh designed environment (Figure 67f).

5. Application of WiSIO to the Roncovetro landslide case study

To apply the method on Roncovetro landslide, a laser scanner survey was carried out to obtain the 3D point cloud, the main input of WiSIO. The survey interested only the central part of the landslide, namely the area of interest for installing the network. Since the reliability of the code is strongly influenced by the resolution of the point cloud, and due also to the high presence of vegetation in the area, seven scans have been acquired from different positions, in order to limit the shadow areas (Figure 68). The survey was carried out on December 5, 2018 using the terrestrial laser scanner RIEGL VZ-1000 (Figure 69).

To obtain a vegetation point cloud (PCV) and a terrain one (PCT) a vegetation filter was applied to the original point cloud. In particular, the filtering procedure was carried out thanks to the echo registered by the laser scanner. The RiSCAN PRO software (RIEGL LMS, RiSCAN PRO version 2.6.2) allowed to detect four different echoes of the point cloud:

i. single targets;
ii. first targets;
iii. other targets;
iv. last targets.

The removal of the first (ii) and other targets (iii) allow to the vegetation removal. Figure 70 shows the split point cloud; the one drawn with only single and last targets is the terrain one, while the one drawn with first and other targets is the vegetation one.

Due to the intense vegetation of the area, a further clean made by the user was then necessary, in particular in areas where dense grass was present. The final result is the one shown in Figure 68.

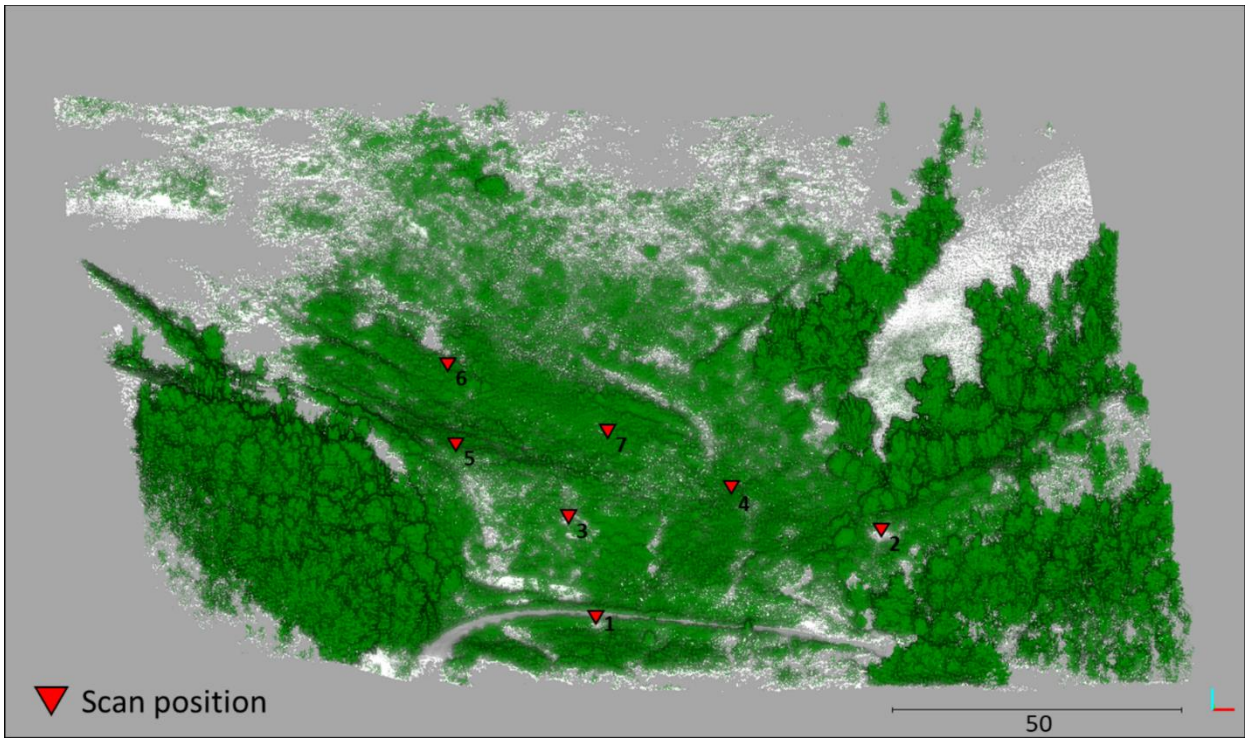

Figure 68. 3D Point cloud of the Roncovetro landslide. The red triangles show the position of the seven scans that were carried out with the terrestrial laser scanner RIEGL VZ-1000. Green and grey colors represent respectively vegetation and terrain (i.e. PCT and PCV).

Figure 69. Laser scanner survey. a) the employed RIEGL VZ-1000 laser scanner; b) picture taken during the survey (scan position 1 of Figure 68).

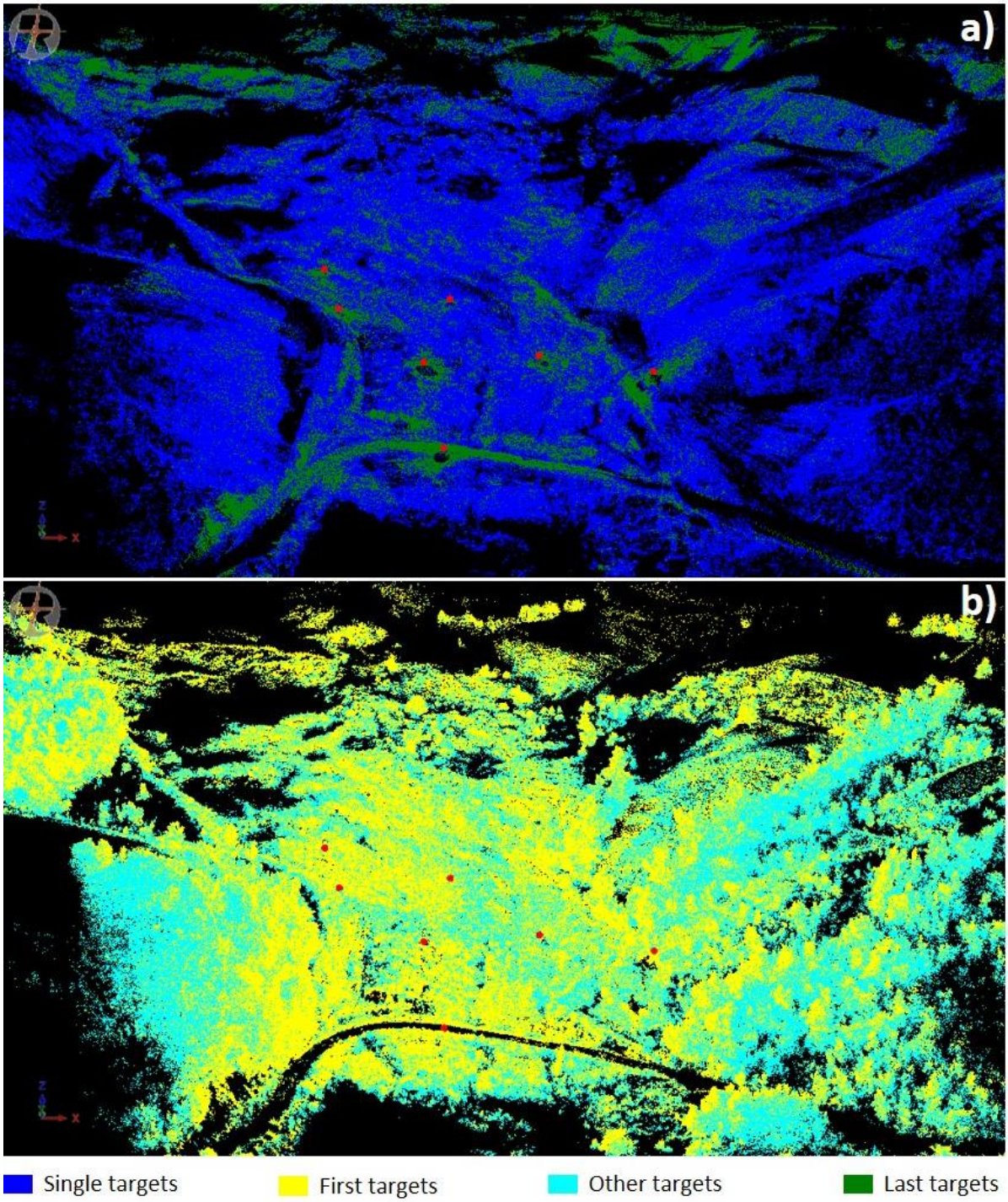

Figure 70. Representation of the 3D point clouds echoes. a) single and last targets, i.e. the terrain point cloud (PCT); b) first and other targets, i.e. the vegetation point cloud (PCV). RIEGL LMS, RiSCAN PRO version 2.6.2 software.

5.1 Selection of the Priority Areas

Several tests were carried out by varying the Priority Areas (PAs) to assess which ones would have produce the best configuration and to understand its influence.

In all cases, *h*, the sensor's support high, was set equal to 1.5 m, according to the first installation of the system made in 2016, while the ROI was fixed at 100 m. However, all the input parameters used for Roncovetro tests are listed in Table 11.

h*	1.5 m	**R sector 1**	3593 m
ROI	100 m	**R sector 2**	18010 m
ROI_{P1}	5 m	**R sector 3**	71700 m
m **	20%	**R sector 4**	180104 m
Iterations for P_1	5	**R sector 5**	285446 m
*Iron poles' height **The value is expressed as the percentage of the points visible from P_i			

Table 11. Summary of the input parameters used for Roncovetro tests.

The first test was performed considering as PAs the areas with the highest displacement values. For this purpose, data of the Robotic Total Station (RTS) installed in the area were analysed and interpolated by kriging, a powerful type of spatial interpolation that uses complex mathematical formulas to estimate values at unknown points based on the values at known points. As previously mentioned (see section 3.2), during the first installation each node had been indeed equipped with a RTS target and it was therefore possible to interpolate the displacement values obtaining a continuous map. Figure 71a shows the displacement map (resulted from the kriging process carried out on ArcGIS, ARCMAP v. 10.4) with the location of the old Cluster 1, namely the points of known displacement. Points of the terrain point cloud (PCT) located on areas with a displacement rate higher than 0.1 m was considered as Pas in this first test (Figure 71b), and the obtained configuration is shown in Figure 71c. One can note that the two nodes of the old configuration that had been installed in stable areas (i.e. nodes 1 and 7, Figure 71a) allow to identify stationary areas, whereas in the middle area, corresponding to the landslide flow channel, the highest displacement values were observed. Despite this, the analysis was not so significant, since the source data were few and punctual. Moreover, the resulted configuration was not satisfying at all due to its high concentration in one sector of the landslide and its total absence in the other areas (Figure 71c).

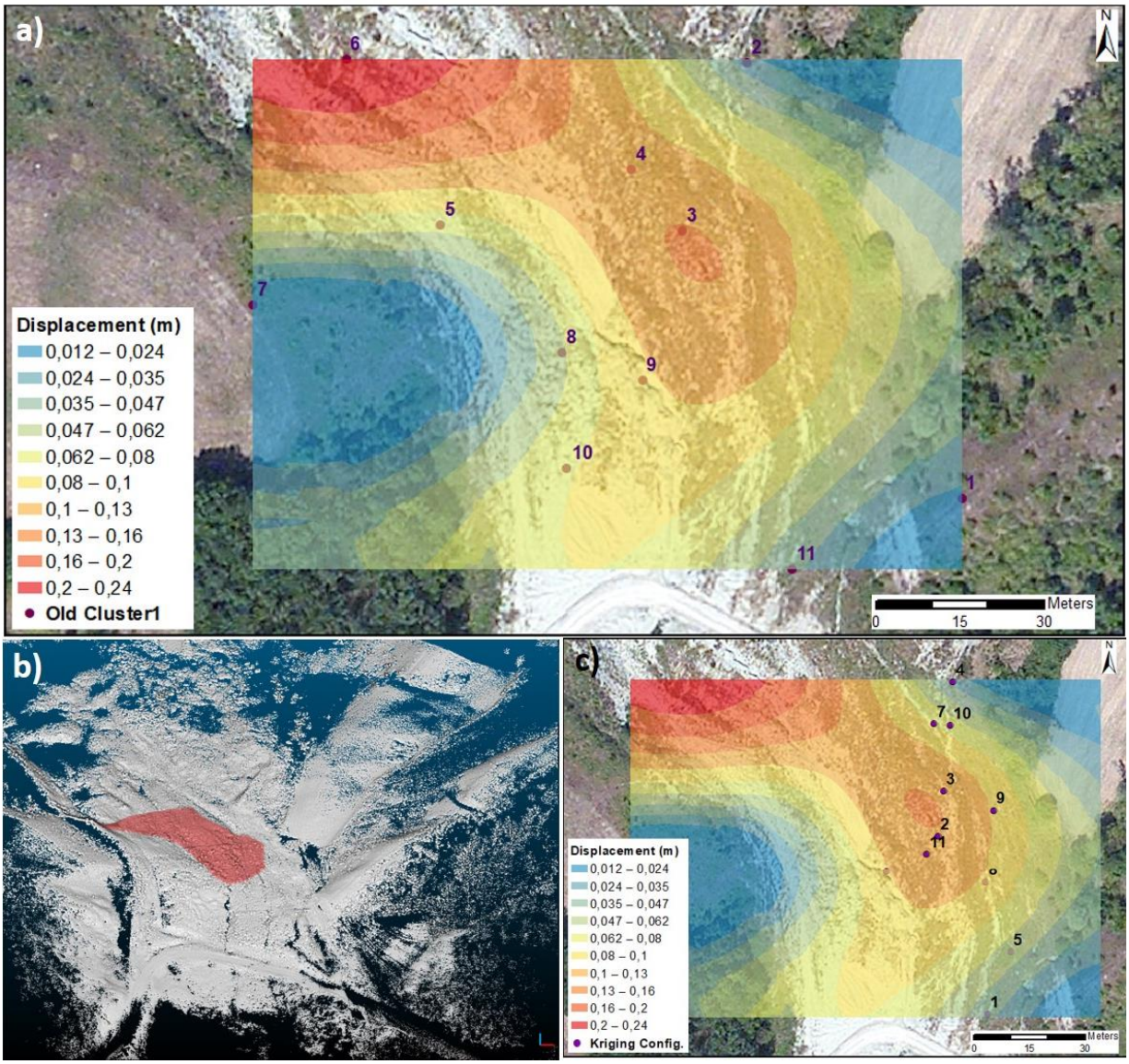

Figure 71. Results of WiSIO using RTS values to define Priority Areas (PAs). a) aerial picture of Roncovetro landslide with the results of the interpolation procedure (i.e. Kriging) obtained with the RTS values acquired from old Cluster 1 positions; b) Roncovetro terrain 3D point cloud (PCT) with the PAs detected by the kriging procedure in red; c) configuration obtained considering areas characterised by displacement values higher than 0.1 m as PAs.

A second test was still performed considering the landslides movement, but this time considering the differences between two 3D point clouds obtained by means of two terrestrial laser scanner survey performed in two different times, one on March 3, 2015 and the other on December 2, 2018 (i.e. the same on which WiSIO runs). The absolute distances were calculated from the mesh generated from the first terrain point cloud and the second terrain point cloud; a direct evaluation of the point to point distance would have indeed produced only relative distances values, not allowing to understand depletion and accumulation zones. Unfortunately, the 2015 point cloud, which was the results of merging only three scansion and considering the strong presence of vegetation as well as terrain

roughness and slopes, did not generates a high resolution cloud as the one obtained in 2018. For this reason, and due also to the strong changes in terms of vegetation and morphology, the obtained results were not so satisfying, especially for the lower part of the area of interest, where the obtained displacement does not seem to follow the actual morphology of the area. Conversely, they seem to be significant and reliable in the upper part, where the depletion areas coincide with the numerous channels where the material flows (Figure 72).

Areas with a displacement values higher than +0.5 m (i.e. depletion zones) were therefore considered as PAs. Two different configurations are shown in Figure 72b and Figure 72c, obtained by WiSIO moving P_1 on the middle and on the lower part of the area of interest, respectively. Both configurations are distributed in space and the influence of the PAs is clearly visible. However, they were both excluded, the first one because the main intention was to install sensors close to the ones installed in 2016; the latter because as above mentioned the PAs in this case were not considered reliable.

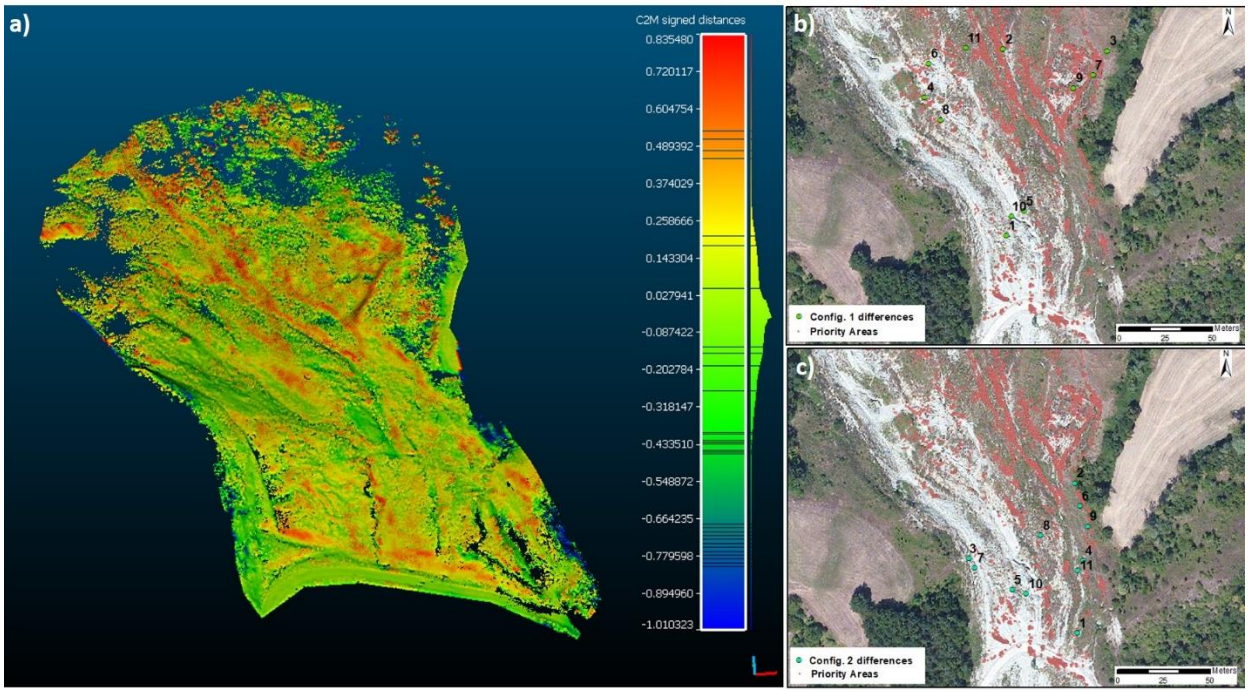

Figure 72. Results of WiSIO using differences between terrestrial laser scanner point clouds obtained in 2015 and 2018. Points with a displacement higher than +0.5 m have been considered as PAs. The differences were calculated by means of CloudCompare software (CloudCompare v. 2.10). a) differences from the mesh generated from the 2005 point cloud and the 2018 point cloud; b) first configuration obtained; c) second configuration obtained.

With the aim of installing the sensors in a position close to the old configuration to obtain a significant comparison of the results, a test was carried out considering as PAs the location of the 2016 nodes. In particular, 11 spheres, having a 10 m radius and centred in the location of the old configuration sensors, were drawn, projected on the 3D point cloud and considered as PAs (Figure 73). WiSIO was

consequently run positioning P_1 close to the old P_1; the result is showed in Figure 73b. This configuration was however discarded since P_1 was the only stable point out of the landslide and this would not be enough to assess the non-relative position of sensors trough triangulation processes, since at least three stable points are required for this purpose.

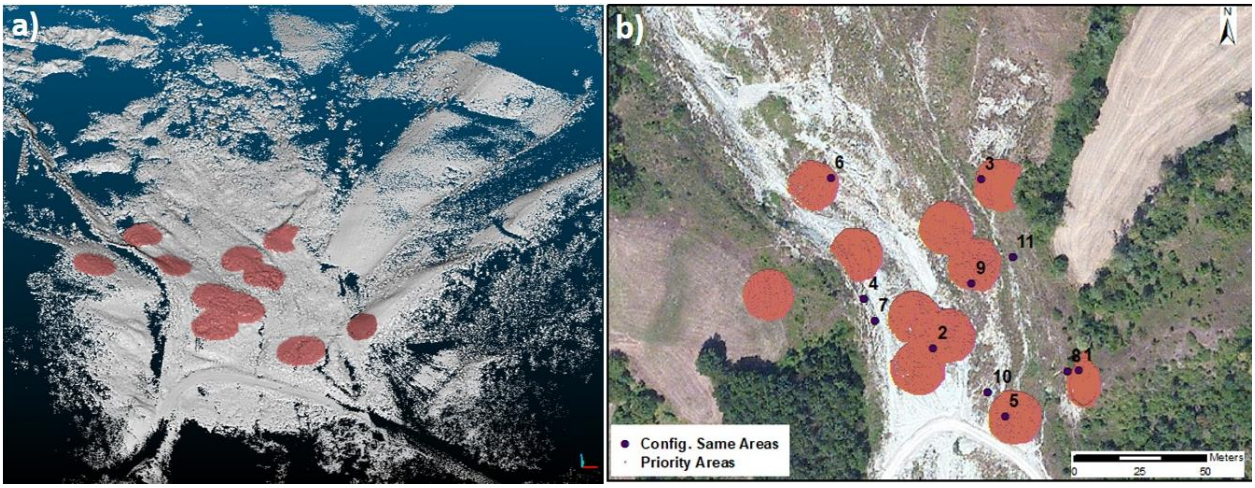

Figure 73. Results of WiSIO using the position of the sensors in the old configuration as PAs. a) in red the PAs on Roncovetro 3D terrain point cloud (PCT); b) the obtained configuration.

A fourth test was finally carried out with the aim of ensuring the best geometrical positioning in terms of visibility despite the presence of several geomorphological ups and down in the landslide body.

Due to the low visibility of the site, it is in fact necessary to avoid locating by WiSIO of one or more sensors in areas with scarce visibility, since it would compromise the best positioning of the subsequent sensors. WiSIO indeed, place devices in LOS one to each other, but without considering if the surrounding areas are highly visible. In a stress condition like Roncovetro landslide, due to the presence of vegetation as well as terrain roughness and slopes, it may happen that a sensor is correctly positioned in LOS with the others and following the distance criteria, but in an area with few visible points, sacrificing the positioning of the succeeding devices. To prevent this, the geomorphological highest locations were selected as PAs. To automatically select these areas, a simple computation was performed. Cells were extracted by ideally moving a sampling cube of fixed dimension (side of 5 m in this work) on the terrain point cloud. For each of them the mean elevation value (Z_{med}) and the average of the 10 highest elevation values (Z_{max}) were calculated. PAs were thus defined as points located in cells whose (Z_{max} - Z_{med}) was greater than 2 m (Figure 74). Note that calculating Z_{med} as above mentioned, instead of using the maximum elevation value of each cell, allow to avoid outliers' issues. In a 3D point cloud of a vegetated area, outliers with a Z_{max} out of the range can be indeed quite common. Figure 74c shows the obtained configuration.

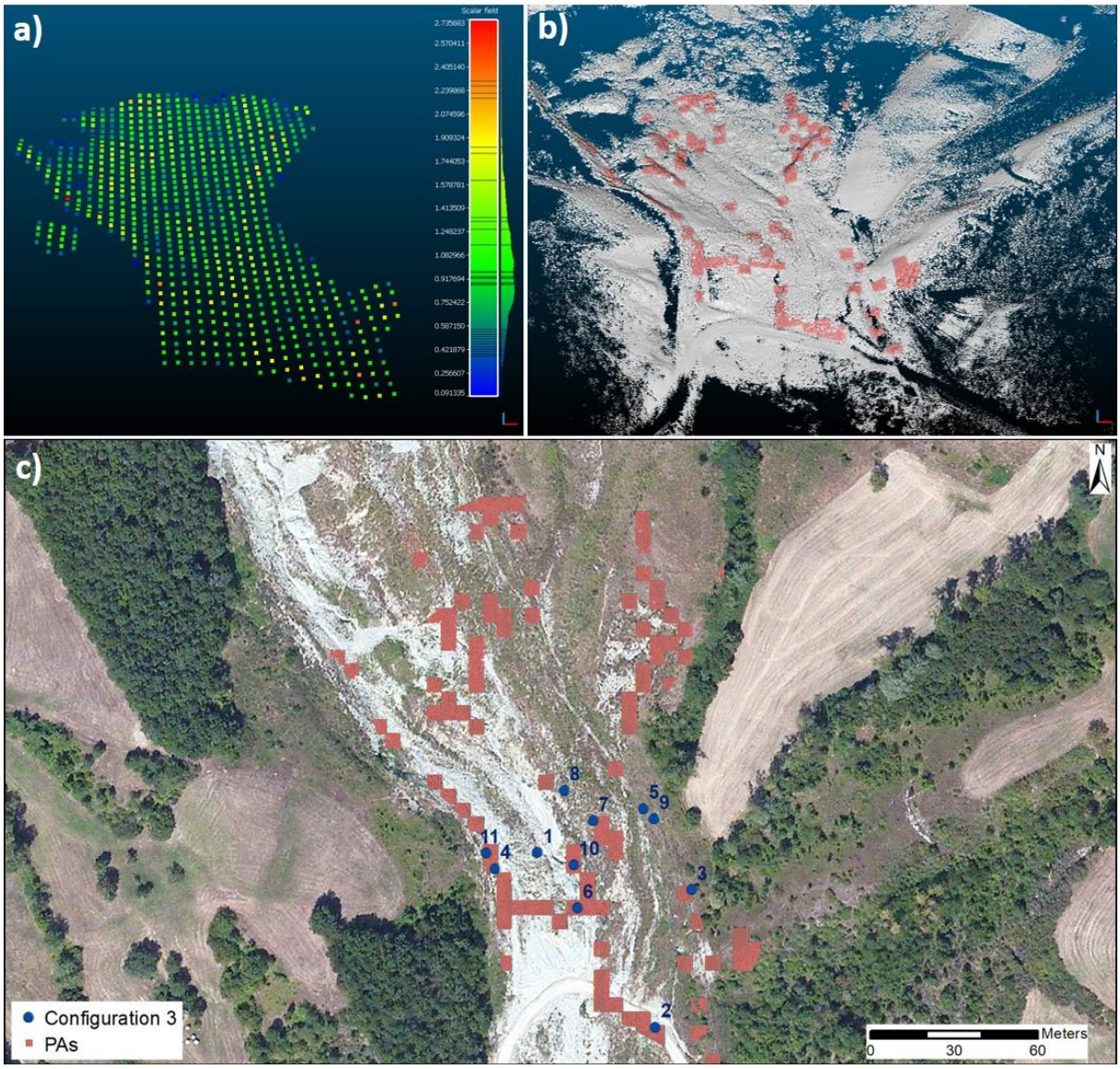

Figure 74. Results of WiSIO obtained using the cube method for the PAs selection. a) cube centres coloured in function of the Z_{max} - Z_{med} values. b) Roncovetro 3D point cloud (PCT) with the PAs (i.e. points in cubes whose Z_{max} - Z_{med} was greater than 2m) highlighted in red; c) one of the obtained configurations.

A further detail to take into account is that the selection of P_1 strongly influenced the whole deployment. As an example, Figure 75 shows three different configurations obtained changing the original position ROI_{P1}, which framed an area of 5 m around P_1. In case 1 and 3, it is located in central and easy to reach positions (Figure 75a and Figure 75c), while in case 2 it is situated a bit further upstream (Figure 75c). The most satisfying configuration is in Case 3, due to the point distribution in the landslides body and to the presence of one or more stable points located outside the landslide (i.e. Nodes 3, 5, 9 and 11).

Therefore, since the interest was to install the system in the same area where it was in 2016, aiming at a complete comparison of the collected data, on February 2019 the new installation of the Wi-GIM system was done following Configuration 3 (Figure 75c).

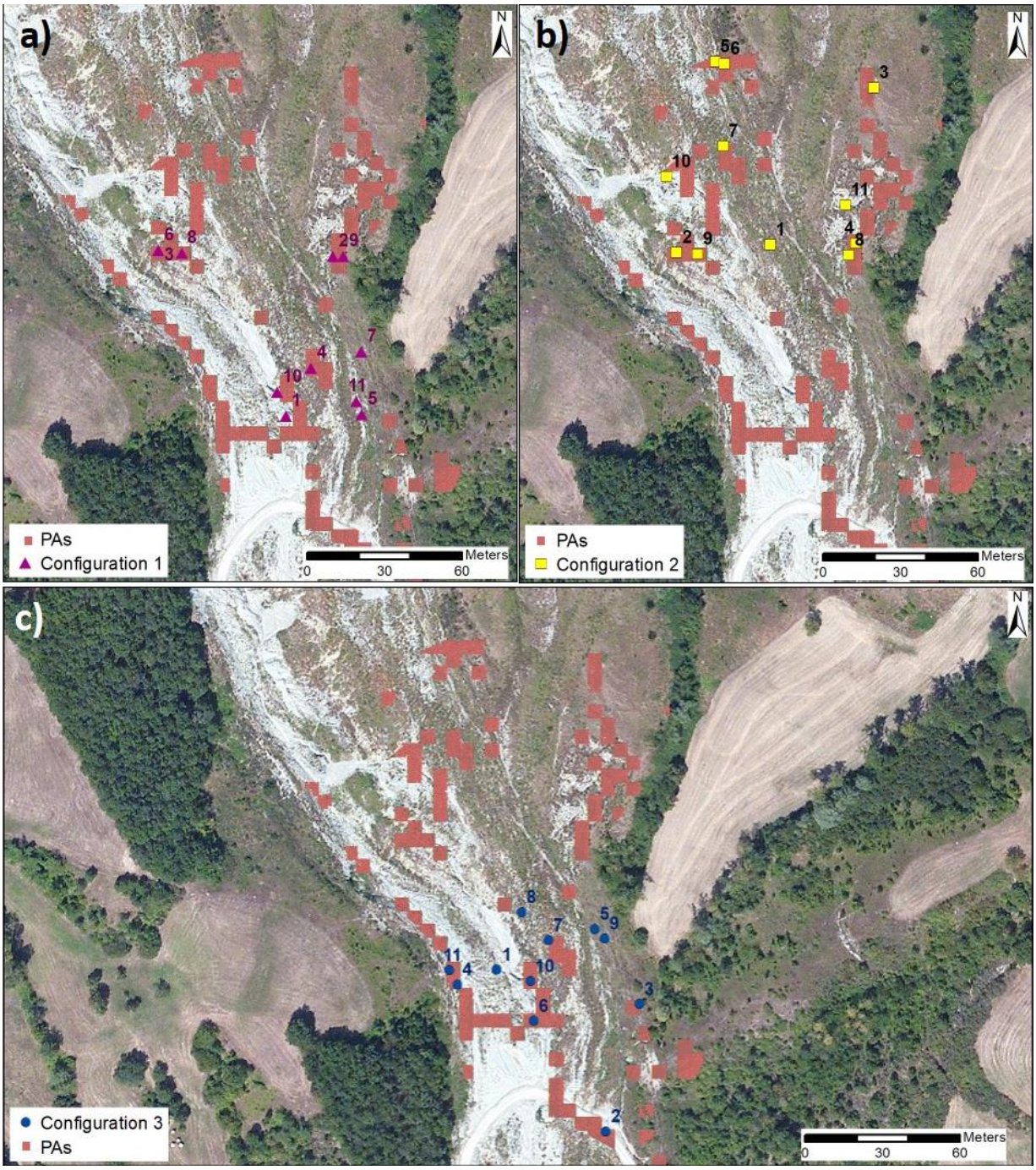

Figure 75. Different configurations obtained changing the position of P_1 using the cube method for the PAs selection. Red dots represent points in cubes whose Z_{max} -Z_{med} was greater than 2m, i.e. the PAs. a) configuration 1; b) configuration 2; c) configuration 3, i.e. the one used for the new installation of the Wi-GIM system.

5.2 Wi-GIM new installation

On February 27nd, 2019, sensors were installed on 1,5 m high iron poles (as already done in 2016, and as considered in the parameter settings reported in Table 11), following the configuration showed in Figure 75c.

To place the poles in the locations detected by WiSIO, the point finder function of the Emlid Reach RS+ GPS (see Emlid Reach GPS official web site, in bibliography) was exploited. The X, Y, Z point coordinates were thus uploaded in the GPS that directed the user on them through a navigation system. Points were then marked on the ground with a spray paint, where the iron poles were subsequently embedded (Figure 76).

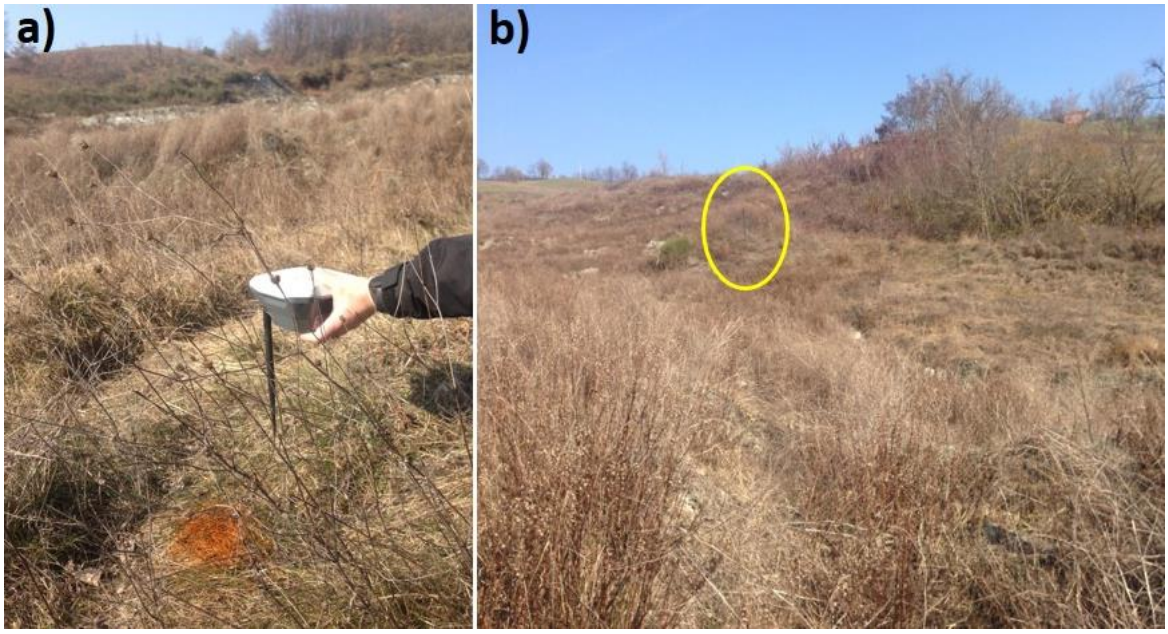

Figure 76. Wi-GIM installation after the implementation of WiSIO. a) Emlid Reach RS+ GPS point finder function used to localise the Points detected by the algorithm; b) installation of the new Cluster 1 Node 8 (highlighted with a yellow circle).

As explained in Section 3.2.2, the power consumption was been a critical point during the first installation of the Wi-GIM system in Roncovetro, since the scarce duration of batteries' life caused too frequent batteries replacements increasing the costs of the monitoring. For this reason, for the second installation, each battery was equipped with a photovoltaic panel (Figure 77a), that was placed in situ on the top of each battery and facing south. Thanks to the panels, all batteries remained charged during the whole monitoring period, except the one at Node 5 which died on 2019/03/15 probably due to a tension overload occurred on 2019/03/01 (Figure 77b).

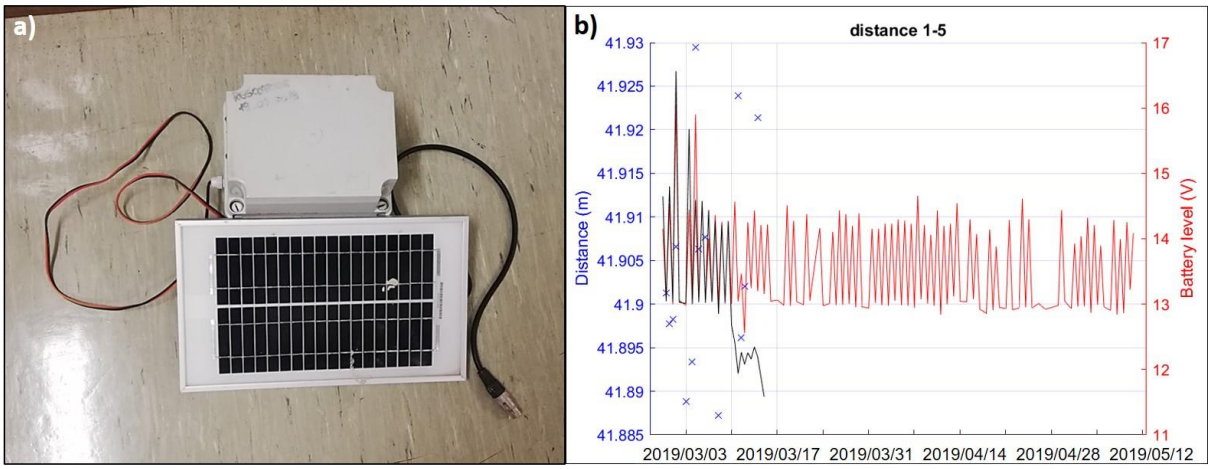

Figure 77. Effect of photovoltaic panels. a) one of the batteries equipped with the photovoltaic panel 5 W 21.2 V, whose dimensions are 180 mm X 340 mm X 23 mm; b) displacement time series of Nodes 1–5 plotted with the battery level, where the daily influence on the panel voltage is clearly visible. The red line is referred to Node 1 battery; the black one is referred to Node 5 battery who died on 2019/03/15 probably due to a tension overload occurred on 2019/03/01. One can note that no data can be acquired after the loss of one of the two involved batteries.

As shown in Figure 75c, 7 devices out of 11 lie on PAs. One of the non-PAs points is however P_1, whose position was manually picked out. The remaining 3 are out of them as a result of the relationship between the distance and the *m* value (set equal to the 20% of the points visible from P_i). All sensors were effectively in LOS, as demonstrated by an analysis carried out with the camera/eye centre visualization function in CloudCompare. Despite this, the acquired data show the lack of three pairs, i.e. 3–11; 2–7 and 4–5 (Figure 78). This leak could be due to changes in vegetation or to problems related to the Decawave. Concerning vegetation, please note that due to logistic problems, three months passed from the scan survey to the installation. This period may have led to some changes on the field, due to animals' transition or branches fall. Secondly, some problems have already been encountered in the past because of the low-cost nature of the Decawave, as already discussed in the previous sections.

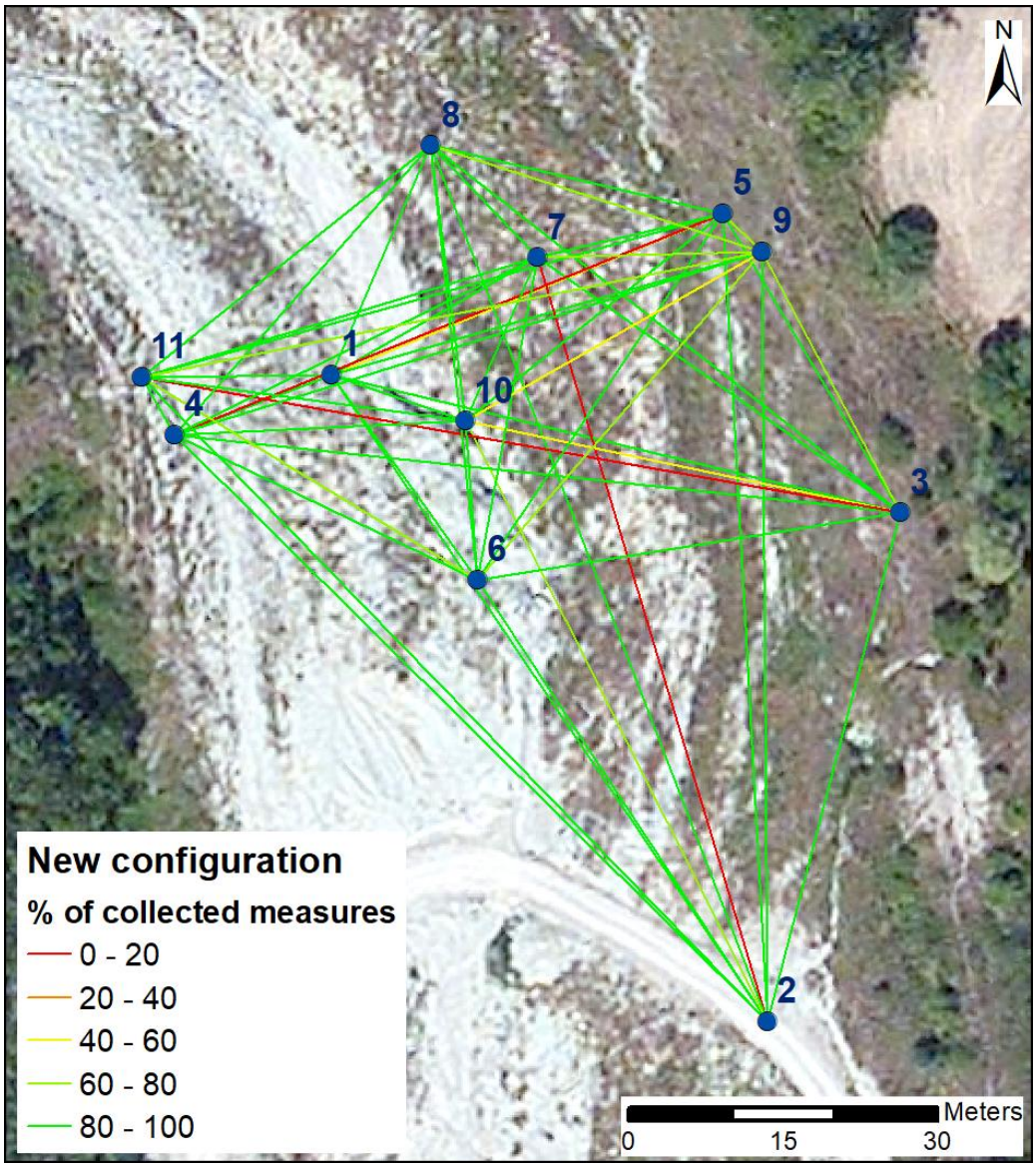

Figure 78. Percentage of collected measures in the new configuration, index of the LOS condition.

Figure 79 and Figure 80 show two examples of the acquired data in the new configuration, i.e. the displacement time series of pairs 4–8 and 7–10 for the period from 2019/02/27 to 2019/05/12. All processing steps are reported in the images, such as the outlier's removal using a threshold of 1 m and the daily averages that strongly increase data precision.

Furthermore, it is interesting to note the temperature effect in the presented data, where a slight daily influence is visible in Figure 79b and in Figure 80b, that are attenuated after the correction using a factor equal to 0.003 (Figure 79c – Figure 80c).

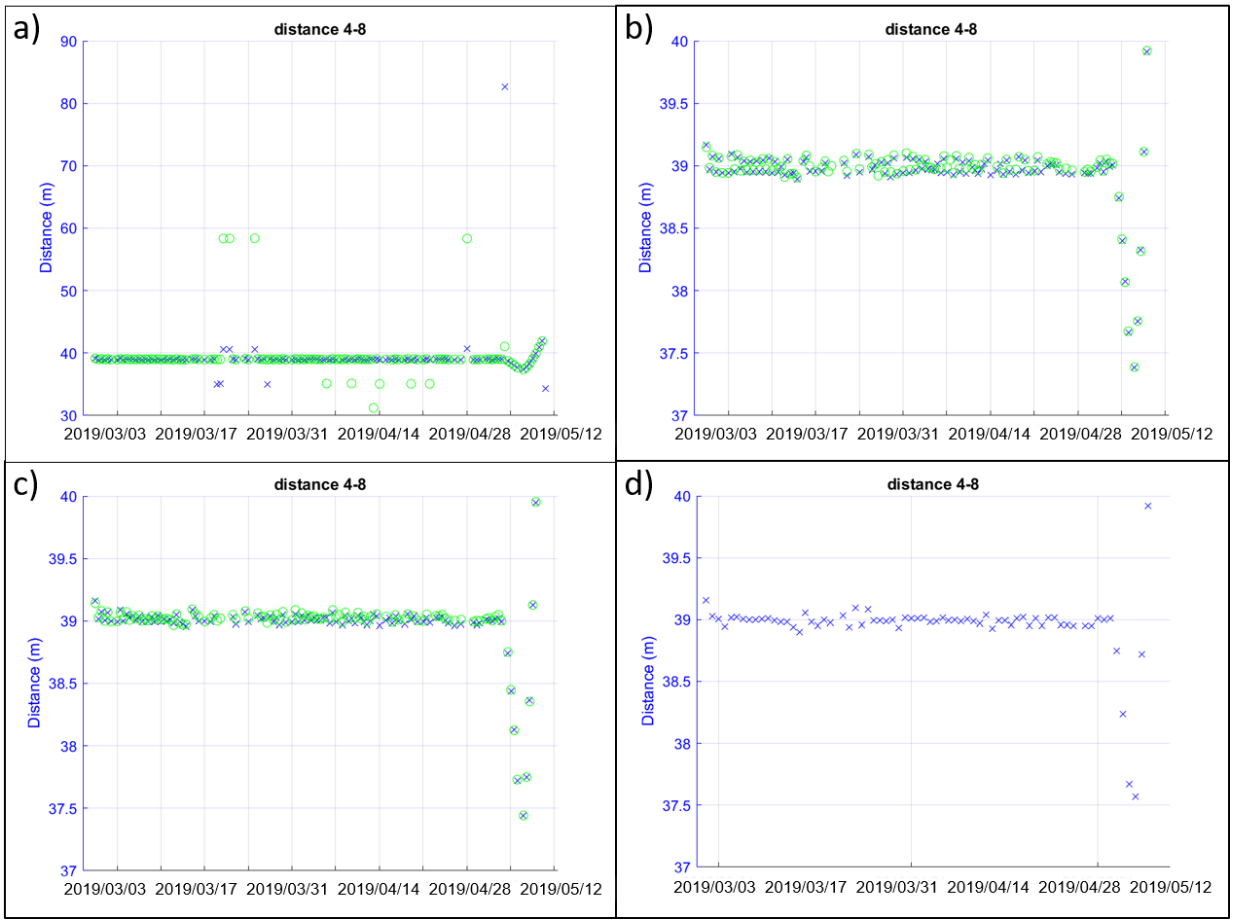

Figure 79. Displacement time series of the pair of nodes 4–8. a) raw distance values; b) distance validated values, considering a threshold of 1 m for the outlier's removal; c) distance validated values after the temperature correction made using a correction factor of 0.003; d) distance daily mean values. Green circles and blue crosses represent the distance measured from one node to the other and vice versa. Where measurement points are extremely dense, the blue crosses are overlaid by the green circles.

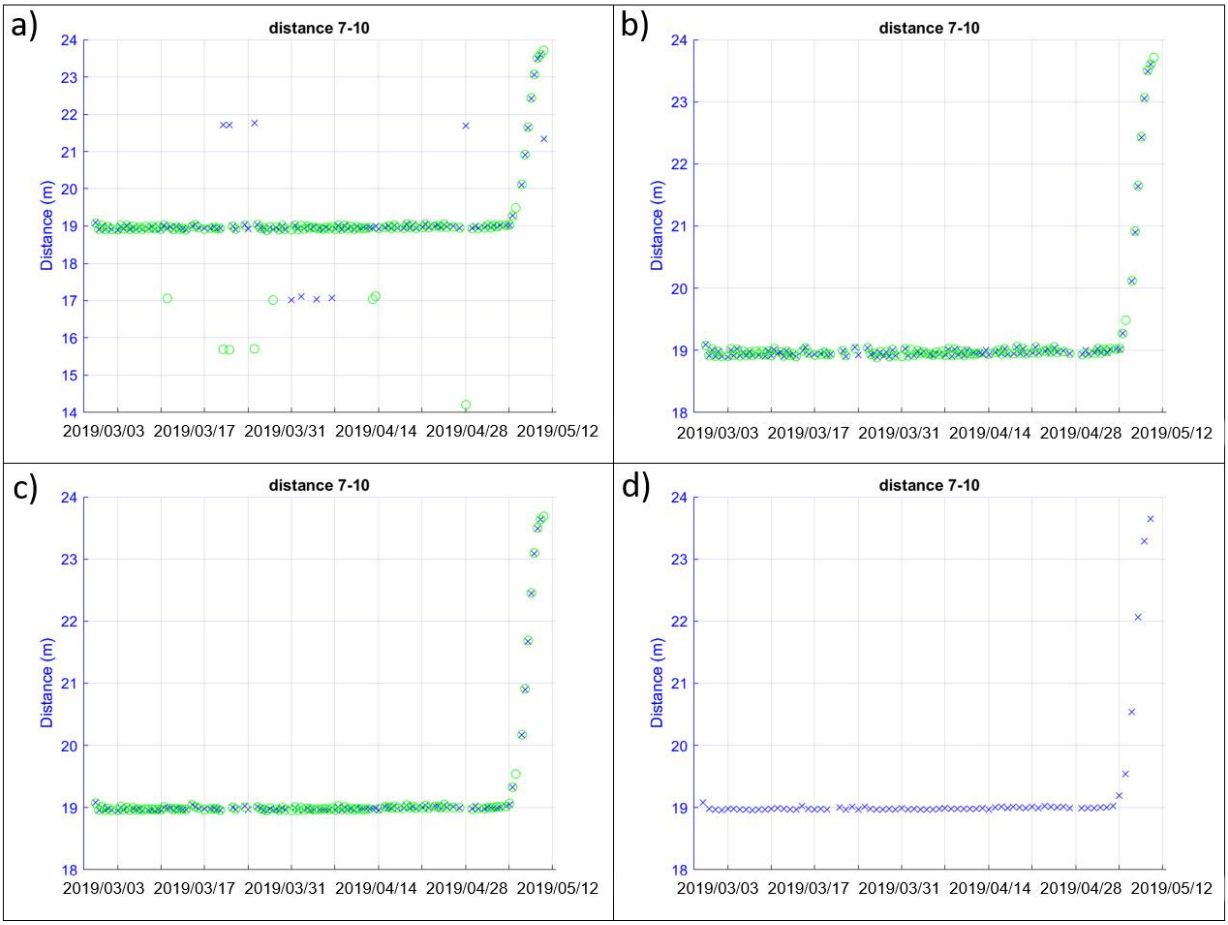

Figure 80. Displacement time series of the pair of nodes 7–10. a) raw distance values; b) distance validated values, considering a threshold of 1 m for the outlier's removal; c) distance validated values after the temperature correction made using a correction factor of 0.003; d) distance daily mean values. Green circles and blue crosses represent the distance measured from one node to the other and vice versa. Where measurement points are extremely dense, the blue crosses are overlaid by the green circles.

5.2.1 The event of May 5th, 2019

Looking at data presented in Figure 79 and Figure 80, one can note that a significant movement is clearly visible starting from the 5th of May 2019. The displacement, 1.5 m for the pair 4–8 and about 5 m for the pair 7–10, occurred during intense rainfall (Figure 81), and it is the higher that has been registered during the whole monitoring period started in 2016.

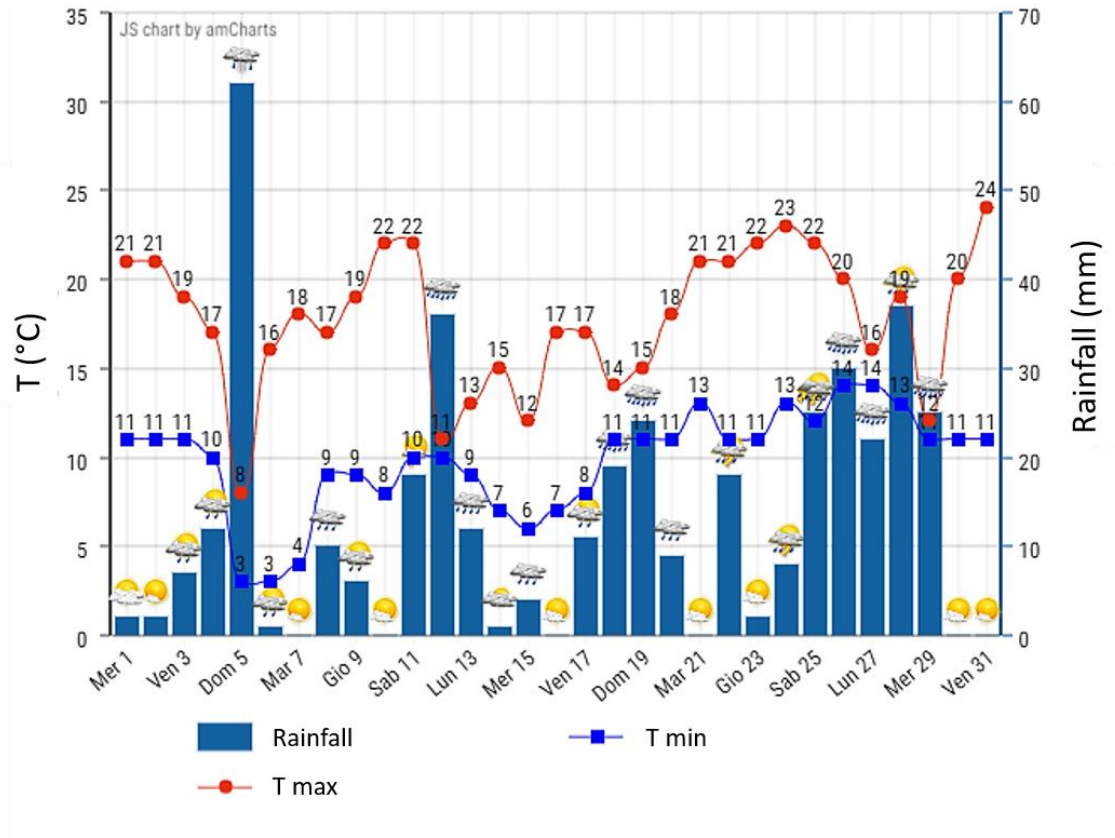

Figure 81. Rainfall and temperature data recorded in May in the close weather station of Canossa (RE, Italy).

It is interesting to note how the pair 4–8 registered a movement in opposite directions, first measuring shorter distances (as if they were approaching one to each other) and then bigger (that is moving away) (Figure 79). This change in direction is due to the pole instability: during the displacement it probably fell down tilting and thus measuring the displacement in a different direction. Pole instability may indeed occur in case of large displacements along the slopes, compromising the reliability of the measured distances. Unfortunately, in these extreme cases, it is hard to imagine an appropriate low cost solution with a low environmental impact. However, it is important to note that while the direction of the movement is in question, the system is capable to record a movement, remaining a good solution in emergency conditions.

Figure 82 shows the daily average values recorded by some other significant pair of nodes during the event.

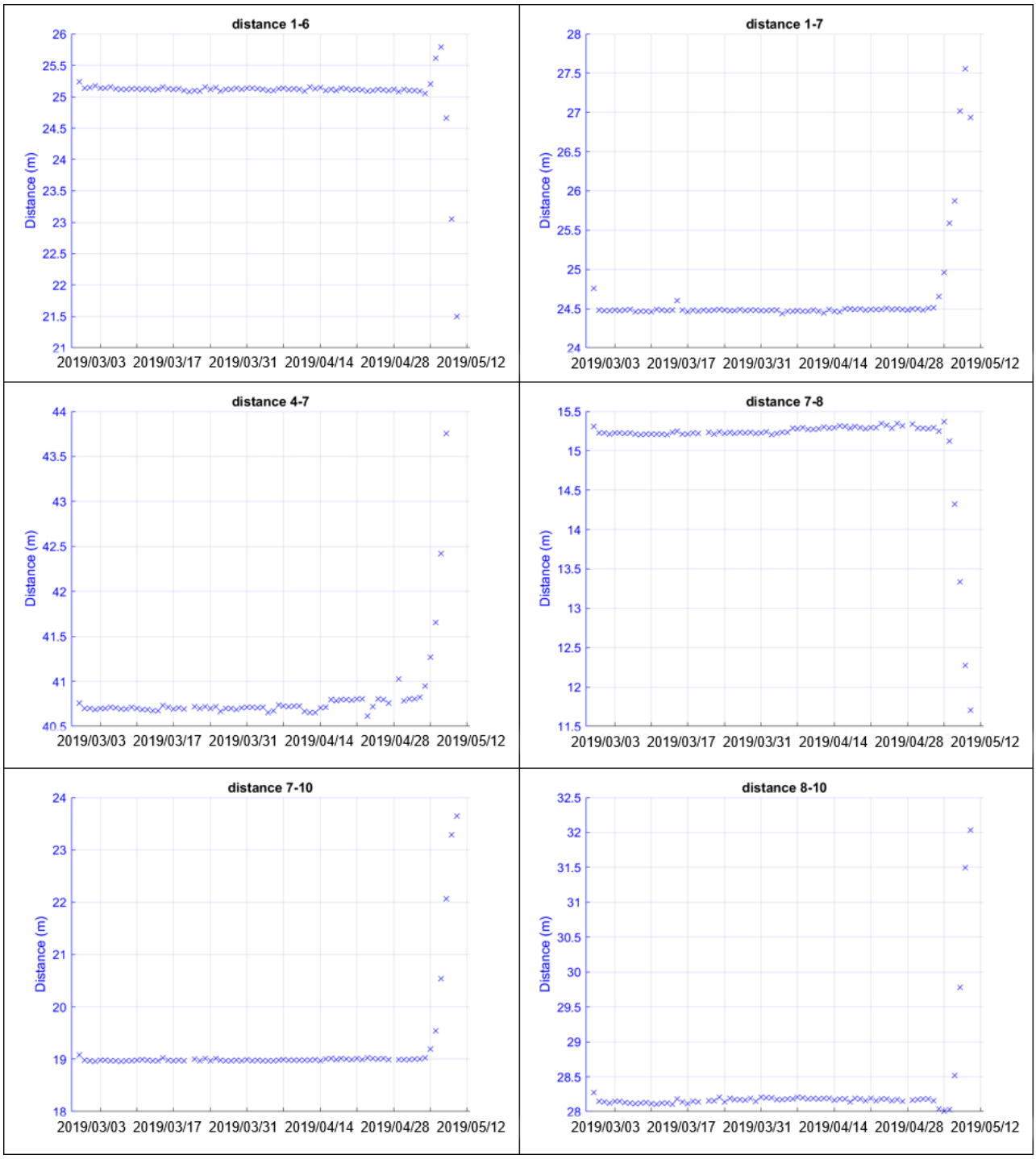

Figure 82. Displacement time series, daily mean values of some pair of nodes recording the event started on the 5th of May 2019.

The differences between the first acquired measurements (specifically the medium value of the first 5) and the last ones were evaluated to estimate the maximum displacement recorded by the network. The values were plotted in a links representation (Figure 83), allowing to understand which nodes

moved more. In Figure 83, warm colours show negative values which refer to an approach between the two sensors; conversely, cold colours show positive values, indicating two sensors moving away.

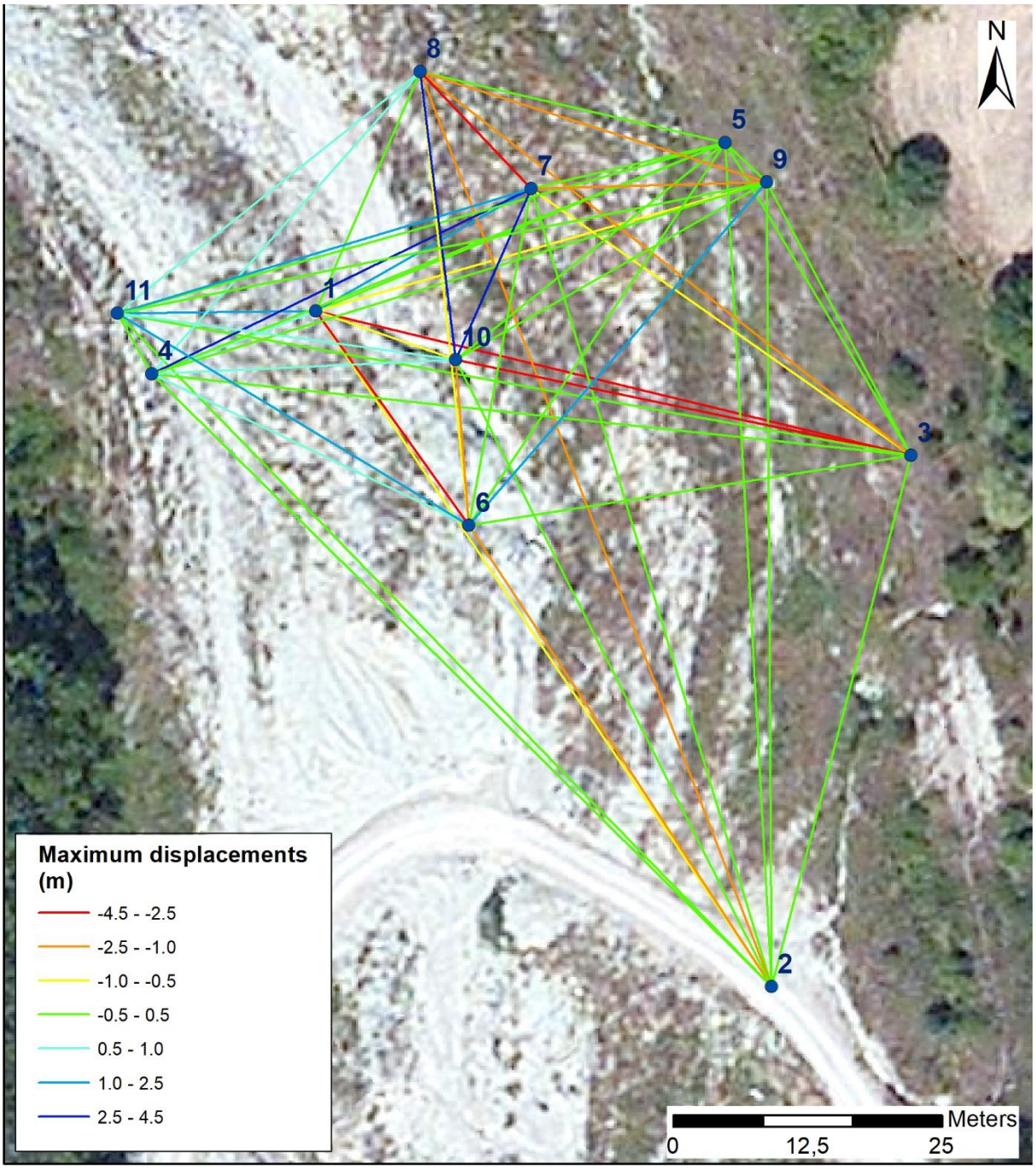

Figure 83. Difference between the first 5 distance values acquired by Wi-GIM and the last one.

However, due to the instability of the pole, as in the case of Nodes 4–8 (Figure 79), those directions could not be always significant. Therefore, it may be more appropriate to consider the absolute values, that anyway give an exhaustive idea of which sector of the landslide are exposed to higher displacements (Figure 84).

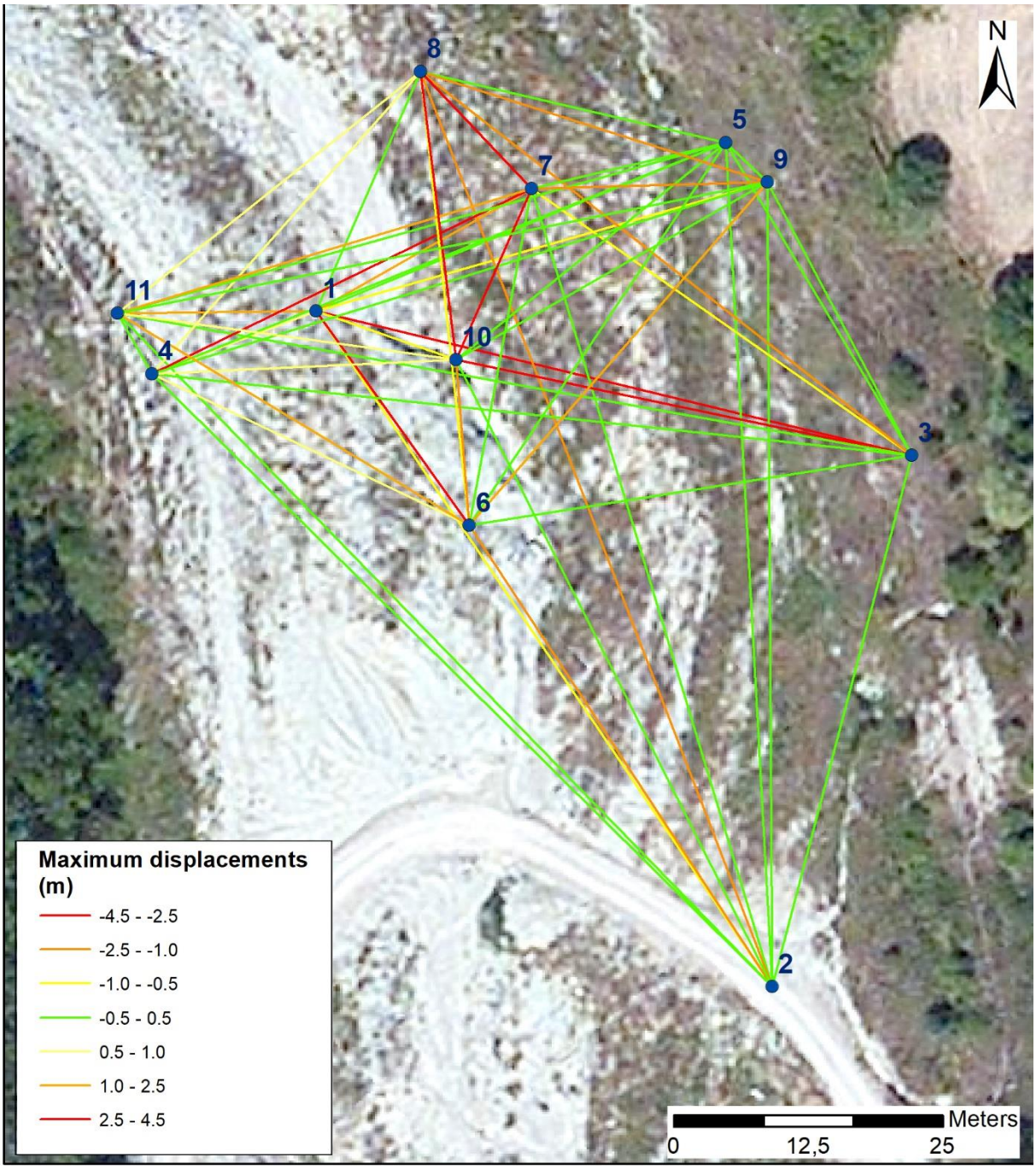

Figure 84. Absolute values of the difference between the first 5 distance values acquired by Wi-GIM and the last one.

During the event, the landslide completely destroyed the road close to Cluster 1, as can be seen in Figure 85 where pictures of the road taken before and after the event are reported.

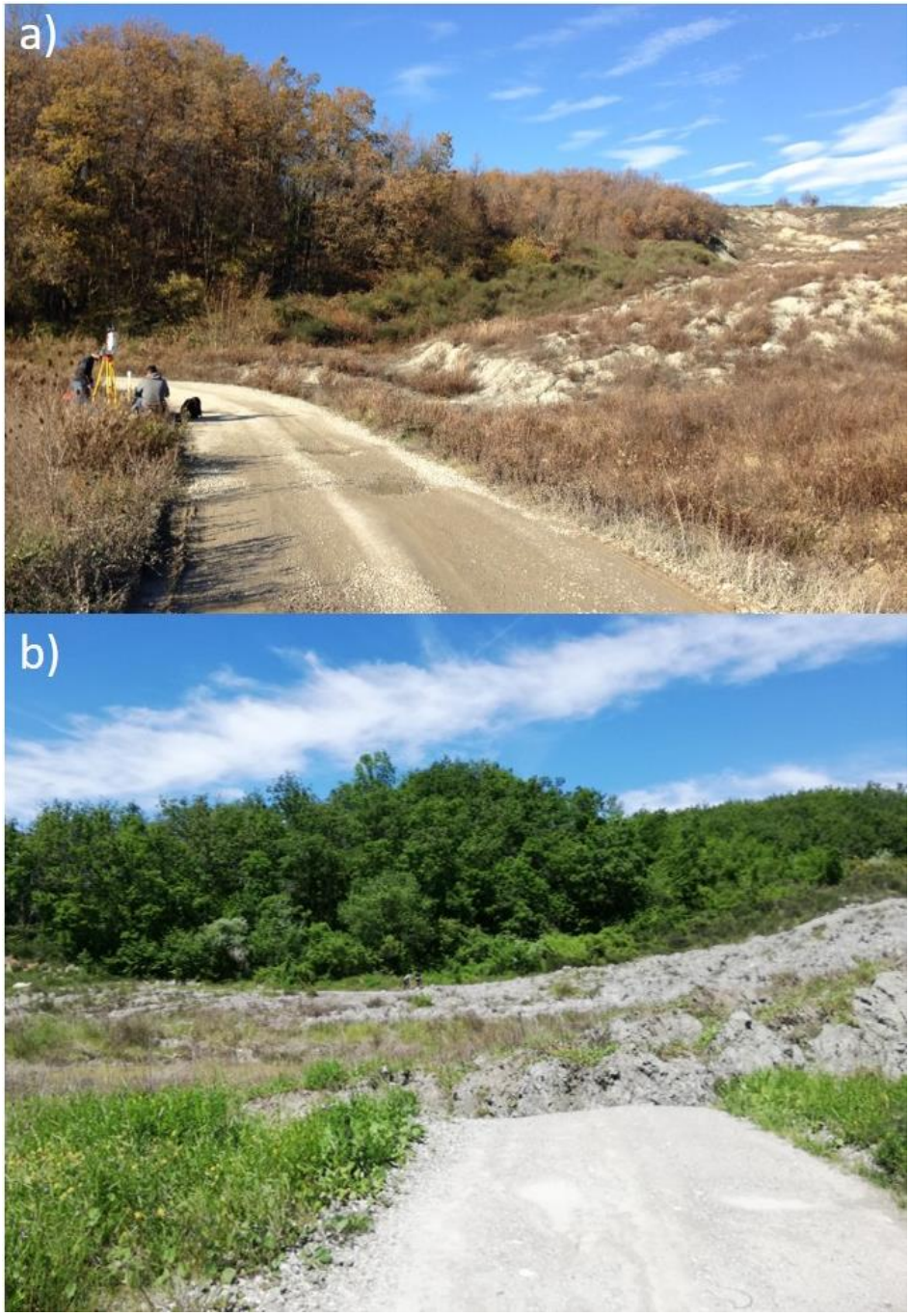

Figure 85. Pictures of the road crossing the landslide taken in December 2018 (a) and May 2019 (b).

Unfortunately, the master node was damaged during the event, and no more data have been acquired after the 10th of May. In sight of this, the whole Cluster was removed from the site on 2019/05/31.

6. Results and discussion

The last part of this thesis presents several considerations on the effectiveness of the Wi-GIM system, allowing to a better comprehension of its feasibility, highlighting both its advantages and limitations, together with the importance of using WiSIO for its deployment.

In particular, in the first part of this chapter, observations about the performance of the system are presented. The results of the validation which was carried out using the data from the Robotic Total Station (RTS), comparing the two measurements and computing the motion tracking of the nodes, are presented and discussed in Section 6.1.1; the influence of atmospheric effects such as rain and snow are pointed out in Section 6.1.2. Moreover, further remarks can be done looking at the Performance Index (PI), a parameter that allow to quantify the system performances over time, as well as the Cost-Benefit analysis, carried out comparing Wi-GIM with two traditional monitoring instruments, namely RTS and Ground-Based InSAR.

Additionally, the second part of this chapter shows the result obtained by applying WiSIO for the installation of the WI-GIM system in Roncovetro landslide. The comparison between the data obtained from the first installation (first configuration) and the second one (second configuration, i.e. the one set considering the output of WiSIO) allows to quantify the improvements achieved by using the developed algorithm.

6.1 Feasibility and reliability of the Wi-GIM system

6.1.1 Validation with the RTS, positioning and pathfinding

A validation of the system was carried out by using the results from the Robotic Total Station. As mentioned in Section 3.2 in fact, each node was equipped with an RTS target, allowing to have the same distances acquired by the two different monitoring system.

The comparison between the two sets of measurements shows an offset on the absolute distance values (Figure 86a – Figure 87a). In the here presented cases, the offset was equal to 83 cm and 90 cm, respectively for pairs 1–6 of Cluster 1 and 1–10 of Cluster 3. For all the examined pairs of nodes, the offset was more in general about 80 cm, and it was due to both problem of signal obstruction and problem related to the low-cost nature of the Decawave sensor. Concerning the first, the obstructed Line of Sight (LOS) of some pairs of nodes (due mainly to vegetation) caused a change in the direction of the signal, that consequently measured higher distances. However, as already mentioned, an error was introduced by the Decawave since, even in free LOS conditions, offsets in the order of the decimetre have been found.

Although the offset is not relevant for a monitoring aimed to record the distance variation, since it is constant for a given pair of nodes, it was corrected (Figure 86b – Figure 87b), and the result highlighted a very good correlation between the two sets of measurements.

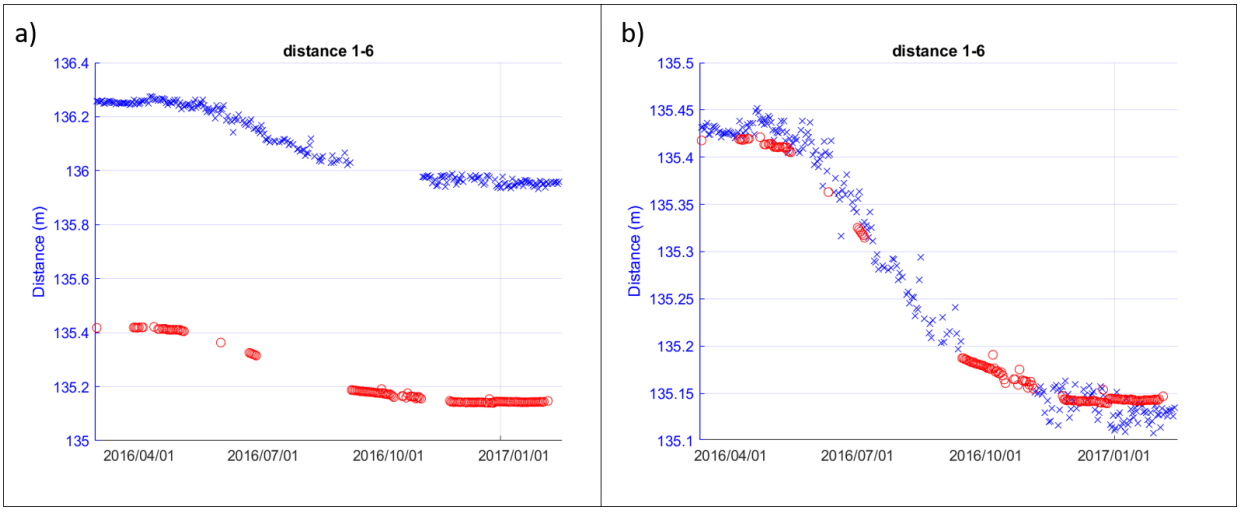

Figure 86. Displacement time series of the pair of nodes 1–6 of Cluster 1 from February 2016 to March 2017. Blue crosses: daily averages of filtered Wi-GIM data. Red circles: RTS data. a) data without offset compensation. b) compensated data.

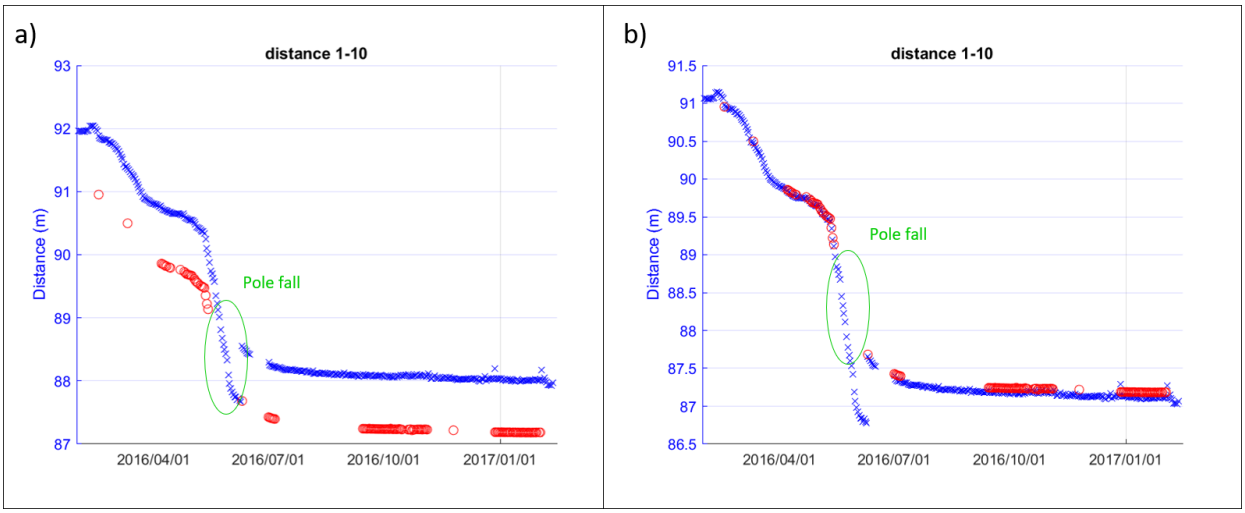

Figure 87. Displacement time series of the pair of nodes 1–10 of Cluster 3 from February 2016 to March 2017. Blue crosses: daily averages of filtered Wi-GIM data. Red circles: RTS data. The green circle highlights the pole fall. a) data without offset compensation. b) compensated data.

Interestingly, between May and June 2016 Wi-GIM nodes 1–10 of Cluster 3 recorded a movement while RTS did not generate any acquisition (Figure 87). This was due to the pole that slowly tilted and finally fell down. Whereas RTS lost sight of the target mounted on the pole and was not able to perform further measurements, the Wi-GIM nodes continued to detect displacements. Data from the RTS (represented by red circles in Figure 87) reappears only when the pole has been put back in place re-establishing the LOS condition. This is a key point of the proposed monitoring system, since although the free LOS strongly improves data reliability, it is not a sine qua non condition, as it is for the RTS.

In case a node is visible at least by other 3 nodes, Wi-GIM system also enables to determine its planimetric position and track its variation over time. To find out the absolute positions of a node, a circle is traced, considering the sensor coordinates as its centre and the measured distance with the other nodes as its radius. The intersection of three circles individuates an elliptic triangle whose centre is taken as the position of the node. Since for a reliable and significant positioning, a node must be seen by three stable nodes, the tracking of Cluster 1 was carried out considering nodes 1, 2 and 7 as stable points (being placed outside the landslide's body). This procedure has been repeated for each daily average measurements, and a motion tracking feature was tested and compared with the results from the geodetic monitoring (Figure 88 – Figure 89 – Figure 90 – Figure 91). Note that, for a better comparison, the offset that affect the Wi-GIM measurements is already removed in the following images.

Concerning the following cases of Cluster 1, the accuracy of the positioning is in the order of the decimetre, but it varies with the scale: lower is the displacement and lower is the precision. Moreover, please note that this positioning has been done in 2D, without taking into account the elevations of

the points, considering the area as a planar one and thus making an approximation. However, looking at the slopes at a node-to-node scale, the error can be judged acceptable. As a matter of fact, in the following cases the two tracks run parallel due to the offset affecting the Wi-GIM measurements, nevertheless Wi-GIM is able to correctly trace the direction and module of the displacement vector.

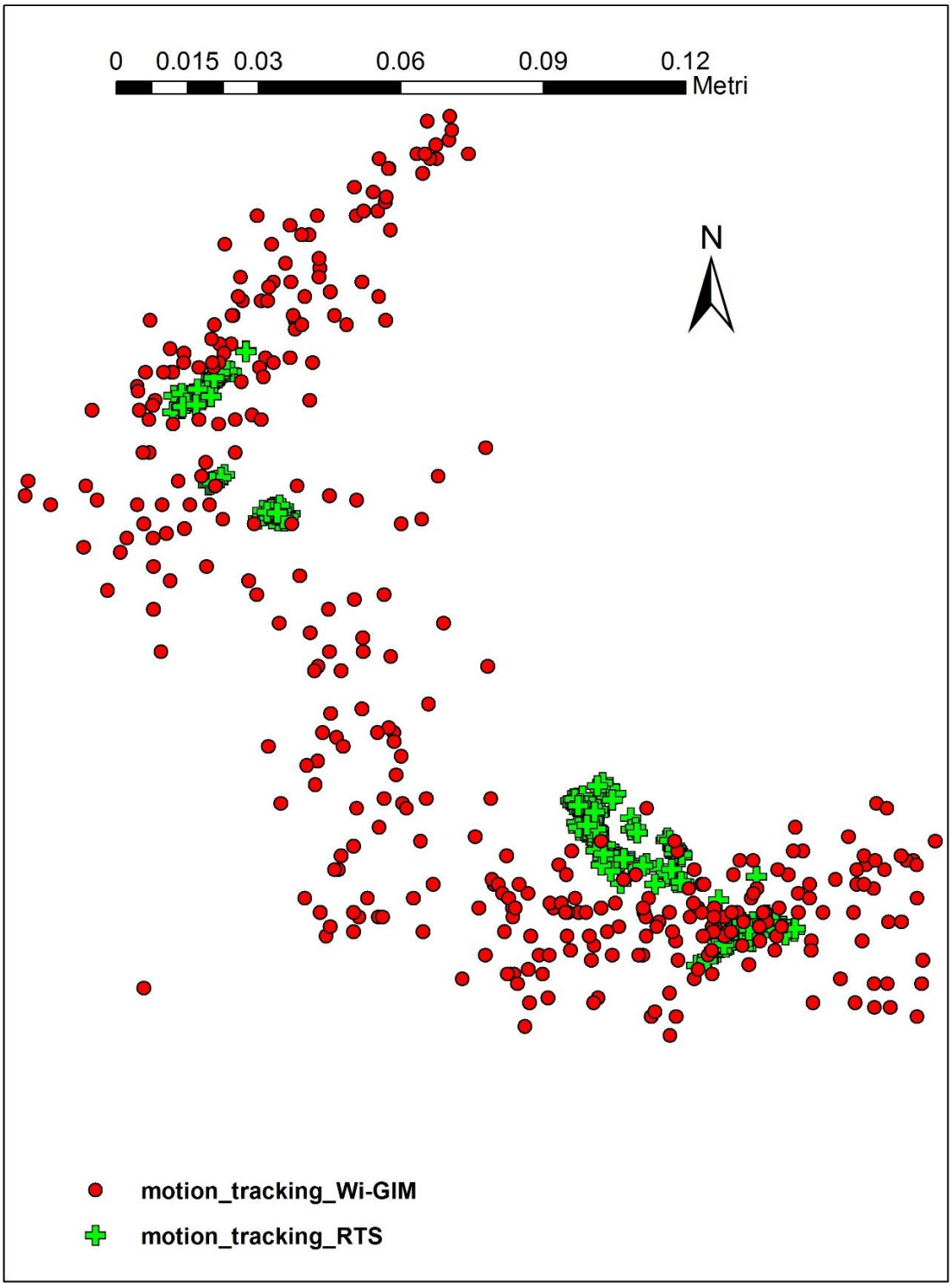

Figure 88. Motion tracking of node 3 from Roncovetro cluster 1 considering data of the whole monitoring period. Crosses refer to RTS and circles to Wi-GIM measurements, respectively.

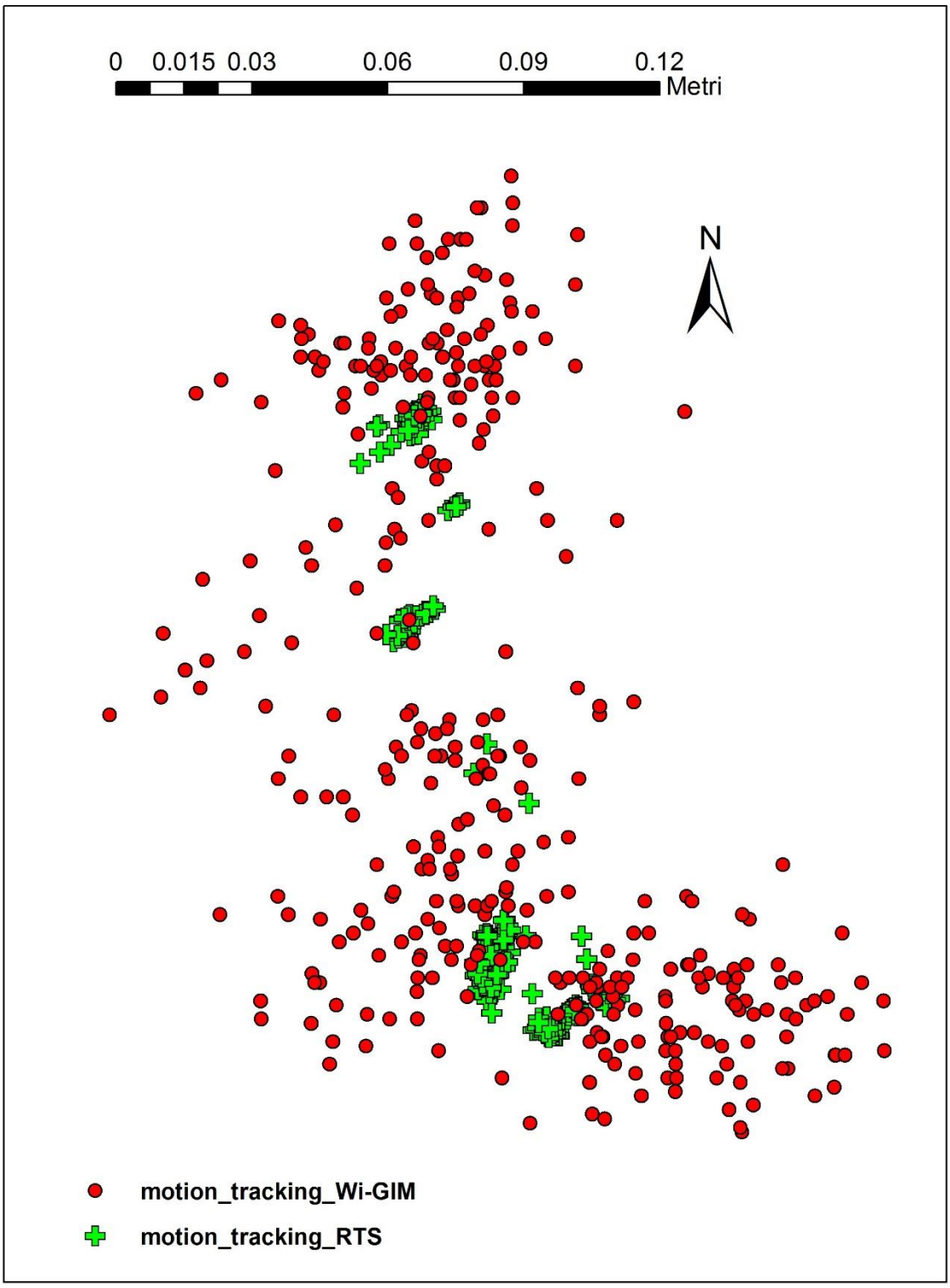

Figure 89. Motion tracking of node 4 from Roncovetro cluster 1 considering data of the whole monitoring period. Crosses refer to RTS and circles to Wi-GIM measurements, respectively.

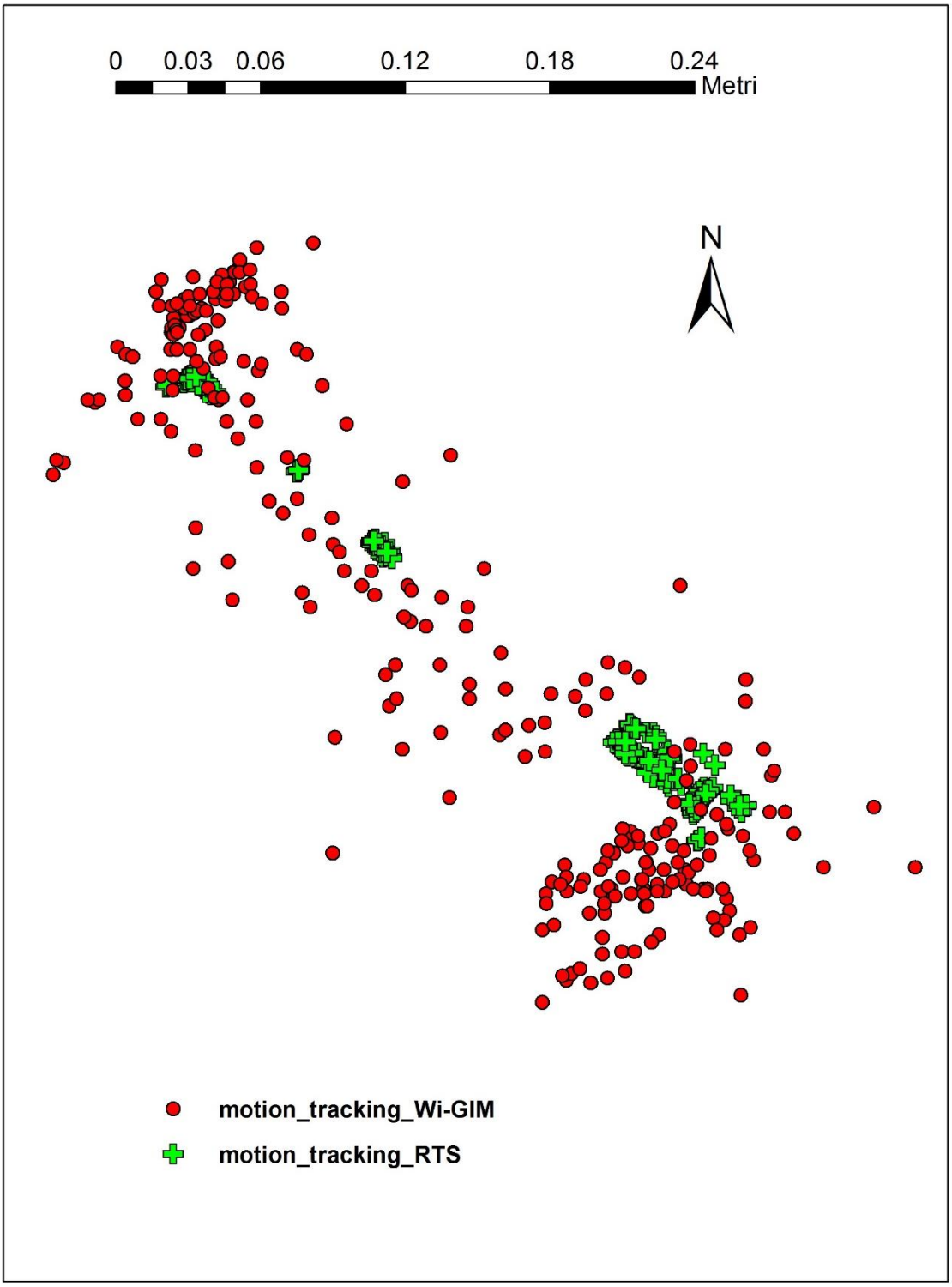

Figure 90. Motion tracking of node 6 from Roncovetro cluster 1 considering data of the whole monitoring period. Crosses refer to RTS and circles to Wi-GIM measurements, respectively.

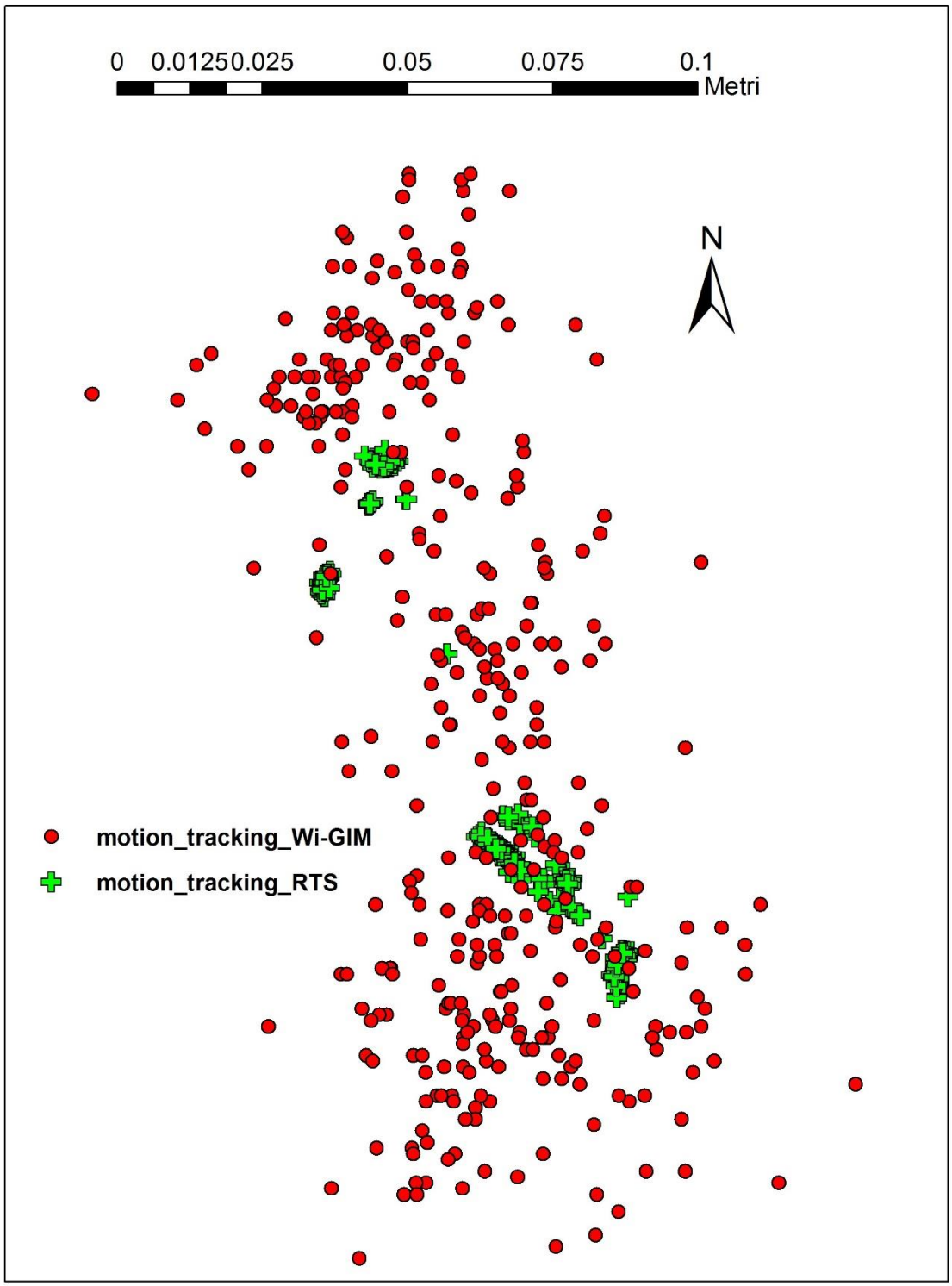

Figure 91. Motion tracking of node 8 from Roncovetro cluster 1 considering data of the whole monitoring period. Crosses refer to RTS and circles to Wi-GIM measurements, respectively.

An example showing how the precision improves increasing the displacement is reported in Figure 92. It concerns the motion tracking of node 10 of Cluster 3. In this case, the nodes considered as stable for the analysis were nodes 1, 2 and 6. Actually, they were not out of the landslides, and therefore their location could not be as reliable as the one carried out for Cluster 1. However, the data showed

minimum movements, so the results can be considered satisfactory. One can note how at this scale, the precision is higher (in the order of millimetres in some cases) and that both systems are able to track movement of around 3.8 m toward SSE from February to September 2016.

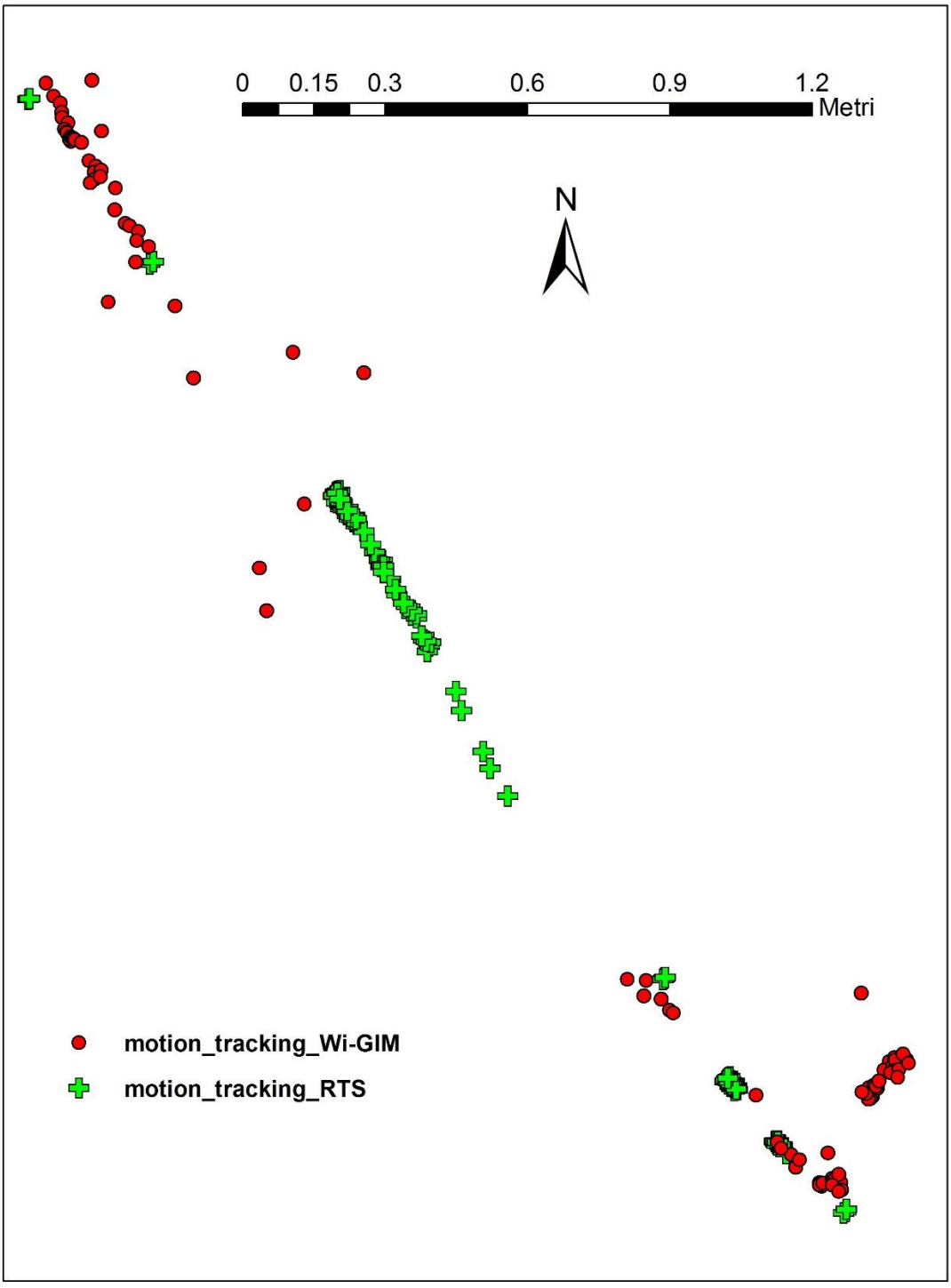

Figure 92. Motion tracking of node 10 from Roncovetro cluster 3 considering data acquired from February to September 2016. Crosses refer to RTS and circles to Wi-GIM measurements, respectively.

Moreover, in Figure 93 a different representation to analyse the positioning over time, i.e. the motion tracking of one node month by month, is reported. If the representations of Figure 88 to Figure 92 can be useful to understand the capability of the Wi-GIM system to correctly track a real movement, the one that follow allows a better comprehension of the periods in which the landslide has had higher displacements.

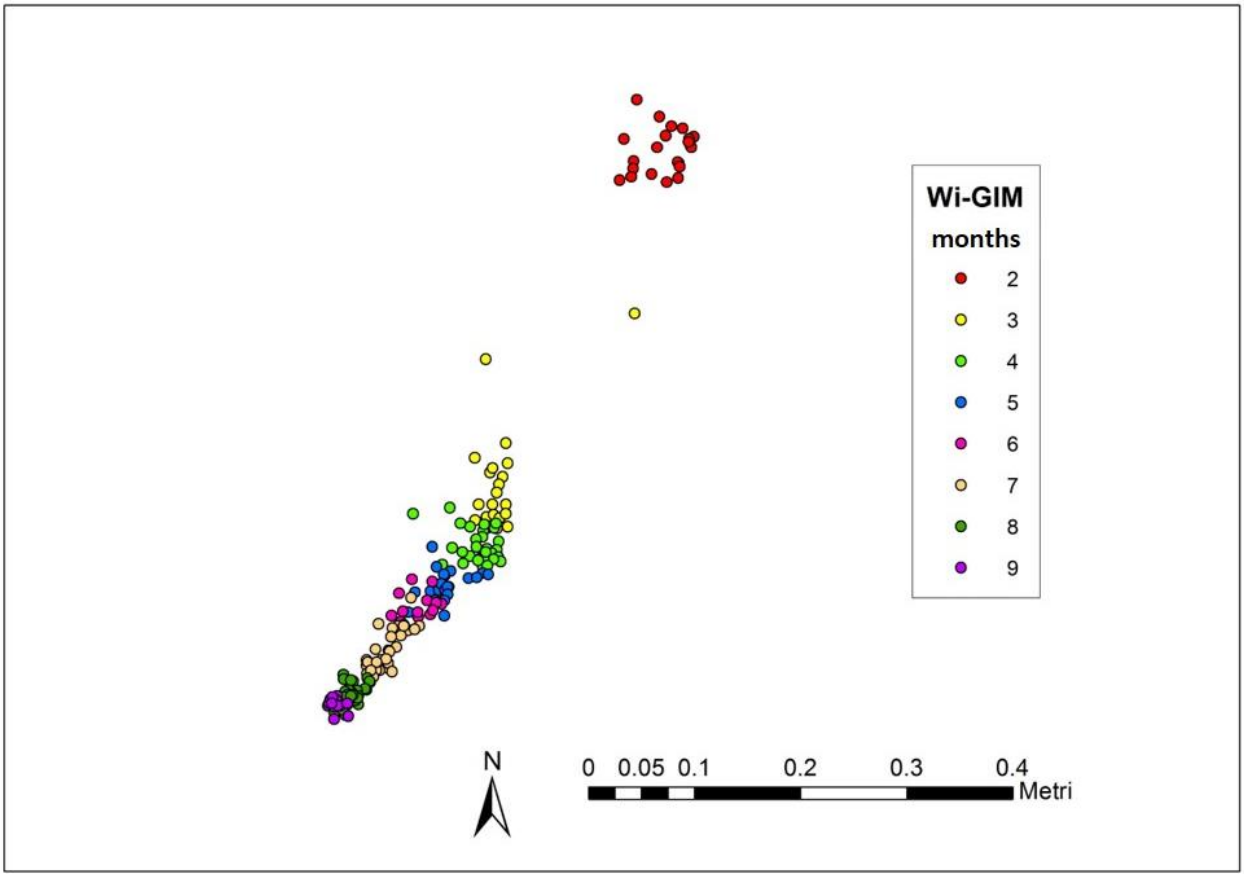

Figure 93. Motion tracking of node 12 from Roncovetro cluster 3 considering data from February to September 2016. Different colours point out months.

6.1.2 Rain and snow effects

A further study was conducted to investigate the effects of rain and snow on Roncovetro's clusters. The attention was in this framework not much focused in seeing how rain and snow affected the landslide, but how they affected the monitoring system. For rainfall, rain gauge data from a meteorological station previously installed in the area were used. For snow, only information about the occurrence of snowy days was available. Here are reported some examples highlighting a basically stable situation and how rainfall and snowy days are not associated with spikes or increased noise (Figure 94 – Figure 95). Indeed, no relation between the atmospheric events and data was observed, in particular referred to data dispersion, acquired data percentage or valid data percentage.

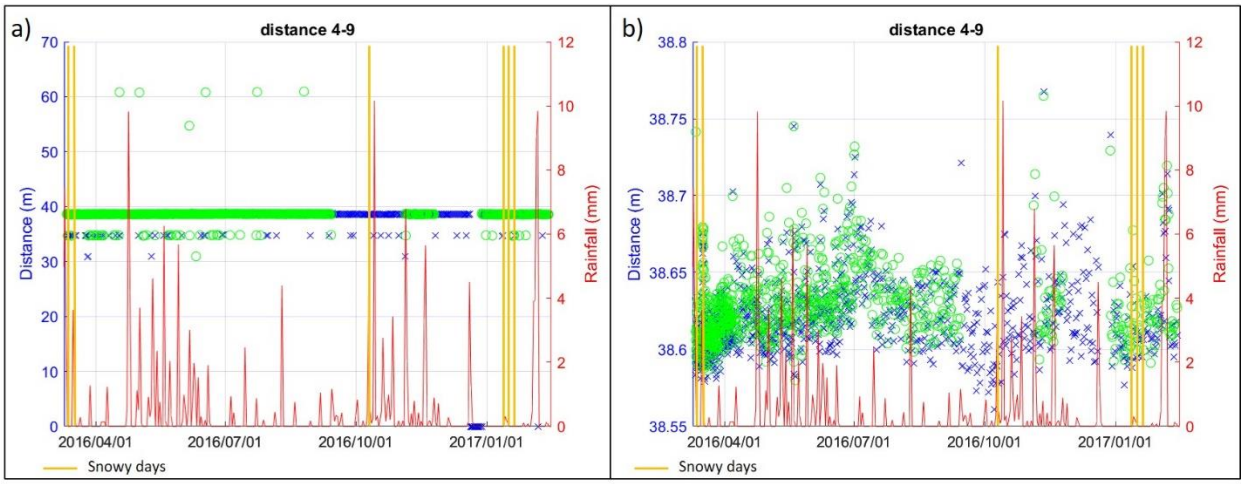

Figure 94. Atmospheric effect on the Wi-GIM system. a) raw distances of nodes 4–9 belonging to Cluster 1. b) distance validated values of nodes 4–9 belonging to Cluster 1.

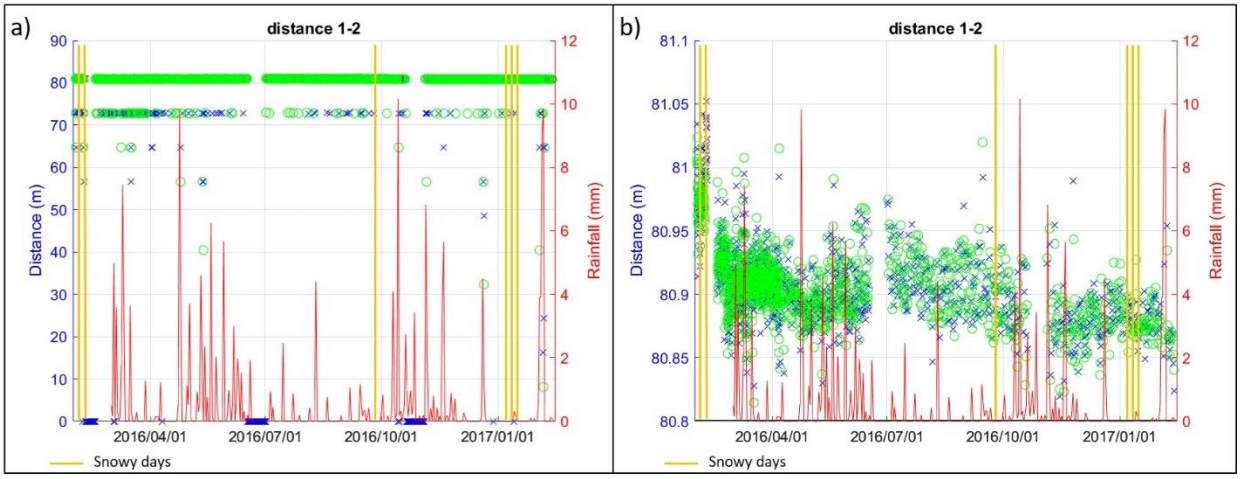

Figure 95. Atmospheric effect on the Wi-GIM system. a) raw distances of nodes 1–2 belonging to Cluster 3. b) distance validated values of nodes 1–2 belonging to Cluster 3.

6.1.3 Performance Index (PI)

In order to quantitatively evaluate the Wi-GIM performance and its variation over time, a specific index, called Performance Index (PI), was introduced in this study. The analysis of the PI values plotted vs time allowed to assess possible local anomalies, making possible to change the system settings in progress, in order to achieve the best results in terms of data quality and continuity. The Performance Index (PI) is calculated daily for each pairs of nodes, and it is defined as the product of two parameters:

PI = P1 x P2

Each parameter is defined as follows:

- P1= N_v/N_{tot}
- P2=1-D

where:

- N_v is the number of valid distance readings (outliers and invalid measurements excluded) for each pair of nodes;
- N_{tot} is the total numbers of readings requested by the master node;
- D is the difference between the RTS distance and the compensated Wi-GIM distance expressed in metres.

Since each parameters P1 and P2 varies from 0 to 1, PI ranges from 0 (minimum performance) to 1 (maximum performance). Thus, the index expresses the quality of each link over time by considering the communication capacity of each pair of nodes and the correctness of the performed readings. In the case study of Roncovetro, the PI allowed to continuously evaluate the performance of each component of Wi-GIM system, as well as to make some local interventions to maximize the quality of monitoring data.

Naturally, the assessment of P2 can be done only in case a parallel monitoring is installed in the area, as for the Roncovetro landslide, or if, more in general, the actual position of each sensor is known. In case this is not applicable, only P1, which is however worthwhile to monitor the system performance, can be estimated.

As mentioned, the P1 parameter is the ratio between the valid distances over the total measures that the master node should acquire. This value is calculated on a moving average considering e.g. days or months. Depending on the chosen time interval, the information given by the PI are visualised differently. To give an example, the variation of P1, P2 and PI for the pair 3–9 of Cluster 1 over time is presented in Figure 96 and Figure 97 considering respectively 20 days and 1 day as time interval for the evaluation of P1. Results are discussed considering the acquired data, and in particular the valid ones and the daily averaged ones compared with the RTS compensated measurements (Figure 98).

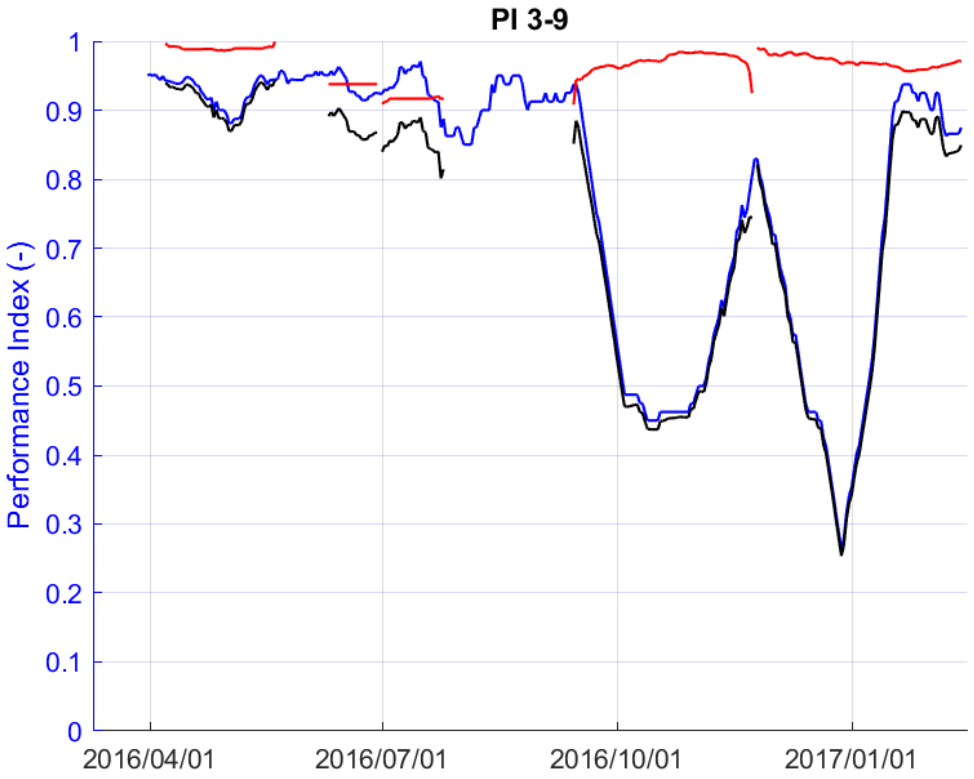

Figure 96. Variation of performance parameters P1 (blue line) and P2 (red line) and Performance Index (PI: black line) over time, considering a time interval of 20 days. Data are relative to Cluster 1 pair of nodes 3–9.

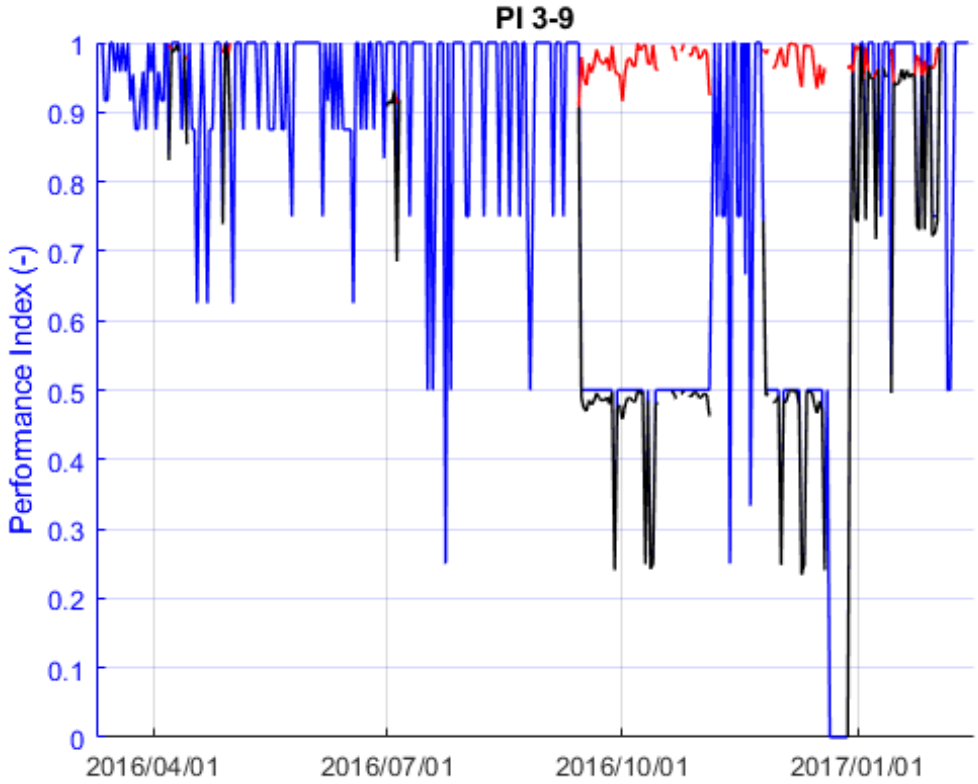

Figure 97. Variation of performance parameters P1 (blue line) and P2 (red line) and Performance Index (PI: black line) over time, considering a time interval of 1 day. Data are relative to Cluster 1 pair of nodes 3–9.

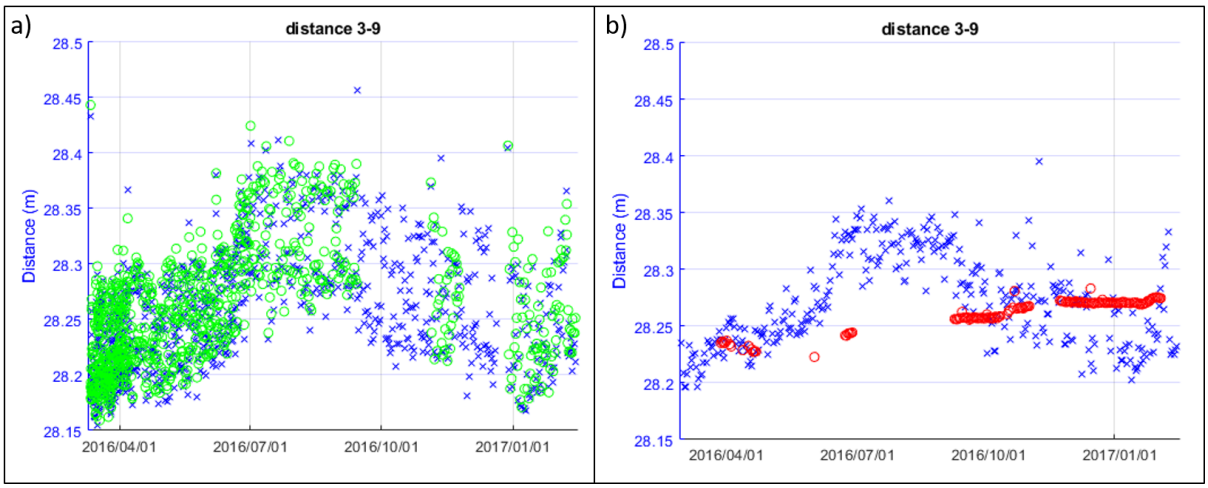

Figure 98. Displacement time series from the pair of nodes 3-9 of Roncovetro Cluster 1. a) distance validated values. Green circles and blue crosses represent the distance measured from one node to the other and vice versa. b) Daily averages of compensated Wi-GIM data (blue crosses) and RTS data (red circles).

As a general rule, one can note that P1 is the parameter which mainly affects the PI values, and this is mainly due to environmental disturbances (such as vegetation growth) which obstruct the LOS making the communication more unstable. In the presented case, i.e. nodes 3–9 of Cluster 1, P1 strongly decreases from October 2010 to January 2017, reaching values of about 0.5, with an interval in correspondence of the end of November, when its values reach 1 again (Figure 96–Figure 97). This trend is due to the number of measures recorded by Wi-GIM, that are halved in the just mentioned periods, as clearly visible in Figure 98, where only measurements from one node to the other are acquired. This has been a recurring behaviour of the system, whose causes are still unclear but that is probably due to a UWB module bug. Another anomalous case is the one occurred at the end of December 2016, when P1 was equal to zero, meaning no data recorded at all, due to the low battery of one of the nodes (Figure 97). Concerning the P2 parameter (the red line in Figure 96 and Figure 97), please note that its repeatedly absence in the graph is simply due to the absence of the RTS data, as visible in Figure 98. Apart from these particular cases, the PI fluctuates in between 0 and 1, and, whereas it gives more detailed but sometimes chaotic information if evaluated daily (Figure 97), its trend over time is better represented when considering a wider time interval, even if less precise (Figure 96).

The same elaboration is then reported for the pair 1–7 of Cluster 3 (Figure 99 to Figure 101).

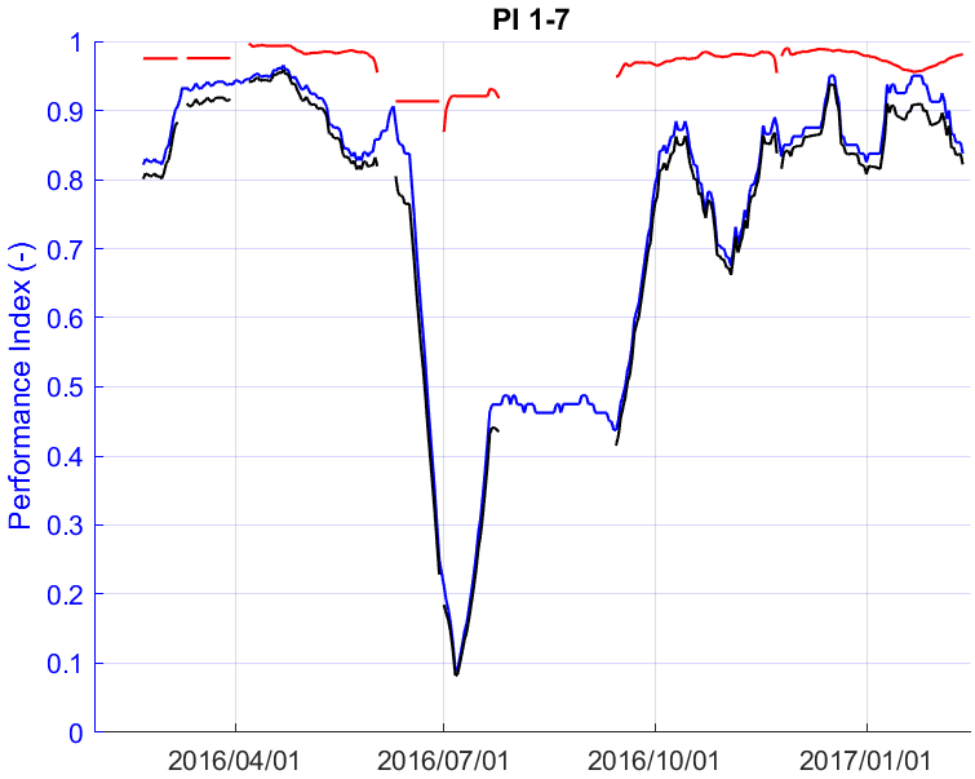

Figure 99. Variation of performance parameters P1 (blue line) and P2 (red line) and Performance Index (PI: black line) over time considering a time interval of 20 days. Data are relative to Cluster 3 pair of nodes 1–7.

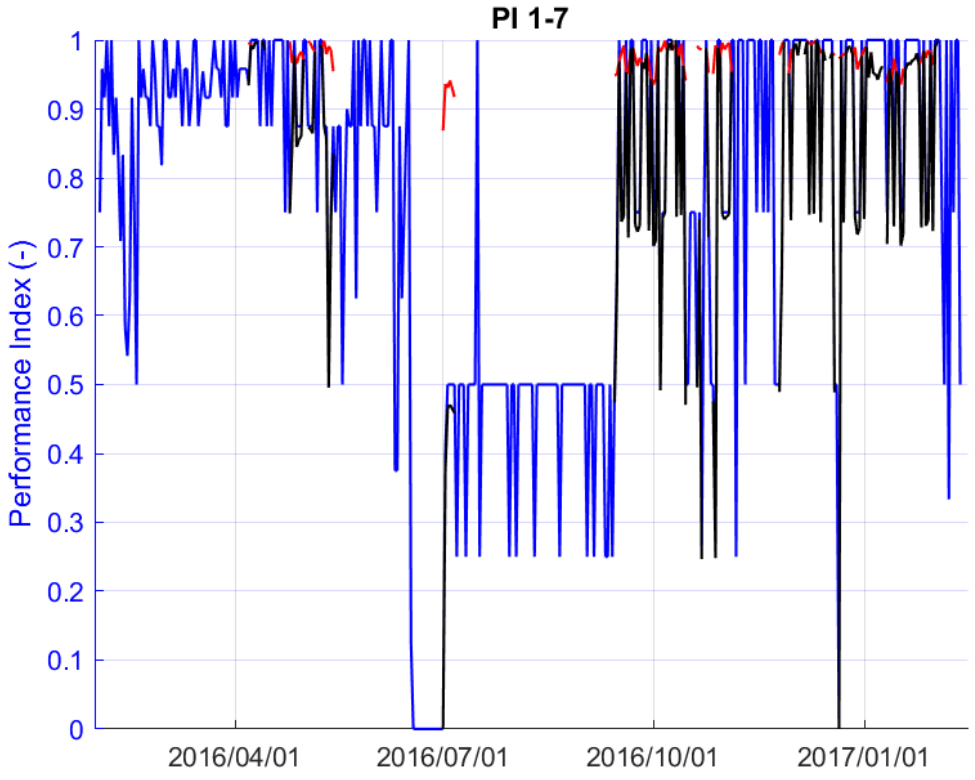

Figure 100. Variation of performance parameters P1 (blue line) and P2 (red line) and Performance Index (PI: black line) over time, considering a time interval of 1 day. Data are relative to Cluster 3 pair of nodes 1–7.

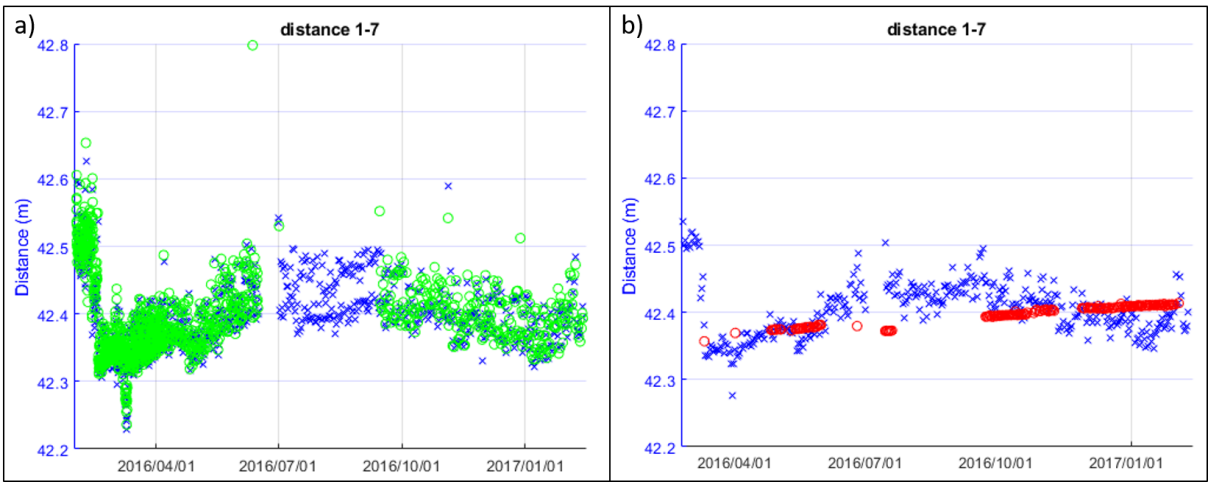

Figure 101. Displacement time series from the pair of nodes 1-7 of Roncovetro Cluster 3. a) distance validated values. Green circles and blue crosses represent the distance measured from one node to the other and vice versa. b) Daily averages of compensated Wi-GIM data (blue crosses) and RTS data (red circles).

Also in the case of nodes 1–7 of Cluster 3, the absence of the RTS data and therefore of the P2 parameter is recurrent, as well as the presence of the Wi-GIM measures in only one direction (from July 2016 to September 2016) and the absence of data due to a low battery (end of June 2016 and end of December 2016) that caused the total absence of the Wi-GIM data and therefore the zero value of the P1 parameter (Figure 99 to Figure 101).

At the end of the monitoring period it has been possible to calculate the mean performance parameters and index for each link, and represent it on a map, as can be observed in Figure 102, Figure 103 and Figure 104. In this case, the Performance Index has been calculated doing an average of all the values obtained by considering a daily time interval.

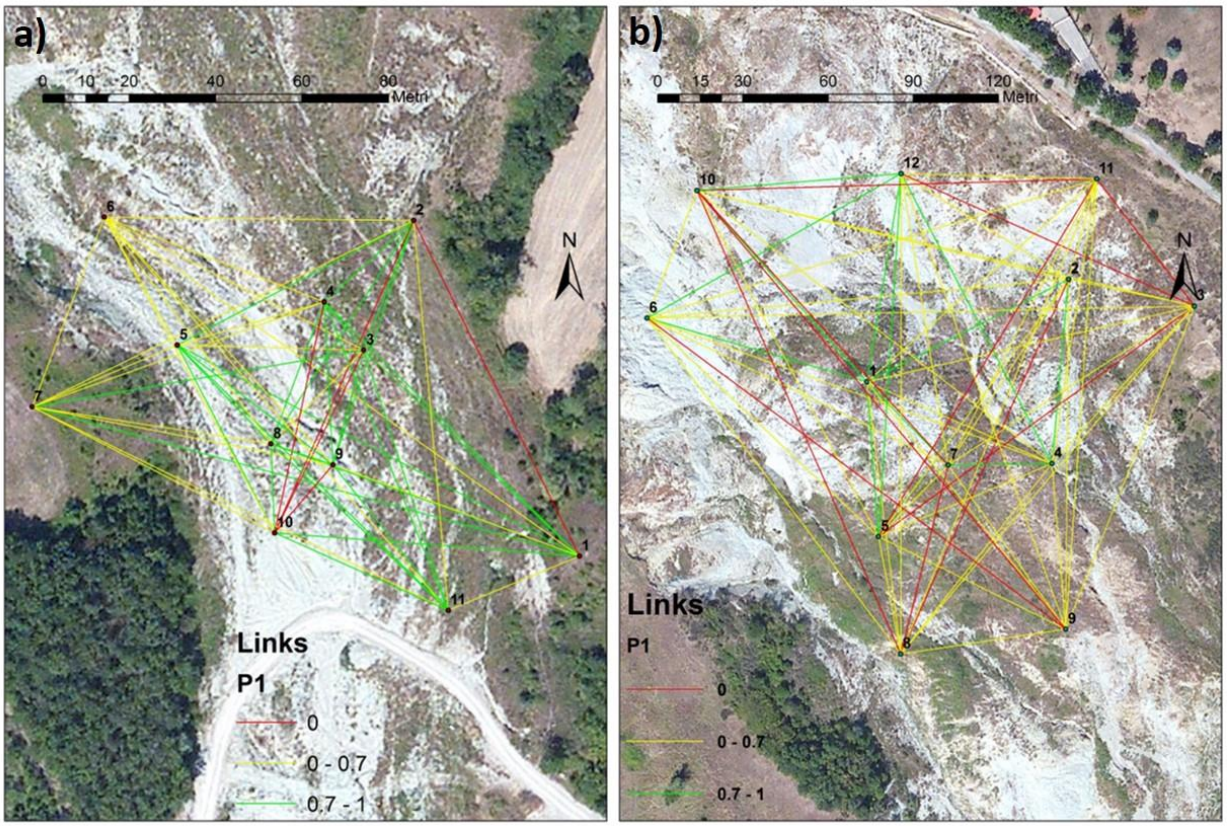

Figure 102. Mean performance parameter P1 for the node links of Cluster 1 (a) and Cluster 3 (b).

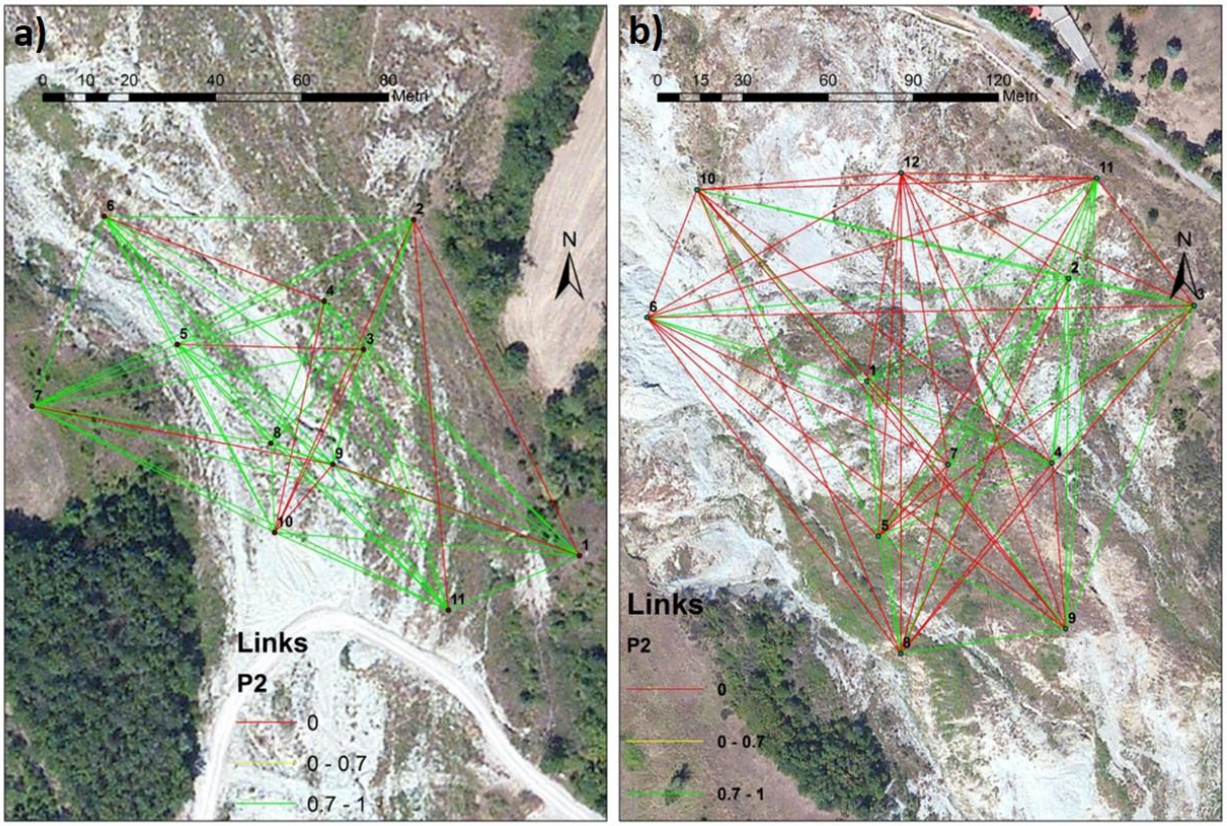

Figure 103. Mean performance parameter P2 for the node links of Cluster 1 (a) and Cluster 3 (b).

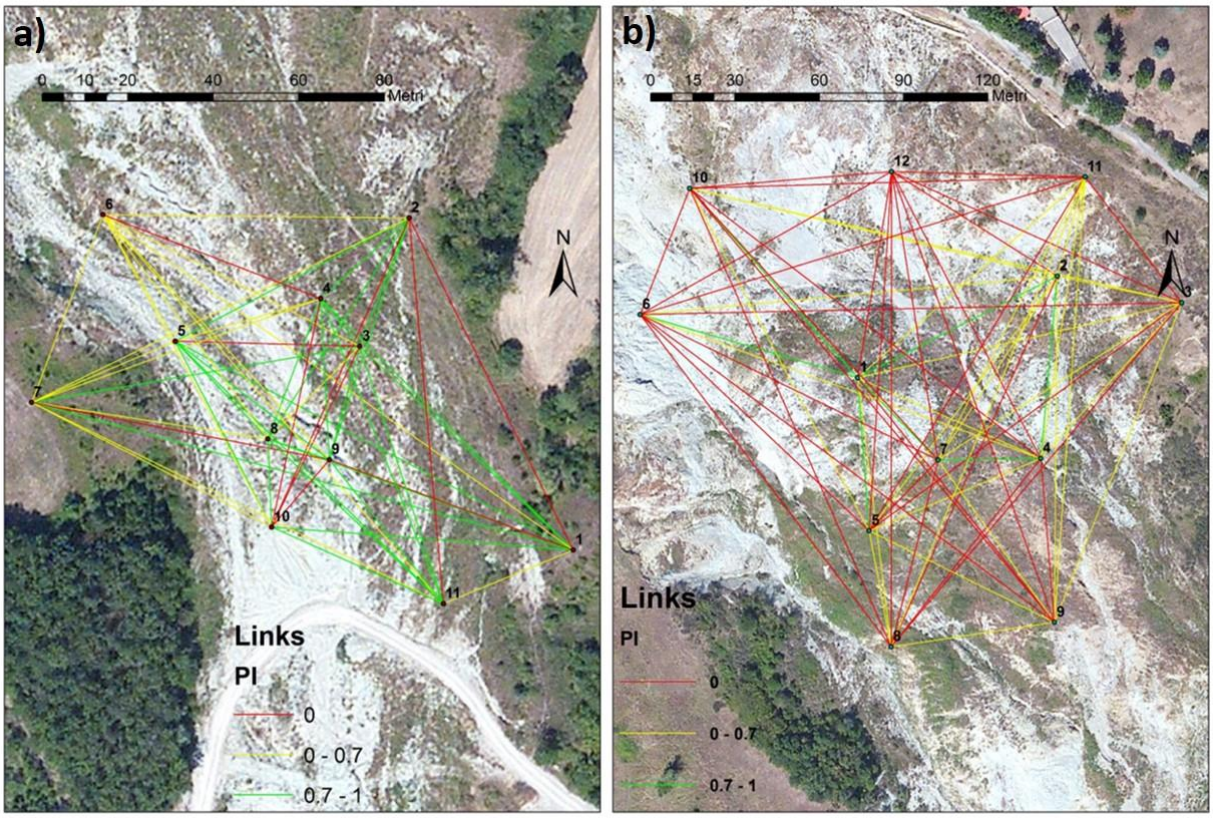

Figure 104. Mean Performance Index (PI) for the node links of Cluster 1 (a) and Cluster 3 (b).

6.1.4 Cost-Benefit analysis

Using the cost-benefit analysis template provides costs and benefits information that can be used to analyse and evaluate the Wi-GIM system. Three different systems usually exploited for monitoring ground instability phenomena have been compared in terms of costs and benefits. In particular, a ground-based radar and a Robotized Total Station (RTS) have been considered together with Wi-GIM.

Concerning costs, to better comprehend the advantages of the examined monitoring systems, a distinction between two different areas has been done:

i. Area 1: an area of 500 m^2;
ii. Area 2: an area of 100000 m^2.

Note that as regard the RTS and the radar, as 'direct costs' the renting cost of the systems for 1 year has been considered, since the actual cost would be too high and so not comparable with Wi-GIM. A detailed analysis of the direct costs for each instrumentation is described in Table 12. Concerning the Wi-GIM system direct costs, note that one battery and one photovoltaic panel or two batteries are actually included in the price of a single battery. To keep the system running for more than one month in fact, it is necessary to replace the batteries (so two for each node are required) or to equip each one with a photovoltaic panel.

Direct costs					
Wi-GIM		**RTS**		**Radar**	
Item	**cost (€)**	**Item**	**cost (€)**	**Item**	**cost (€)**
Battery	20	Total Station	11000[(1)]	Radar	54000[(2)]
UWB module	20	Target	120		
Micro-controller	30				
TOT (€)	**70**		**11120**		**54000**

[(1)]Price taken from a one-year rental made by the Department of Earth Sciences of the University of Florence for the monitoring of the Lungarno Diaz sinkhole (FI, Italy) with the Pizzi Instruments S.r.l company in 2019.
[(2)]Price taken from a one-year rental made by the Department of Earth Sciences of the University of Florence for the monitoring of the Pomarico landslide (MT, Italy) with the ELLEGI-LiSALab S.r.l. company in 2019.

Table 12. Direct costs considered for the Cost-Benefit analysis.

As for the benefits, to more easily understand the advantages and the disadvantages of Wi-GIM than the other two monitoring systems, a table that summarized benefits with a score from 1 to 5 has been realised. The scores have been assigned as follows:

1: poor;

2: fair;

3: good;

4: very good;

5: excellent.

Results of the Cost-Benefit analysis are shown in Table 13. Due mainly to the low scores assigned to precision, vulnerability (caused by the instability of the nodes) and maximum range at which the system works, Wi-GIM has a final mark lower than the other two systems, but anyway classified as good. However, the benefits results must be considered together with the costs one: if Wi-GIM has some limits, on the other hand it is characterized by a really low cost. Looking at the following table in fact, one can note that there is a big difference between the total price of Wi-GIM (5220 € in the worst scenario analysed) and the price of the other two systems (18150 € for the RTS and 58100 € for the radar), although for the lasts only the rent for one year has been considered. Furthermore, the total price of the Wi-GIM system can be even reduced with the use of photovoltaic panels, since the high maintenance costs are due to the field trips for the batteries replacements.

Therefore, the cost-benefit analysis points out that where a high precision is not requested or big distances are not involved, Wi-GIM can be a good compromise (Table 13).

COSTS										
		area (m^2)	number of nodes/targets	**Direct costs (€)**	**Energy consumption (€)**	**Maintenance costs (€)**	**Installation costs (€)**		**Data trasmission costs (€)**	**TOT (€)**
							Materials	Labor		
Wi-GIM	Area 1	500	5	350	20	1500	50 [(1)]	200	700 [(4)]	2820
	Area 2	100000	30	2100	120	1800	300 [(1)]	200	700 [(4)]	5220
RTS	Area 1	500	5	11600	150	200	1600 [(2)]	500	700 [(4)]	14750
	Area 2	100000	30	14600	200	350	1600 [(2)]	700	700 [(4)]	18150
Radar	Area 1	500	-	54000	300	100	2500 [(3)]	500	700 [(4)]	58100
	Area2	100000	-	54000	300	100	2500 [(3)]	500	700 [(4)]	58100

[(1)]Price of the supports for the UWB modules. [(2)]Sum of the prices of the protection structure (1200€) plus the reinforced concrete pillar on which the instrument lean (400€). [(3)]Sum of the prices of the protection structure (2000 €) plus the supporting structure needed for the ground based radar (500 €). [(4)]Sum of the prices of the sim card (200 €) plus the modem necessary for the data trasmission (500€).

BENEFITS								
	Vulnerability	**Precision**	**Maximum range**	**Environmental impact**	**Influence of atmospheric events**		**Installation effort**	**TOT**
					Rain	Snow		
Wi-GIM	2	3	2	3	4	4	5	3,3
RTS	3	4	5	4	3	3	3	3,6
Radar	5	5	5	4	4	1	4	4,0

Table 13. The Cost-Benefit analysis.

6.2 Evaluation of the effectiveness of WISIO by comparing the two installations of the Wi-GIM system

To highlight the effectiveness of WiSIO, a comparison was made between the results from the Wi-GIM system with the old 2016 installation and the new one, which was supported by WiSIO optimizing procedure, considering both the amount of acquired data and their worth.

The percentage of collected and valid data (data without no outliers or zero values) both in the old and in the new configuration is shown in Figure 105 where the percentages of respectively collected and valid measures in the whole monitoring periods are represented by means of coloured links for each pair of nodes.

In the new configuration (Figure 105a,b), the percentage of collected data ranges between 90% and 100% for all the pairs, except for the 4 previously mentioned pairs (see Section 5) and for pairs 1–5; 3–10; 9–10. In these last three cases, both collected and valid data are in between 45% and 50%).

In the old configuration (Figure 105c,d), the percentage of collected data is less than 60% for 10 pairs and the percentage of valid measures do not reach the 60% for 22 pairs. That means that not only in the old configuration less data were acquired due to non-LOS problems, but most importantly that the quality of data was worse as well. Indeed, in the old configuration the acquisition of a value did not guarantee its validity, as it is for the new configuration, where there is no discrepancy from the percentage of collected and valid data.

Considering as suitable pairs the ones whose percentage of valid data is at least 60%, and that consequently 50 out of 56 pairs are suitable in the new configuration (i.e. the 89,3%), instead of 34 out of 56 in the old one (i.e. the 60,7%), it follows that thanks to WiSIO the amount of valid data increased by the 28.6%.

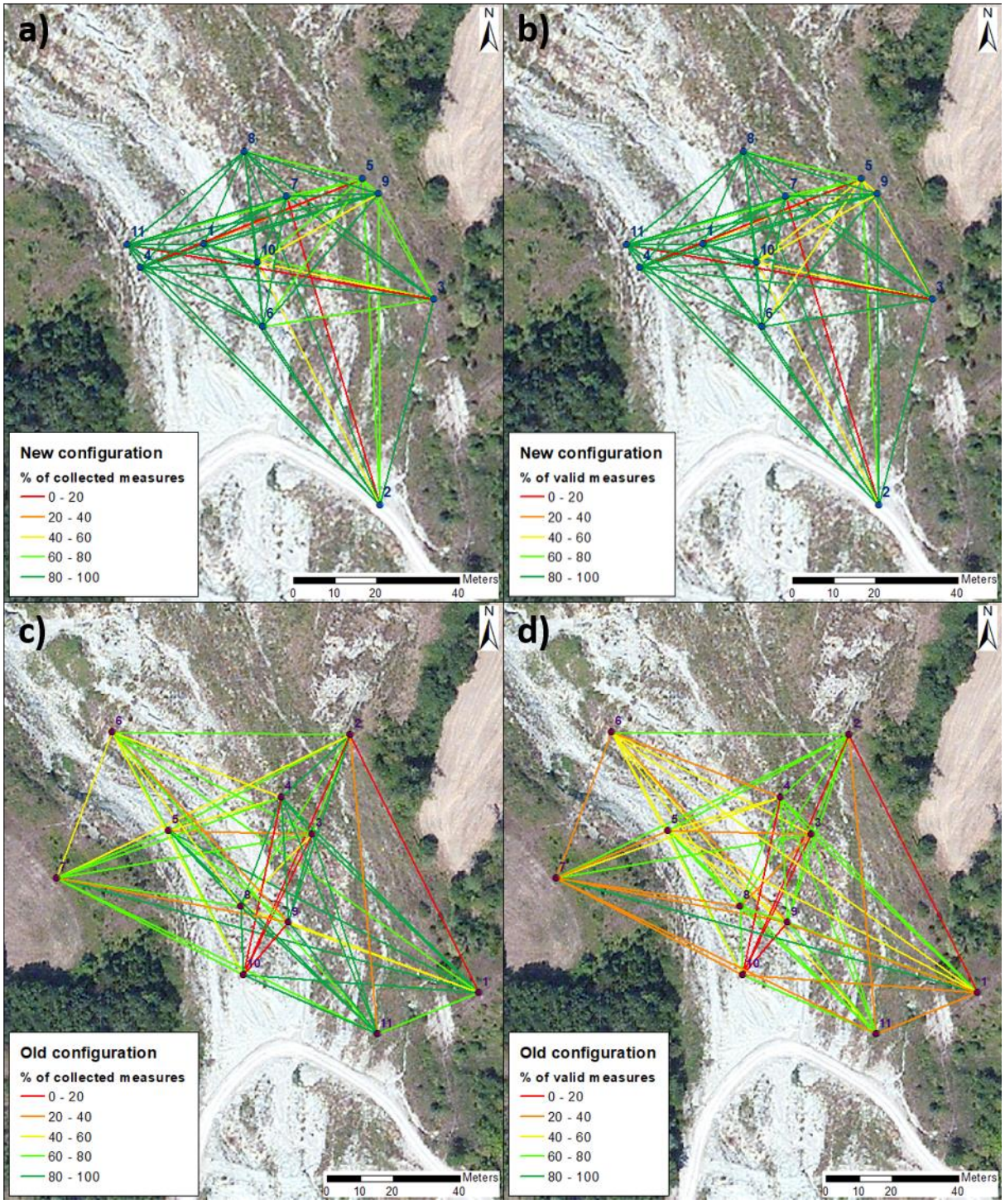

Figure 105. Comparison between measures recorded in the old and in the new configuration of the Wi-GIM system, considering data acquired during the whole monitoring periods. a) Percentage of collected measures in the new configuration. b) Percentage of valid measures in the new configuration. c) Percentage of collected measures in the old configuration. d) Percentage of valid measures in the old configuration.

As mentioned, the analysis has been carried out taking into account data acquired during the whole monitoring periods, i.e. from March 11th, 2016 to March 7th, 2017 and from February 27th, 2019 to May 10th, 2019, respectively as regards the old and the new configuration. For a more precise analysis, the

elaboration has been carried out also considering data recorded in the same time interval and in particular in the same period, to exclude the influence of seasonal variables on the percentage of collected and valid measures. Such factors could be the rainfall intensity or the temperature, as well as the vegetation growth. Considering both periods of acquisition, data recorded in the month of April (2016 for the old configuration and 2019 for the new one) have been processed and compared (Figure 106).

As noticeable in Figure 106, results are not contradictory when considering equal time intervals. This is particularly true for data belonging to the new configuration, but it was expected since the monitoring period considered in Figure 105 is really close to the one examined in this phase. Even in this case in fact, the couples that do not reach the 60% of valid data are 50 out of 59 (i.e. the 89.3 %). On the other hand, the old configuration presents some differences. Now, following the same procedure done before, both the percentages of collected and valid data are less than 60% for 29 pairs (i.e. the 48.2 %). Thus, when considering the same time interval and mostly the same period, the amount of valid data increased by the 41.1% instead of the 28.6%, meaning that the month of April was one of the worst in terms of data quality during the first installation of the Wi-GIM system.

The main cause may lie in the vegetation growth that occurs in April and that could have obstructed several LOS between couples of nodes. The old configuration was indeed installed on March 11th, when brushes and grass were still dry. The growth in April could have then changed the morphology at a small scale compromising several Line Of Sights. However, it is interesting to note that this does not occurred in the new configuration, even if the network was installed at the end of February and thus in similar conditions.

It is reasonable to think that the different behaviour (i.e. the loss of the LOS condition in the old configuration and the unchanged situation in the new one) is due to the application of WiSIO. As previously discussed in Sections 6.1.1 and 6.2, the algorithm produces a few false negatives around the objects, i.e. visible points marked as non visible. This preventative measure, although reducing the number of exploitable points, ensure the LOS between two sensors even in case of small changes around an obstacle, at least as long as these are limited in the buffer area of the false negatives. Therefore, if the vegetation grows within this precautionary area, it does not compromise LOS between two nodes when using WiSIO for their positioning.

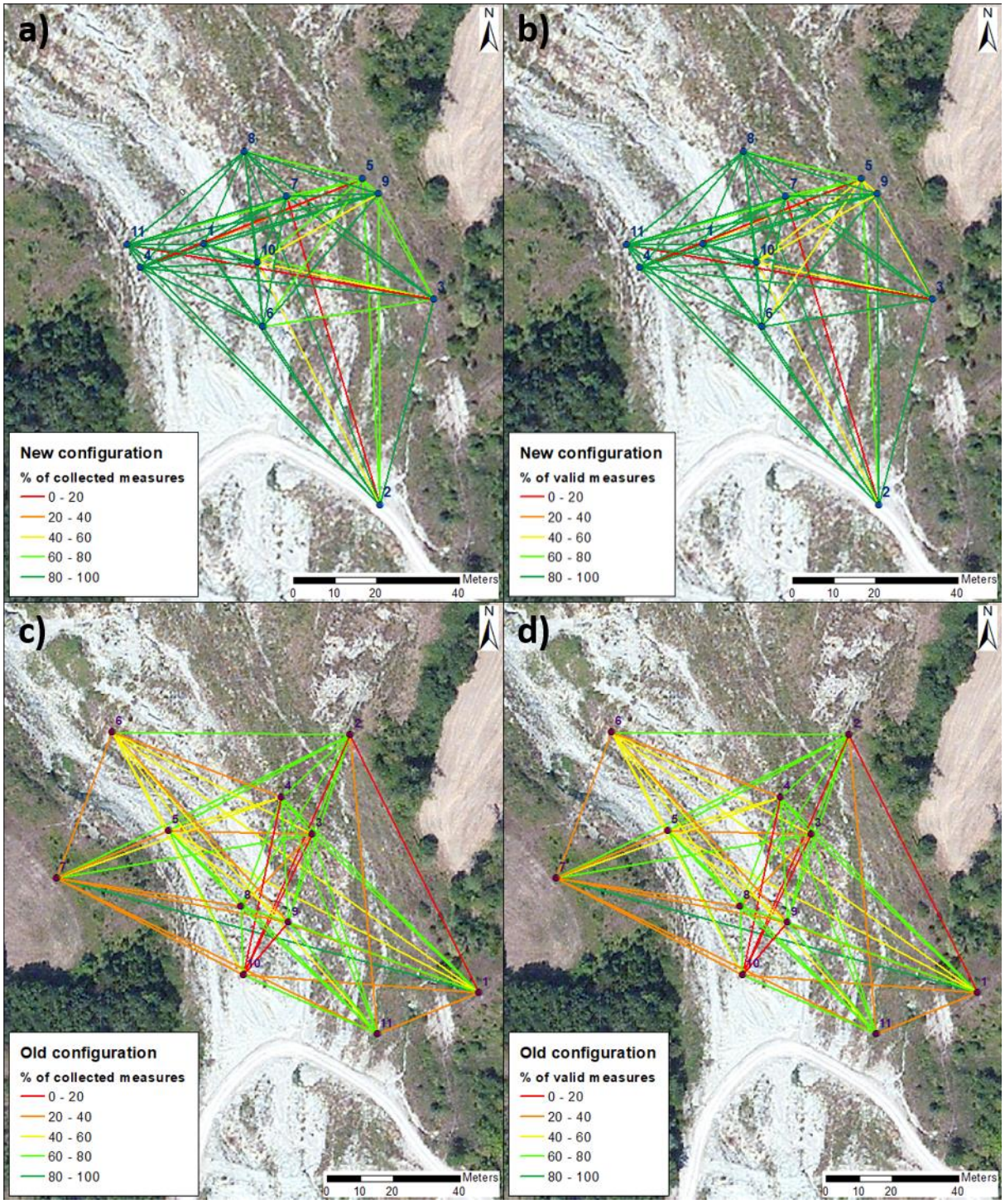

Figure 106. Comparison between measures recorded in the old and in the new configuration of the Wi-GIM system, considering data acquired in the same period, i.e. April 2016 for the old configuration and April 2019 for the new configuration. a) Percentage of collected measures in the new configuration. b) Percentage of valid measures in the new configuration. c) Percentage of collected measures in the old configuration. d) Percentage of valid measures in the old configuration.

Some examples showing this improvement on the distance measurements acquired by the system are reported in Figure 107. The image shows three cases in which data recorded in the old and in the new configuration (respectively during April 2016 and April 2019) are compared. The two pairs that are part of each case have been selected due to their similar positioning in the landslide and therefore visibility conditions (Case A and Case B), or to their similar distance (Case C). Observing these examples, it is evident how the pairs belonging to the old configuration are more affected by outliers and multipath effects. This is a general aspect, occurring regardless the percentage of collected and valid data, as in the case of pairs 2–7 and 4–9 (Case B in Figure 107). Despite their high percentage of collected and valid data (more that 80% for both), the pair 2–7 is affected by a higher number of outliers.

Looking at the acquisition of pair 1–11 of the old configuration (the one presented in Case A – Figure 107), one can note that the measurements have been recorded only from one node to the other and then vice versa. This anomaly is however probably related to a problem of the UWB module (as discussed in Section 6.1.3) and it is not clear if it can be connected to LOS problems.

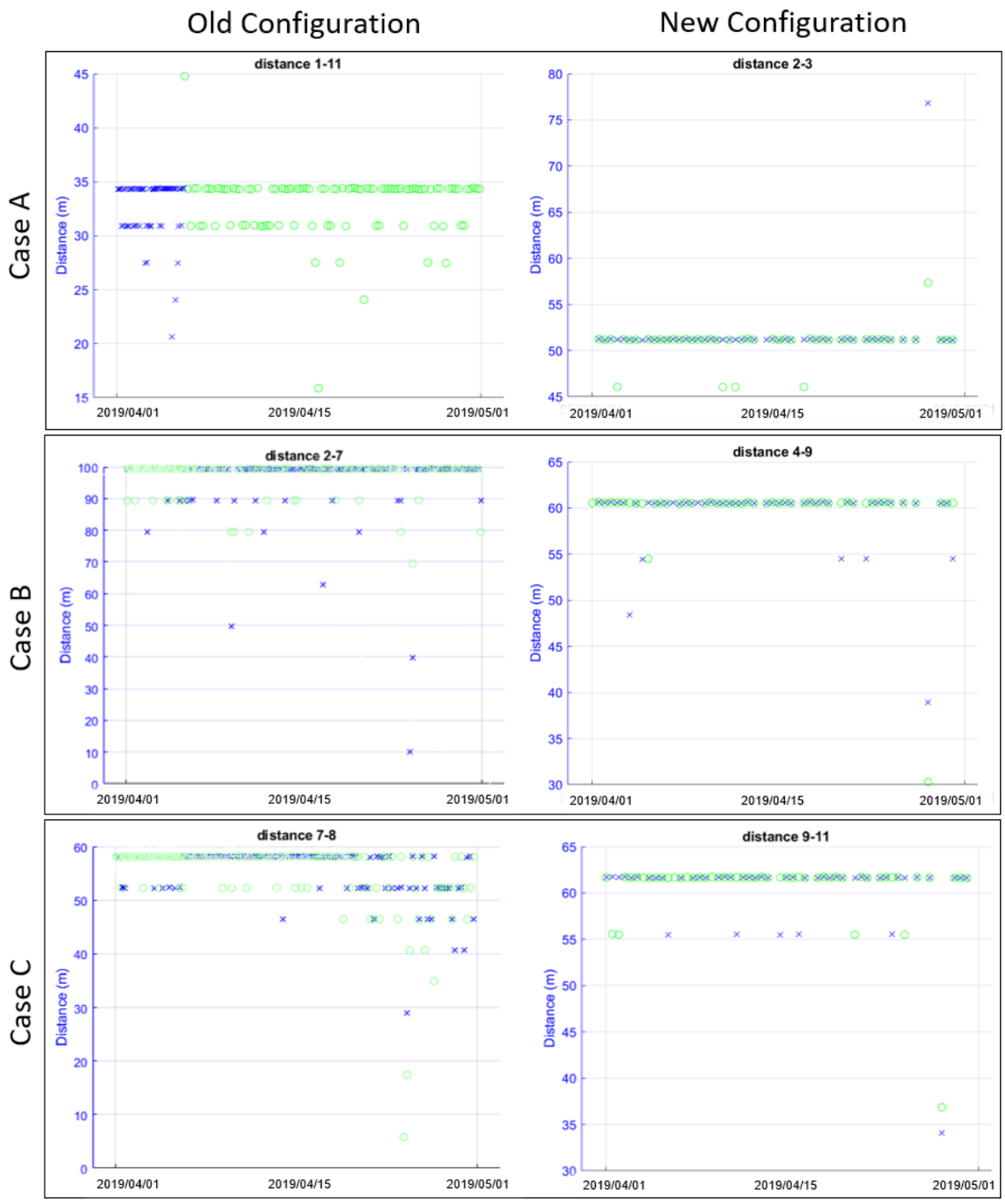

Figure 107. Comparison between data acquired in the new and in old configurations. Case A) Pairs of nodes 1–11 and 2–3 from the old and the new configurations, respectively. Case B) Pairs of nodes 2–7 and 4–9 from the old and the new configurations, respectively. Case C) Pairs of nodes 7–8 and 9–11 from the old and the new configurations, respectively. Blue crosses and green circles represent measurements in the two directions, i.e. the signals from node x to node y and vice versa.

Contrary to precision, whose values remain in the range of 2 to 5 cm once outliers are removed, WiSIO has also an effect on the accuracy of the data, affected by the presence of obstacles. Comparing the offset between 'actual' distances and Wi-GIM measured distances, it is clear how the place of sensors in LOS contributes to increase accuracy (Figure 108). The histogram shows the offset between real and measured distances (named "Error" in the graph) for all the pairs of nodes in the two configurations. The real distances have been calculated using the values of the RTS for the old configuration and the GPS coordinates for the new one. On the other hand, as values measured by Wi-GIM it is intended the average of one-month acquisition for each link (the months of April 2016 for the old configuration and April 2019 for the new one). The error has been then evaluated for each pair of nodes and displayed on a histogram. It is clearly visible that in the old configuration the error is higher in almost all the pairs due to the presence of obstacles, whereas it is lower and much more distributed in the new configuration.

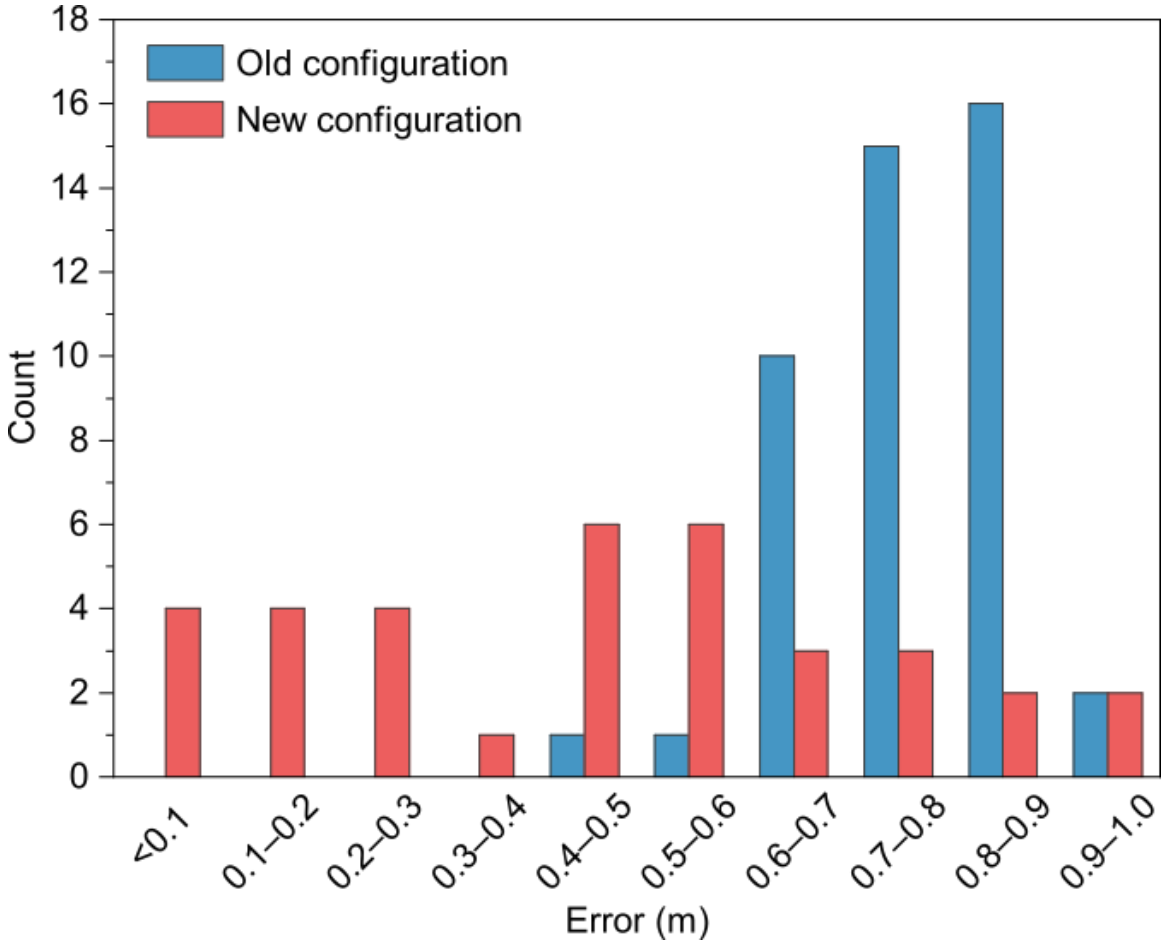

Figure 108. Histogram of the errors in the new and in the old configurations. On the x-axis, Error is expressed as the offset between the real distances and the ones evaluated by Wi-GIM. On the y-axis there is reported the frequency, i.e. the number of pairs. For the old configurations, real distances have been evaluated by means of a robotic total station, while in the new one they have been measured using the GPS coordinates.

7. Conclusions

In the field of ground stability control there is a general lack of low cost instruments able to monitor displacements over broad areas. The main reason is the difficulty in providing good performances especially in terms of precision, acquisition frequency and robustness. In this framework, thanks to the European Life+ financing program for the environment, a new prototypical ground instability monitoring instrument, called Wi-GIM (Wireless sensor network for Ground Instability Monitoring), has been developed. It consists in a Wireless sensor network (WSN) constituted by nodes (organized in clusters, each consisting of one master node and a number of slaves) able to determine their mutual inter-distances by measuring the time of flight of an Ultra-Wide Band impulse. Therefore, no sensors are implemented in the network, as the same signals used for transmission are also used for ranging.

As part of the activities carried out in the framework of the present thesis, the system was tested in a controlled outdoor environment and applied for the monitoring of the displacements of an actual active landslide, the Roncovetro mudflow in Central Italy. The outputs are displacement time series showing the distance of each pair of nodes belonging to the same cluster. Data retrieved from the performed tests revealed a precision of 2–5 cm (when they are opportunely filtered and averaged) and that measurements are influenced by the temperature. Since the correlation with this parameter has proved to be linear, a simple correction made it possible to improve the precision and remove the effect of temperature. The results of this study also revealed that measurements were not affected by rain or snow, and that the system can efficiently communicate up to 150 m with a 360° angle of view without affecting precision.

All the further key features of the Wi-GIM system can be summarized as follows:

i. Easy installation. Wi-GIM is easy to deploy and to set up in the target areas. The setup of the system is simple: firstly, the sensors are put in the area to be monitored, if the node position is requested, at least three reference nodes are put in a known position in a stable area.

ii. Quick installation. The system has very low setup time. Only the reference nodes have to be localized once they have been positioned in the stable area around the unstable ones.

iii. Flexibility. Wi-GIM can be easily adapted to different types of landslide, subsidence cases or other ground displacements. The total absence of wired structures allows the monitoring of harsh environment and decreases its vulnerability.

iv. Cost effective. Wi-GIM has a reasonable cost. This makes it suitable to monitor large areas without prohibitive expenses, especially if compared with traditional systems as Robotic Total Stations (RTSs).

v. Real-time monitoring. Wireless transmission permits to interpret data from any remote location in order to perform a real-time hazard assessment. This is achieved comparing the measured data with appropriate thresholds based on the knowledge of the kinematic behaviour of the phenomenon and on previous monitoring data.

vi. Frequency changeability. The acquisition frequency can be modified whenever the landslides features vary. It is a trade-off with the duration of the batteries and can be as high as 1 measurement every minute (or less if necessary).

Despite the implementation of a sleep mode for the survey on the test site, battery's life was a critical point during the first monitoring period, since a replacement per month was necessary. The problem was solved by equipping each node with a photovoltaic panel.

The parallel monitoring performed by RTS allowed to validate the system. Whenever a node is visible from at least other three stable sensors, it is possible to track its movement by means of a pathfinding. The comparison of both the distance measurements and the pathfinding shows the capacity of Wi-GIM to correctly trace the direction and module of the displacement vector. Nevertheless, the obtained results pointed out the presence of an offset (in an order that vary from centimetric to decametric) constant for each single pair of nodes, due to the low-cost nature of the antenna used (and probably to a miscalibration) and to the presence of obstacles that obstruct the LOS. However, it is important to remark that this error does not influence the measurement of the displacements (and therefore the potential of Wi-GIM as an early warning tool) but only of the absolute distance between the nodes, which, in this case, is not a meaningful parameter. The system in fact, aims at the reconstruction of the displacement over a landslide using the measurement of the relative distances between the nodes.

The presence of vegetation is the main cause of the obstruction of the LOS between two nodes, which translates in a longer path of the signals and therefore to a less accurate distance measurements. In this context, several tests were carried out proving the strong influence of the vegetation over both data quantity and quality. To improve them, avoiding the obstruction of the LOS between nodes, a MATLAB tool (R2018a, MAthWorks, Natick, MA, USA) called WiSIO (Wireless Sensor network Installation Optimizer) was developed. The algorithm finds the best devices deployment following

three criteria: inter-visibility by means of the Hidden Point Removal modified operator; equal distribution; positioning in pre-selected Priority Areas. With respect to the existing viewshed analysis, the main novelty is that it works directly with 3D point clouds, without rendering them or performing any surface. This lead to skip the process of generating surface models avoiding errors and approximations, that is essential when dealing with vegetation.

Within the framework of this thesis, WiSIO procedure was applied to Roncovetro landslide's 3D point cloud, but it can be applied to several natural scenarios such as vertical cliffs, gentle as well as steep slopes and terraces. Its employment can also be extended to buildings, small objects, and, more generally, to every artificial structure without geometrical or size limits. Moreover, the manual selection of the area in which the first point of the network must fall, and the weights associated to each Priority Area make sure that the user puts his knowledge in the procedure, despite the automatic approach of the code. The validation on a 3D artificial model, especially created to reconstruct a harsh environment with low visibility, pointed out a good correspondence with the reality, showing just few false negative (i.e. visible points marked as non-visible). Precision can be improved increasing the number of sectors to divide the area under study and evaluating the radius for each of them. The more the sectors are, the fewer the false negatives or/and false positives, and the higher the running time. The continuous growth of new technologies for the development of increasingly high-resolution 3D point clouds (i.e., drone laser scanners and high-resolution cameras) could still improve the reliability of the presented approach that is highly dependent on the data source.

A second installation of the Wi-GIM system on Roncovetro landslide was therefore carried out considering the deployment suggested by WiSIO. The comparison of data acquired by the Wi-GIM system positioned with and without the help of the proposed algorithm allowed a complete analysis of the effectiveness of the method. The results obtained showed that almost all devices of the latest installation were in LOS with each other, evenly distributed in space, and seven out of eleven devices lay in Priority Areas. As a matter of fact, 87.5% of measurements were collected by the master node and, between them, 89.3% was good enough to be considered reliable data with respect to the previous installation, when during the whole monitoring period the acquired measurements where 82% and only 60.7% were valid.

The presented results are very promising, showing how a simple elaboration can be essential to have more and more reliable data, improving the Wi-GIM system performances and making it even more usable in very complex environments and increasing its flexibility.

The significant movement that occurred at Roncovetro landslide on the 5th of May 2019 allowed to point out the suitability of the system, confirming its capacity to detect displacement in real-time and emphasizing its high potential in emergency conditions.

The most significant limitation of Wi-GIM system is currently the precision. Such issue is connected to the aim of using only low-cost components, and it can be prospectively overcome if the system undergoes an industrialization process. Since the system architecture is re-adaptable, it is prone to enhancements as soon as the technology advances and new low cost hardware enters the market. As a perspective, it would be in fact interesting to replace the Ultra-Wide Band module with a more recent one, analysing the improvements with particular attention on the offset that was caused by the miscalibration of the antennas.

Another interesting development could be the installation of the network in different type of landslides such as rockslides, clay rotational slides or subsidence. The deployment could be moreover supported by the use of WiSIO applied to a UAV-LiDAR 3D point cloud. A further aspect to deepen is certainly the absolute positioning, that has been faced in this thesis considering a 2D surface. The same process carried out in 3D could avoid some errors, making the system even more applicable in different scenarios. Finally, a more in-depth study about the influence of the temperature on the Wi-GIM measurements is already ongoing, but it will require several experimentations. This analysis will allow to comprehend the nature of this relation that is not really clear up to now.

In conclusion, albeit it is still a prototypal system and, as such, is prone to improvements, the Wi-GIM system appears as a suitable instrument for monitoring velocities classified from slow (of the order of m/year) to rapid (m/min) (Cruden and Varnes 1996), typical for example of earth flows, subsidence in mining areas, earth slides and rockslides before failure. More in general, it fits for every ground movements characterized by periods of acceleration that leads to significant movements (at least in the order of cm), and when strong precisions are not required. In a few words, it is optimal in emergency condition, where a quick and low-cost installation, the remote control of the monitoring data and the detection of unexpected accelerations are fundamental requirements.

References

Adam, N., Rodriguez-Gonzalez, F., Parizzi, A., Liebhart, W. (2011). Wide area persistent scatterer interferometry. In Geoscience and Remote Sensing Symposium (IGARSS), 2011 IEEE International, 1481–1484.

Akyildiz, I. F., Su, W., Sankarasubramaniam, Y., Cayirci, E. (2002). Wireless sensor networks: a survey. Computer Networks, 38(4): 393–422.

Almagià, R. (1907). Studi geografici sulle frane in Italia. Memorie Società Geografica, 13: 1–342.

Alwan, N. A., Mahmood, A. S. (2015). Distributed gradient descent localization in wireless sensor networks. Arabian Journal for Science and Engineering, 40(3): 893–899.

Amitrano, D., Grasso, J. R., Senfaute, G. (2005). Seismic precursory patterns before a cliff collapse and critical point phenomena. Geophysical Research Letters, 32(8).

Angeli, M. G., Pasuto, A., Silvano, S. (1999). Monitoring and warning systems: methodological approach and case studies. In Floods and Landslides: Integrated Risk Assessment. Springer Berlin Heidelberg, 295–303.

Arampatzis, T., Lygeros, J., Manesis, s. (2005). A survey of applications of wireless sensors and wireless sensor networks. Intelligent Control. Proceedings of the 2005 IEEE International Symposium on, Mediterrean Conference on Control and Automation, 719–724.

Ardizzone, F., Cardinali, M., Galli, M., Guzzetti, F., Reichenbach, P. (2007). Identification and mapping of recent rainfall-induced landslides using elevation data collected by airborne Lidar. Natural Hazards and Earth System Sciences, 7: 637–650.

Arnhardt, C., Asch, K., Azzam, R., Bill, R., Fernandez-Steeger, T. M., Homfeld, S. D., Kallash, A., Niemeyer, F., Ritter, H., Toloczyki, M., Walter, K. (2007). Sensor based Landslide Early Warning System-SLEWS. Development of a geoservice infrastructure as basis for early warning systems for landslides by integration of real-time sensors. Geotechnologien science report, 10: 75–88.

Atzeni, C., Barla, M., Pieraccini, M., Antolini, F. (2015). Early warning monitoring of natural and engineered slopes with ground-based synthetic-aperture radar. Rock Mechanics and Rock Engineering, 48(1): 235–246.

Auken, E., Pellerin, L., Christensen, N. B., Sorensen, K. (2006). A survey of current trends in near-surface electrical and electromagnetic methods. Geophysics, 71(5): G249–G260.

Barla, M., Antolini, F., Bertolo, D., Thuegaz, P., D'Aria, D., Amoroso, G. (2017). Remote monitoring of the Comba Citrin landslide using discontinuous GBInSAR campaigns. Engineering Geology, 222: 111–123.

Barla, M., Antolini, F. (2016). An integrated methodology for landslides' early warning systems. Landslides, 13(2): 215–228.

Barla, G., Antolini, F., Barla, M., Mensi, E., Piovano, G. (2010). Monitoring of the Beauregard landslide (Aosta Valley, Italy) using advanced and conventional techniques. Engineering Geology, 116: 218–235.

Baltsavias, E. P. (1999). Airbone laser scanning: basic relations and formulas. ISPRS J Photogramm Remote Sensing, 54: 199–214.

Bamler, R., P. Hartl. (1998). Synthetic aperture radar interferometry. Inverse Problems, 14: 1–54.

Berardino, P., Fornaro, G., Lanari, R., Sansosti, E. (2002). A new algorithm for surface deformation monitoring based on small baseline differential SAR interferograms. IEEE Transactions on Geoscience and Remote Sensing, 40(11): 2375–2383.

Bertolini, G., Fioroni, C. (2013). Large Reactivated Earth Flows in the Northern Apennines (Italy): An Overview. In Landslide Science and Practice. Springer, Berlin, Heidelberg, 51–58.

Bertolini, G., Gorgoni, C. (2001). La lavina di Roncovetro (Vedriano, Comune di Canossa, Provincia di Reggio Emilia). Quad. Geolog. Appl, 8: 1–21.

Bhardwaj, G. S., Metha, M., Ahmed, M. Y., Chowdhury, M. A. I. (2014). Landslide monitoring by using sensor and wireless technique: a review. International Journal of Geomatics and Geosciences, 5(1): 1.

Bianchini, S., Pratesi, F., Nolesini, T., Casagli, N. 2015. Building deformation assessment by means of persistent scatterer interferometry analysis on a landslide-affected area: the Volterra (Italy) case study. Remote Sensing, 7(4): 4678–4701.

Bitelli, G., Dubbini, M., Zanutta, A. (2004). Terrestrial laser scanning and digital photogrammetry techniques to monitor landslide bodies. International Archives of Photogrammetry, Remote Sensing and Spatial Information Sciences, 35(Part B5): 246–251.

Bock, Y., Shimada, S. (1990). Continuously monitoring GPS networks for deformation measurements. In Global Positioning System: An Overview. Springer, New York, NY, 40–56.

Bonnard, C., Steinman, G. (1990). Continuous measurement of landslide movements. Geotechnical Instruments in Practices. Institute of Civil Engineers, Thomas Telford, London.

Borlat, C., Epard, J. L., Jaboyedoff, M. (2007) Use of a laser-DTM for geological survey, structural interpretation and update of existing maps: example in the Jura Mountains (Switzerland). Geophys Res Abst, 9: 07424.

Brückl, E., Brunner, F. K., & Kraus, K. (2006b). Kinematics of a deep-seated landslide derived from photogrammetric, GPS and geophysical data. Engineering Geology, 88(3–4): 149–159.

Brückl, E., Mertl, S. (2006a). Seismic monitoring of deep-seated mass movements. In Proceedings of the INTERPRAEVENT International Symposium, Disaster Mitigation of Debris Flows, Slope Failures and Landslides, Marui, H., Niigata, Japan, 571–580.

Brunsden, D., Chandler, J. H., (1996). Development of an episodic landform change model based upon the Black Ven mudslide, 1946–1995. In: Anderson, M.G., Brooks, S.M. (Eds.), Advances in Hillslope Processes. Wiley, Chichester, UK, 869–896.

Canuti, P., N. Casagli, F. Catani, G. Falorni, P. Farina. (2007). Integration of remote sensing techniques in different stages of landslide response. In Progress in landslide science. Berlin Heidelberg: Springer, 251–260.

Cardenal, J., Mata, E., Perez-Garcia, J. L., Delgado, J., Andez, M., Gonzalez, A., Diaz-de-Teran, J. R. (2008). Close range digital photogrammetry techniques applied to landslide monitoring. International Archives of Photogrammetry, Remote Sensing and Spatial Information Sciences, 37(Part B8).

Casagli, N., Frodella, W., Morelli, S., Tofani, V., Ciampalini, A., Intrieri, E., Raspini, F., Rossi, G., Tanteri, L., Lu, P. (2017a). Spaceborne, UAV and ground-based remote sensing techniques for landslide mapping, monitoring and early warning. Geoenvironmental Disasters, 4(1): 9.

Casagli, N., Guzzetti, F., Jaboyedoff, M., Nadim, F., Petley, D. (2017b). Hydrological risk: landslides. In: Poljanšek, K., Marín Ferrer, M., De Groeve, T., Clark, I. (Eds.). Science for disaster risk management 2017: knowing better and losing less. EUR 28034 EN, Publications Office of the European Union, Luxembourg, Chapter 3.5.

Casagli, N., Catani, F., Del Ventisette, C., Luzi, G. (2010). Monitoring, prediction, and early warning using ground-based radar interferometry. Landslides, 7(3): 291–301.

Castillo-Effer, M., Quintela, D. H., Moreno, W., Jordan, R., & Westhoff, W. (2004). Wireless sensor networks for flash-flood alerting. In Proceedings of the Fifth IEEE International Caracas Conference on Devices, Circuits and Systems, 1: 142–146.

Chae, B. G., Park, H. J., Catani, F., Simoni, A., Berti, M. (2017). Landslide prediction, monitoring and early warning: a concise review of state-of-the-art. Geosciences Journal, 21(6): 1033–1070.

Chen, D., Liu, Z., Wang, L., Dou, M., Chen, J., Li, H. (2013). Natural disaster monitoring with wireless sensor networks: a case study of data-intensive applications upon low-cost scalable systems. Mobile Networks and Applications, 18(5): 651–663.

Cho, C., Chou, P., Chung, Y., King, C., Tsai, M., Lee, B., Chou, T. (2008). Wireless sensor networks for debris flow observation. Paper presented at the 5th Annual IEEE Communications Society Conference on Sensor, Mesh and Ad Hoc Communications and Networks, 16–20 June, San Francisco, CA, USA, 615–617.

Ciampalini, A., Raspini, F., Lagomarsino, D., Catani, F., Casagli, N. (2016). Landslide susceptibility map refinement using PSInSAR data. Remote Sensing of Environment, 184: 302–315.

Ciampalini, A., Bardi, F., Bianchini, S., Frodella, W., Del Ventisette, C., Moretti, S., Casagli, N. (2014). Analysis of building deformation in landslide area using multisensor PSInSAR™ technique. International Journal of Applied Earth Observation and Geoinformation, 33: 166–180.

Colomina, I., Molina, P. (2014). Unmanned aerial systems for photogrammetry and remote sensing: A review. ISPRS Journal of photogrammetry and remote sensing, 92: 79–97.

Corominas, J., Moya, J., Lloret, A., Gili, J. A., Angeli, M. G., Pasuto, A., Silvano, S. (2000). Measurement of landslide displacements using a wire extensometer. Engineering Geology, 55(3): 149–166.

Corominas, J., Copons, R., Moya, J., Vilaplana, J. M., Altimir, J., Amigo, J. (2005). Quantitative assessment of the residual risk in a rockfall protected area. Landslides, 2(4): 343–357.

Corsini, A., Borgatti, L., Coren, F., Vellico, M. (2007). Use of multitemporal airborne LiDAR surveys to analyse post- failure behaviour of earthslides. Canadian Journal of Remote Sensing, 33: 116–120.

Crosetto, M., Monserrat, O., Cuevas-González, M., Devanthéry, N., Crippa, B. (2016). Persistent scatterer interferometry: a review. ISPRS Journal of Photogrammetry and Remote Sensing, 115: 78–89.

Cruden, D. M., Varnes, D. J. (1996). Landslides: investigation and mitigation. Chapter 3-Landslide types and processes. Transportation research board special report, 247.

Dai, K., Chen, S. (2009). Strong ground movement induced by mining activities and its effect on power transmission structures. Min. Sci. Technol., 19: 563–568.

Dardari, D., Conti, A., Ferner, U., Giorgetti, A., Win, M. Z. (2009). Ranging with ultrawide bandwidth signals in multipath environments. Proceedings of the IEEE, 97(2): 404–426.

Decawave. Decawave DWM1000 Datasheet. (2018). Available online: https://www.decawave.com/sites/default/files/resources/DWM1000-Datasheet-V1.6.pdf (accessed on 30 August 2018).

DeLong, S. B., Prentice, C. S., Hilley, G. E., Ebert, Y. (2012). Multitemporal ALSM change detection, sediment delivery, and process mapping at an active earthflow. Earth Surf. Process. Landf., 37: 262–272.

Dixon, T. H. (1991). An introduction to the Global Positioning System and some geological applications. Reviews of Geophysics, 29(2): 249–276.

Dodd, H. M. (2001). The validity of using a geographic information system's viewshed function as a predictor for the reception of line-of-sight radio waves (Doctoral dissertation, Virginia Tech).

Dunnicliff, J., La Fonta, J. G. (2001). In-place Inclinometers - A Significant Test Program. Geotechnical News Vancouver, 19(1): 33–34.

Dunning, S. A., Massey, C. I., Rosser, N. J. (2009). Structural and geomorphological features of landslides in the Bhutan Himalaya derived from terrestrial laser scanning. Geomorphology, 103(1): 17–19.

Duranthon, J. P. (2000). Application de la méthode GPS de localisation par satellite à la surveillance de sites naturels instables. BULLETIN LABORATOIRES DES PONTS ET CHAUSSEES, 47–58.

Eeckhaut, M. V. D., Poesen, J., Verstraeten, G., Vanacker, V., Nyssen, J., Moeyersons, J., Van Beek, L. P. H., Vandekerckhove, L. (2007). Use of LIDAR-derived images for mapping old landslides under forest. Earth Surface Processes and Landforms, 32(5): 754–769.

Eberhardt, E., Clague, J. J., Stead, D. (2012). Landslide monitoring: The role of investigative monitoring to improve understanding and early warning of failure. In Landslides: Types, Mechanisms and Modeling. Cambridge Univ. Press, 222–234.

El Houssaini, D., Guesmi, A., Khriji, S., Keutel, T., Besbes, K., Kanoun, O. (2019). Experimental Investigation on Weather Changes Influences on Wireless Localization System. In 2019 IEEE International Symposium on Measurements & Networking, 1–6.

Emlid Reach GPS official web site: https://docs.emlid.com/reachrs/.

Estrin, D., Culler, D., Pister, K., Sukhatme, G. (2002). Connecting the physical world with pervasive networks. IEEE pervasive computing, 1(1): 59–69.

Farina, P., Coli, N., Yön, R., Eken, G., Ketizmen, H. (2013). Efficient real time stability monitoring of mine walls: the çöllocar mine case study. Proc. International Mining Congress and Exhibition of Turkey, Antalya, Turkey, 16-19 April 2013, 111–117.

Farina, P., Leoni, L., Babboni, F., Coppi, F., Mayer, L., Ricci, P. (2011). IBIS-M, an innovative radar for monitoring slopes in open-pit mines. In Proceedings of the Slope Stability 2011: International Symposium on Rock Slope Stability in Open Pit Mining and Civil Engineering, Vancouver, BC, Canada, 18–21.

Feng, L., Pazzi, V., Intrieri, E., Gracchi, T., Gigli, G. (2019). Rockfall seismic features analysis based on in situ tests: frequency, amplitude, and duration. Journal of Mountain Science, 16(5): 955–970.

Ferretti, A., Prati, C., Rocca, F. (2001). Permanent Scatterers in SAR interferometry. IEEE Transactions on Geoscience and Remote Sensing, 39(1): 8–20.

Fiorucci, F., Cardinali, M., Carlà, R., Rossi, M., Mondini, A. C., Santurri, L., Ardizzone, F., Guzzetti, F. (2011). Seasonal landslide mapping and estimation of landslide mobilization rates using aerial and satellite images. Geomorphology, 129(1–2): 59–70.

Fisher, P. F. (1991). First experiments in viewshed uncertainty: the accuracy of the viewshed area. Photogrammetric engineering and remote sensing, 57(10): 1321–1327.

Frodella, W., Ciampalini, A., Gigli, G., Lombardi, L., Raspini, F., Nocentini, M., Scardigli, C., Casagli, N. (2016). Synergic use of satellite and ground based remote sensing methods for monitoring the San Leo rock cliff (Northern Italy). Geomorphology, 264: 80–94.

Fruneau, B., Achache, J., Delacourt, C. (1996). Observation and modeling of the Saint-Etienne-de-Tine'e Landslide using SAR interferometry. Tectonophysics, 265.

García, A., Hördt, A., Fabian, M. (2010). Landslide monitoring with high resolution tilt measurements at the Dollendorfer Hardt landslide, Germany. Geomorphology, 120(1–2): 16–25.

Gezici, S., Tian, Z., Giannakis, G. B., Kobayashi, H., Molisch, A. F., Poor, H. V., Sahinoglu, Z. (2005). Localization via ultra-wideband radios: a look at positioning aspects for future sensor networks. IEEE signal processing magazine, 22(4): 70–84.

Gigli, G., Casagli, N. (2011). Semiautomatic extraction of rock mass structural data from high resolution LIDAR point clouds. Int J Rock Mech Min Sci, 48(2): 187–198.

Gili, J. A., Corominas, J., Rius, J. (2000). Using Global Positioning System techniques in landslide monitoring. Engineering Geology, 55(3): 167–192.

Giordan, D., Allasia, P., Manconi, A., Baldo, M., Santangelo, M., Cardinali, M., Corazza, A., Albanese, V., Lollino, G., Guzzetti, F. (2013). Morphological and kinematic evolution of a large earthflow: The Montaguto landslide, southern Italy. Geomorphology, 187: 61–79.

Giorgetti, A., Lucchi, M., Tavelli, E., Barla, M., Gigli, G., Casagli, N., Chiani, M., Dardari, D. (2016). A robust wireless sensor network for landslide risk analysis: system design, deployment, and field testing. IEEE sensors journal, 16(16): 6374–6386.

Glennie, C. L., Carter, W. E., Shrestha, R. L., Dietrich, W. E. (2013). Geodetic imaging with airborne LiDAR: The Earth's surface revealed. Rep. Prog. Phys., 76: 086801.

Godio, A., Strobbia, C., De Bacco, G. (2006). Geophysical characterisation of a rockslide in an alpine region. Engineering Geology, 83: 273–86.

Gracchi, T., Gigli, G., Noël, F., Jaboyedoff, M., Madiai, C., Casagli, N. (2019). Optimising Wireless Sensor Network installations by Visibility Analysis on 3D Point Clouds. ISPRS International Journal of Geo-Information, 8 (10), 460.

Gracchi, T., Lotti, A., Saccorotti, G., Lombardi, L., Nocentini, M., Mugnai, F., Gigli, G., Barla, M., Giorgetti, A., Antolini, F., Fiaschi, A., Matassoni, L. (2017). A method for locating rockfall impacts using signals recorded by a microseismic network. Geoenvironmental Disasters, 4(1): 26.

Groves, P.D. (2013). Principles of GNSS, Inertial, and Multisensor Integrated Navigation Systems, 2nd ed.; Artech House: Norwood, MA, USA.

Guth, P.L. (2009). Incorporating vegetation in viewshed and line-of-sight algorithms: Proceedings ASPRS/MAPPS 2009 Conference, San Antonio, Texas, November 16–19.

Guzzetti, F., Reichenbach, P., Cardinali, M., Ardizzone, F., Galli, M. (2003). The impact of landslides in the Umbria region, central Italy. Natural Hazards and Earth System Sciences, 3: 469–486.

Hervás, J., Barredo, J., Rosin, P., Pasuto, A., Mantovani, F., Silvano, S. (2003). Monitoring landslide from optical remotely sensed imagery: the case story of Tessina landslide, Italy. Geomorphology, 54: 63–75.

Intrieri, E., Gigli, G., Gracchi, T., Nocentini, M., Lombardi, L., Mugnai, F., Frodella, W., Bertolini, G., Carnevale, E., Favalli, M., Fornaciai, A., Marturià Alavedra, J., Mucchi, L., Nannipieri, L., Rodriguez-Lloveras, X., Pizziolo, M., Schina, R., Trippi, F. & Casagli, N. (2018). Application of an ultra-wide band sensor-free wireless network for ground monitoring. Engineering Geology, 238: 1–14.

Intrieri, E., Gigli, G., Mugnai, F., Fanti, R., Casagli, N. (2012). Design and implementation of a landslide early warning system. Engineering Geology, 147–148: 124–136.

Itakura, Y., Inaba, H., Sawada, T. (2005). A debris-flow monitoring devices and methods bibliography. Natural Hazards and Earth System Science, 5(6): 971–977.

James, M. R., Robson, S. (2012). Straightforward reconstruction of 3D surfaces and topography with a camera: Accuracy and geoscience application. Journal of Geophysical Research: Earth Surface, 117. F3.

Jaboyedoff, M., Metzger, R., Oppikofer, T., Couture, R., Derron, M. H., Locat, J., Durmel, D. (2007). New insight techniques to analyze rock-slope relief using DEM and 3D imaging cloud points: COLTOP-3D software. In: Eberhardt E, Stead D, Morrison T (eds) Rock mechanics: meeting society's challenges and demands. Taylor & Francis Group, London, 61–68.

Jaboyedoff, M., Demers, D., Locat, J., Locat, A., Locat, P., Oppikofer, T., Turmel, D. (2009). Use of terrestrial laser scanning for the characterization of retrogressive landslides in sensitive clay and rotational landslides in riverbanks. Canadian Geotechnical Journal, 46(12): 1379–1390.

Jaboyedoff, M., Oppikofer, T., Abellan, A., Derron, M. H., Loye, A., Metzger, R., Pedrazzini, A., (2012). Use of LIDAR in landslide investigations: a review. Natural Hazards, 61: 5–28.

Jongmans, D., Garambois, S. (2007). Geophysical investigation of landslides: a review. Bulletin de la Société géologique de France, 178(2): 101–112.

Kääb, A., Haeberli, W., Gudmundsson, G. H. (1997). Analysing the creep of mountain permafrost using high precision aerial photogrammetry: 25 years of monitoring Gruben Rock glacier, Swiss Alps. Permafrost and Periglacial Processes, 8: 409–426.

Kamal, A. R. M., Hamid, M. A. (2013). Reliable data approximation in wireless sensor network. Ad Hoc Networks 11(8): 2470–2483.

Katz, S., Tal, A., Basri, R. (2007). Direct visibility of point sets. In ACM Transactions on Graphics, ACM, 26(3): 24.

Khara, S. (2017). A Review on Security Issues in Wireless Sensor Network. Int J Sens Netw Data Commun S1: 001. doi: 10.4172/2090-4886.S1-001.

Kilburn, C. R. J., Petley, D. N. (2003). Forecasting giant, catastrophic slope collapse: lessons from Vajont, northern Italy. Geomorphology 54(1–2): 21–32.

Kolesnikov, Y. I., Nemirovich-Danchenko, M. M., Goldin, S. V., Seleznev, V. S. (2003). Slope stability monitoring from microseismic field using polarization methodology. Natural Hazards and Earth System Sciences, 3(6): 515–521.

Lapenna, V., Lorenzo, P., Perrone, A., Piscitelli, S., Rizzo, E., Sdao, F. (2005): Case history: 2D electrical resistivity imaging of some complex landslides in Lucanian Apennine (Southern Italy). Geophysics, 70: B11–B18.

Liu, D.A., Yang, Z.F., Tang, C.H., Wang, J., Liu, Y., 2004. An automatic monitoring system for the shiplock slope of Wuqiangxi Hydropower Station. Engineering Geology, 76: 79–91.

Lombardi, L., Nocentini, M., Frodella, W., Nolesini, T., Bardi, F., Intrieri, E., Carlà, T., Solari, L., Dotta, G., Ferrigno, F., Casagli, N. (2017). The Calatabiano landslide (southern Italy): Preliminary GB-InSAR monitoring data and remote 3D mapping. Landslides, 14: 685–696.

Lowry, A. R., Hamburger, M. W., Meertens, C. M., Ramos, E. G. (2001). GPS monitoring of crustal deformation at Taal Volcano, Philippines. Journal of Volcanology and Geothermal Research, 105(1-2): 35–47.

Luzi, G. (2010). Ground based SAR interferometry: a novel tool for Geoscience. In Geoscience and Remote Sensing New Achievements. IntechOpen.

Machan, G., Bennett, V. G. (2008). Use of inclinometers for geotechnical instrumentation on transportation projects: State of the practice. Transportation Research E-Circular, (E-C129).

Mainsant, G., Larose, E., Brönnimann, C., Jongmans, D., Michoud, C., Jaboyedoff, M. (2012). Ambient seismic noise monitoring of a clay landslide: Toward failure prediction, Journal of Geophysical Research, 117, F01030.

Mantovani, F., Pasuto, A., Silvano, S., Zannoni, A. (2000). Collecting data to define future hazard scenarios of the Tessina landslide. Int. J. Appl. Earth Obs. Geoinf., 2: 33–40.

Martinez, K., Ong, R., Hart, J. (2004). Glacsweb: a sensor network for hostile environments. Proceedings of the First IEEE Communications Society Conference on Sensor and Ad Hoc Communications and Networks, October, Santa Clara, CA, USA.

Martins, A. C., Elis, V., Tomi, G. D., Bettencourt, J., Marin, T. (2016). Resistivity and induced polarization to support morphological modeling in limestone mining. Geofísica internacional, 55(4): 227–238.

Medina-Cetina, Z., Nadim, F. (2008). Stochastic design of an early warning system. Georisk: Assessment and Management of Risk for Engineered Systems and Geohazards, 2(4): 223–236.

Mehta, P., Chander, D., Shahim, M., Tejaswi, K., Merchant, S. N., Desai, U. B. (2007). Distributed detection for landslide prediction using wireless sensor network. In Proceedings of the First International Global Information Infrastructure Symposium, Marrakech, Morocco, 2–6 July 2007.

Meisina, C., Zucca, F., Notti, D., Colombo, A., Cucchi, A., Savio, G., Giannico, C., Bianchi, M. (2008). Geological interpretation of PSInSAR data at regional scale. Sensors, 8(11): 7469–7492.

Meisina, C., Notti, D., Zucca, F., Ceriani, M., Colombo, A., Poggi, F., Roccati, A., Zaccone, A. (2013). The use of PSInSAR™and SqueeSAR™techniques for updating landslide inventories. In Landslide science and practice, Berlin Heidelberg: Springer, ed. Margottini, C., Canuti, P., and Sassa, K. 81–87.

Meng, Y. S., Lee, Y. H., Ng, B. C. (2009). Study of propagation loss prediction in forest environment. Progress In Electromagnetics Research, 17: 117–133.

Meric, O., Garambois, S., Jongmans, D., Wathelet, M., Chatelain, J. L., Vengeon, J. M. (2005). Application of geophysical methods for the investigation of the large gravitational mass movement of Sechilienne France Canadian Geotechnical Journal, 42: 1105–15.

Montealegre, A., Lamelas, M., Riva, J. (2015). Interpolation routines assessment in ALS-derived digital elevation models for forestry applications. Remote Sensing, 7: 8631–8654.

Mora, P., Baldi, P., Casula, G., Fabris, M., Ghirotti, M., Mazzini, E., Pesci, A. (2003). Global Positioning Systems and digital photogrammetry for the monitoring of mass movements: application to the Ca'di Malta landslide (northern Apennines, Italy). Engineering Geology, 68(1-2): 103–121.

Mora, O. E., Lenzano, M. G., Toth, C. K., Grejner-Brzezinska, D. A., Fayne, J. V. (2018). Landslide change detection based on multi-temporal Airborne LiDAR-derived DEMs. Geosciences, 8: 23.

Mucchi, L., Jayousi, S., Martinelli, A., Caputo, S., Intrieri, E., Gigli, G., Gracchi, T., Mugnai, F., Favalli, M., Fornaciai, A., Nannipieri, L. (2018). A Flexible Wireless Sensor Network Based on Ultra-Wide Band Technology for Ground Instability Monitoring. Sensors, 18(9): 2948.

Murgoitio, J. J., Shrestha, R., Glenn, N. F., Spaete, L. P. (2013). Improved visibility calculations with tree trunk obstruction modeling from aerial LiDAR. International Journal of Geographical Information Science, 27(10): 1865–1883.

Nadim, F., Kjekstad, O., Peduzzi, P., Herold, C., Jaedicke, C. (2006). Global landslide and avalanche hotspots. Landslides, 3(2): 159–173.

Nolesini, T., Frodella, W., Bianchini, S., Casagli, N. (2016). Detecting Slope and Urban Potential Unstable Areas by Means of Multi-Platform Remote Sensing Techniques: The Volterra (Italy) Case Study. Remote Sensing, 8(9): 746.

Oppikofer, T., Jaboyedoff, M., Keusen, H. R. (2008). Collapse at the eastern Eiger flank in the Swiss Alps. Nature Geoscience, 1(8): 531–535.

Pazzi, V., Ceccatelli, M., Gracchi, T., Masi, E. B., Fanti, R. (2018). Assessing subsoil void hazards along a road system using H/V measurements, ERTs and IPTs to support local decision makers. Near Surface Geophysics, 16(3), 282–297.

Perrone, A., Lapenna, V., Piscitelli, S. (2014). Electrical resistivity tomography technique for landslide investigation: a review. Earth-Science Reviews, 135: 65–82.

Pesci, A., Casula, G., Bonali, E., Boschi, E. (2011). Un metodo per lo studio di edifici storici mediante misure laser a scansione terrestre: le Due Torri di bologna.

Petley, D. N., Mantovani, F., Bulmer, M. H., Zannoni, A. (2005). The use of surface monitoring data for the interpretation of landslide movement patterns. Geomorphology, 66: 133–147.

Petley, D. (2012). Global patterns of loss of life from landslides. Geology, 40(10): 927–930.

Petrie, G., Toth, C. K. (2008). I. Introduction to laser ranging, profiling and scanning, II. Airbone and spaceborne laser profiles and scanners, III. Terrestrial laser scanners (chapters 1 to 3). In: Shan, J., Toth, C. K. (eds) Topographic laser ranging and scanning: principles and processing, CRC Press, Taylor & Francis.

Rizzo, V., Leggeri, M. (2004). Slope instability and sagging reactivation at Maratea (Potenza, Basilicata, Italy). Engineering Geology, 71: 181–198.

Rosen, P. A., Hensley, S., Joughin, I. R., Li, F. K., Madsen, S. N., Rodriguez, E., Goldstein, R. M. (2000). Synthetic aperture radar interferometry. Proc. IEEE 88(3): 333–382.

Rosi, A., Berti, M., Bicocchi, N., Castelli, G., Corsini, A., Mamei, M., Zambonelli, F. (2011). Landslide monitoring with sensor networks: experiences and lessons learnt from a real-world deployment. International Journal of Sensor Networks, 10(3): 111–122.

Rossi, G., Tanteri, L., Tofani, V., Vannocci, P., Moretti, S., Casagli, N. (2018). Multitemporal UAV surveys for landslide mapping and characterization. Landslides, 15(5), 1045-1052.

Rossi, G., Tanteri, L., Salvatici, T., Casagli, N. (2017). The use of multi-copter drones for landslide investigations. In 3rd North American Symposium on Landslides, Roanoke, VA, 978–984.

Roth, M., Dietrich, M., Blikra, L. H., Lecomte, I. (2006). Seismic monitoring of the unstable rock slope site at Åknes, Norway. In Symposium on the Application of Geophysics to Engineering and Environmental Problems 2006. Society of Exploration Geophysicists, 184–192.

Rowlands, K. A., Jones, L. D., Whitworth, M. (2003). Landslide laser scanning: a new look at an old problem. Quarterly Journal of Engineering Geology and Hydrogeology, 36(2): 155–157.

Sahinoglu, Z., Gezici, S., Guvenc, I. (2008). Ultra-wideband positioning systems. Cambridge, New York.

Savvaidis, P. D. (2003). Existing landslide monitoring systems and techniques. From Stars to Earth and Culture, 242–258.

Schroder-Preikschat, W., Kapitza, R., Kleinoder, J., Felser, M., Karmeier, K., Labella, T. H., Dressler, F. (2007). Robust and efficient software management in sensor networks. In Communication Systems Software and Middleware, 2007. COMSWARE 2007. 2nd International Conference, 1–6.

Sheth, A., Thekkath, C. A., Mehta, P., Tejaswi, K., Parekh, C., Singh, T. N., Desai, U. B. (2007). Senslide: a distributed landslide prediction system. SIGOPS Operating Systems Review, 41: 75–87.

Sheth, A., Tejaswi, K., Mehta, P., Parekh, C., Bansal, R., Merchant, S., Singh, T., Desai, U. B., Thekkath, C. A., Toyama, K. (2005). Senslide: A sensor network based landslide prediction system. In Proceedings of the 3rd International Conference on Embedded Networked Sensor Systems, San Diego, CA, USA, 2–4 November 2005, 280–281.

Shrestha, R. L., Carter, W. E., Lee, M., Finer, P., Sartori, M. (1999). Airborne laser swath mapping: Accuracy assessment for surveying and mapping applications. J. Am. Congr. Surv. Mapp., 59: 83–94.

Singhroy, V., Mattar, K. E., Gray, A. L. (1998). Landslide characterisation in Canada using interferometric SAR and combined SAR and TM images. Advances in Space Research, 21(3): 465–476.

Spillmann, T., Maurer, H., Green, A. G., Heincke, B., Willenberg, H., Husen, S. (2007). Microseismic investigation of an unstable mountain slope in the Swiss Alps. Journal of Geophysical Research, 112(B7): B07301.

Squarzoni, C., Delacourt, C., Allemand, P. (2005). Differential single-frequency GPS monitoring of the La Valette landslide (French Alps). Engineering Geology, 79(3-4): 215–229.

Stark, T. D., Choi, H. (2008). Slope inclinometers for landslides. Landslides, 5(3): 339.

Sumner J. S. (1976). Principles of Induced Polarization for Geophysical Exploration. Elsevier Scientific Publishing Co., Amsterdam, 227.

Tan, G., Jarvis, S. A., Kermarrec, A. M. (2009). Connectivity-guaranteed and obstacle-adaptive deployment schemes for mobile sensor networks. IEEE Transactions on Mobile Computing, 8(6): 836–848.

TAOGLAS DXP.02.A SMD L1/L2/L5 SAW Diplexer For GNSS Band Applications https://www.taoglas.com/product/dxp-02-a/.

Tapete, D., Casagli, N., Luzi, G., Fanti, R., Gigli, G., Leva, D. (2013). Integrating radar and laser-based remote sensing techniques for monitoring structural deformation of archaeological monuments. Journal of Archaeological Science, 40(1): 176–189.

Teja, G. N. L. R., Harish, V. K. R., Khan, D. N. M., Krishna, R. B., Singh, R., Chaudhary, S. (2014). Land Slide detection and monitoring system using wireless sensor networks (WSN). In Proceedings of the 2014 IEEE International Advance Computing Conference (IACC), Gurgaon, New Delhi, India, 21–22 February, 149–154.

Teza, G., Galgaro, A., Zaltron, N., Genevois, R. (2007). Terrestrial laser scanner to detect landslide displacement fields: a new approach. International Journal of Remote Sensing, 28(16): 3425–3446.

Tofani, V., Raspini, F., Catani, F., Casagli, N. (2013). Persistent Scatterer Interferometry (PSI) technique for landslide characterization and monitoring. Remote Sensing, 5(3): 1045–1065.

Wang, G. (2013). Millimeter-accuracy GPS landslide monitoring using precise point positioning with single receiver phase ambiguity resolution: A case study in Puerto Rico. J. Géod. Sci., 3: 22–31.

Wang, X., Wang, Z., O'Dea, B. (2003). A TOA-based location algorithm reducing the errors due to non-line-of-sight (NLOS) propagation. IEEE Transactions on Vehicular Technology, 52(1): 112–116.

Wehr, A., Lohr, U. (1999). Airborne laser scanning - an introduction and overview. ISPRS J Photogramm Remote Sensing, 54: 68–82.

Weirich, F., Blesius, L. (2007). Comparison of satellite and air photo based landslide susceptibility maps. Geomorphology, 87: 352–364.

Werner-Allen, G., Lorincz, K., Welsh, M., Marcillo, O., Johnson, J., Ruiz, M., Lees, J. (2006). Deploying a wireless sensor network on an active volcano. IEEE Internet Computing, 10: 18–25.

Whiteley, J. S., Chambers, J. E., Uhlemann, S., Wilkinson, P. B., Kendall, J. M. (2019). Geophysical Monitoring of Moisture-Induced Landslides: A Review. Reviews of Geophysics.

Wi-GIM Project Official Web Site. Available online: http://www.life-wigim.eu/ (accessed on 31 August 2018).

Win, M. Z., Dardari, D., Molisch, A. F., Wiesbeck, W., Zhang, J. (2009). History and Applications of UWB. Proc. IEEE, 97: 198–204.

Win, M. Z., Scholtz, R. A. (1998). Impulse radio: How it works. IEEE Commun. Lett., 2: 36–38.

Xiong, L., Wang, G., Bao, Y., Zhou, X., Sun, X., Zhao, R. (2018). Detectability of Repeated Airborne Laser Scanning for Mountain Landslide Monitoring. Geosciences, 8(12): 469.

Yavari, M., Nickerson, B. G. (2014). Ultra wideband wireless positioning systems. Dept. Faculty Comput. Sci., Univ. New Brunswick, Fredericton, NB, Canada, Tech. Rep. TR14–2*30*.

Yick, J., Mukherjee, B., Ghosal, D. (2008). Wireless sensor network survey. Computer networks, 52(12): 2292–2330.

Zanella, A., Zorzi, M. (2006). Reti di sensori: dalla teoria alla pratica. SIGNET (Special Interest Group on NETworking) presso il Dipartimento di Ingegneria dell'Informazione dell'Università di Padova.

Zhang, G., Van Oosterom, P., Verbree, E. (2017). Point Cloud Based Visibility Analysis: first experimental results. In Societal Geo-Innovation: short papers, posters and poster abstracts of the 20th AGILE Conference on Geographic Information Science.

Zou, Y., Chakrabarty, K. (2003). Sensor deployment and target localization based on virtual forces. In INFOCOM 2003. Twenty-Second Annual Joint Conference of the IEEE Computer and Communications. IEEE Societies, 2: 1293–1303.

Full publication list

Articles on international journals

Gracchi, T., Gigli, G., Noël, F., Jaboyedoff, M., Madiai, C., Casagli, N. (2019). Optimising Wireless Sensor Network installations by Visibility Analysis on 3D Point Clouds. ISPRS International Journal of Geo-Information, 8 (10), 460.

Feng, L., Pazzi, V., Intrieri, E., **Gracchi, T.**, Gigli, G. (2019). Seismic features analysis of rockfalls based on in situ tests: frequency, amplitude, and duration. Journal of Mountain Science, 16(5), 955–970.

Intrieri E., Gigli G., **Gracchi T.**, Nocentini M., Lombardi L., Mugnai F., Frodella W., Bertolini G., Carnevale E., Favalli M., Fornaciai A., Marturià Alavedra J., Mucchi L., Nannipieri L., RodriguezLloveras X., Pizziolo M., Schina R., Trippi F., Casagli N. (2018). Application of an ultrawide band sensorfree wireless network for ground monitoring. Engineering Geology, 238, 1–14.

Mucchi, L., Jayousi, S., Martinelli, A., Caputo, S., Intrieri, E., Gigli, G., **Gracchi, T.**, Mugnai, F., Favalli, M., Fornaciai, A., Nannipieri, L. (2018). A Flexible Wireless Sensor Network Based on UltraWide Band Technology for Ground Instability Monitoring. Sensors, 18(9), 2948.

Pazzi, V., Ceccatelli, M., **Gracchi, T.**, Masi, E. B., Fanti, R. (2018). Assessing subsoil void hazards along a road system using H/V measurements, ERTs and IPTs to support local decision makers. Near Surface Geophysics, 16(3), 282–297.

Gracchi, T., Lotti, A., Saccorotti, G., Lombardi, L.., Nocentini, M., Mugnai, F., Gigli, G., Barla, M., Giorgetti, A., Antolini, F., Fiaschi, A., Matassoni, L.., Casagli, N. (2017). A method for locating rockfall impacts using signals recorded by a microseismic network. Geoenvironmental Disasters, 4(1), 26.

Proceedings and abstracts

Gracchi, T., Gigli, G., Noël, F., Jaboyedoff, M., Casagli, N. (2019). Automatic positioning of a Wireless Sensor Network by visibility analysis on 3D point cloud. XI Convegno Nazionale dei Giovani Ricercatori in Geologia Applicata AIGAA, Matera 19–22 Settembre 2019.

Feng, L., Pazzi, P., Intrieri, E., **Gracchi, T.**, Gigli, G. (2019). An algorithm for rockfall events automatic detection and classification is seismic monitoring. In EGU General Assembly Conference Abstracts (Vol. 21, p. 9097).

Noël, F., Wyser, E., Jaboyedoff, M., Hibert, C., Talib, M., Malet, J.P., Toussaint, R., Desrues, M., Bourrier, F., Toe, D., Brenguier, O., **Gracchi, T.**, Derron, M.H., Cloutier, C., Locat, J. (2019). Realsize rockfall experiment: Applying observed impact dynamics to 3D rockfall simulations on highly detailed terrain models. In EGU General Assembly Conference Abstracts (Vol. 21, p. 16778).

Gracchi, T., Gigli, G., Intrieri E., Nocentini M., Lombardi L., Mugnai F., Frodella W., Bertolini G., Carnevale E., Favalli M., Fornaciai A., Marturià Alavedra J., Mucchi L., Nannipieri L., RodriguezLloveras X., Pizziolo M., Schina R., Trippi F., Casagli N. (2018). Using a new UltraWide Band wireless sensor network for realtime landslide monitoring. 6° Convegno Nazionele AIGA 2729 Giugno 2018, Courmayeur.

Gracchi, T., Noël, F., Derron, M. H., Jaboyedoff, M. (2018). Finding the best locations of monitoring devices based on visibility analysis with 3D point clouds. In EGU General Assembly Conference Abstracts (Vol. 20, p. 7445).

Morelli, S., Pazzi, V., Bandecchi, A. E., Valori, L., Gambacciani, L., Ceccatelli, M., **Gracchi, T.**, Marini, F., Masi, E.B., Pastonchi, L., Lotti, A., Fontanelli, K, Casagli, N. (2018). A multidimensional and interdisciplinary strategy for geohydrological risk reduction oriented towards minors. In EGU General Assembly Conference Abstracts (Vol. 20, p. 15669).

Nannipieri, L., Fornaciai, A., Favalli, M., Intrieri, E., Gigli, G., **Gracchi, T.**, Nocentini M., Lombardi L., Mugnai F., Frodella W., Bertolini G., Carnevale E., Marturià Alavedra J., Mucchi L., RodriguezLloveras X., Pizziolo M., Schina R., Trippi F., Casagli, N. (2018). Realtime landslide monitoring with a wireless sensor network based on ultrawide band technology: applications and perspectives. Abstract NH21B0809 presented at 2018 Fall Meeting, AGU, Washington, D.C., 1014 Dec. http://abstractsearch.agu.org/meetings/2018/FM/NH21B0809.html

Gracchi, T., Gigli, G., Intrieri, E., Mucchi, L.., Casagli, N. (2018). Experimental study of a new wireless sensor network for landslide monitoring. Journées Biennales des Géosciences et de l'Environnement, Université de Lausanne. Poster Session, February 15th.

Appendix A: WiSIO MATLAB tool

```
% A file named 'Points_coordinates.txt' with the obtained configuration
coordinates is saved
% File named 'visiblearray' contains points visible from the ith point
clearvars;

%INPUT DATA
load PtCloud_VEG.txt;                                %Point cloud_Vegetation
Clean_V=PtCloud_VEG;
p_V=[Clean_V(:,1),Clean_V(:,2),Clean_V(:,3)];
load PtCloud_TERR.txt;                               %Point cloud_Terrain
Clean_T=PtCloud_TERR;
p_T=[Clean_T(:,1),Clean_T(:,2),Clean_T(:,3)];
p=[p_T;p_V];                                         %Point cloud_all
load PAs_cubi.txt;                                   %Priority Areas
Dangerous_Areas=PAs_cubi;
DangerousAreas=[Dangerous_Areas(:,1),Dangerous_Areas(:,2),Dangerous_Areas(:
,3)];

tic
Pole_h=1.5;                          %Pole's height
Nodes=11;                            %Number of nodes
FontSize=18;                         %Point label
max_distanza=90;                     %ROI extension
ROI_C_Extension=5;                   %ROI for Point1
iteration_for1=5;                    %Iteration for Point1
Sector=5;                            %Number of sectors
param_all=[1.6,2.3,2.9,3.3,3.5];     %Radius
values_PA=5;                         %m
%%%%%%%%%%%%%%%%%%%%%%%%%%%%%%%%%%%%%%%%%%%%%%%%%%%%%%%%%%%%%%%%%%%%%%%%

%FIGURE
figure;
grey=[0.5 0.5 0.5];
plot3(p_T(:,1),p_T(:,2),p_T(:,3),'.','Color',grey);
%plot3(p_V(:,1),p_V(:,2),p_V(:,3),'.','Color','g');
hold on
grid on
xlabel('MN95 Longitude [m]');
ylabel('MN95 Latitude [m]');
zlabel('Altitude [m]');
sz=6;
scatter3(DangerousAreas(:,1),DangerousAreas(:,2),DangerousAreas(:,3),sz,'Ma
rkerFaceColor','r','MarkerEdgeColor','r','MarkerFaceAlpha',.2,'MarkerEdgeAl
pha',.2);

%SELECTION OF THE FIRST POINT OF VIEW, C
%by pointer
datacursormode on
dcm_obj=datacursormode;
set(dcm_obj,'DisplayStyle','window','SnapToDataVertex','off','Enable','on')
pause
c_info=getCursorInfo(dcm_obj);
C=[c_info.Position(1,1),c_info.Position(1,2),c_info.Position(1,3)];
%by coordinates
% C=[-600.77343750 -425.23242188 199.84852600];
plot3(C(1,1),C(1,2),C(1,3),'*','Color','r');
```

```
%Preallocating
COLPLUS=zeros(1,3);
Point_all={zeros(size(p,1),3)};
Point_all_dist={zeros(size(p,1),3)};
Point={zeros(1,3)};
roi={zeros(1,6)};
indices={zeros(size(p,1),1)};
p_roi={zeros(size(p,1),3)};
Inters_weight={zeros(size(DangerousAreas,1),3)};
Point1_ntime={zeros(1,3)};
visiblearray_ntime={zeros(size(p,1),3)};
length_visarray={zeros(1,1)};
sector={zeros(1,6)};
index={zeros(size(p,1),1)};
p_sector={zeros(size(p,1),3)};
p_sec={zeros(size(p,1),3)};
visiblearray_sect_diff={zeros(size(p,1),3)};
indicess={zeros(size(p,1),1)};
visiblearray_sect_all={zeros(size(p,1),3)};
visiblearray={zeros(size(p_T,1),3)};
visiblearray_sect={zeros(size(p_T,1),3)};

for i=1:Nodes
    disp(num2str(i));
    %COLORS
    COL=rand(1,3);
    plus=[0.2500 0.2500 0.2500];
    for j=1:length(COL)
       if COL(1,j)+plus(1,j)>1
          COLPLUS(1,j)=1;
         else
          COLPLUS(1,j)=COL(1,j)+plus(1,j);
       end
    end
             if i==1
                if iteration_for1==0
                    Point{i}=[C(1,1) C(1,2) C(1,3)+Pole_h];
                    roi{i}=[Point{i}(1,1)-
max_distanza,Point{i}(1,1)+max_distanza,Point{i}(1,2)-
max_distanza,Point{i}(1,2)+max_distanza,Point{i}(1,3)-
max_distanza,Point{i}(1,3)+max_distanza];
                    indicess{i}=findPointsInROI(ptCloud,roi{i});
                    p_roi{i}=select(ptCloud,indicess{i});
                    p=p_roi{i}.Location;
                    ptCloud=pointCloud(p);
                    [indices,dist]=findNearestNeighbors(ptCloud,C,K);
                    FurthestPoint=ptCloud.Location(indices(K),:);
                    Radius=dist(K);
                    Radius_roi=Radius/Sector;
                    for n=1:Sector
                    XROI=Radius_roi*n;
                    sector{n}=[Point{i}(1,1)-
XROI,Point{i}(1,1)+XROI,Point{i}(1,2)-
XROI,Point{i}(1,2)+XROI,Point{i}(1,3)-XROI,Point{i}(1,3)+XROI];
                    index{n}=findPointsInROI(ptCloud,sector{n});
                    p_sector{n}=select(ptCloud,index{n});
                    p_sec{n}=p_sector{n}.Location;
                    % KATZ_2007
                    p=p_sec{n};
                    param=param_all(1,n);
```

```
                    dim=size(p,2);
                    numPts=size(p,1);
                    pnew=p-repmat(Point{i},[numPts 1]);
                    normp=sqrt(dot(pnew,pnew,2));
                    R=repmat(max(normp)*(10^param),[numPts 1]);
                    P=pnew+2*repmat(R-normp,[1 dim]).*pnew./repmat(normp,[1
dim]);
                    a=convhulln(P);
                    visiblePtInds=unique(a);
                    I=visiblePtInds;
                    visiblearray_sect_all{n}=[p(I,1) p(I,2) p(I,3)];
visiblearray_sect{n}=intersect(visiblearray_sect_all{n},p_T,'rows');
                    if n==1
                       visiblearray_sect_diff{n}=visiblearray_sect{n};
                       else
                        visiblearray_sect_diff{n}=setdiff(visiblearray_sect
                  {n},p_sec{n-1},'rows');
                    end
                    visiblearray{i}=vertcat(visiblearray_sect_diff{:});
                    end
                else
                %Selection of the small ROI for Point1
                roi_C=[C(1,1)-
ROI_C_Extension,C(1,1)+ROI_C_Extension,C(1,2)-
ROI_C_Extension,C(1,2)+ROI_C_Extension,C(1,3)-
ROI_C_Extension,C(1,3)+ROI_C_Extension];
                ptCloud=pointCloud(p);
                indici=findPointsInROI(ptCloud,roi_C);
                punti_roi_C=select(ptCloud,indici);
                punti_inroi_C=punti_roi_C.Location(:,:);
                   for Num_iterationFor1=1:iteration_for1
                           Point{1}=datasample(punti_inroi_C,1,1);
Point{1}=[Point{1}(1,1),Point{1}(1,2),Point{1}(1,3)+Pole_h];
                           roi{i}=[Point{i}(1,1)-
max_distanza,Point{i}(1,1)+max_distanza,Point{i}(1,2)-
max_distanza,Point{i}(1,2)+max_distanza,Point{i}(1,3)-
max_distanza,Point{i}(1,3)+max_distanza];
                           indicess{i}=findPointsInROI(ptCloud,roi{i});
                           p_roi{i}=select(ptCloud,indicess{i});
                           p=p_roi{i}.Location;
                           ptCloud=pointCloud(p);
                           K=size(p,1);
                          [indices,dist]=findNearestNeighbors(ptCloud,C,K);
                           FurthestPoint=ptCloud.Location(indices(K),:);
                           Radius=dist(K);
                           Radius_roi=Radius/Sector;
                               for n=1:Sector
                               XROI=Radius_roi*n;
                               sector{n}=[Point{i}(1,1)-
XROI,Point{i}(1,1)+XROI,Point{i}(1,2)-
XROI,Point{i}(1,2)+XROI,Point{i}(1,3)-XROI,Point{i}(1,3)+XROI];
                               index{n}=findPointsInROI(ptCloud,sector{n});
                               p_sector{n}=select(ptCloud,index{n});
                               p_sec{n}=p_sector{n}.Location;
                               % KATZ_2007
                               p=p_sec{n};
                               param=param_all(1,n);
                               dim=size(p,2);
                               numPts=size(p,1);
                               pnew=p-repmat(Point{i},[numPts 1]);
```

```
                                normp=sqrt(dot(pnew,pnew,2));
                                R=repmat(max(normp)*(10^param),[numPts 1]);
                                P=pnew+2*repmat(R-normp,[1
dim]).*pnew./repmat(normp,[1 dim]);
                                a=convhulln(P);
                                visiblePtInds=unique(a);
                                I=visiblePtInds;
                                visiblearray_sect_all{n}=[p(I,1) p(I,2)
p(I,3)];
                               visiblearray_sect{n}=intersect(visiblearray_
sect_all{n},p_T,'rows');
                                 if n==1
                            visiblearray_sect_diff{n}=visiblearray_sect{n};
                                 else
                           visiblearray_sect_diff{n}=setdiff(visiblearray
_sect{n},p_sec{n-1},'rows');
                                 end
                           visiblearray{i}=vertcat(visiblearray_sect_diff
{:});
                                 end
                         Point1_ntime{Num_iterationFor1}=Point{i};
                        visiblearray_ntime{Num_iterationFor1}=visiblearray{
i};
                        length_visarray{Num_iterationFor1}=size(visiblearra
y_ntime{Num_iterationFor1},1);
                     end
                      %Ordering in ascending order Num_iter in function of
                      %the visible points and choice of the first one
                   lenght_visarray_matr=vertcat(length_visarray{:});
                   [lenght_visarray_matr_ord,lenght_visarray_index]=sort(len
                   ght_visarray_matr,'descend');
                   visiblearray{i}=visiblearray_ntime{lenght_visarray_index(
:,:)};
                    Points1_ntime=vertcat(Point1_ntime{:});
                   Points_maxVisibility=Points1_ntime(lenght_visarray_index,
:);
                    Point{1}=Points_maxVisibility(1,:);
                   Point{1}=[Point{1}(1,1),Point{1}(1,2),Point{1}(1,3)+Pole_
h];
                end

                  plot3(Point{i}(1,1),Point{i}(1,2),Point{i}(1,3),'*','Mark
                  erSize',10,'Color',COL);

                  text(Point{i}(1,1),Point{i}(1,2),Point{i}(1,3),num2str(i)
                  ,'Color','k','FontSize',FontSize);
             elseif i==2
                        %DISTANCE EVALUATION
                        AbsDistance_xyz=abs(Point{1}-visiblearray{1});
                       AbsDistance_Single=abs(AbsDistance_xyz(:,1)-
                       AbsDistance_xyz(:,2)-
                       AbsDistance_xyz(:,3));[AbsDistance_Descend,AbsDista
                       nce_Descend_Index]=sort(AbsDistance_Single,'descend
                       ');

                       Visiblearray_maxDist=visiblearray{1}(AbsDistance_De
                       scend_Index,:);
            n__values=floor(size(Visiblearray_maxDist,1)/values_PA);
            Point_all_dist{2}=Visiblearray_maxDist(1:n__values,:);
```

```
%PRIORITY AREAS
      Inters_weight{2}=intersect(DangerousAreas,Point_all_dist{2},'rows');
                              if Inters_weight{2}~=0
                                 Point{2}=datasample(Inters_weight{2},1);
                                   else
                                  Point{2}=Point_all_dist{2}(1,:);
                                end
                            znew=Point{2}(1,3)+Pole_h;
                            Point{2}=[Point{2}(1,1),Point{2}(1,2),znew];

plot3(Point{i}(1,1),Point{i}(1,2),Point{i}(1,3),'*','MarkerSize',10,'Color'
,COL);

text(Point{i}(1,1),Point{i}(1,2),Point{i}(1,3),num2str(i),'Color','k','Font
Size',FontSize);
                            ptCloud=pointCloud(p);
                            roi{i}=[Point{i}(1,1)-
max_distanza,Point{i}(1,1)+max_distanza,Point{i}(1,2)-
max_distanza,Point{i}(1,2)+max_distanza,Point{i}(1,3)-
max_distanza,Point{i}(1,3)+max_distanza];
                            indicess{i}=findPointsInROI(ptCloud,roi{i});
                            p_roi{i}=select(ptCloud,indicess{i});
                            p=p_roi{i}.Location;
                            ptCloud=pointCloud(p);
                            K=size(p,1);

[indices,dist]=findNearestNeighbors(ptCloud,Point{i},K);
                            FurthestPoint=ptCloud.Location(indices(K),:);
                            Radius=dist(K);
                            Radius_roi=Radius/Sector;
                               for n=1:Sector
                               XROI=Radius_roi*n;
                               sector{n}=[Point{i}(1,1)-
XROI,Point{i}(1,1)+XROI,Point{i}(1,2)-
XROI,Point{i}(1,2)+XROI,Point{i}(1,3)-XROI,Point{i}(1,3)+XROI];
                                index{n}=findPointsInROI(ptCloud,sector{n});
                                p_sector{n}=select(ptCloud,index{n});
                                p_sec{n}=p_sector{n}.Location;
                                % KATZ_2007
                                p=p_sec{n};
                                param=param_all(1,n);
                                dim=size(p,2);
                                numPts=size(p,1);
                                pnew=p-repmat(Point{i},[numPts 1]);
                                normp=sqrt(dot(pnew,pnew,2));
                                R=repmat(max(normp)*(10^param),[numPts 1]);
                                P=pnew+2*repmat(R-normp,[1
dim]).*pnew./repmat(normp,[1 dim]);
                                a=convhulln(P);
                                visiblePtInds=unique(a);
                                I=visiblePtInds;
                                visiblearray_sect_all{n}=[p(I,1) p(I,2) p(I,3)];

                                  visiblearray_sect{n}=intersect(visiblearray_se
                                  ct_all{n},p_T,'rows');
                                 if n==1
                                 visiblearray_sect_diff{n}=visiblearray_sect{n};
                                   else
                                         visiblearray_sect_diff{n}=setdiff(visibl
                                  earray_sect{n},p_sec{n-1},'rows');
```

```
                            end
                              visiblearray{i}=vertcat(visiblearray_sect_diff
                        {:});
                            end

               else        %FROM POINT 3
                           Point_all{2}=visiblearray{1};
                           Point_all{i}=intersect(Point_all{i-
1},visiblearray{i-1},'rows');
                           Distance={zeros(size(Point_all{i},1),1)};
                             for jj=1:(i-1)
                                  for jjj=1:size(Point_all{i},1)
                                  Distance{jj}(jjj,1)=sqrt((Point{jj}(1,1)-
Point_all{i}(jjj,1)).^2+((Point{jj}(1,2)-
Point_all{i}(jjj,2)).^2+((Point{jj}(1,3)-Point_all{i}(jjj,3)).^2)));
                                  end
                             end
                           Distance_all=horzcat(Distance{:});
                           ProdOfDistanceAll=prod(Distance_all,2);

[Prod_Desc,Prod_Desc_Index]=sort(ProdOfDistanceAll,'descend');

Distance_all_Weight=[Distance_all(Prod_Desc_Index,:),ProdOfDistanceAll(Prod
_Desc_Index,:)];

Point_all_Dist_Sort=Point_all{i}(Prod_Desc_Index,:);
                                  if size(Point_all_Dist_Sort,1)>5000

nvalues=floor(size(Point_all_Dist_Sort,1)/values_PA);
                                  elseif size(Point_all_Dist_Sort,1)==1
                                      nvalues=1;
                                  else

nvalues=floor(size(Point_all_Dist_Sort,1)/4);
                                  end
Point_all_dist{i}=Point_all_Dist_Sort(1:nvalues,:);

Inters_weight{i}=intersect(DangerousAreas,Point_all_dist{i},'rows');
                             if  size(Inters_weight{i},1)>1
                                 Point{i}=datasample(Inters_weight{i},1,1);
                             else
                                  Point{i}=Point_all_dist{i}(1,:);
                             end
                           znew=Point{i}(1,3)+Pole_h;
                           Point{i}=[Point{i}(1,1),Point{i}(1,2),znew];
plot3(Point{i}(1,1),Point{i}(1,2),Point{i}(1,3),'*','MarkerSize',10,'Color'
,COL);

text(Point{i}(1,1),Point{i}(1,2),Point{i}(1,3),num2str(i),'Color','k','Font
Size',FontSize);
                           ptCloud=pointCloud(p);
                           roi{i}=[Point{i}(1,1)-
max_distanza,Point{i}(1,1)+max_distanza,Point{i}(1,2)-
max_distanza,Point{i}(1,2)+max_distanza,Point{i}(1,3)-
max_distanza,Point{i}(1,3)+max_distanza];
                           indicess{i}=findPointsInROI(ptCloud,roi{i});
                           p_roi{i}=select(ptCloud,indicess{i});
                           p=p_roi{i}.Location;
                           ptCloud=pointCloud(p);
                           K=size(p,1);
```

```
[indices,dist]=findNearestNeighbors(ptCloud,Point{i},K);
                          FurthestPoint=ptCloud.Location(indices(K),:);
                          Radius=dist(K);
                          Radius_roi=Radius/Sector;
                            for n=1:Sector
                            XROI=Radius_roi*n;
                            sector{n}=[Point{i}(1,1)-
XROI,Point{i}(1,1)+XROI,Point{i}(1,2)-
XROI,Point{i}(1,2)+XROI,Point{i}(1,3)-XROI,Point{i}(1,3)+XROI];
                            index{n}=findPointsInROI(ptCloud,sector{n});
                            p_sector{n}=select(ptCloud,index{n});
                            p_sec{n}=p_sector{n}.Location;
                            % KATZ_2007
                            p=p_sec{n};
                            param=param_all(1,n);
                            dim=size(p,2);
                            numPts=size(p,1);
                            pnew=p-repmat(Point{i},[numPts 1]);
                            normp=sqrt(dot(pnew,pnew,2));
                            R=repmat(max(normp)*(10^param),[numPts 1]);
                            P=pnew+2*repmat(R-normp,[1
dim]).*pnew./repmat(normp,[1 dim]);
                            a=convhulln(P);
                            visiblePtInds=unique(a);
                            I=visiblePtInds;
                            visiblearray_sect_all{n}=[p(I,1) p(I,2) p(I,3)];

visiblearray_sect{n}=intersect(visiblearray_sect_all{n},p_T,'rows');
                             if n==1

visiblearray_sect_diff{n}=visiblearray_sect{n};
                               else

visiblearray_sect_diff{n}=setdiff(visiblearray_sect{n},p_sec{n-1},'rows');
                             end

visiblearray{i}=vertcat(visiblearray_sect_diff{:});
                            end
             end
plot3(visiblearray{i}(:,1),visiblearray{i}(:,2),visiblearray{i}(:,3),'o','C
olor',COLPLUS);
end

rotate3d on
Points_coordinates=vertcat(Point{:});
dlmwrite('Points_coordinates_9.txt',Points_coordinates,'precision',10);

time=toc/60;
disp([num2str(time),' minutes']);.
```